AD 744491

AFCRL-72-0258 013630-10-T

THE UNIVERSITY OF MICHIGAN

COLLEGE OF ENGINEERING
DEPARTMENT OF ELECTRICAL AND COMPUTER ENGINEERING
Radiation Laboratory

Scattering of Electromagnetic Waves by a Periodic Surface with Arbitrary Profile

By

TOMMY C-H. TONG and THOMAS B. A. SENIOR

April 1972

Scientific Report No. 13
Contract No. F19628-68-C-0071
Project No. 5635
Task No. 563502
Work Unit No. 56350201

DDC
RECEIVED
AUG 28 1972
D

Approved for public release; distribution unlimited.

Contract Monitor: JOHN K. SCHINDLER
MICROWAVE PHYSICS LABORATORY

Reproduced by
NATIONAL TECHNICAL
INFORMATION SERVICE
U S Department of Commerce
Springfield VA 22151

Prepared for:

Air Force Cambridge Research Laboratories
Air Force Systems Command
Laurence G. Hanscom Field
Bedford, Massachusetts 01730

Ann Arbor, Michigan 48105

R 230

ACCESSION for
NTIS White Section
DDC Buff Section
UNANNOUNCED
JUSTIFICATION .....
BY .....
DISTRIBUTION/AVAILABILITY CODES
Dist. AVAIL. and/or SPECIAL
A

Qualified requestors may obtain additional copies from the Defense Documentation Center. All others should apply to the National Technical Information Service.

UNCLASSIFIED

Security Classification

DOCUMENT CONTROL DATA - R & D

(Security classification of title, body of abstract and indexing annotation must be entered when the overall report is classified)

1. ORIGINATING ACTIVITY (Corporate author)

The University of Michigan Radiation Laboratory
2216 Space Research Bldg., North Campus
Ann Arbor, Michigan 48105

2a. REPORT SECURITY CLASSIFICATION

UNCLASSIFIED

2b. GROUP

---

3. REPORT TITLE

SCATTERING OF ELECTROMAGNETIC WAVES BY A PERIODIC SURFACE WITH ARBITRARY PROFILE

4. DESCRIPTIVE NOTES (Type of report and inclusive dates)

Scientific Interim

5. AUTHOR(S) (First name, middle initial, last name)

Tommy C-H. Tong
Thomas B.A. Senior

6. REPORT DATE

April 1972

7a. TOTAL NO. OF PAGES

214

7b. NO. OF REFS

64

8a. CONTRACT OR GRANT NO.

F19628-68-C-0071

b. ———

Project, Task, Work Unit Nos.

c. 5635-02-01

DoD Element 61102F

d. DoD Sublement 681305

9a. ORIGINATOR'S REPORT NUMBER(S)

013630-10-T
Scientific Report No. 13

9b. OTHER REPORT NO(S) (Any other numbers that may be assigned this report)

AFCRL-72-0258

10. DISTRIBUTION STATEMENT

A - Approved for public release; distribution unlimited.

11. SUPPLEMENTARY NOTES

TECH, OTHER

12. SPONSORING MILITARY ACTIVITY

Air Force Cambridge Research Laboratories (LZ)
L. G. Hanscom Field
Bedford, Massachusetts 01730

13. ABSTRACT

Numerical procedures are developed for the digital solution of the integral equations for the current induced on a perfectly conducting, two-dimensional periodic surface of arbitrary profile when a plane electromagnetic wave is incident. By using Floquet's theorem the range of integration is reduced to a single period, and special summation techniques consisting of a Poisson summation and the subtraction of the dc term are used to improve the convergence of the infinite series representation of the Green's function. The integral equations are then solved numerically using the moment method and an interpolation scheme.

Data are obtained for both the surface and far fields for a variety of sinusoidal, full-wave rectified, inverted full-wave rectified and triangular profiles for plane waves of either polarization at oblique as well as normal incidence, and the results are compared with the predictions of physical optics.

The numerical results are used to illustrate some interesting physical phenomena, notably the P-type and S-type Wood anomalies associated with the frequency and angular responses of diffraction gratings, and to develop a scheme to estimate back scattering from a sinusoidal surface at oblique incidence.

The knowledge gained in the study of scattering from periodic surfaces is then applied to the study of rough surfaces by treating the surface as a small scale roughness superimposed upon a periodic base (representing the large scale roughness). The small scale roughness is approximated by a random function with a Gaussian distribution.

DD FORM 1 NOV 65 1473

UNCLASSIFIED

Security Classification

UNCLASSIFIED

Security Classification

14. KEY WORDS	LINK A ROLE	LINK A WT	LINK B ROLE	LINK B WT	LINK C ROLE	LINK C WT
Periodic Surfaces						
Diffraction Gratings						
Surface Currents						
Diffraction Modes						
Wood Anomalies						
Rayleigh's Assumption						
Physical Optics						
Numerical Techniques						
Rough Surfaces						

UNCLASSIFIED

AFCRL-72-0258 013630-10-T

Scattering of Electromagnetic Waves by a Periodic Surface with Arbitrary Profile

by

Tommy C-H. Tong and Thomas B. A. Senior
The University of Michigan
Radiation Laboratory
2455 Hayward Street
Ann Arbor, Michigan 48105

Scientific Report No. 13

April 1972

Scientific Report No. 13
Contract F19628-68-C-0071
Project No. 5635
Task No. 563502
Work Unit No. 56350201

Approved for public release; distribution unlimited.

Contract Monitor: John K. Schindler
Microwave Physics Laboratory

Prepared For

Air Force Cambridge Research Laboratories
Air Force Systems Command
Laurence G. Hanscom Field
Bedford, Massachusetts 01730

DDC
RECEIVED
AUG 1972
D

TABLE OF CONTENTS

		Page
	LIST OF TABLES	v
	LIST OF ILLUSTRATIONS	vii
	LIST OF APPENDICES	xv
I.	INTRODUCTION	1
II.	FORMULATION OF THE INTEGRAL EQUATIONS FOR NUMERICAL SOLUTION	7
	2.1 Formulation	7
	2.1.1 E (or horizontal) Polarization	9
	2.1.2 H (or vertical) Polarization	10
	2.2 Reduction of Integral Equations for Periodic Surfaces	12
	2.2.1 E Polarization	12
	2.2.2 H Polarization	16
	2.3 Comments on the Green's Function of the Integral equations	19
	2.4 Numerical Procedures	20
	2.5 Convergence and Accuracy of the Numerical Solutions	24
	2.6 Computational Time	26
III.	SURFACE FIELD FOR E POLARIZATION	28
	3.1 Surfaces of Small Period ($d/\lambda \leqslant 0.2$)	30
	3.2 Surfaces of Slightly Larger Period ($0.2 \leqslant d/\lambda \leqslant 0.6$)	46
	3.3 Surfaces of Large Period ($d/\lambda \geqslant 0.6$)	46
	3.4 Coupling Among Cells	70
	3.5 Accuracy Checks and Computational Time	70
IV.	SCATTERED FIELD FOR E POLARIZATION	82
	4.1 Diffracted Mode Amplitudes	82
	4.2 Diffracted Energy and Wood Anomalies	86
	4.2.1 Discussion	86
	4.2.2 Computed Data for the Diffracted Energy	88
	4.3 Conservation of Energy	96
	4.4 Approximate Techniques	100
V.	SURFACE FIELD FOR H POLARIZATION	107
	5.1 Surfaces of Small Period ($d/\lambda \leqslant 0.2$)	107
	5.2 Surfaces of Slightly Larger Period ($0.2 \leqslant d/\lambda \leqslant 0.6$)	123
	5.3 Surfaces of Large Period ($d/\lambda \geqslant 0.6$)	128
	5.4 Coupling Among Cells	146
	5.5 Accuracy Checks and Computational Time.	146

TABLE OF CONTENTS (Cont'd)

		Page
VI.	Scattered Field for H Polarization	156
	6.1 Diffracted Mode Amplitude	156
	6.2 Diffracted Energy and Wood Anomalies	158
	6.2.1 Discussion	158
	6.2.2 Computed Data for the Diffracted Energy	159
	6.2.3 Blazed Gratings	167
	6.3 Conservation of Energy	167
	6.4 Approximate Techniques	168
VII.	RAYLEIGH'S METHOD	171
	7.1 History	171
	7.2 Numerical Results by the Exact and Rayleigh's Method	173
VIII.	APPLICATION TO ROUGH SURFACE SCATTERING	182
	8.1 Discussion	182
	8.2 Perturbation of the Surface Current	183
IX.	CONCLUSION	198
	REFERENCES	200

LIST OF TABLES

Table		Page
3-1	Computational Time for E Polarization.	81
4-1	Amplitudes of Diffracted Waves for a Sinusoidal Surface ($d = 0.2\lambda$, $a = 0.1\lambda$)	84
4-2	Amplitudes of Diffracted Waves for a Sinusoidal Surface ($d = 1.9\lambda$, $a = 0.25\lambda$, $\theta = 0$).	85
4-3	Amplitudes of Diffracted Waves for a Sinusoidal Surface ($d = 0.4\lambda$, $a = 0.2\lambda$).	85
4-4	Amplitudes of Diffracted Waves for a Sinusoidal Surface ($d = 0.2\lambda$, $a = 0.03\lambda$, $\theta = 0$).	85
4-5	Conservation of Energy for a Sinusoidal Surface.	86
4-6	Comparison of the Energy Backscattered by a Sinusoidal Surface: $d = 1.155\lambda$, $\theta = 60^{\circ}$, Computed Using the Exact and Stationary Phase Methods.	101
4-7	Comparison of Normalized Current Modulus over the Illuminated Region for the Sinusoidal Surface with $d = 1.155\lambda$ and $\theta = 60^{\circ}$.	106
5-1	Computational Time for H Polarization.	155
6-1	Amplitudes of Diffracted Waves for a Sinusoidal Surface ($d = 0.2\lambda$, $a = 0.1\lambda$).	157
6-2	Amplitudes of Diffracted Waves for a Sinusoidal Surface ($d = 1.90\lambda$, $a = 0.25\lambda$, $\theta = 0$).	157
6-3	Amplitudes of Diffracted Waves for a Sinusoidal Surface ($d = 0.4\lambda$, $a = 0.2\lambda$).	157
6-4	Amplitudes of Diffracted Waves for a Sinusoidal Surface ($d = 0.2\lambda$, $a = 0.03\lambda$, $\theta = 0$).	158
6-5	Conservation of Energy for a Sinusoidal Surface.	168
6-6	Comparison of the Energy Backscattered by a Sinusoidal Surface: $d = 1.155\lambda$ and $\theta = 60^{\circ}$, Computed Using the Exact and Stationary Phase Methods.	169
6-7	Comparison of the Current Modulus over the Illuminated Region of a Sinusoidal Surface: $d = 1.155\lambda$, $\theta = 60^{\circ}$, Computed using the Exact Method and the Imaginary Part of the Physical Optics Approximation.	170

LIST OF TABLES (Cont'd)

		Page
7-1	E Polarization - Comparison of Scattered Fields at the Surface Trough Obtained by the Exact and Rayleigh Methods.	177
7-2	H Polarization - Comparison of Scattered Fields at the Surface Trough Obtained by the Exact and Rayleigh Methods.	180

LIST OF ILLUSTRATIONS

Figure		Page
2-1	Geometry for the Application of Green's Theorem.	8
2-2	Illustration of the Interpolation Procedure.	8
3-1	Profiles of Periodic Surfaces: (a) Sinusoidal, (b) Inverted Full-wave Rectified, (c) Full-wave Rectified, and (d) Triangular.	29
3-2	Normalized Surface Field for a Sinusoidal Surface ($d = 0.2\lambda$, $a = 0.1\lambda$ and $\theta = 0$) for E polarization.	31
3-3	Normalized Surface Field for a Sinusoidal Surface ($d = 0.2\lambda$, $a = 0.1\lambda$ and $\theta = 30^{o}$) for E polarization.	32
3-4	Normalized Surface Field for a Sinusoidal Surface ($d = 0.2\lambda$, $a = 0.1\lambda$ and $\theta = 60^{o}$) for E polarization.	33
3-5	Normalized Surface Field for an Inverted Full-wave Rectified Surface ($d = 0.2\lambda$, $a = 0.1\lambda$ and $\theta = 0$) for E polarization.	34
3-6	Normalized Surface Field for an Inverted Full-wave Rectified Surface ($d = 0.2\lambda$, $a = 0.1\lambda$ and $\theta = 30^{o}$) for E polarization.	35
3-7	Normalized Surface Field for an Inverted Full-wave Rectified Surface ($d = 0.2\lambda$, $a = 0.1\lambda$ and $\theta = 60^{o}$) for E polarization.	36
3-8	Normalized Surface field for a Full-wave Rectified Surface ($d = 0.2\lambda$, $a = 0.1\lambda$ and $\theta = 0$) for E polarization.	37
3-9	Normalized Surface Field for a Full-wave Rectified Surface ($d = 0.2\lambda$, $a = 0.1\lambda$ and $\theta = 30^{o}$) for E polarization.	38
3-10	Normalized Surface Field for a Full-wave Rectified Surface ($d = 0.2\lambda$, $a = 0.1\lambda$ and $\theta = 60^{o}$) for E polarization.	39
3-11	Normalized Surface Field for a Triangular Surface ($d = 0.2\lambda$, $a = 0.1\lambda$, $\ell = 0.1\lambda$, and $\theta = 0$) for E polarization.	40

LIST OF ILLUSTRATIONS

Figure		Page
3-12	Normalized Surface Field for a Triangular Surface ($d = 0.2\lambda$, $a = 0.1\lambda$, $\ell = 0.1\lambda$, and $\theta = 30^{\circ}$) for E polarization.	41
3-13	Normalized Surface Field for a Triangular Surface ($d = 0.2\lambda$, $a = 0.1\lambda$, $\ell = 0.1\lambda$, and $\theta = 60^{\circ}$) for E polarization.	42
3-14	Normalized Surface Field for a Sinusoidal Surface ($d = 0.2\lambda$, $a = 0.03\lambda$ and $\theta = 0$) for E polarization.	47
3-15	Normalized Surface Field for a Sinusoidal Surface ($d = 0.2\lambda$, $a = 0.01\lambda$ and $\theta = 0$) for E polarization.	48
3-16	Normalized Surface Field for a Sinusoidal Surface ($d = 0.4\lambda$, $a = 0.2\lambda$ and $\theta = 0$) for E polarization.	49
3-17	Normalized Surface Field for a Sinusoidal Surface ($d = 0.4\lambda$, $a = 0.2\lambda$ and $\theta = 60^{\circ}$) for E polarization.	50
3-18	Normalized Surface Field for an Inverted Full-wave Rectified Surface ($d = 0.6\lambda$, $a = 0.3\lambda$ and $\theta = 60^{\circ}$) for E polarization.	51
3-19	Normalized Surface Field for a Full-wave Rectified Surface ($d = 0.6\lambda$, $a = 0.3\lambda$ and $\theta = 60^{\circ}$) for E polarization.	52
3-20	Normalized Surface Field for a Sinusoidal Surface ($d = 0.95\lambda$, $a = 0.25\lambda$ and $\theta = 0$) for E polarization.	53
3-21	Normalized Surface Field for a Sinusoidal Surface ($d = 1.90\lambda$, $a = 0.25\lambda$ and $\theta = 0$) for E polarization.	54
3-22	Normalized Surface Field for a Sinusoidal Surface ($d = 1.6\lambda$, $a = 0.1\lambda$ and $\theta = 45^{\circ}$) for E polarization.	56
3-23	Normalized Surface Field for a Sinusoidal Surface ($d = 1.155\lambda$, $a = 0.05\lambda$ and $\theta = 60^{\circ}$) for E polarization.	58
3-24	Normalized Surface Field for a Sinusoidal Surface ($d = 1.155\lambda$, $a = 0.1\lambda$ and $\theta = 60^{\circ}$) for E polarization.	59
3-25	Normalized Surface Field for a Sinusoidal Surface ($d = 1.155\lambda$, $a = 0.2\lambda$ and $\theta = 60^{\circ}$) for E polarization.	60
3-26	Normalized Surface Field for a Sinusoidal Surface ($d = 1.155\lambda$, $a = 0.3\lambda$ and $\theta = 60^{\circ}$) for E polarization.	61

LIST OF ILLUSTRATIONS

Figure		Page
3-27	Normalized Surface Field for a Sinusoidal Surface ($d = 1.155\lambda$, $a = 0.4\lambda$ and $\theta = 60^\circ$) for E polarization.	62
3-28	Normalized Surface Field for a Sinusoidal Surface ($d = 1.155\lambda$, $a = 0.5\lambda$ and $\theta = 60^\circ$) for E polarization.	63
3-29	Normalized Surface Field for a Sinusoidal Surface ($d = 1.155\lambda$, $a = 0.6\lambda$ and $\theta = 60^\circ$) for E polarization.	64
3-30	Normalized Surface Field for a Sinusoidal Surface ($d = 1.155\lambda$, $a = 0.7\lambda$ and $\theta = 60^\circ$) for E polarization.	65
3-31	Normalized Surface Field for a Half-wave Rectified Surface ($d = 1.155\lambda$, $a = 0.5\lambda$ and $\theta = 60^\circ$) for E polarization.	66
3-32	Normalized Surface Field for a Full-wave Rectified Surface ($d = 0.75\lambda$, $a = 0.6\lambda$ and $\theta = 41.8^\circ$) for E polarization.	67
3-33	Normalized Surface Field for a Triangular Profile ($d = 1.75\lambda$, $\theta_1 = 20^\circ$, $\theta_2 = 66^\circ$ and $\theta = 12.2^\circ$) for E polarization.	68
3-34	Normalized Surface Field for an Inverted Full-wave Rectified Surface ($d = 0.95\lambda$, $a = 0.25\lambda$ and $\theta = 0$) for E polarization.	69
3-35	Normalized Surface Field for a Modified Full-wave Rectified Surface ($d = 0.3\lambda$, $a = 0.3\lambda$, $\theta = 60^\circ$ and $\ell = 0.3\lambda$) for E polarization.	71
3-36	Normalized Surface Field for a Modified Full-wave Rectified Surface ($d = 0.3\lambda$, $a = 0.3\lambda$, $\theta = 60^\circ$ and $\ell = 0.4\lambda$) for E polarization.	72
3-37	Normalized Surface Field for a Modified Full-wave Rectified Surface ($d = 0.3\lambda$, $a = 0.3\lambda$, $\theta = 60^\circ$ and $\ell = 0.5\lambda$) for E polarization.	73
3-38	Normalized Surface Field for a Modified Full-wave Rectified Surface ($d = 0.3\lambda$, $a = 0.3\lambda$, $\theta = 60^\circ$ and $\ell = 0.6\lambda$) for E polarization.	74

LIST OF ILLUSTRATIONS

Figure		Page
3-39	Normalized Surface Field for a Modified Full-wave Rectified Surface ($d = 0.7\lambda$, $a = 0.3\lambda$, $\theta = 60^{\circ}$ and $\ell = 0.7\lambda$) for E polarization.	75
3-40	Normalized Surface Field for a Sinusoidal Surface ($d = 0.2\lambda$, $a = 0.1\lambda$ and $\theta = 0$), Computed using 4, 10 and 12 Sampling Points, for E polarization.	77
3-41	Normalized Surface Field for a Sinusoidal Surface ($d = 0.2\lambda$, $a = 0.0005\lambda$ and $\theta = 0$) for E polarization.	78
3-42	Normalized Surface Field for a Sinusoidal Surface ($d = 1.9\lambda$, $a = 0.25\lambda$ and $\theta = 0$) for E polarization.	79
3-43	Surface Field for a Triangular Surface ($d = 1.75\lambda$, $\theta_1 = 20^{\circ}$, $\theta_2 = 66^{\circ}$ and $\theta = 12.2^{\circ}$) for E polarization.	80
4-1	Diffracted Energy for Two Radiating Modes for E polarization.	89
4-2	Diffracted Energy for a Modified Full-wave Rectified Surface ($a = 0.3\lambda$, $\theta = 60^{\circ}$ and $d = 0.3\lambda$.) for E polarization.	94
4-3	Diffracted Energy for a Sinusoidal Surface ($d = 1.155\lambda$, and $\theta = 60^{\circ}$) for E polarization.	95
4-4	Diffracted Energy for a Sinusoidal Surface ($d = 1.155\lambda$ and $\theta = 60^{\circ}$) for E polarization.	97
4-5	Diffracted Energy for a Sinusoidal Surface ($d = 1.155\lambda$ and $\theta = 60^{\circ}$), Computed Using the Modified Physical Optics Method (without shadow), for E polarization.	98
4-6	Diffracted Energy for a Sinusoidal Surface ($d = 1.155\lambda$ and $\theta = 60^{\circ}$) for E polarization.	99
4-7	Approximation of the Surface Current Modulus over the Illuminated Region of the Sinusoidal Surface by that on a Circular Cylinder.	102
4-8	Approximation of the Surface Current Modulus over the Illuminated Region of the Sinusoidal Surface by that on a Parabolic Cylinder.	104
5-1	Normalized Surface Field for a Sinusoidal Surface ($d = 0.2\lambda$, $a = 0.1\lambda$ and $\theta = 0$) for H polarization.	108

LIST OF ILLUSTRATIONS

Figure		Page
5-2	Normalized Surface Field for a Sinusoidal Surface ($d = 0.2\lambda$, $a = 0.1\lambda$ and $\theta = 30^{\circ}$) for H polarization.	109
5-3	Normalized Surface Field for a Sinusoidal Surface ($d = 0.2\lambda$, $a = 0.1\lambda$ and $\theta = 60^{\circ}$) for H polarization.	110
5-4	Normalized Surface Field for an Inverted Full-wave Rectified Surface ($d = 0.2\lambda$, $a = 0.1\lambda$ and $\theta = 0$) for H polarization.	112
5-5	Normalized Surface Field for an Inverted Full-wave Rectified Surface ($d = 0.2\lambda$, $a = 0.1\lambda$ and $\theta = 30^{\circ}$) for H polarization.	113
5-6	Normalized Surface Field for an Inverted Full-wave Rectified Surface ($d = 0.2\lambda$, $a = 0.1\lambda$ and $\theta = 60^{\circ}$) for H polarization.	114
5-7	Normalized Surface Field for a Full-wave Rectified Surface ($d = 0.2\lambda$, $a = 0.1\lambda$ and $\theta = 0$) for H polarization.	115
5-8	Normalized Surface Field for a Full-wave Rectified Surface ($d = 0.2\lambda$, $a = 0.1\lambda$ and $\theta = 30^{\circ}$) for H polarization.	116
5-9	Normalized Surface Field for a Full-wave Rectified Surface ($d = 0.2\lambda$, $a = 0.1\lambda$ and $\theta = 60^{\circ}$) for H polarization.	117
5-10	Normalized Surface Field for a Triangular Surface ($d = 0.2\lambda$, $a = 0.1\lambda$, $\ell = 0.1\lambda$ and $\theta = 0$) for H polarization.	118
5-11	Normalized Surface Field for a Triangular Surface ($d = 0.2\lambda$, $a = 0.1\lambda$, $\ell = 0.1\lambda$ and $\theta = 30^{\circ}$) for H polarization.	119
5-12	Normalized Surface Field for a Triangular Surface ($d = 0.2\lambda$, $a = 0.1\lambda$, $\ell = 0.1\lambda$ and $\theta = 60^{\circ}$) for H polarization.	120
5-13	Normalized Surface Field for a Sinusoidal Surface ($d = 0.2\lambda$, $a = 0.03\lambda$ and $\theta = 0$) for H polarization.	124

LIST OF ILLUSTRATIONS

Figure		Page
5-14	Normalized Surface Field for a Sinusoidal Surface ($d = 0.2\lambda$, $a = 0.01\lambda$ and $\theta = 0$) for H polarization.	125
5-15	Normalized Surface Field for a Sinusoidal Surface ($d = 0.4\lambda$, $a = 0.2\lambda$ and $\theta = 0$) for H polarization.	126
5-16	Normalized Surface Field for a Sinusoidal Surface ($d = 0.4\lambda$, $a = 0.2\lambda$ and $\theta = 60^{\circ}$) for H polarization.	127
5-17	Normalized Surface Field for a Full-wave Rectified Surface ($d = 0.6\lambda$, $a = 0.3\lambda$ and $\theta = 60^{\circ}$) for H polarization.	129
5-18	Normalized Surface Field for a Full-wave Rectified Surface ($d = 0.6\lambda$, $a = 0.3\lambda$ and $\theta = 75^{\circ}$) for H polarization.	130
5-19	Normalized Surface Field for a Sinusoidal Surface ($d = 0.95\lambda$, $a = 0.25\lambda$ and $\theta = 0$) for H polarization.	131
5-20	Normalized Surface Field for a Sinusoidal Surface ($d = 1.9\lambda$, $a = 0.25\lambda$ and $\theta = 0$) for H polarization.	132
5-21	Normalized Surface Field for a Sinusoidal Surface ($d = 1.6\lambda$, $a = 0.25\lambda$ and $\theta = 45^{\circ}$) for H polarization.	134
5-22	Normalized Surface Field for a Sinusoidal Surface ($d = 1.155\lambda$, $a = 0.05\lambda$ and $\theta = 60^{\circ}$) for H polarization.	135
5-23	Normalized Surface Field for a Sinusoidal Surface ($d = 1.155\lambda$, $a = 0.1\lambda$, and $\theta = 60^{\circ}$) for H polarization.	136
5-24	Normalized Surface Field for a Sinusoidal Surface ($d = 1.155\lambda$, $a = 0.2\lambda$ and $\theta = 60^{\circ}$) for H polarization.	137
5-25	Normalized Surface Field for a Sinusoidal Surface ($d = 1.155\lambda$, $a = 0.3\lambda$ and $\theta = 60^{\circ}$) for H polarization.	138
5-26	Normalized Surface Field for a Sinusoidal Surface ($d = 1.155\lambda$, $a = 0.4\lambda$ and $\theta = 60^{\circ}$) for H polarization.	139
5-27	Normalized Surface Field for a Sinusoidal Surface ($d = 1.155\lambda$, $a = 0.5\lambda$ and $\theta = 60^{\circ}$) for H polarization.	140
5-28	Normalized Surface Field for a Sinusoidal Surface ($d = 1.155\lambda$, $a = 0.6\lambda$ and $\theta = 60^{\circ}$) for H polarization.	141

LIST OF ILLUSTRATIONS

Figure		Page
5-29	Normalized Surface Field for a Sinusoidal Surface ($d = 1.155\lambda$, $a = 0.7\lambda$ and $\theta = 60^{\circ}$) for H polarization.	142
5-30	Normalized Surface Field for a Half-wave Rectified Surface ($d = 1.155\lambda$, $a = 0.5\lambda$ and $\theta = 60^{\circ}$) for H polarization.	143
5-31	Normalized Surface Field for a Full-wave Rectified Surface ($d = 0.85\lambda$, $a = 0.3\lambda$ and $\theta = 36^{\circ}$) for H polarization.	144
5-32	Normalized Surface Field for a Triangular Surface ($d = 1.75\lambda$, $\theta_1 = 20^{\circ}$, $\theta_2 = 66^{\circ}$ and $\theta = 12.2^{\circ}$) for H polarization.	145
5-33	Normalized Surface Field for a Modified Full-wave Rectified Surface ($d = 0.3\lambda$, $a = 0.3\lambda$, $\theta = 60^{\circ}$ and $\ell = 0.3\lambda$) for H polarization.	147
5-34	Normalized Surface Field for a Modified Full-wave Rectified Surface ($d = 0.3\lambda$, $a = 0.3\lambda$, $\theta = 60^{\circ}$ and $\ell = 0.4\lambda$) for H polarization.	148
5-35	Normalized Surface Field for a Modified Full-wave Rectified Surface ($d = 0.3\lambda$, $a = 0.3\lambda$, $\theta = 60^{\circ}$ and $\ell = 0.5\lambda$) for H polarization.	149
5-36	Normalized Surface Field for a Modified Full-wave Rectified Surface ($d = 0.3\lambda$, $a = 0.3\lambda$, $\theta = 60^{\circ}$ and $\ell = 0.6\lambda$) for H polarization.	150
5-37	Normalized Surface Field for a Modified Full-wave Rectified Surface ($d = 0.3\lambda$, $a = 0.3\lambda$, $\theta = 60^{\circ}$ and $\ell = 0.7\lambda$) for H polarization.	151
5-38	Normalized Surface Field for a Sinusoidal Surface ($d = 0.2\lambda$, $a = 0.1\lambda$ and $\theta = 0$), Computed Using 4, 6 and 8 Sampling Points, for H polarization.	152
5-39	Normalized Surface Field for a Sinusoidal Surface ($d = 1.9\lambda$, $a = 0.25\lambda$ and $\theta = 0$) for H polarization.	153
5-40	Surface Field for a Triangular Surface ($d = 1.75\lambda$, $\theta_1 = 20^{\circ}$, $\theta_2 = 66^{\circ}$ and $\theta = 12.2^{\circ}$) for H polarization.	154

LIST OF ILLUSTRATIONS

Figure		Page
6-1	Diffracted Energy for Two Radiating Modes, for H polarization.	160
6-2	Diffracted Energy for a Modified Full-wave Rectified Surface ($a = 0.3\lambda$, $\theta = 60^{\circ}$ and $d = 0.30\lambda$) for H polarization.	161
6-3	Diffracted Energy for a Full-wave Rectified Surface ($d = 0.6\lambda$, and $a = 0.3\lambda$) for H polarization.	162
6-4	Diffracted Energy for a Sinusoidal Surface ($d = 1.155\lambda$ and $\theta = 60^{\circ}$) for H polarization.	164
6-5	Diffracted Energy for a Sinusoidal Surface ($d = 1.155\lambda$ and $\theta = 60^{\circ}$), Computed Using the Physical Optics Method (with shadow) for H polarization.	165
6-6	Diffracted Energy for a Sinusoidal Surface ($d = 1.155\lambda$ and $\theta = 60^{\circ}$) for H polarization.	166
7-1	Partitioning the Periodic Surface into Two Parts, S^{+} and S^{-}.	175
8-1	Geometry of a Rough Surface Consisting of a Periodic Base and a Small Scale Random Roughness.	184
8-2	Scattered Intensity Pattern ($T = 0.5d$), E-Polarization.	190
8-3	Scattered Intensity Pattern ($T = d$), E-Polarization.	190
8-4	Scattered Intensity Pattern ($T = 3d$), E-Polarization.	191
8-5	Scattered Intensity Pattern ($T = 0.5d$), H-Polarization.	191
8-6	Scattered Intensity Pattern ($T = d$), H-Polarization.	192
8-7	Scattered Intensity Pattern with Finite Source Illumination ($p = 3d$, $T = d$), E-Polarization.	192
8-8	Scattered Intensity Pattern with Finite Source Illumination ($p = 3d$, $T = d$), H-Polarization.	197
B-1	Scattering by a Cylindrical Surface.	210
B-2	Geometry of Orthogonal Vectors.	210

LIST OF APPENDICES

		Page
APPENDIX A:	PHYSICAL OPTICS APPROXIMATION	205
APPENDIX B:	AN ALTERNATIVE INTEGRAL EQUATION FOR E POLARIZATION	209

Chapter I

INTRODUCTION

Periodic structures find a variety of applications in fields ranging from acoustics and electromagnetics to optics. Typical examples are the diffraction gratings used in optical spectrometers and as resonator components in sub-optical lasers, the slow-wave structures in microwave tubes, and for microwave lenses and broadband absorbers. They are also important to oceanographers in the study of acoustic or low-frequency radio wave scattering from an idealized sea.

Mathematically, the problem of the scattering of waves by a periodic surface is one which is easy to formulate but difficult to solve. It consists of solving the wave equation subject to boundary conditions imposed at a surface whose shape can be very complicated. For this reason, an exact analytical treatment of the problem is seldom possible, and it is only recently, with the advent of the high speed computer, that reliable results have been obtained.

Prior to this time, a variety of approximate analytical treatments were developed, most of them based on an approach originated by Lord Rayleigh (1878). Assuming the surface to be infinite in extent and making use of the periodicity in (say) the coordinate x, Rayleigh expanded the scattered field in a discrete spectrum of outgoing plane waves, which representation was assumed to hold right down to the surface. Application of the boundary condition leads to an infinite set of linear algebraic equations, valid for all x, from which to determine the complex amplitudes of the scattered waves, infinite in number.

The crucial and unjustified step (see Lippmann, 1953) in this procedure is the assumption that the representation of the scattered field holds everywhere above and on the boundary. This has ever since been a subject of controversy (see, for example, Lysanov, 1958). Thus, for a perfectly conducting sinusoidal surface, Rayleigh (1878) obtained a solution by successive approximation based on the initial neglect of all attenuated waves and assuming that

the amplitudes of the corrugations are small irregularities compared to the wavelength. Later, for the small surface, Tai (1948) proceeded via an orthogonal mode expansion, followed by matrix truncation, and others have pursued essentially the same path. An analogous treatment for a corrugated interface between two homogeneous media was developed by Rayleigh (1907), and applied to a sinusoidal profile by Pavageau (1963) and to a triangular profile by Bousquet (1963).

A refinement of Rayleigh's method was developed by Uretsky (1965). His method starts in the same way as Rayleigh's, but instead of merely assuming that the scattered field can be expanded as an infinite set of plane waves, Uretsky proved that this is possible for observation points not too close to the boundary. To avoid Rayleigh's assumption that the representation holds right down to the surface, Uretsky used Green's theorem to express the scattered field as an integral over the elementary sources induced on the boundary by the incident wave. Numerical results were obtained for a sinusoidal surface with a Dirichlet boundary condition.

Methods of small perturbations similar to Rayleigh's were used by Miles (1954) and Katsenelenbaum (1955). The typical procedure is as follows: the boundary conditions specified on the uneven surface $y = f(x)$ are transformed to the plane $y = 0$ by expansion in a power series with respect to $f(x)$. Thus the problem of scattering from an uneven periodic surface is reduced to solving the wave equation subject to specified boundary conditions on a plane.

At best, all such solutions are valid only for corrugations whose height is much smaller than the free space wavelength, and in an attempt to overcome this restriction, Meecham (1956a) used a variational method to find the angular distribution of scattered energy for a perfectly conducting grating. The scattered field was represented as a linear combination of known solutions of the wave equation whose coefficients were obtained by a least square fit to the boundary condition at the surface, and the procedure was then applied to a triangular (or sawtooth) profile.

A somewhat different approach was taken by Eckart (1953). He expressed the scattered field as a Helmholtz integral involving the scattered field itself and its normal derivative on the boundary. The integral was then evaluated after assuming that the reflection took place at an equivalent flat surface, and approximating the scattered field and its normal derivative on the boundary by the incident field alone. Another method also based on variations on the Kirchhoff approximation was used by Brekhovskikh (1952). The method assumed that the field at the uneven surface was local in nature and could be specified in terms of the laws of geometrical optics. The field at each point on the surface was assumed to be the same as if the reflection from that point were to occur from an infinite plane tangent to the surface at the specified point.

A method based on physical optics was used by Senior (1959). Once again the determination of the field is reduced to quadratures, and Senior showed that for a plane wave at normal incidence on a sinusoidal grating, the physical optics integral can be evaluated exactly to give the complex amplitudes of the scattered waves. As indicated in Appendix A, the same is true (if shadowing is ignored) for both polarizations, and for oblique incidence as well as normal. It should be emphasized, however, that the solution is still approximate by virtue of the postulated surface field distribution, and the failures of the physical optics estimate of the surface fields are examined in Chapters III and V of this work.

A method which is quite distinct from all of the above was developed by Sivov (1964) who used conformal transformation and a consideration of the static limit to analyze reflections from periodic surfaces with shallow and deep corrugations. The procedure is similar to that recently employed by Millar (1969, 1971) to investigate the inherent limitation of Rayleigh's method (see Chapter VII). As first noted by Lippmann (1953), it is not in general valid to assume that the expansion of the scattered field as a discrete spectrum of outgoing waves alone holds over the entire scattering surface, and this fact was later verified by Petit and Cadilhac (1964) in the case of a sinusoidal grating.

In any general treatment of the grating problem it is therefore necessary to allow "ingoing" waves in the immediate vicinity of the surface.

All of the methods considered so far are very limited (satisfactory only for certain classes of structures) and have little success in predicting certain characteristics of periodic structures (for example the P-type Wood anomalies). In the desire for a better understanding of Wood anomalies (see Chapters IV and VI), a different point of view was proposed by Hessel and Oliver (1965). They used a guided wave approach and replaced the uneven surface by a plane which had a modulated surface reactance. Their theory is more general than the previous theories and predicts the general location and shapes of the anomalies. Since the surface geometry and the modulated plane reactance cannot be related quantitatively, information about the performance of a specific structure cannot be obtained.

Recently, another approach based on function theoretic techniques was used by Tseng, Hessel and Oliner (1968), and Itoh and Mittra (1969). Unfortunately structures for which such methods are possible are very few.

Without exception, all of these analytical attempts to determine the fields scattered by periodic surfaces are subject to approximation, either implicit or explicit, and it is only with the use of high speed computers permitting the direct digital solution of the integral equations that reliable results have been obtained.

Most of the initial work in this area was carried out by the French investigators, such as Petit, Cadilhac and Wirgin, and was motivated by the desire for more efficient optical diffraction gratings. In his early papers Petit (e.g. 1963) followed Rayleigh's approach in expressing the scattered field as a discrete spectrum of outgoing waves alone, leading to a matrix equation for the determination of the spectral amplitudes. Since the matrix was then truncated and inverted numerically, it will be appreciated that the method is no more than a digitization of that originated by Rayleigh. However, in later papers (Petit,

1967), the Rayleigh assumption was circumvented by using an integral equation formulation. Series expansions were adopted for the incident and scattered fields and the integral equation converted to a matrix equation which was solved numerically. Specific results were obtained for plane wave incidence on gratings with triangular profiles, and the efficiencies computed. A rather different approach was taken by Pavageau (1967) who derived the integral equation directly in terms of the unknown surface current. The equation was cast in the form of a nonhomogeneous Fredholm equation of the second kind and solved by iteration.

Methods which are very similar to that which we shall use have recently been employed by Neureuther and Zaki (1968, 1971a, b) and by Green (1970). The former considered scattering by periodic structures, either dielectric or perfectly conducting. The integral equation was obtained from Green's theorem and the modified Green's function expressed in either of two ways depending on the parameters of the surface. The first (space harmonic) representation is analogous to that used by Petit; the second consists of an infinite series of Hankel functions, and was computed using a Mellin transform and an asymptotic comparison scheme. Numerical data were obtained for sinusoidal profiles, and very recently data were obtained also for triangular profiles by Kalhor and Neureuther (1971). Green (1970) also used the space harmonic representation, but improved its convergence by summation techniques. Data were presented for the surface field and diffraction efficiencies of perfectly conducting gratings with triangular profiles.

The present work also employs the numerical approach, and is concerned with the scattering of electromagnetic waves by infinite, perfectly conducting, two-dimensional periodic surfaces of arbitrary but continuous profile. Plane wave incidence is assumed, with either E or H polarization, and both normal and oblique incidence are considered. A representation of the Green's function is employed which is similar to that used by Green (1970), and the convergence is improved still further by subtracting the dc terms. This has the added advantage of making explicit the behavior of the Green's function in a neighborhood

of its singularity. The integral equations are formulated on the basis of the Green's theorem, and the range of integration is reduced to a single period by application of Floquet's theorem. Using the moment method and an interpolation scheme, the integral equations are converted into a matrix equation which is solved to yield the unknown surface current.

Chapter II is concerned with the formulation of the integral equations and the development of numerical procedures for solving them. Numerical data for E polarization are presented in Chapters III and IV. Chapter III is concerned with the surface field while Chapter IV is devoted to the scattered field. Numerical results are obtained for a variety of surface profiles such as sinusoidal, full-wave rectified, inverted full-wave rectified and triangular, having various combinations of amplitudes, periods and for various incidence angles. In presenting the numerical data in Chapter IV, particular attention is given to the Wood anomalies (P-type), and in both chapters, the data are compared with the physical optics predictions.

The numerical results for H polarization are presented in Chapters V and VI and the S-type Wood anomalies discussed. The results support Palmer's experimental observation that the S-type anomalies are generally stronger than the P-type and can occur on structures with relatively shallow grooves.

Chapter VII is devoted to Rayleigh's method. After a brief historical survey of the assumption, numerical data are obtained for the scattered field using the exact representation as well as Rayleigh's.

Lastly, in Chapter VIII, the knowledge gained from the study of periodic surfaces is applied to an investigation of scattering from rough surfaces. The rough surface is treated as a small scale roughness superimposed on a periodic base (large scale roughness) with the small scale roughness represented by a random variable having a Gaussian distribution.

Chapter II

FORMULATION OF THE INTEGRAL EQUATION FOR NUMERICAL SOLUTION

We consider here an infinite, perfectly conducting periodic surface illuminated by a plane electromagnetic wave. Since the surface is assumed two dimensional in the sense of being independent of a Cartesian coordinate z, the entire problem is two dimensional, and the most general solution can be deduced from the particular solutions appropriate to incident plane waves having either $\underline{E}$ or $\underline{H}$ in the z direction, i.e. parallel to the corrugations. In either case, the problem is essentially scalar.

2.1 Formulation

It is convenient to develop first the integral equation in the somewhat simpler case of a scattering surface of finite extent. Let S (see Fig. 2-1) be this surface, and surround it by another closed surface S_R. Let $\psi(\underline{r})$ and $G(\underline{r}|\underline{r}')$ be two scalar functions which are continuous, together with their first and second derivatives, on S and S_R and throughout the volume V enclosed by them. Assume, moreover, that $\psi(\underline{r})$ satisfies the homogeneous wave equation

$$(\nabla^2 + k^2)\psi(\underline{r}) = 0 \tag{2.1}$$

inside and on the boundaries of V, whereas

$$(\nabla^2 + k^2)G(\underline{r}|\underline{r}') = -\delta(\underline{r} - \underline{r}') \ . \tag{2.2}$$

Applying Green's theorem to the volume V, we obtain

$$\int_{S+S_R} \left\{ G(\underline{r}|\underline{r}')\frac{\partial}{\partial n'}\psi(\underline{r}') - \psi(\underline{r}')\frac{\partial}{\partial n'}G(\underline{r}|\underline{r}') \right\} dS'$$

$$= \int_V \left\{ G(\underline{r}|\underline{r}')(\nabla^2 + k^2)\psi(\underline{r}') - \psi(\underline{r}')(\nabla^2 + k^2)G(\underline{r}|\underline{r}') \right\} dV' = \psi(\underline{r}) \tag{2.3}$$

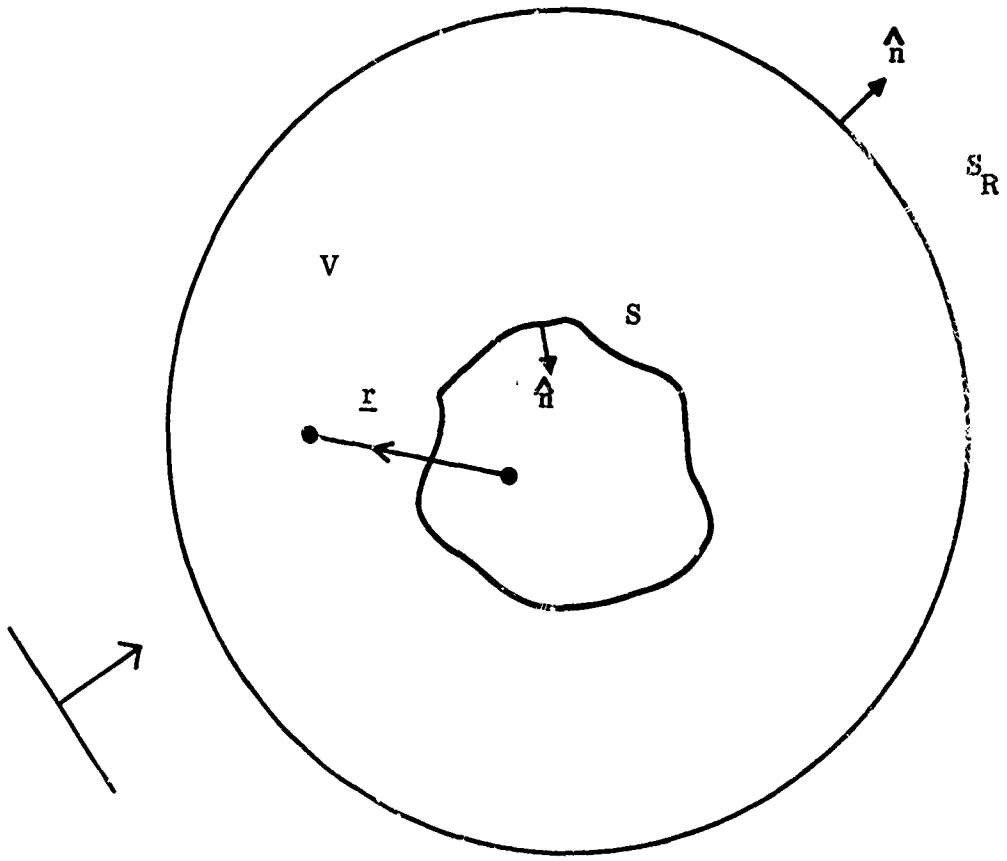

Fig. 2-1: Geometry for the Application of Green's Theorem.

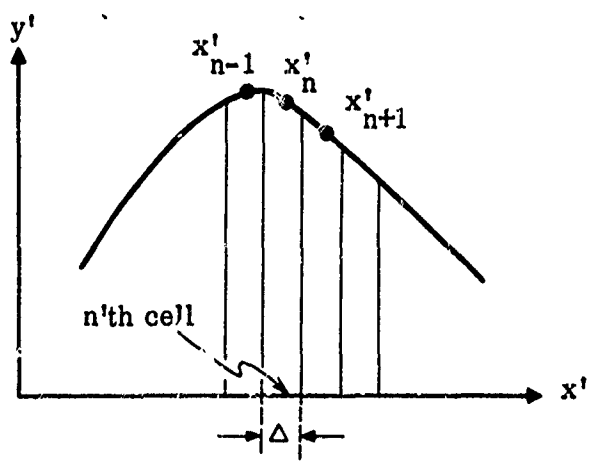

Fig. 2-2: Illustration of the interpolation procedure.

by virtue of the properties of the delta function. We now identify $\psi(\underline{r})$ with a total field

$$\psi^{tot}(\underline{r}) = \psi^{i}(\underline{r}) + \psi^{s}(\underline{r})$$

where $\psi^{i}(\underline{r})$ is an incident plane wave originated by a source at infinity (and therefore outside V), and $\psi^{s}(\underline{r})$ is the field scattered by the surface S. Since $\psi^{s}(\underline{r})$ must satisfy a radiation condition at infinity, its contribution to the integral over S_R decreases to zero as the surface S_R recedes to infinity, whereas $\psi^{i}(\underline{r})$ contributes itself. Equation (2.3) then becomes

$$\psi^{tot}(\underline{r}) = \psi^{i}(\underline{r}) + \int_S \left\{ G(\underline{r}|\underline{r}') \frac{\partial}{\partial n'} \psi(\underline{r}') - \psi(\underline{r}') \frac{\partial}{\partial n'} G(\underline{r}|\underline{r}') \right\} dS' \qquad (2.4)$$

and in spite of the assumptions of an incident plane wave and a surface of finite extent, Eq. (2.4) is also valid for an arbitrary incident field and for a surface S extending to infinity. In the latter case, however, the proof is by no means trivial (Jones, 1952).

The particular situation of concern to us is that in which S is doubly infinite and divides space into two regions. It is then sufficient to integrate over only the upper ("illuminated") side of the surface. We also assume that S is independent of the coordinate z, and this allows us to distinguish two particular cases according to the polarization of the incident field. Mks units are employed and a time factor $e^{j\omega t}$ suppressed throughout.

2.1.1 <u>E (or horizontal) Polarization</u>

If $\underline{E}^{i} = E_z^{i}\hat{z}$, the electric vector in the scattered field will also be confined to the z direction, and we can make the identification

$$\psi(\underline{r}) = E_z^{tot}(\underline{r}) \; . \qquad (2.5)$$

Since the normal derivative of E_z^{tot} is related to the surface current density K_z by the equation

$$\frac{\partial}{\partial n'} E_z^{tot}(\underline{r}') = -j\omega\mu K_z(\underline{r}') \quad , \tag{2.6}$$

where μ is the permeability of free space, Eq. (2.4) can be written as

$$E_z^{tot}(\underline{r}) = E_z^i(\underline{r}) - j\omega\mu \int_S \left\{ G(\underline{r}|\underline{r}')K_z(\underline{r}') + \frac{1}{j\omega\mu} E_z^{tot}(\underline{r}') \frac{\partial}{\partial n'} G(\underline{r}|\underline{r}') \right\} dS' \ . \tag{2.7}$$

At the perfectly conducting surface S the boundary condition is

$$E_z^{tot}(\underline{r}) = 0 \tag{2.8}$$

and hence, on allowing $\underline{r}$ to approach the surface, Eq. (2.7) gives rise to the integral equation

$$\int_S G(\underline{r}|\underline{r}')K_z(\underline{r}')dS' = \frac{1}{j\omega\mu} E_z^i(\underline{r}) \ . \tag{2.9}$$

For a two dimensional problem the free space Green's function is

$$G(\underline{r}|\underline{r}') = -\frac{j}{4} H_0^{(2)}(k|\underline{r}-\underline{r}'|) \tag{2.10}$$

where $H_0^{(2)}$ is the zero order Hankel function of the second kind. The final integral equation is therefore

$$\int_S K_z(\underline{r}')H_0^{(2)}(k|\underline{r}-\underline{r}'|)\, d\ell' = \frac{4}{\omega\mu} E_z^i(\underline{r}) \tag{2.11}$$

from which K_z has to be determined.

2.1.2 <u>H (or vertical) Polarization</u>

If $\underline{H}^i = H_z^i \hat{z}$, the total magnetic field is likewise in the z direction, and on making the identification

$$\psi(\underline{r}) = H_z^{tot}(\underline{r}) , \tag{2.12}$$

Eq. (2.4) becomes

$$H_z^{tot}(\underline{r}) = H_z^i(\underline{r}) + \int_S \left\{ G(\underline{r}|\underline{r}')\frac{\partial}{\partial n'} H_z^{tot}(\underline{r}') - H_z^{tot}(\underline{r}') \frac{\partial}{\partial n'} G(\underline{r}|\underline{r}') \right\} dS' . \tag{2.13}$$

The boundary condition at the perfectly conducting surface S is

$$\frac{\partial}{\partial n'} H_z^{tot}(\underline{r}) = 0 \tag{2.14}$$

and on allowing $\underline{r}$ to approach the surface, Maue (1949) has shown that (2.13) reduces to

$$\frac{1}{2} H_z^{tot}(\underline{r}) = H_z^i(\underline{r}) - \int_S H_z^{tot}(\underline{r}') \frac{\partial}{\partial n'} G(\underline{r}|\underline{r}') \, dS' . \tag{2.15}$$

The quantity H_z^{tot} is the induced current density, and since this current flows tangential to the surface in a plane perpendicular to the z direction, we can write

$$\underline{K}_t(\underline{r}) = H_z^{tot}(\underline{r})\hat{t} \tag{2.16}$$

where $\hat{t}$ is a unit vector tangential to S. Inserting finally the expression (2.10) for the free space Green's function, we have

$$\int_S K_t(\underline{r}) \frac{\partial}{\partial n'} H_0^{(2)}(k|\underline{r} - \underline{r}'|) d\ell' = 4j \left\{ H_z^i(\underline{r}) - \frac{1}{2} K_t(\underline{r}) \right\} , \tag{2.17}$$

i.e.

$$\int_S K_t(\underline{r}) H_1^{(2)}(k|\underline{r}-\underline{r}'|) \cos(\hat{n}, |\underline{r}-\underline{r}'|) d\ell' = 4j \left\{ H_z^i(\underline{r}) - \frac{1}{2} K_t(\underline{r}) \right\} . \tag{2.18}$$

This is an integral equation from which to determine K_t.

2.2 Reduction of the Integral Equations for the Periodic Surfaces

We now make use of the fact that the incident field is a plane wave and that the surface $y = f(x)$ is periodic with period d, i.e.

$$f(x+md) = f(x) , \qquad m = \pm 1, \pm 2, \pm 3, \ldots \quad . \tag{2.19}$$

As before, it is convenient to consider separately the cases of E and H polarization.

2.2.1 E Polarization

Let us assume that

$$E_z^i(\underline{r}) = e^{-jk(x \sin\theta - y \cos\theta)} \tag{2.20}$$

where θ is the angle of incidence with respect to the normal to the mean surface. The integral equation is as shown in Eq. (2.11), but since the integration extends from $-\infty$ to ∞, this is not appropriate for a numerical solution. However, by invoking the periodic property of the surface, the integral can be reduced to one over a single period alone at the expense of a more complicated form for the kernel.

From Floquet's theorem, we have that

$$K_z(\underline{r}+md\hat{x}) = K_z(\underline{r}) e^{-jkmd \sin\theta}, \quad m = \pm 1, \pm 2, \pm 3, \ldots \quad . \tag{2.21}$$

Moreover,

$$d\ell' = \sqrt{1+\{f'(x')\}^2}\, dx'$$

where $f'(x)$ is the derivative of f with respect to x. This allows us to express the integral as one along the x' axis, and since

$$|\underline{r}-\underline{r}'| = \sqrt{(x-x'-md)^2+(y-y')^2}\,,$$

we obtain

$$\int_0^d \sum_{m=-\infty}^{\infty} H_0^{(2)}\left(k\sqrt{(x-x'-md)^2+(y-y')^2}\right) e^{-jkmd\sin\theta}\sqrt{1+\left\{f'(x')\right\}^2}\,K_z(x')dx'$$

$$= \frac{4}{\omega\mu}\, e^{-jk(x\sin\theta - y\cos\theta)}\,, \tag{2.22}$$

valid for $0 \le x \le d$ with $y = f(x)$, $y' = f(x')$.

In arriving at (2.22) we have implicitly assumed that interchanging the order of integration and summation is valid (a fact which is by no means obvious), but even so Eq. (2.21) is not a very promising equation for numerical purposes because of the extremely poor convergence of the infinite series constituting the kernel. To rectify this situation, consider

$$P_1 = \sum_{m=-\infty}^{\infty} H_0^{(2)}\left(k\sqrt{(x-x'-md)^2+(y-y')^2}\right) e^{-jkmd\sin\theta}\,. \tag{2.23}$$

Using the Fourier integral representation of the Hankel function, the Poisson summation formula (see, for example, Morse and Feshbach, 1953) applied to (2.23) gives

$$P_1 = \frac{2}{d}\sum_{m=-\infty}^{\infty} \frac{1}{X_m}\, e^{-j\left(\frac{2m\pi}{d}+k\sin\theta\right)(x-x')}\, e^{-j|y-y'|X_m}\,, \tag{2.24}$$

where

$$X_m = \sqrt{k^2 - \left(\frac{2m\pi}{d}+k\sin\theta\right)^2} \tag{2.25}$$

and the chosen branch of the square root is that for which

$$\operatorname{Im} X_m \le 0$$

in order to satisfy the radiation condition.

The expression (2.23) for P_1 has been used by Yen (1962) and Green (1970), and is equivalent to that obtained by Neureuther and Zaki (1968) using a space harmonic expansion. The features that should be noted are that if $y \neq y'$ the successive terms decrease exponentially with increasing $|m|$ for all

$$\left| m + \frac{kd}{2\pi} \sin\theta \right| > \frac{kd}{2\pi} \quad ,$$

and that in addition there is an algebraic decrease (proportional to m^{-1}) provided by the factor X_m in the denominator.

We can produce still a further improvement in the convergence properties of the series by separating out the zero-frequency ($k = 0$) terms, and this has the added advantage of making explicit the behavior of P_1 in the vicinity of the singular point $x' = x$, $y' = y$. Putting $k = 0$ in (2.24), we have

$$P_1\Big|_{k=0} = -\frac{2}{d} \sum_{m=-\infty}^{\infty} \frac{1}{j|m| \frac{2\pi}{d}} e^{-j\frac{2m\pi}{d}(x-x')} e^{-\frac{2\pi}{d}|m(y-y')|} \tag{2.26}$$

and since

$$\sum_{m=1}^{\infty} = -\frac{d}{2\pi j} \log \left[1 - e^{-j\frac{2\pi}{d}(x-x') - \frac{2\pi}{d}|y-y'|} \right]$$

$$\sum_{m=-\infty}^{-1} = \frac{d}{2\pi j} \log \left[1 - e^{j\frac{2\pi}{d}(x-x') - \frac{2\pi}{d}|y-y'|} \right]$$

(see, for example, Collin, 1960), provided $y' \neq y$, it follows that

$$P_1\Big|_{k=0} = (m=0 \text{ term}) - \frac{j}{\pi} \log \left[\left\{ 1 - e^{-\frac{2\pi}{d}\left[|y-y'| + j(x-x')\right]} \right\} \right.$$

$$\left. \left\{ 1 - e^{-\frac{2\pi}{d}\left[|y-y'| - j(x-x')\right]} \right\} \right] . \tag{2.27}$$

Hence, by subtracting the zero frequency value of each term of (2.24) and then adding (2.27), the integral equation (2.21) takes the form

$$\int_0^d G_1(x,y;\, x',y') K_z(x') e^{jkx'\sin\theta} \sqrt{1 + \left\{f'(x')\right\}^2}\, dx' = \frac{2d}{\omega\mu} e^{jky\cos\theta} ,$$

$$0 \le x \le d , \tag{2.28}$$

where

$$G_1(x,y;x',y') = \frac{1}{k\cos\theta} e^{-jk|y-y'|\cos\theta}$$

$$- \frac{jd}{2\pi} \log \left[\left\{ 1 - e^{-\frac{2\pi}{d}\left[|y-y'| + j(x-x')\right]} \right\} \left\{ 1 - e^{-\frac{2\pi}{d}\left[|y-y'| - j(x-x')\right]} \right\} \right]$$

$$+ \sum_{m=1}^{\infty} e^{-j\frac{2m\pi}{d}(x-x')} \left\{ \frac{e^{-j|y-y'|X_m^+}}{X_m^+} + \frac{e^{-\frac{2m\pi}{d}|y-y'|}}{j\frac{2m\pi}{d}} \right\}$$

$$+ \sum_{m=1}^{\infty} e^{j\frac{2m\pi}{d}(x-x')} \left\{ \frac{e^{-j|y-y'|X_m^-}}{X_m^-} + \frac{e^{-\frac{2m\pi}{d}|y-y'|}}{j\frac{2m\pi}{d}} \right\} \tag{2.29}$$

with

$$X_m^+ = \sqrt{k^2 - \left(\frac{2m\pi}{d} + k\sin\theta\right)^2} , \qquad X_m^- = \sqrt{k^2 - \left(\frac{2m\pi}{d} - k\sin\theta\right)^2} . \tag{2.30}$$

We observe that the Green's function has now been expressed as the sum of a term involving explicitly the amplitude and the angle of incidence, a logarithmic function representing the true behavior of G in a neighborhood of its singularity, and two series which are themselves differences of two convergent series.

2.2.2 H Polarization

The incident field in this case is taken to be

$$H_z^i(\underline{r}) = e^{-jk(x\sin\theta - y\cos\theta)} \tag{2.31}$$

and the reduction of the integral equation (2.17) to a form suitable for numerical solution proceeds in much the same way as for E polarization. Since

$$\frac{\partial}{\partial n'} = \frac{-1}{\sqrt{1+\{f'(x')\}^2}}\left\{f'(x')\frac{\partial}{\partial x'} - \frac{\partial}{\partial y'}\right\},$$

Eq. (2.17) can be written as

$$\int_0^d P_2 K_t(x')dx' = 4j\left\{H_z^i(\underline{r}) - \frac{1}{2}K_t(\underline{r})\right\} \tag{2.32}$$

where

$$P_2 = \left\{1+\{f'(x')\}^2\right\}\frac{\partial}{\partial n'}\sum_{m=-\infty}^{\infty} H_0^{(2)}\left(k\left[(x-x'-md)^2+(y-y')^2\right]^{\frac{1}{2}}\right)e^{-jkmd\sin\theta}$$

$$= -\frac{2j}{d}\sum_{m=-\infty}^{\infty}\frac{1}{X_m}\left[f'(x')\left(\frac{2m\pi}{d}+k\sin\theta\right) - X_m\,\mathrm{sgn}(y-y')\right] \times$$

$$\times\, e^{-j\left(\frac{2m\pi}{d}+k\sin\theta\right)(x-x')}\, e^{-j|y-y'|X_m} \tag{2.33}$$

in which $\mathrm{sgn}(\tau)$ is the signum function and X_m is given in (2.25). The zero frequency ($k = 0$) limit of P_2 is

$$P_{2\,|k=0} = \frac{2}{d}\sum_{m=-\infty}^{\infty}\left\{\frac{m}{|m|}\,f'(x')+j\,\mathrm{sgn}(y-y')\right\} e^{-j\frac{2m\pi}{d}(x-x')}\, e^{-\frac{2\pi}{d}|m(y-y')|}$$

$$= \frac{2}{d}\left\{f'(x')+j\,\mathrm{sgn}(y-y')\right\} + \frac{2}{d}\left\{f'(x')+j\,\mathrm{sgn}(y-y')\right\}\sum_{m=1}^{\infty} e^{-j\frac{2m\pi}{d}\{(x-x')-|y-y'|\}}$$

$$+\frac{2}{d}\left\{-f'(x')+j\,\mathrm{sgn}(y-y')\right\}\sum_{m=1}^{\infty} e^{j\frac{2m\pi}{d}\{(x-x')+j|y-y'|\}} ,$$

and since

$$\sum_{m=1}^{\infty} e^{jm\tau} = -\frac{1}{2}+\frac{j}{2}\cot\frac{\tau}{2} ,$$

we have

$$P_{2\,|k=0} = \frac{2}{d}f'(x')+\frac{j}{d}\left\{f'(x')+j\,\mathrm{sgn}(y-y')\right\}\cot\left\{-\frac{\pi}{d}(x-x')+j\frac{\pi}{d}|y-y'|\right\}$$

$$+\frac{j}{d}\left\{-f'(x')+j\,\mathrm{sgn}(y-y')\right\}\cot\left\{\frac{\pi}{d}(x-x')+j\frac{\pi}{d}|y-y'|\right\} . \qquad (2.34)$$

Hence, by subtracting the zero-frequency value of each term of (2.33) and then adding (2.34), the integral equation (2.32) takes the form

$$\int_0^d G_2(x,y;x',y')K_t(x')dx' = jd\left\{2H_z^i(x)-K_t(x)\right\} , \quad 0 \le x \le d , \qquad (2.35)$$

where

$$
\begin{aligned}
&G_2(x,y;x',y') \\
&= -j\,\mathrm{sgn}(y-y') - j\left\{f'(x')\tan\theta - \mathrm{sgn}(y-y')\right\} e^{-jk\sin\theta(x-x') - jk\cos\theta\,|y-y'|} - \\
&- j\,e^{-jk\sin\theta(x-x')} \sum_{m=1}^{\infty} e^{-j\frac{2m\pi}{d}(x-x')} \left[\frac{e^{-j|y-y'|X_m^+}}{X_m^+} \wedge \right. \\
&\wedge \left\{ f'(x')\left(\frac{2m\pi}{d} + k\sin\theta\right) - X_m^+\,\mathrm{sgn}(y-y') \right\} - e^{-\frac{2m\pi}{d}|y-y'|} \left\{ jf'(x') - \mathrm{sgn}(y-y') \right\} - \\
&- j\,e^{-jk\sin\theta(x-x')} \sum_{m=1}^{\infty} e^{j\frac{2m\pi}{d}(x-x')} \left[\frac{e^{-j|y-y'|X_m^-}}{X_m^-} \wedge \right. \\
&\wedge \left\{ f'(x')\left(-\frac{2m\pi}{d} + k\sin\theta\right) - X_m^-\,\mathrm{sgn}(y-y') \right\} + \\
&+ e^{-\frac{2m\pi}{d}|y-y'|} \left\{ jf'(x') + \mathrm{sgn}(y-y') \right\} \Bigg] + \\
&+ \frac{j}{2}\left\{ f'(x') + j\,\mathrm{sgn}(y-y') \right\} \cot\left\{ -\frac{\pi}{d}(x-x') + j\frac{\pi}{d}|y-y'| \right\} + \\
&+ \frac{j}{2}\left\{ -f'(x') + j\,\mathrm{sgn}(y-y') \right\} \cot\left\{ \frac{\pi}{d}(x-x') + j\frac{\pi}{d}|y-y'| \right\} . \qquad (2.36)
\end{aligned}
$$

In spite of the obvious complexity of the Green's function G_2, its form is directly analogous to G_1 in consisting of certain explicit terms, a pair of cotangent functions representing the true behavior of G_2 in a neighborhood of its singularity, and two series which are themselves differences of two convergent series. Once again, therefore, the singularity of the Green's function has been separated out.

We further note that the integral equations (2.28) and (2.35) have been derived without approximation. In consequence, the formulation so far is

exact for any two dimensional perfectly conducting periodic surface which is smooth in the sense of having a continuous first derivative.

2.3 Comments on the Green's Functions of the Integral Equations

Before we discuss the numerical procedures of solving the integral equations shown in Eqs. (2.28) and (2.35), it is appropriate to examine their kernels (modified Green's functions) with some care. Equation (2.28) for E polarization is a Fredholm integral equation of the first kind with a weakly singular kernel. Very little is known about equations of this type, and even the uniqueness of the solution is not assured. On the other hand, Eq. (2.35) for H polarization is a Fredholm integral equation of the second kind with a weakly singular kernel. The advantage of this equation over that for E polarization is that we can use an iterative scheme (Neumann series) to obtain the solution. This has been done by Pavagean and Bousquet (1969) using the geometric optics expression for the surface field as a first approximation. As shown in Appendix B, however, the integral equation for E polarization can be converted from one of the first kind to one of the second kind, so the successive approximation method can be applied here as well.

If we examine the Green's function for E polarization, Eq. (2.29), it is found that the surface slope dependence of the kernel occurs explicitly only in the terms $\sqrt{1+f'(x)^2}$. For surfaces of gentle slope such that $|f'(x)| \ll 1$, it is now obvious that the surface current will be relatively insensitive to slope. The second term of the Green's function has a logarithmic singularity which represents the correct singular behavior for E polarization in two dimensions. The last two terms consist of infinite series. Whenever X_m^+ or X_m^- is purely imaginary, the corresponding terms are exponentially damped. Hence, in a numerical solution of the integral equation, these series can be terminated at a term somewhat beyond that where the exponential decay starts. On physical grounds, it would appear that as functions of K, the values of these series could

change abruptly when an individual mode becomes cut-off. This could then lead to an abrupt change in surface field distribution. However, for surfaces of small periods ($d/\lambda < 0.2$), the contribution of the infinite series is insignificant, and the first two terms dominate.

For H polarization, the Green's function is much more complicated and more dependent on angle of incidence and surface slopes, but its qualitative behavior is not too different from that for E polarization. If $f'(x) = 0$, the surface is a flat sheet and it can be shown that G_2 vanishes. The current distribution is now given by the explicit term alone, and this is just the geometrical optics value. Again the correct singular behavior for H polarization in two dimensions is represented by the last two cotangent functions.

2.4 Numerical Procedures

Methods for the numerical solution of integral equations have been extensively discussed in the literature (see, for example, Harrington, 1968). The general procedure consists of reducing the equation to a finite set of algebraic equations, i.e. to a matrix equation, and can be illustrated by considering

$$\int_0^d G(x,x')K(x')dx' = F(x)\,, \qquad 0 \leq x \leq d. \tag{2.37}$$

We assume that the unknown function $K(x')$ can be expanded in terms of linearly independent base functions $\phi_n(x')$ such that

$$K(x') \simeq \sum_{n=1}^{N} a_n \phi_n(x') \tag{2.38}$$

where the a_n are the associated constants. Substitution of (2.38) into (2.37) gives

$$\sum_{n=1}^{N} a_n \int_0^d G(x,x')\phi_n(x')dx' = F(x) \tag{2.39}$$

and the solution of the integral equation has now been reduced to the determination of the constants, a_n, $n = 1, 2, \ldots, N$.

There are several possible ways of finding the a_n, e.g. least squares fit, Galerkin's method, and the collocation method, and it is the last of these that we shall employ.

The collocation method converts (2.39) into a system of N linear equations by forcing the two sides of (2.39) to be equal at N sampling points in the interval (0, d). This is simply a point-matching procedure and results in the matrix equation

$$\sum_{n=1}^{N} a_n \int_0^d G(x_m, x')\phi_n(x')dx' = F(x_m), \quad 0 \leq x_m \leq d, \; m = 1, 2, \ldots, N. \tag{2.40}$$

There now remains the problem of choosing the base functions $\phi_n(x')$, and here again there are several possible choices, e.g. rectangular, quadratic and sinusoidal. By appropriate choice, we can economize in the number of sampling points requred for an "accurate" approximation to the solution K(x), and experience has shown that a rectangular function is not in general a good choice, whereas sinusoidal interpolation often works rather well.

The particular form of sinusoidal interpolation that we have adopted is predicated on the use of sampling points which are uniformly distributed in $0 \leq x' \leq d$. The range of integration is therefore broken up into N increments of length Δ 'N (see Fig. 2-2). Furthermore, let x'_n be the midpoint of the n'th cell, i.e. $x'_n = (n - \frac{1}{2})\Delta$, and let $\Delta x'_n$ denote the interval $x'_n - \frac{\Delta}{2} \leq x' \leq x'_n + \frac{\Delta}{2}$. We assume that

$$K(x') = \begin{cases} A_n + B_n \sin k(x' - x_n) + C_n \cos k(x' - x_n), & \text{if } x' \in \Delta x'_n \\ 0 & \text{otherwise} \end{cases} \tag{2.41}$$

and specify the constants A_n, B_n and C_n by continuing the form appropriate to $x' \in \Delta x'_n$ out to the centers of the adjacent cells and imposing continuity. Defining $K_n = K(x_n)$ and $K_{n\pm 1} = K(x_{n\pm 1})$, we have

$$K_n = A_n + C_n ,$$

$$K_{n+1} = A_n + B_n \sin k\Delta + C_n \cos k\Delta ,$$

$$K_{n-1} = A_n - B_n \sin k\Delta + C_n \cos k\Delta ,$$

from which we obtain

$$A_n = \frac{-K_{n+1} + 2K_n \cos k\Delta - K_{n-1}}{2(\cos k\Delta - 1)}$$

$$B_n = \frac{K_{n+1} - K_{n-1}}{2 \sin k\Delta} \tag{2.42}$$

$$C_n = \frac{K_{n+1} - 2K_n + K_{n-1}}{2(\cos k\Delta - 1)} .$$

Substitution of (2.41) and (2.42) into (2.40) now gives

$$\sum_{n=1}^{N} \int_{\Delta x_n} G(x_m, x') \; K_n \left\{ \frac{\cos k\Delta - \cos k(x' - x_n)}{\cos k\Delta - 1} \right.$$

$$+ K_{n+1} \left(\frac{-\sin k\Delta + (\cos k\Delta - 1)\sin k(x' - x_n) + \sin k\Delta \cos k(x' - x_n)}{2 \sin k\Delta(\cos k\Delta - 1)} \right)$$

$$+ K_{n-1} \left(\frac{-\sin k\Delta - (\cos k\Delta - 1)\sin k(x' - x_n) + \sin k\Delta \cos k(x' - x_n)}{2 \sin k\Delta(\cos k\Delta - 1)} \right) dx'$$

$$= F(x_m) , \tag{2.43}$$

where $x_m = (m - \frac{1}{2})\Delta$, $m = 1, 2, \ldots, N$. We note in passing that when $n = 1$ or N the periodicity of the problem must be used to determine the constants K_{-1} or K_{n+1} required in (2.43).

The above procedure is immediately applicable to the integral equations for E and H polarizations on inserting the appropriate values for the Green's function and the forcing function, but a brief comment is desirable concerning the treatment of the singular cell. The Green's functions of concern to us are singular when $x = x'$, the singularity being logarithmic for E polarization, and a first order pole for H polarization, and it is therefore necessary to modify the numerical scheme when $x_m = x_n$. In line with the usual practice, we divide the singular cell into three portions:

$$(x_n - \frac{\Delta}{2}, x_n - \frac{\epsilon}{2}), \qquad (x_n - \frac{\epsilon}{2}, x_n + \frac{\epsilon}{2}), \qquad (x_n + \frac{\epsilon}{2}, x_n + \frac{\Delta}{2})$$

with $0 < \epsilon < \Delta$. The first and third segments are handled by the standard numerical technique, whereas the central portion is treated analytically by means of a limiting process (Andreasen, 1964).

It must be mentioned here that the sinusoidal interpolation by no means assumes that the surface current distribution is sinusoidal. In fact other methods based on quadratic or flat-top functions can be used just as well. However, numerical results indicate that good convergence is obtained by using sinusoidal interpolation in this case.

In order to make the computer program applicable to periodic surfaces of arbitrary shape, it is convenient to represent the surface by its Fourier series.

If $y = f(x)$ is a periodic function of period d, then

$$f(x) = \frac{a_0}{2} + \sum_{n=1}^{\infty} \left[a_n \cos\left(\frac{2n\pi}{d}x\right) + b_n \sin\left(\frac{2n\pi}{d}x\right) \right] \tag{2.44}$$

where

$$a_n = \frac{2}{d} \int_0^d f(x) \cos\left(\frac{2n\pi}{d} x\right) dx \qquad (n = 0, 1, 2, \ldots)$$

$$b_n = \frac{2}{d} \int_0^d f(x) \sin\left(\frac{2n\pi}{d} x\right) dx \qquad (n = 1, 2, 3, \ldots)$$

It is known from the theorems of Fourier series that if f(x) is a periodic, continuous and piecewise continuously differentiable function, then the Fourier series (2.44) will converge uniformly to f(x). Subject to these restrictions on f(x), we can therefore synthesize an arbitrary periodic surface to any desired degree of accuracy. In general, more Fourier terms are needed for H polarization than for E polarization to obtain the same degree of accuracy because the Green's function in the former case involves more terms with the first derivative.

2.5 Convergence and Accuracy of the Numerical Solutions

The numerical solution of the integral equations for both polarizations has been programmed for an IBM/67 computer in Fortran IV language. In solving an integral equation numerically it is always desirable to carry out a convergence test for the following reasons:

a) to determine the number of sampling points necessary to achieve the required accuracy, and

b) to test whether or not the numerical solution approaches a stable value as the number of sampling points is increased.

Although it has not been shown mathematically that the accuracy can be improved by increasing the number of sampling points, it would appear reasonable to believe so on physical grounds. In general it is considered that a numerical solution is "satisfactory" if it remains essentially unchanged when additional terms or modes are included in the computation, but there are exceptions to this (see, for example, Lee, Jones and Campbell, 1971).

The accuracy of the numerical solution in this work has been checked using the following criteria:

a) Energy conservation. This furnishes a common check on the accuracy of the solution in electromagnetic scattering from perfectly conducting surfaces. This is essentially the check employed by Petit and Cadilhac (1964), Neureuther and Zaki (1968) and Green (1970) as well as many others. However, as pointed out by Amitay and Galindo (1968), energy conservation does not provide a measure of accuracy of a solution found by the Ritz or other related methods, and hence, in order to use energy conservation to check other than computational round-off errors, care must be exercised in choosing the method of solving the integral equation numerically.

The method that has been adopted in this work is a subsection and sinusoidal interpolation scheme, and since the solution does not automatically satisfy energy conservation, we are able to use this as a check. The relation that must be satisfied is

$$\sum_{m=0}^{N} \left|A_m\right|^2 \mathrm{Re}(X_m) = k\cos\theta \tag{2.45}$$

where N is the number of propagating modes and the A_m's are the scattered field amplitudes. These are derived in Chapters IV and VI for E and H polarizations respectively.

b) Convergence test. The numerical solution is found for the same surface using different numbers of sampling points. As shown later, the numerical solution approaches a stable value as the number of sampling points increases, which value can be considered as the solution. It is found that the number of sampling points necessary to yield accurate results depend on many factors, such as the angle of incidence, the amplitude and period of the profile, the smoothness of the profile as well as polarization of the incident fields. In general, for both polarizations

better convergence is obtained for normal incidence or when the incidence angle is small. The computer program adopted in this work is based on uniform sampling cells, but it may be true that a nonuniform sampling scheme would give faster convergence for the same number of cells. Because the Green's functions are sensitive to a change in the surface slope, particularly for H polarization, it is necessary for us to insert more sampling points into those regions where the surface slope changes most.

c) Flat surface check. A very simple and useful check on the numerical solution is to let the surface become flat. We should then obtain the geometrical optics value for a flat sheet, and this is indeed the case.

d) Check with the result obtained by other authors. It is always desirable to be able to check the results obtained with those obtained by other workers (and other methods). The numerical results obtained here will be compared with those obtained by Zaki and Neureuther, and by Green. Good agreement is indicated.

2.6 Computational Time

Perhaps one of the most serious restrictions imposed on numerical work is the computational time involved. Although the computer programs have been cast in a general form applicable to surfaces of any size, economics dictate that only reasonable sizes (say from 0.2λ to 2λ in period) are explored. It is understood that most of the computational time consumed is used in filling up the matrix elements. The rest is used in the matrix inversion process. In general, the program for H polarization takes more computational time than for E polarization, because of its more complicated Green's function. To save computational time, separate programs have been written for the special case of sinusoidal surfaces. However, in spite of the fact that for the case of normal incidence symmetry can be used to reduce the matrix size by a factor of two, and hence to reduce the

computational time by a factor of four, separate programs were not written to take advantage of this, since most emphasis will be given to the more interesting case of oblique incidence. Examples of the computational time involved are given later.

Chapter III

SURFACE FIELD FOR E POLARIZATION

In this chapter surface field distributions obtained by numerical solution of the integral equation for E polarization are presented. The particular profiles considered are sinusoidal, full-wave rectified, inverted full-wave rectified, and triangular (see Fig. 3-1) with various periods and angles of incidence. In each case the physical optics approximation is also presented as a basis for comparison.

The physical optics method is a widely-used technique for estimating the scattered field. Basically, it is an extension of geometrical optics in which the surface field is approximated by its geometrical optics value, thereby reducing the determination of the scattered field to quadratures. Consequently, the physical optics method is a high frequency approximation technique, and it is suitable only when the "effective" dimensions of the scatterer are large compared with the wavelength, and there is no shadowing involved. How much shadowing affects the solution is still unknown, and a matter that is then of some debate is whether shadowing should be taken into account, and if so, how.

According to the physical optics method the current induced on the surface is

$$K = 2\hat{n} \wedge \underline{H}^i \quad \text{in the illuminated region, and} \tag{3.1}$$

$$= 0 \quad \text{in the geometrical shadow} \tag{3.2}$$

where $\hat{n}$ is the outward normal to the surface, and for a two dimensional surface this is given by

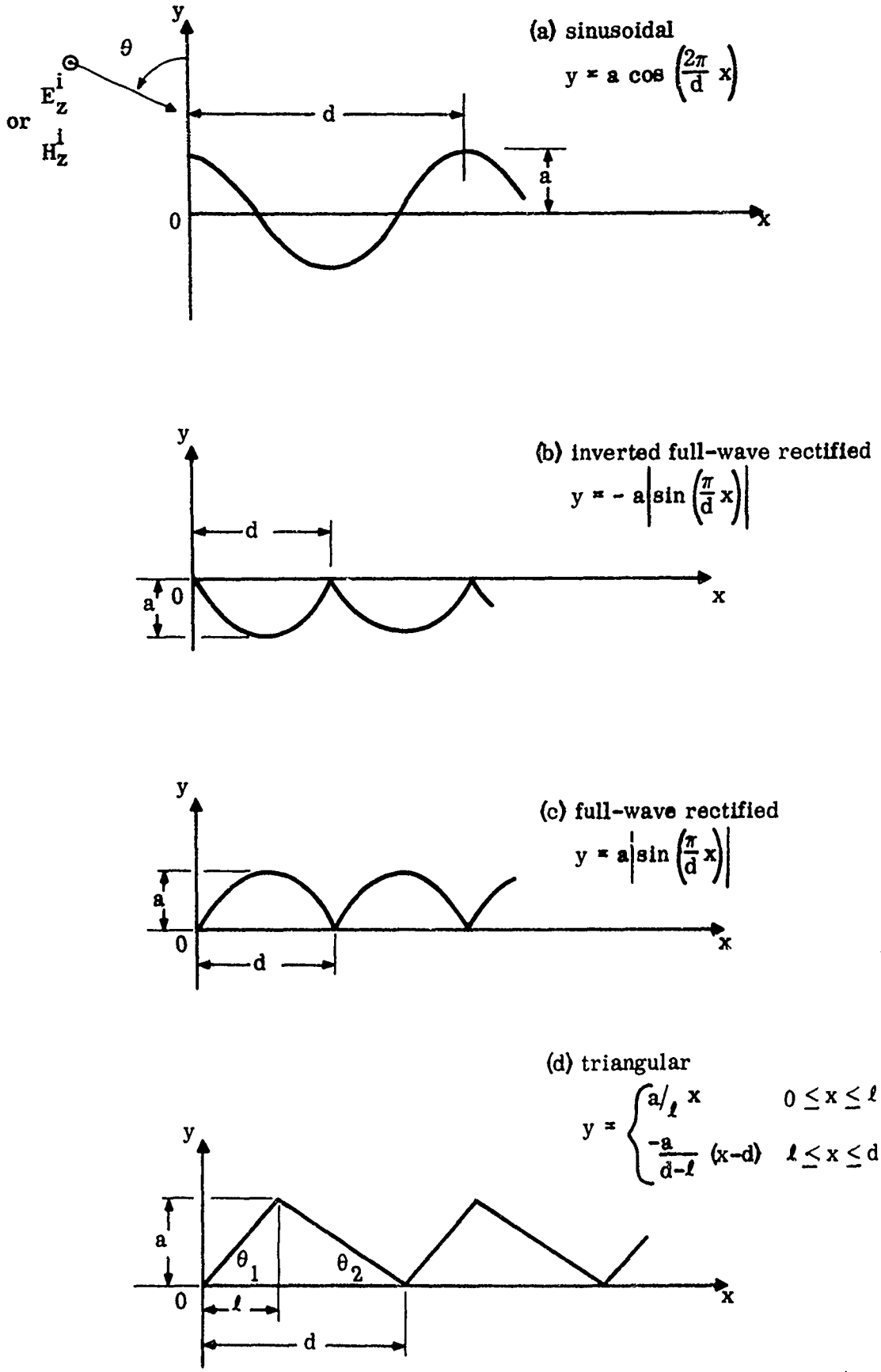

Fig. 3-1: Profiles of Periodic Surfaces.

$$\hat{n} = \frac{1}{\sqrt{1+f'(x)^2}}\left[-f'(x)\hat{x}+\hat{y}\right] \quad . \tag{3.3}$$

Thus, using Eqs. (2.20), (3.1) and (3.3) we obtain for E polarization

$$\underline{K} = \frac{1}{60\pi\sqrt{1+f'(x)^2}}\left[f'(x)\sin\theta+\cos\theta\right] e^{-jk(x\sin\theta - y\cos\theta)}\hat{z} \tag{3.4}$$

in the illuminated region.

By comparison with the exact solution, it is found that in general the physical optics method fails to give accurate results. However, if we consider a "smooth" surface with sufficiently large ratio of period to surface height, we can then rely on the physical optics method.

3.1 Surfaces of Small Period ($d/\lambda \lesssim 0.2$)

Figures 3-2 through 3-13 represent the current distributions on periodic surfaces of four different profiles (see Fig. 3-1). Each surface has a period $d = 0.2\lambda$, and a maximum amplitude $a = 0.1\lambda$. The angles of incidence considered are $\theta = 0$ (normal incidence), $\theta = 30^\circ$ and $\theta = 60^\circ$. In each figure, the exact computed values are shown as circled points, and are joined by a broken line only to guide the eye; the physical optics approximation is shown as a solid line.

Let us examine the sinusoidal surface. We observe that for this relatively small period most of the current is concentrated in the vicinity of the surface peaks, with the current almost zero in the troughs. There is, indeed, almost an exponential decrease in the current modulus away from the peaks, and the main effect of increasing the incidence angle is to scale the curves, leaving the general shape unchanged. In spite of shadowing due to large angles of incidence, the curve for the modulus still retains its symmetry.

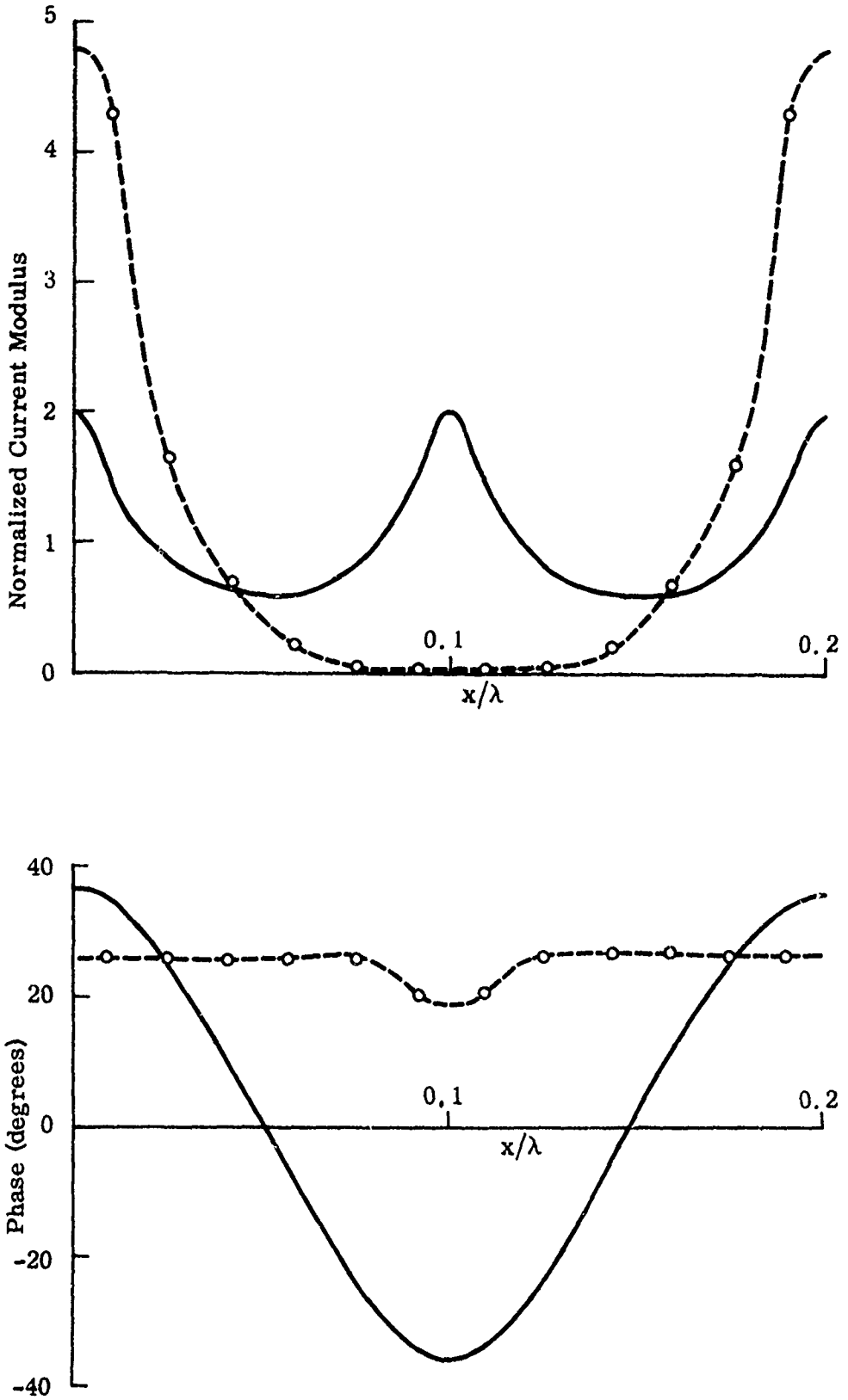

Fig. 3-2: Normalized Surface Field for a Sinusoidal Surface ($d = 0.2\lambda$, $a = 0.1\lambda$ and $\theta = 0$) for E polarization, --o-- exact, — physical optics.

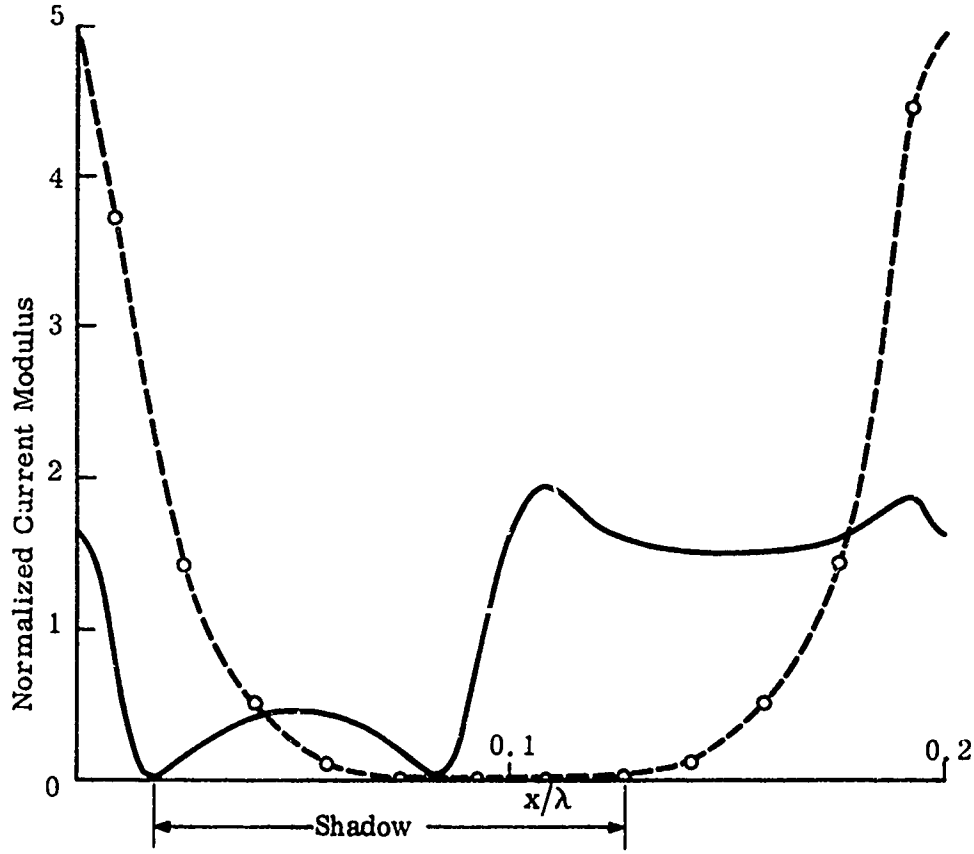

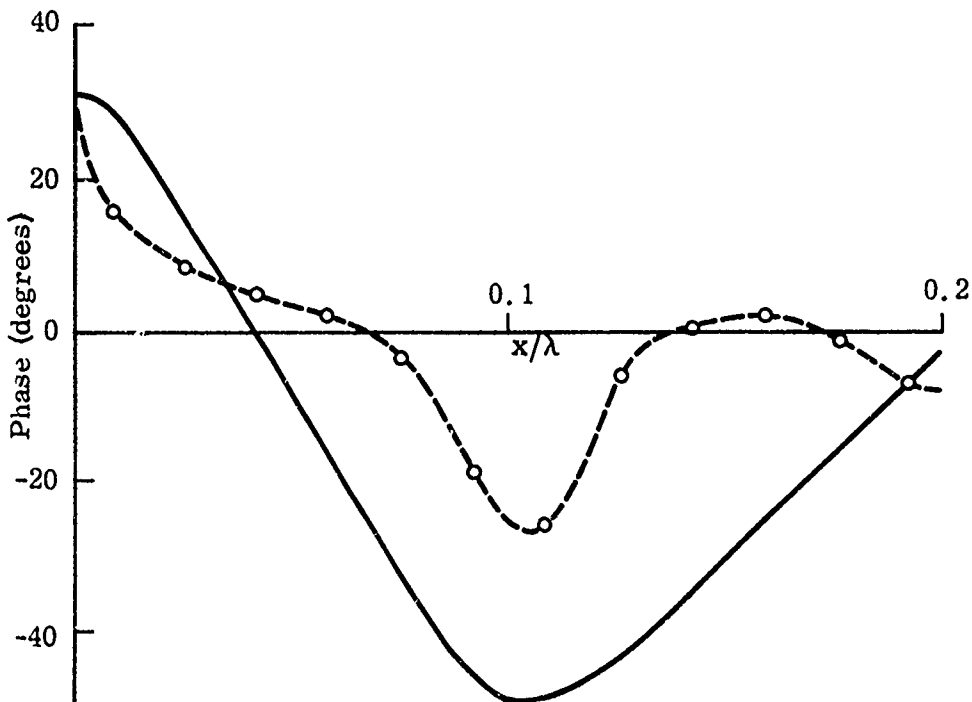

Fig. 3-3: Normalized Surface Field for a Sinusoidal Surface ($d = 0.2\lambda$, $a = 0.1\lambda$ and $\theta = 30^{\circ}$) for E polarization. --o-- exact, — physical optics.

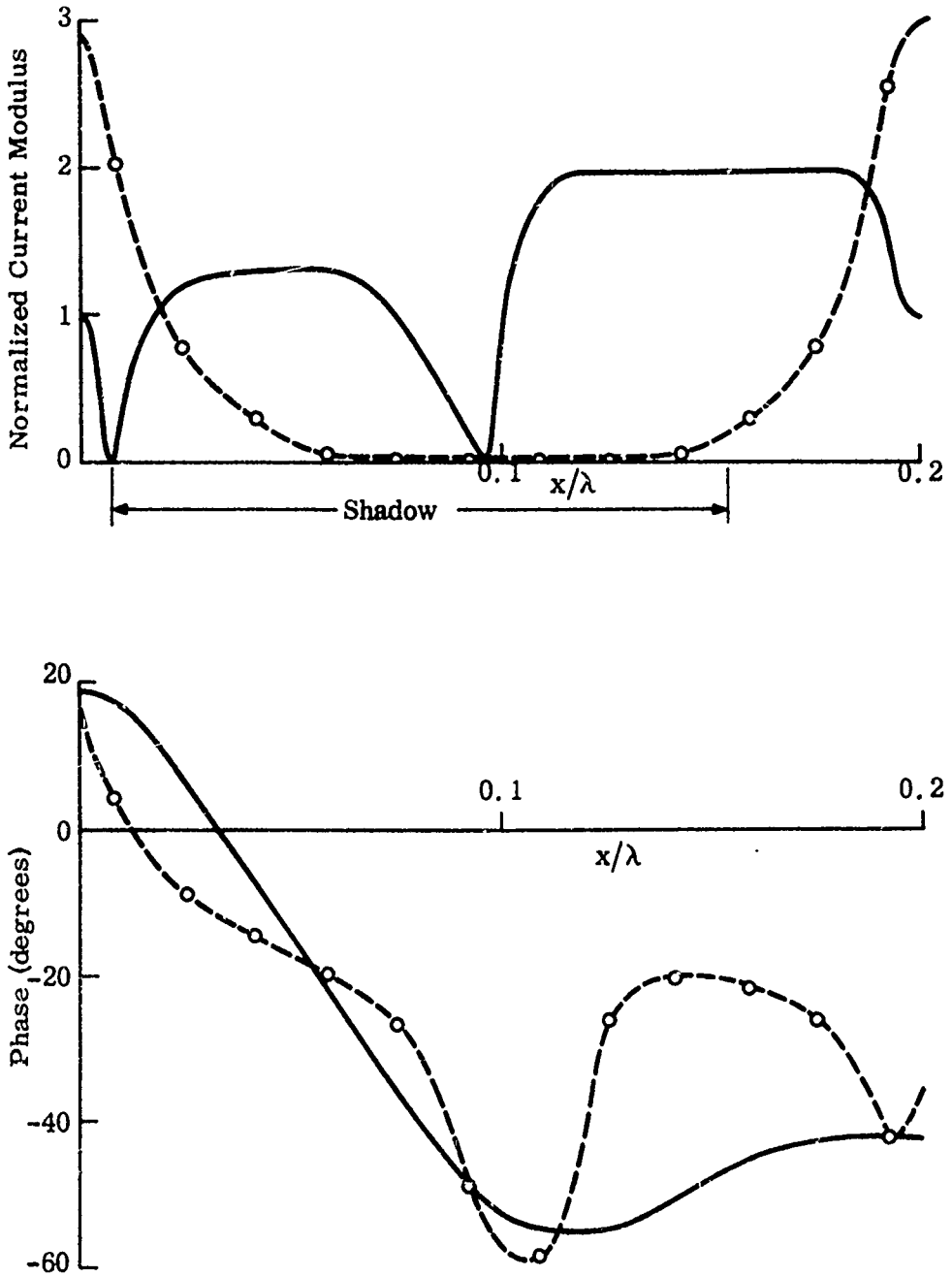

Fig. 3-4: Normalized Surface Field for a Sinusoidal Surface ($d = 0.2\lambda$, $a = 0.1\lambda$ and $\theta = 60^{\circ}$) for E polarization, --o-- exact, — physical optics.

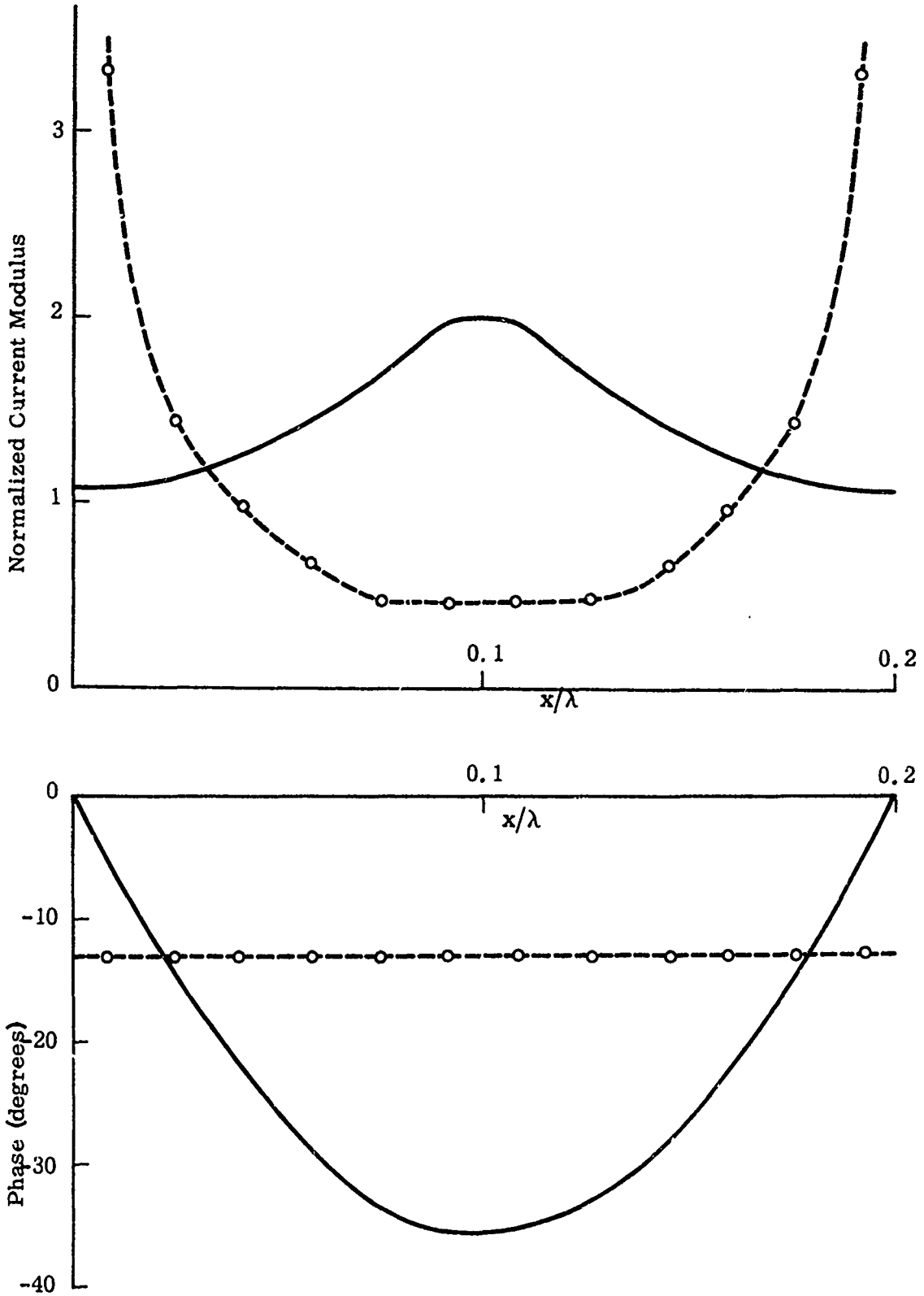

Fig. 3-5: Normalized Surface Field for an Inverted Full-Wave Rectified Surface ($d = 0.2\lambda$, $a = 0.1\lambda$ and $\theta = 0$) for E polarization, --o-- exact, — physical optics.

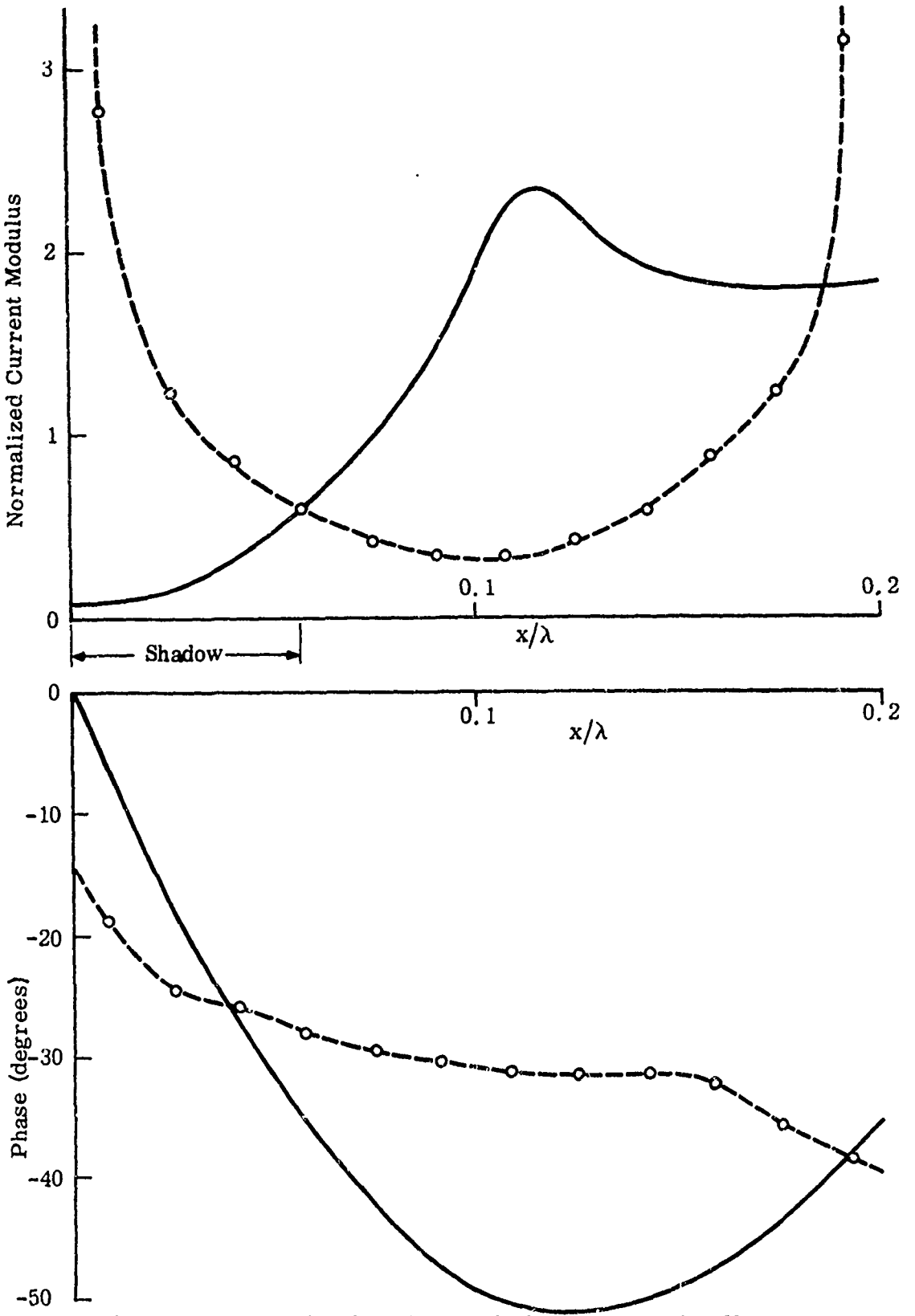

Fig. 3-6: Normalized Surface Field for an Inverted Full-Wave Rectified Surface ($d = 0.2\lambda$, $a = 0.1\lambda$ and $\theta = 30^{\circ}$) for E polarization, --o-- exact, — physical optics.

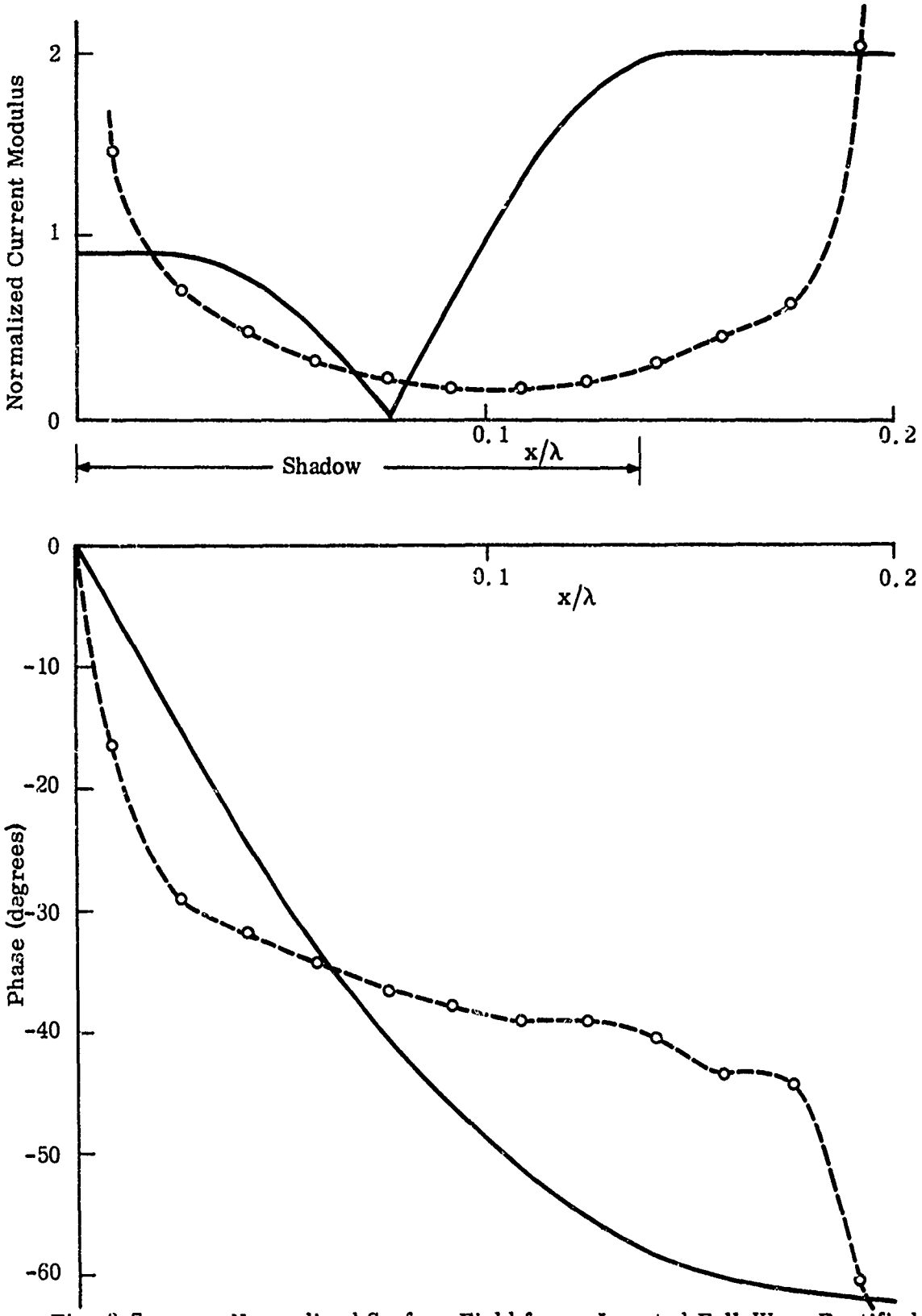

Fig. 3-7: Normalized Surface Field for an Inverted Full-Wave Rectified Surface ($d = 0.2\lambda$, $a = 0.1\lambda$ and $\theta = 60^{\circ}$) for E polarization, ---o--- exact, — physical optics.

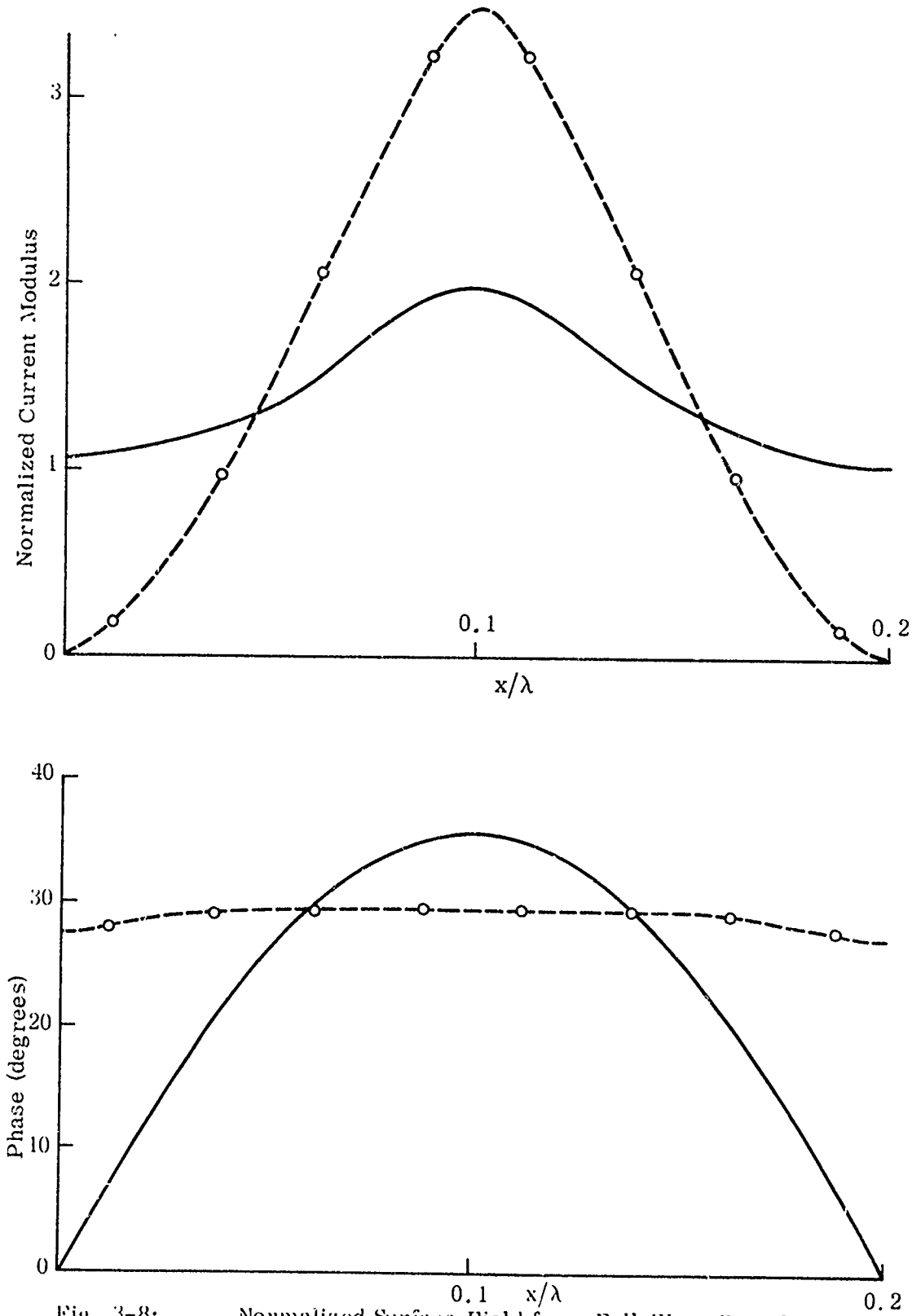

Fig. 3-8: Normalized Surface Field for a Full-Wave Rectified Surface ($d = 0.2\lambda$, $a = 0.1\lambda$ and $\theta = 0$) for E polarization. --o-- exact, — physical optics.

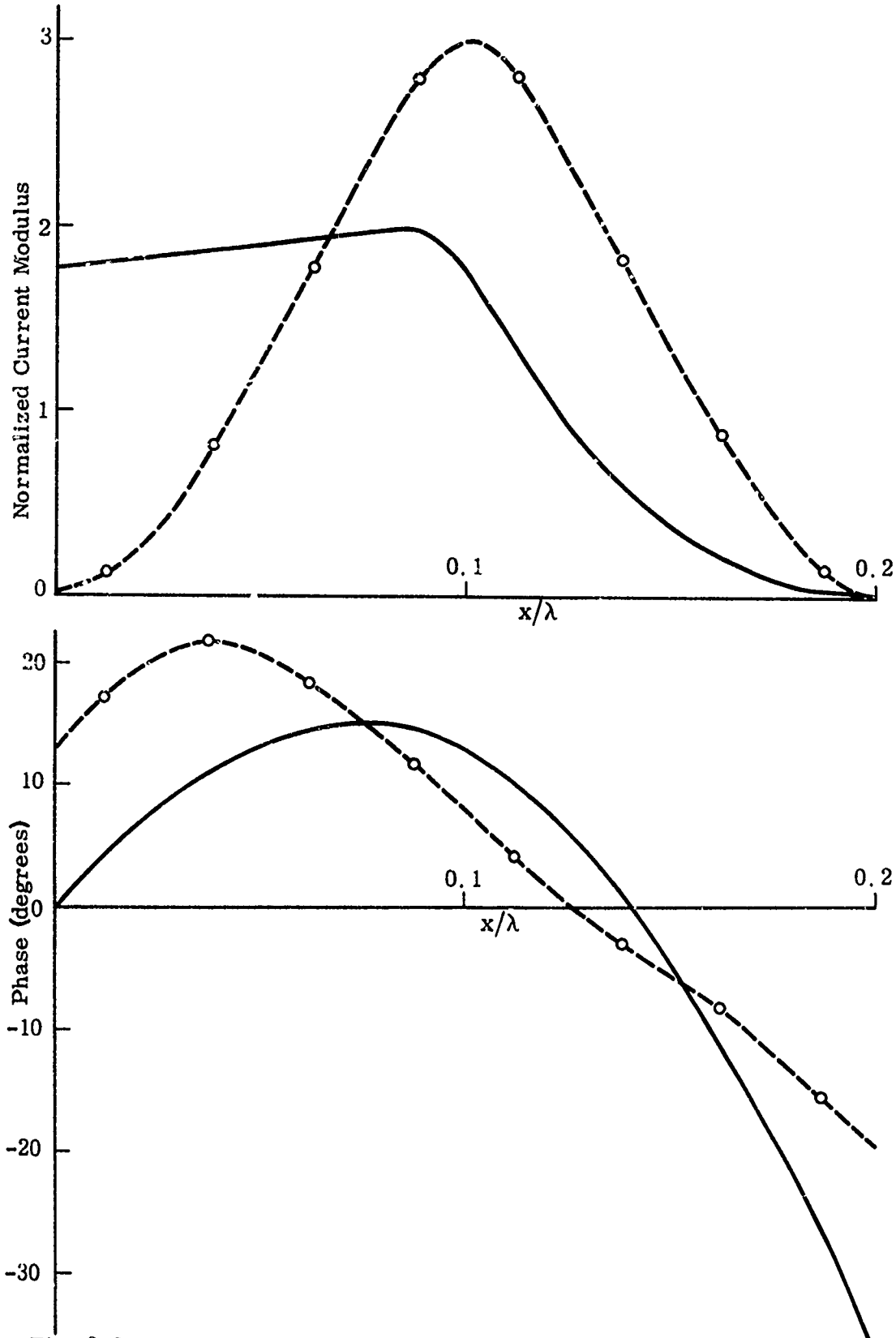

Fig. 3-9: Normalized Surface Field for a Full-Wave Rectified Surface ($d = 0.2\lambda$, $a = 0.1\lambda$ and $\theta = 30^{\circ}$) for E polarization, --o-- exact, — physical optics.

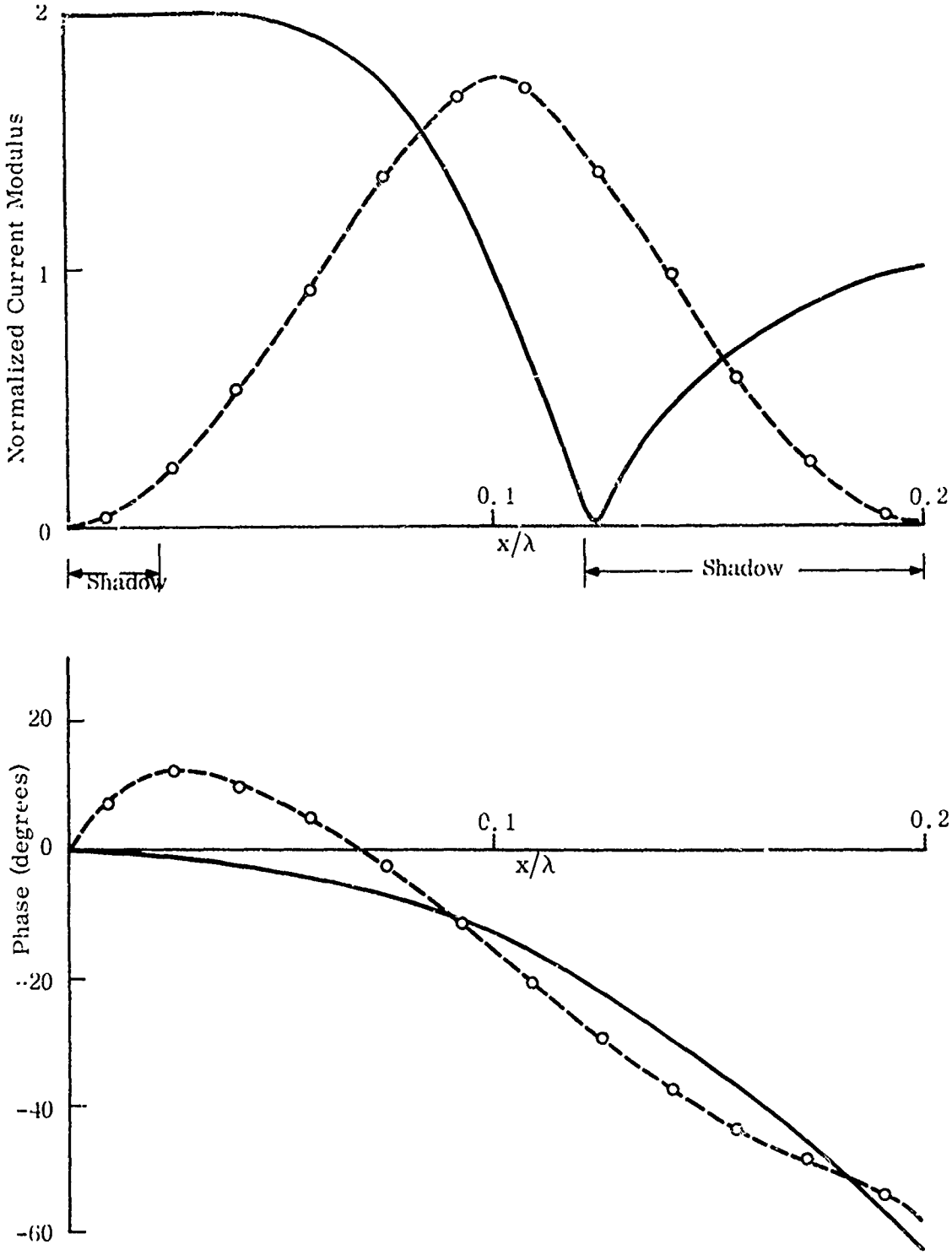

Fig. 3-10: Normalized Surface Field for a Full-Wave Rectified Surface ($d = 0.2\lambda$, $a = 0.1\lambda$ and $\theta = 60^{\circ}$) for E polarization. --o-- exact — physical optics.

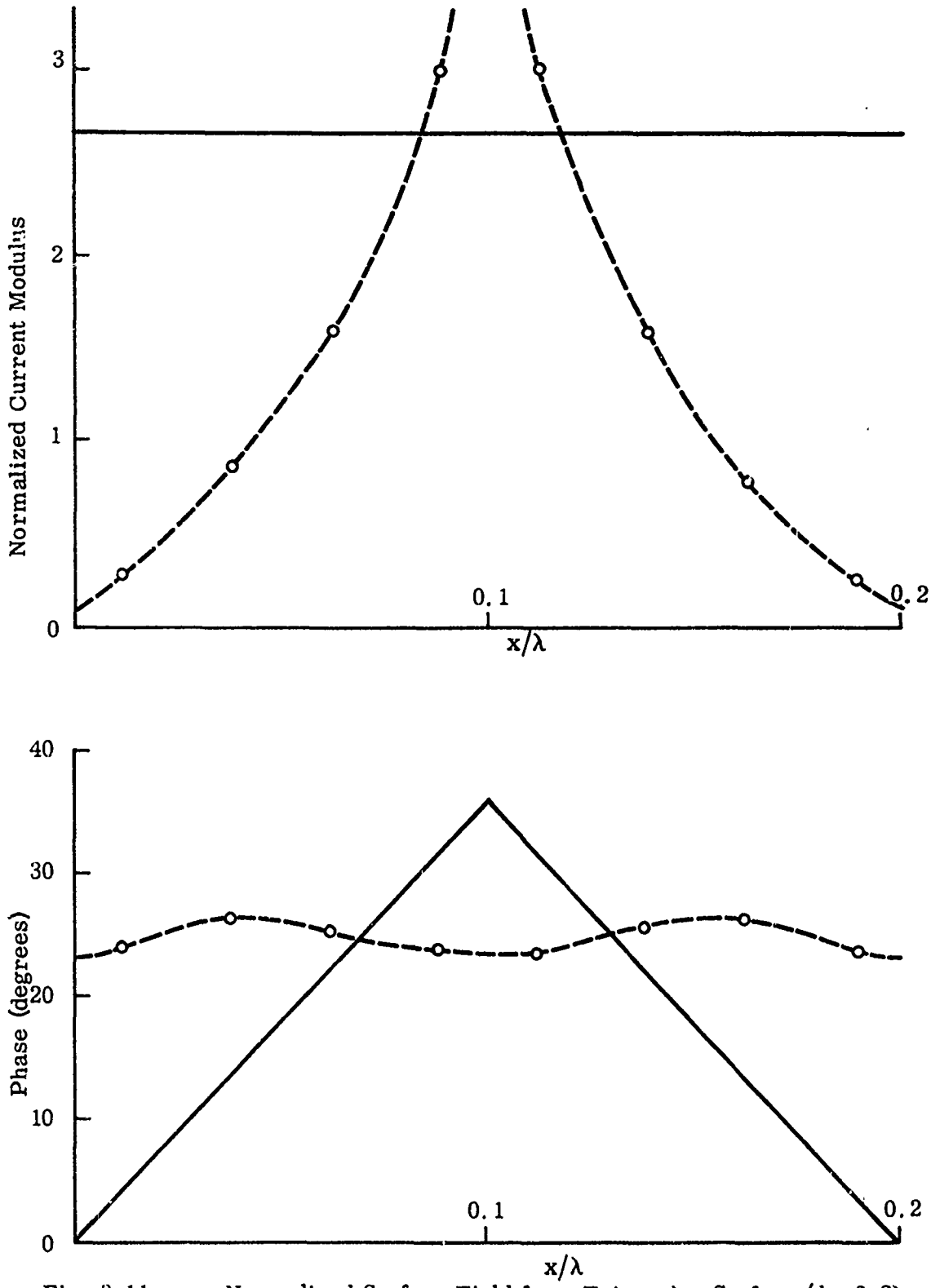

Fig. 3-11: Normalized Surface Field for a Triangular Surface ($d = 0.2\lambda$, $\ell = 0.1\lambda$, $a = 0.1\lambda$ and $\theta = 0$) for E polarization, --o-- exact, — physical optics.

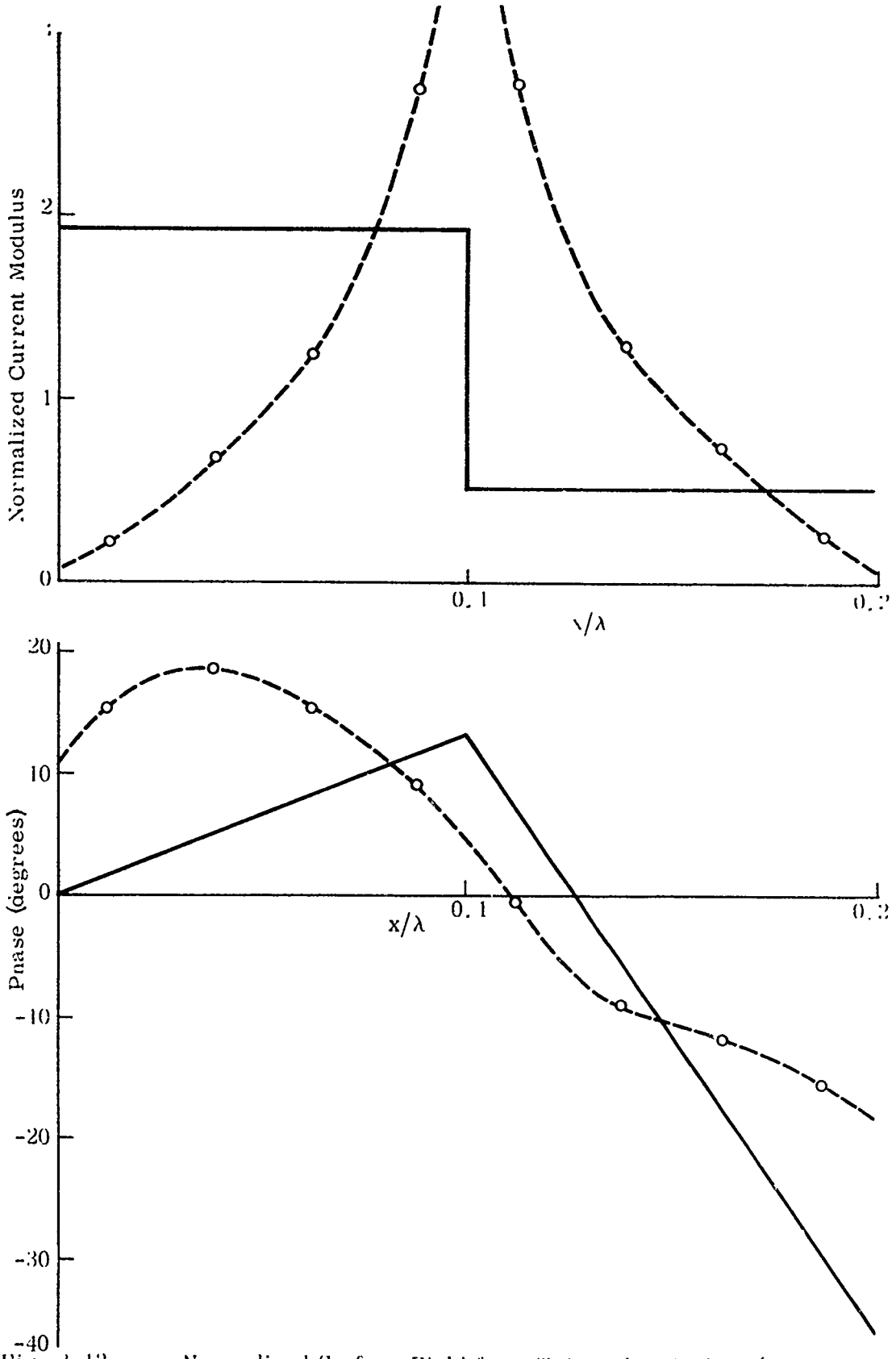

Fig. 3-12: Normalized Surface Field for a Triangular Surface (d = 0.2λ, ℓ = 0.1λ, a = 0.1λ and θ = 30°) for E polarization. --o-- exact — physical optics.

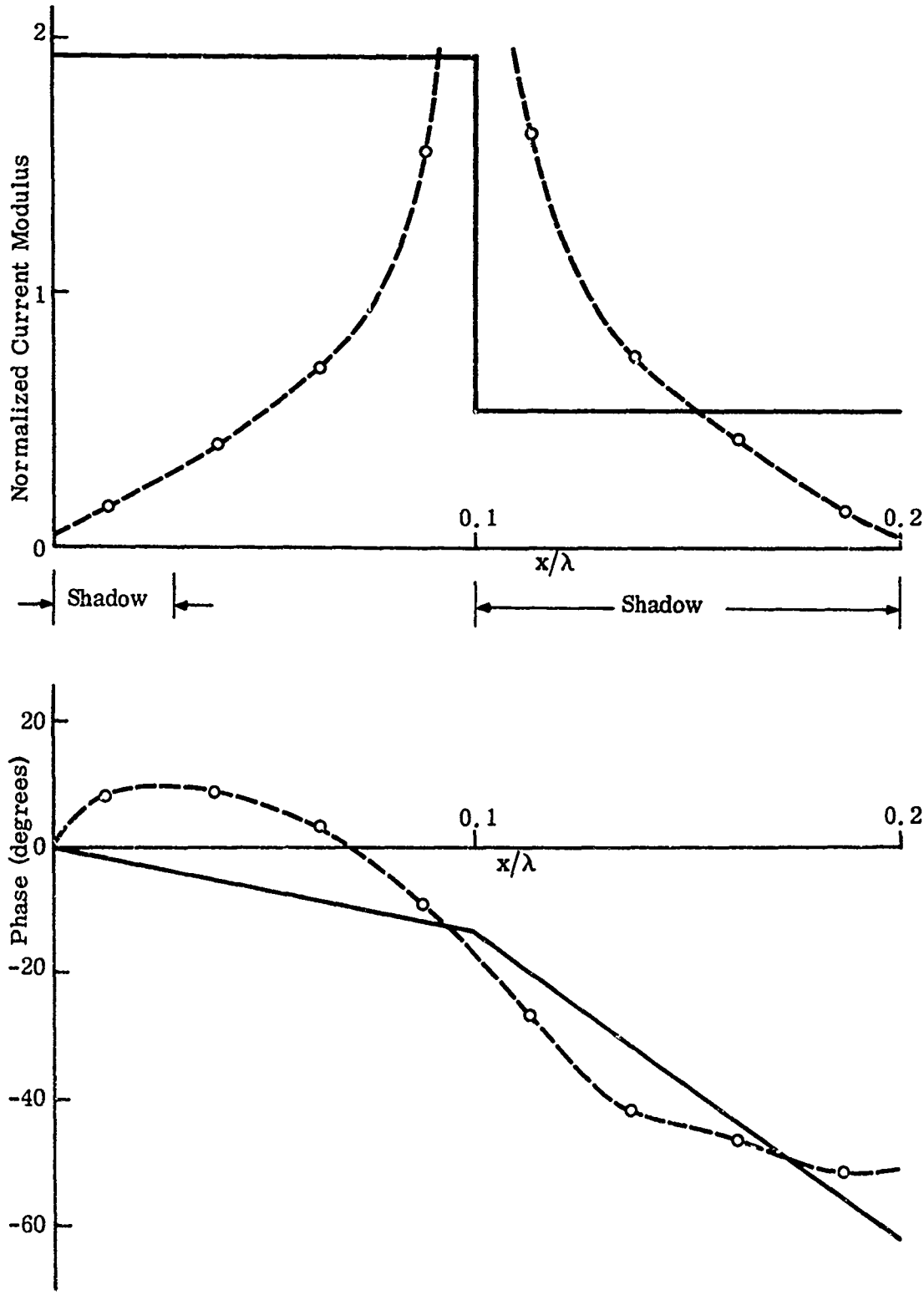

Fig. 3-13: Normalized Surface Field for a Triangular Surface ($d = 0.2\lambda$, $\ell = 0.1\lambda$, $a = 0.1\lambda$ and $\theta = 60^{\circ}$) for E polarization, --o-- exact, — physical optics.

The phase is somewhat more sensitive to θ, and whereas the curve is almost flat for $\theta = 0$, the shape changes noticeably with increase in θ.

Since $k\rho_{min} = 0.064$ (ρ_{min} is the minimum radius of curvature) for the surface, it is not surprising to find that the physical optics approximation bears no resemblance to the exact data. According to physical optics the current within the shadow region should be zero, but exact results prove this is not so, and this is natural because the current must be a continuous function along the surface. The physical optics phase is also poor for $\theta = 0$, but agrees better for large θ, at least in an average sense. In general it is true that the physical optics approximation shows best agreement with the exact data in regions where the radius of curvature is largest. That is, in all cases the maximum discrepancy occurs at the surface peaks and troughs where the radius of curvature is a minimum.

Examination of the remaining profiles show that the shape of the modulus curve is very similar, except in small details, to the corresponding one for the sinusoidal surface, and the phase still remains relatively constant for $\theta = 0$. In general, the above remarks for the sinusoidal surface apply also to these profiles, but each profile has, because of its own geometry, some particular characteristics. For example, in the case of the inverted full-wave rectified profile with $\theta = 60^{\circ}$ (Fig. 3-7), we can see a small standing wave pattern in the phase just outside the shadow. This is probably due to multiple scattering of the incident field by the surface. Another example is the "edge effect" which is clearly evident in the results for the triangular profile.

In order to obtain a better understanding of the surface field, let us go back to the integral equation. If we look at Eq. (2.29) carefully, we observe that for a sufficiently small period we can approximate the kernel by the first two terms, and of these two terms only the first term, which has no singularity, contains the incidence angle. Thus the approximate integral equation becomes

$$\int_0^d G_1^*(x,y;x',y')K_z(x')\,e^{jkx'\sin\theta}\sqrt{1+f'(x')^2}\,dx' \cong \frac{2d}{\omega\mu}\,e^{jky\cos\theta} \tag{3.5}$$

where

$$G_1^*(x,y;x',y') = \frac{1}{k\cos\theta}\,e^{-jk|y-y'|\cos\theta} -$$

$$-\frac{jd}{2\pi}\log\left[\left\{1-e^{-\frac{2\pi}{d}\left[|y-y'|+j(x-x')\right]}\right\}\left\{1-e^{-\frac{2\pi}{d}\left[|y-y'|-j(x-x')\right]}\right\}\right] \tag{3.6}$$

Since the integral equation is singular, a rough estimate of the solution to the integral equation may be obtained by examining the equation in the neighborhood of the singularity. Thus

$$\lim_{\substack{|x-x'|\to 0\\|y-y'|\to 0}} G_1^*(x,y;x',y') = \frac{1}{k\cos\theta} - \frac{jd}{2\pi}\lim_{\substack{|x-x'|\to 0\\|y-y'|\to 0}}\log[\ ], \tag{3.7}$$

where

$$\lim_{\substack{|x-x'|\to 0\\|y-y'|\to 0}}\log[\ ] = \lim_{\substack{|x-x'|\to 0\\|y-y'|\to 0}}\log\left[\left\{1-e^{-\frac{2\pi}{d}\left[|y-y'|+j(x-x')\right]}\right\}\times\left\{1-e^{-\frac{2\pi}{d}\left[|y-y'|-j(x-x')\right]}\right\}\right]$$

$$= \lim_{\substack{|x-x'|\to 0\\|y-y'|\to 0}}\log\left\{1+e^{-\frac{4\pi}{d}|y-y'|}-2e^{-\frac{2\pi}{d}|y-y'|}\cos\left[\frac{2\pi}{d}(x-x')\right]\right\}$$

$$= \lim_{|y-y'|\to 0}\log\left\{1+e^{-\frac{4\pi}{d}|y-y'|}-2e^{-\frac{2\pi}{d}|y-y'|}\right\}.$$

Using the following expression,

$$e^x = 1 + x + \frac{x^2}{2!} + \frac{x^3}{3!} + \ldots ,$$

we obtain

$$\lim_{\substack{|x-x'| \to 0 \\ |y-y'| \to 0}} \log[\ ] \cong \lim_{\epsilon \to 0} \log \epsilon , \tag{3.8}$$

where

$$\epsilon = \frac{12\pi^2}{d^2} |y-y'|^2 .$$

Thus in the neighborhood of singularity, Eq. (3.5) becomes

$$\int_{x-\delta}^{x+\delta} \left(\frac{1}{k\cos\theta} - \frac{jd}{2\pi} \log x' \right) K_z(x') e^{-jkx'\sin\theta} \sqrt{1+f'(x')^2}\, dx' \cong \frac{2d}{\omega\mu} e^{jky\cos\theta} \tag{3.9}$$

where $|x-x'| < \delta$. $\delta > 0$ is an arbitrarily small number. If we assume that the factor $K_z(x') e^{-jkx'\sin\theta} \sqrt{1+f'(x')^2}$ remains constant in this small region, we can solve Eq. (3.9) to get

$$\left[\frac{1}{k\cos\theta} + \frac{jd}{2\pi} \right] \delta K_z(x) e^{-jkx\sin\theta} \sqrt{1+f'(x)^2} \cong \frac{d}{\omega\mu} e^{jky\cos\theta} . \tag{3.10}$$

It now follows immediately that if the period d is sufficiently small, the first term in the square bracket dominates, and so the modulus of the surface field is seen to be proportional to $\cos\theta$, a scaling factor. This is consistent with the numerical results.

The effect on the surface field for a sinusoidal profile due to change in the amplitude as the period is kept constant, and $\theta = 0$ is shown in Figs. 3-2, 3-14 and 3-15. It is observed that as the height decreases, so does the current concentration near the peaks; the phase, on the other hand, is much more nearly constant, and is more akin to that for a flat surface than a sinusoidal one.

3.2 Surface of Slightly Larger Period ($0.2 \lesssim d/\lambda \lesssim 0.6$)

Figures 3-16 and 3-17 show the surface field for a sinusoidal profile with $d = 0.4\lambda$, $a = 0.2\lambda$ and $\theta = 0$, 60° respectively. Comparison with Figs. 3-2 and 3-4 indicates that doubling both d and a has little effect on the modulus of the current, but has a marked effect on the phase. For normal incidence the phase curve still has a small sag at the surface trough region. Results for $d = 0.6\lambda$, $a = 0.3\lambda$ and $\theta = 60^{\circ}$ are shown in Figs. 3-18 and 3-19 for the inverted full-wave rectified and full-wave rectified surfaces respectively. Although the overall shape of the modulus curves bears much resemblance to the previous cases of small period (Figs. 3-7 and 3-10), there is evidence (small undulations along the curves) of stronger multiple scattering here. Again, the physical optics method fails to give satisfactory results in all cases.

3.3 Surfaces of Larger Period ($d/\lambda \gtrsim 0.6$)

Let us now consider surfaces of larger period for which the requirements of physical optics are more nearly satisfied. Referring to Eq. (2.30) it is seen that as d becomes larger, the number m which makes X_m^+ and X_m^- purely imaginary increases (implying more propagating modes), and the infinite series of the kernel therefore becomes more important. One consequence of this is that the surface current distributions for surfaces of large period are much more complicated and quite different from those for surfaces of small period.

Figures 3-20 and 3-21 represent two cases of a sinusoidal surface at normal incidence with $d = 0.95\lambda$ and $a = 0.25\lambda$; $d = 1.90\lambda$ and $a = 0.25\lambda$ respectively. In the first, the modulus displays a strong oscillation having a

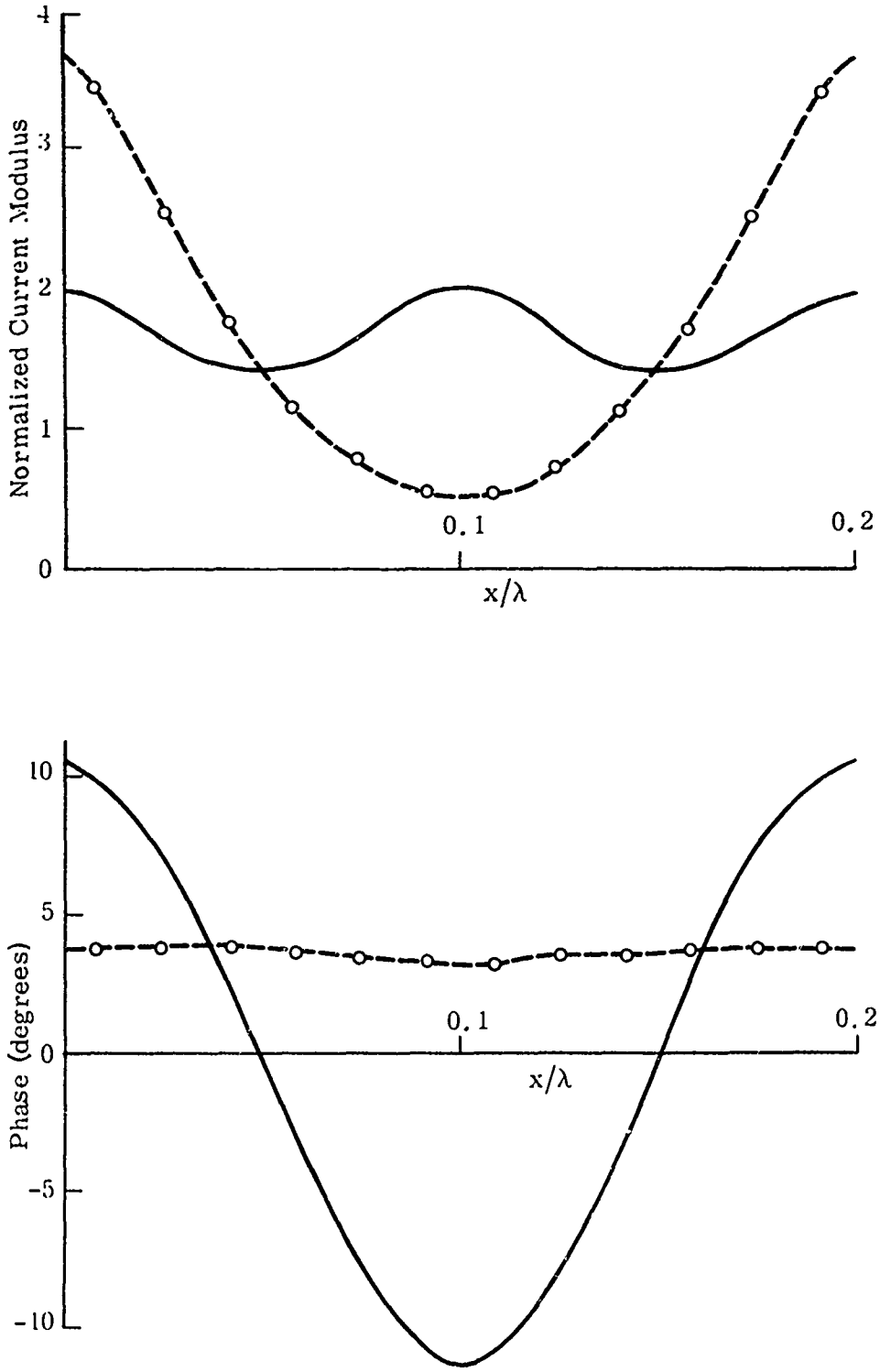

Fig. 3-14: Normalized Surface Field for a Sinusoidal Surface ($d = 0.2\lambda$, $a = 0.03\lambda$ and $\theta = 0$) for E polarization, --o-- exact, — physical optics.

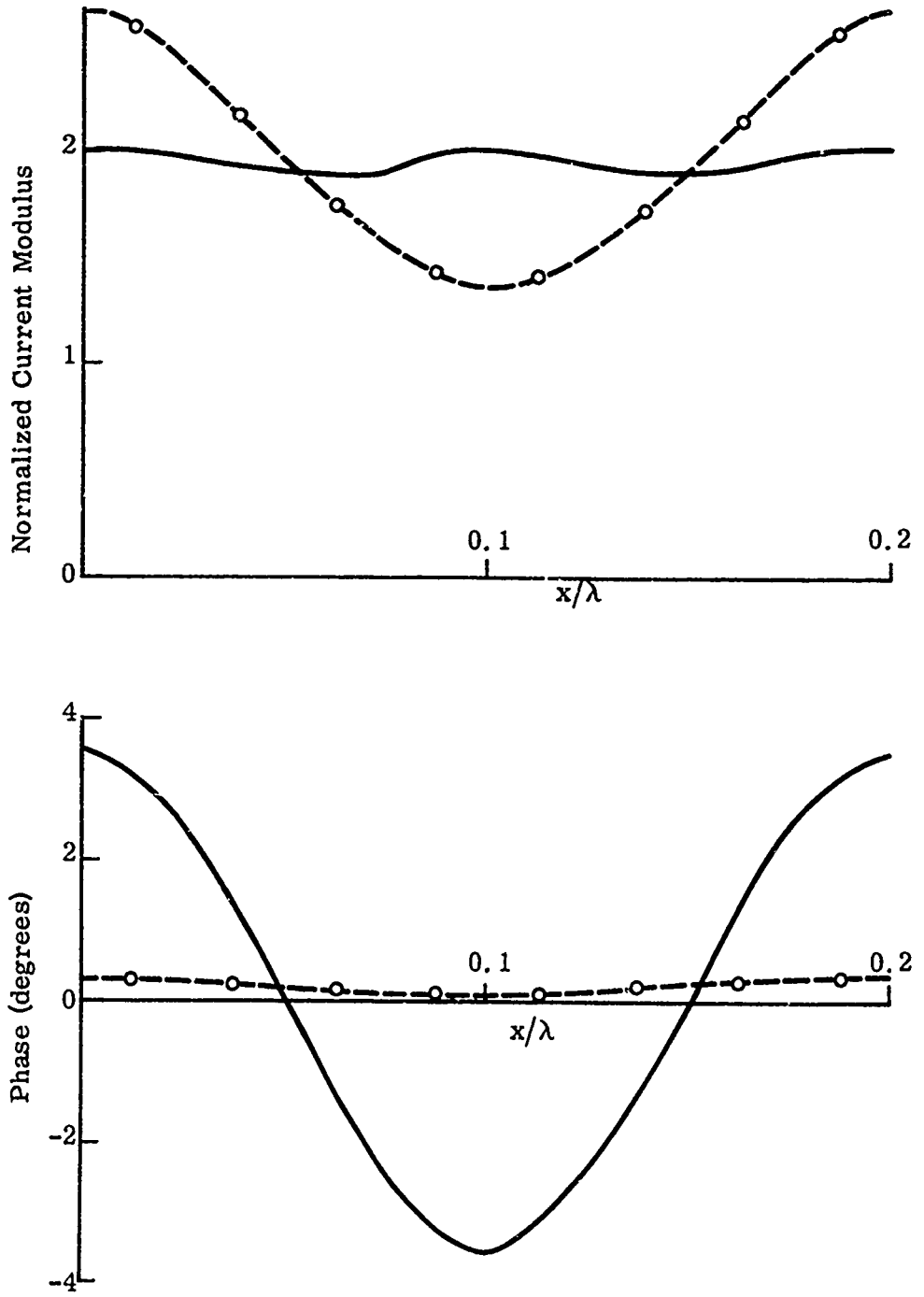

Fig. 3-15: Normalized Surface Field for a Sinusoidal Surface ($d = 0.2\lambda$, $a = 0.01\lambda$ and $\theta = 0$) for E polarization, --o-- exact, — physical optics.

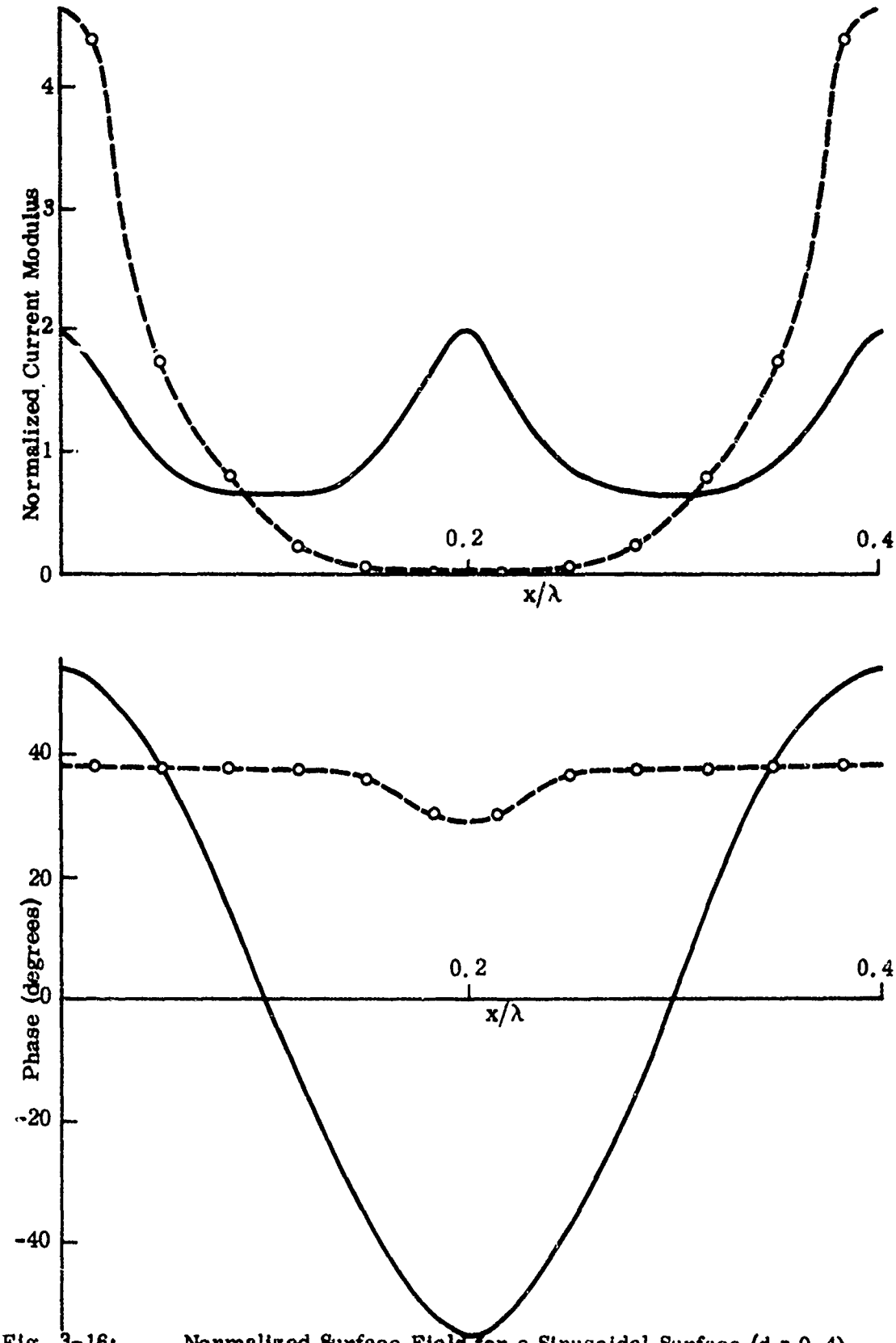

Fig. 3-16: Normalized Surface Field for a Sinusoidal Surface ($d = 0.4\lambda$, $a = 0.2\lambda$ and $\theta = 0$) for E polarization, --o-- exact, — physical optics.

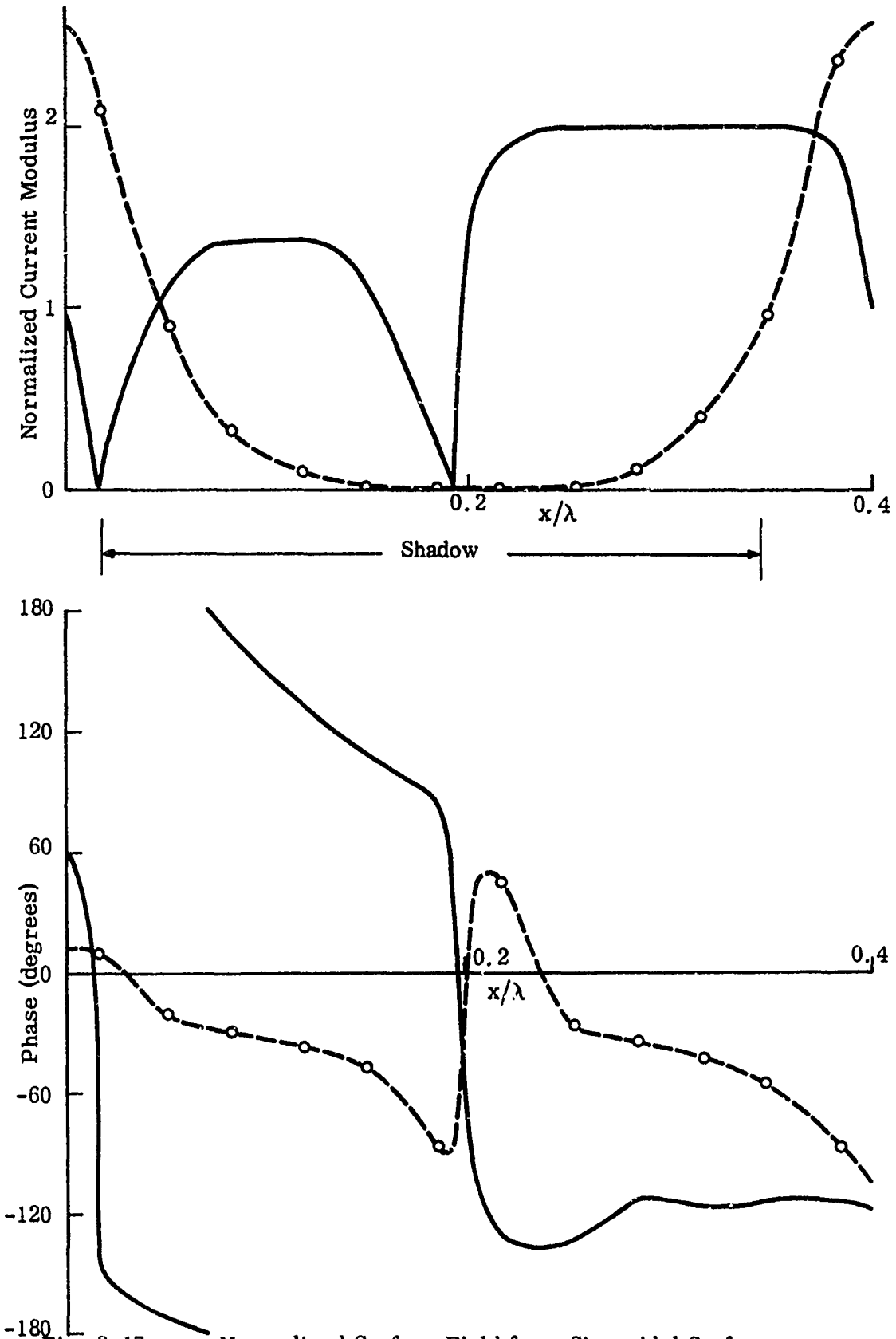

Fig. 3-17: Normalized Surface Field for a Sinusoidal Surface ($d = 0.4\lambda$, $a = 0.2\lambda$ and $\theta = 60^{\circ}$) for E polarization, --o-- exact. — physical optics.

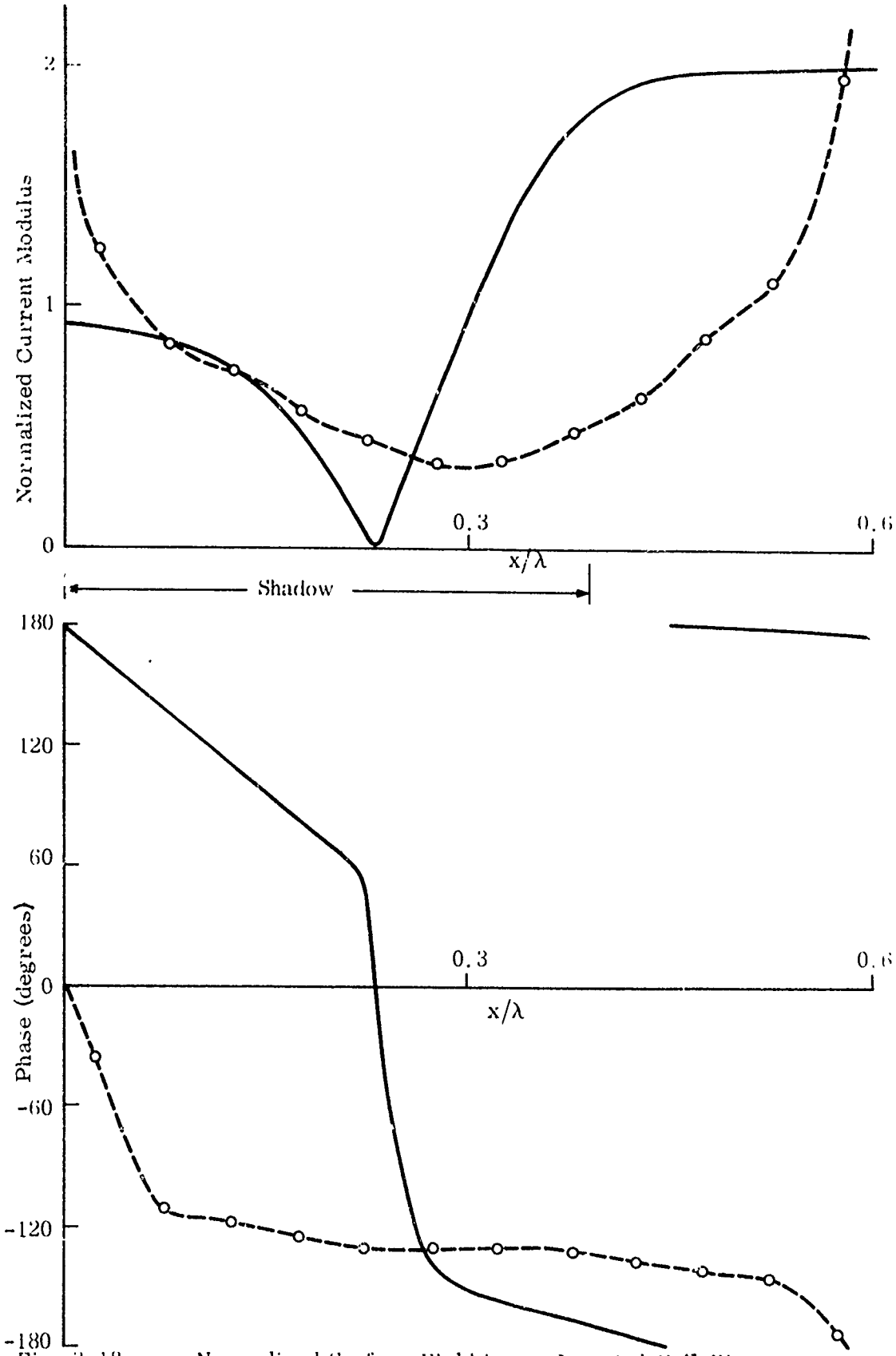

Fig. 3-18: Normalized Surface Field for an Inverted Full-Wave Rectified Surface ($d = 0.6\lambda$, $a = 0.3\lambda$ and $\theta = 60^{\circ}$) for E polarization. --o-- exact. — physical optics.

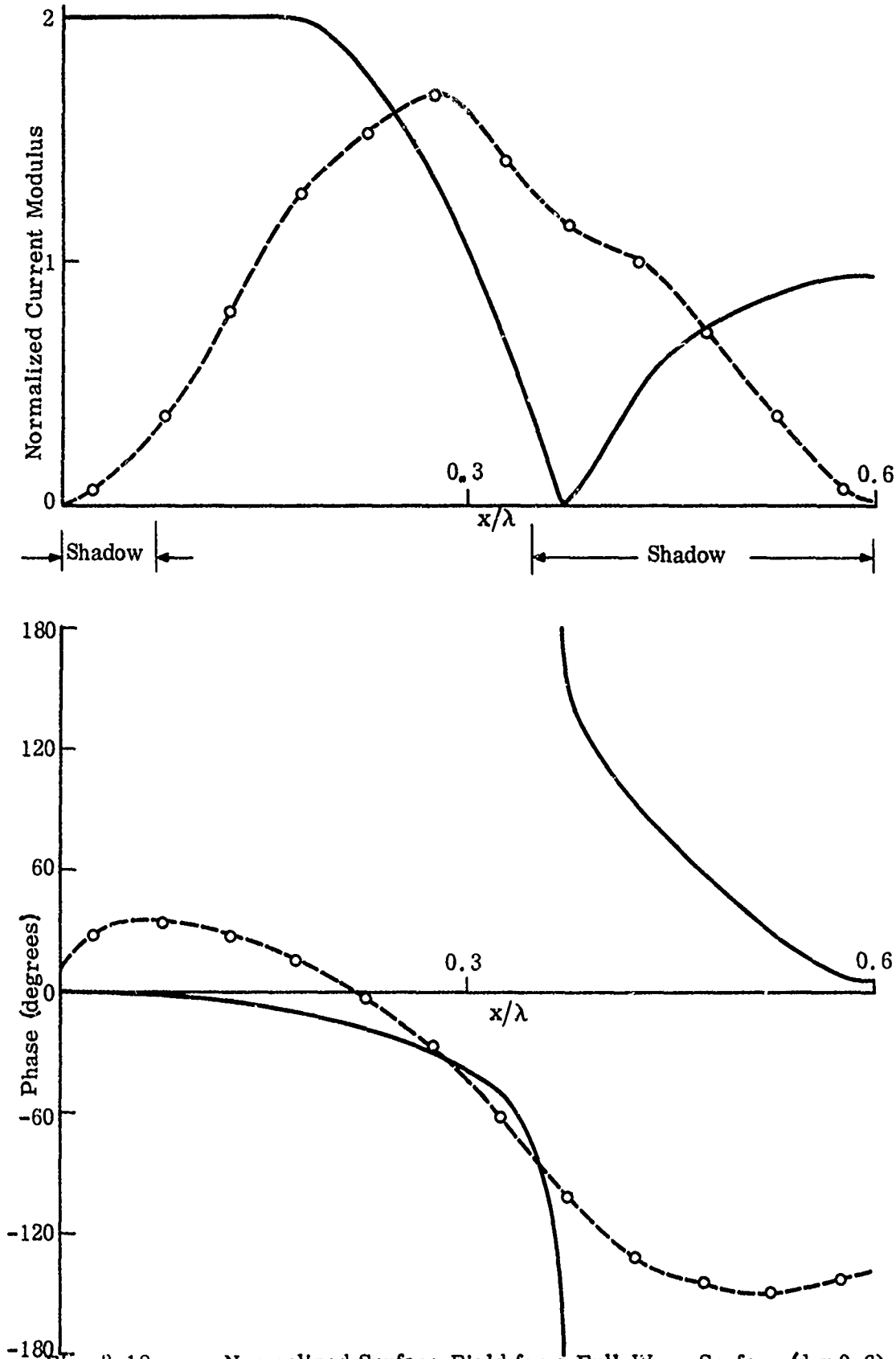

Fig. 3-19: Normalized Surface Field for a Full-Wave Surface ($d = 0.6\lambda$, $a = 0.3\lambda$ and $\theta = 60^{\circ}$) for E polarization, --o-- exact, — physical optics.

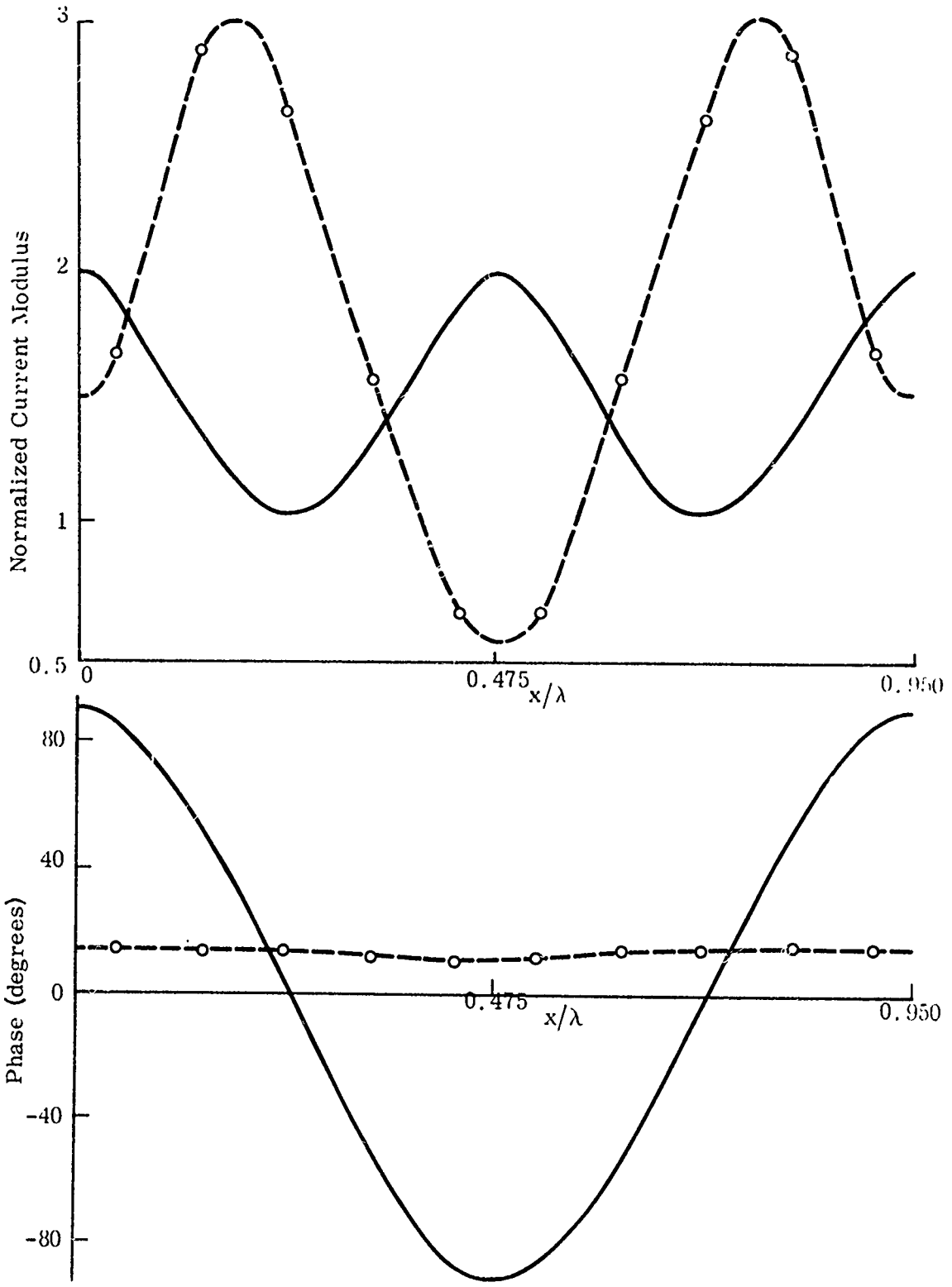

Fig. 3-20: Normalized Surface Field for a Sinusoidal Surface ($d = 0.95\lambda$, $a = 0.25\lambda$ and $\theta = 0$) for E polarization. --o-- exact, — physical optics.

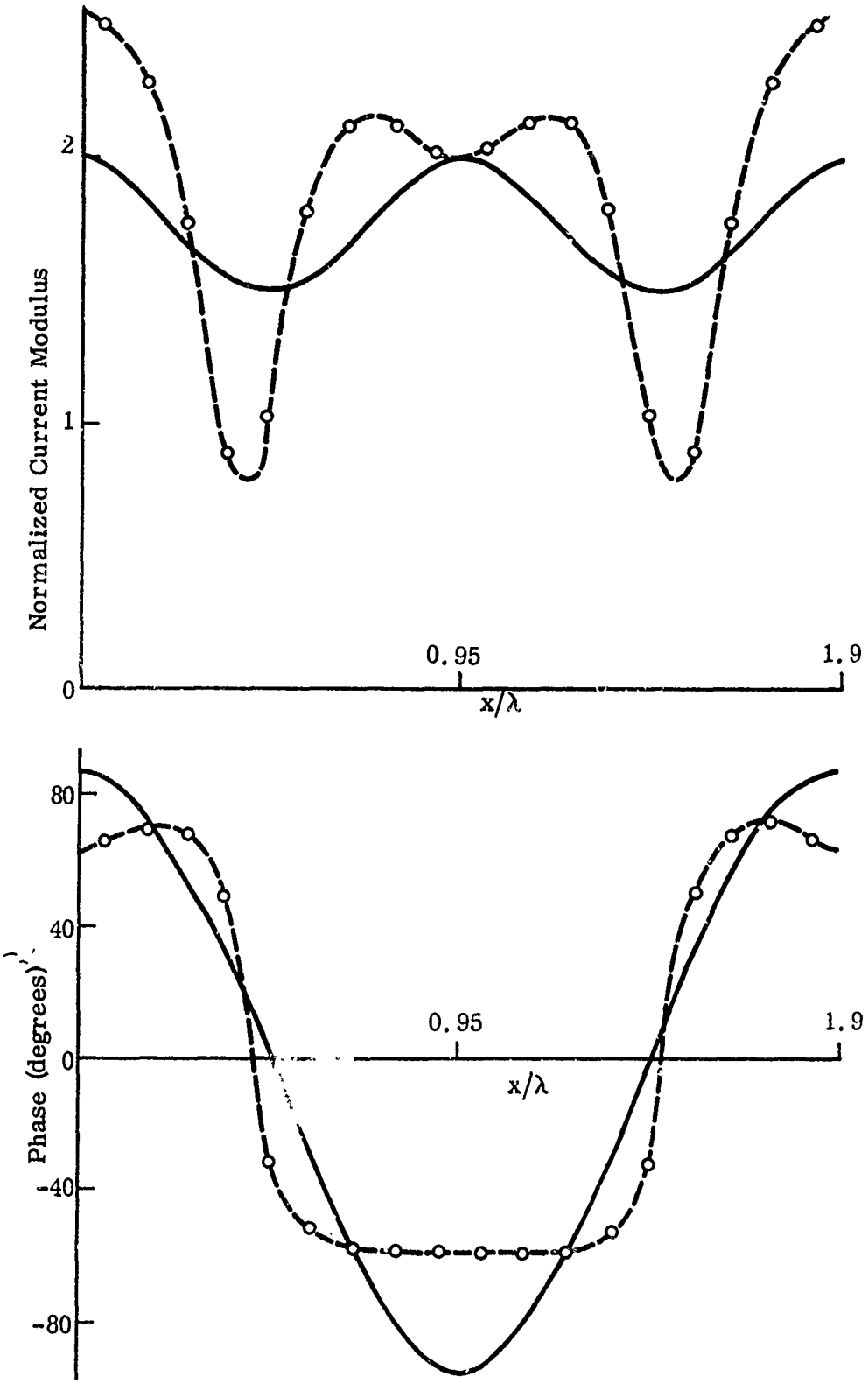

Fig. 3-21: Normalized Surface Field for a Sinusoidal Surface ($d = 1.9\lambda$, $a = 0.25\lambda$ and $\theta = 0$) for E polarization, --o-- exact, — physical optics.

standing wave ratio of about 6 and a period of 0.6λ. Maxima occur at a distance of 0.17λ from the peaks while a minimum exists at the trough of the surface. The exact phase is still characterized by the familiar almost-constant value. The physical optics approximation gives no agreement with the exact solution, but in the second example for which the period has been doubled while keeping the height constant, the physical optics approximation is better, though there are some noticeable discrepancies. The maxima of the modulus still occur at the surface peaks, but minima appear where the surface slope changes sign, that is, where the surface crosses the x axis. The minimum radii of curvature for these two cases are $k\rho_{min} = 0.572$ and 2.30, respectively.

A case showing better agreement between the exact solution and the physical optics approximation is given in Fig. 3-22, where the surface is a sinusoidal one with $d = 1.6\lambda$, $a = 0.1\lambda$ ($k\rho_{min} = 4.07$), and $\theta = 45^{\circ}$. There is no obvious explanation for the apparent shift between the exact and physical optics curves.

To examine the effect on the surface field of a gradual increase in the surface height when the period and angle of incidence are kept fixed, we select the sinusoidal surface with $d = 1.155\lambda$, $\theta = 60^{\circ}$, and a varying from 0.05λ to 0.7λ. The minimum radii of curvature for these cases are as follows:

Amplitude a (λ)	$k\rho_{min}$
0.05	4.260
0.1	2.130
0.2	1.065
0.3	0.710
0.4	0.533
0.5	0.426
0.6	0.355
0.7	0.304

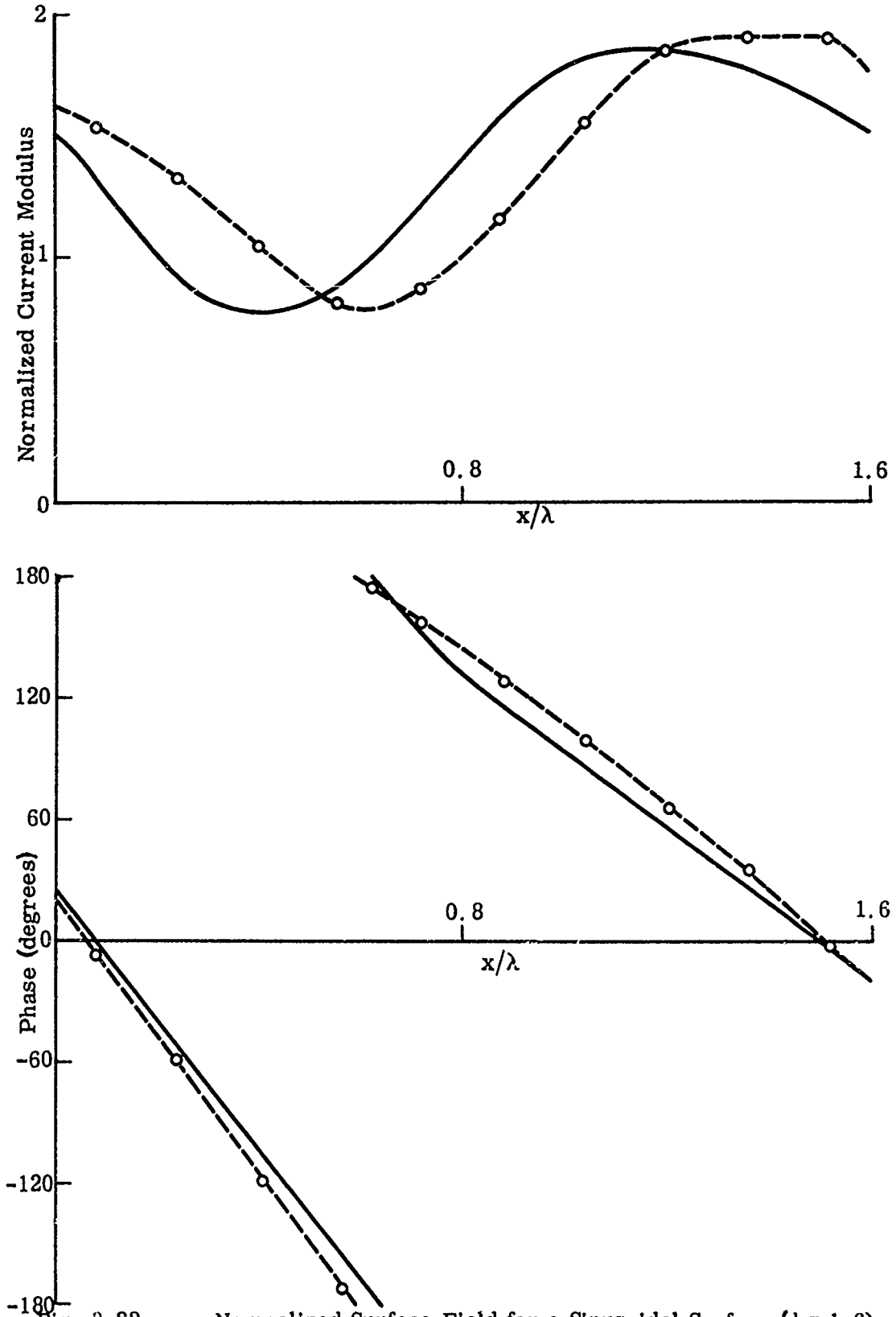

Fig. 3-22: Normalized Surface Field for a Sinusoidal Surface ($d = 1.6\lambda$, $a = 0.1\lambda$ and $\theta = 45^{\circ}$) for E polarization, --o-- exact, — physical optics.

The numerical results are illustrated in Figs. 3-23 through 3-30. It is seen that the agreement between the physical optics prediction and the exact solution deteriorates gradually as the amplitude is increased. If we examine the phase curves with a little care we find that the physical optics phase agrees better with the exact phase in the illuminated region, and both of them are relatively constant there. In contrast to the situation for surfaces of small period, the field is very sensitive to a change in surface height, and it is therefore very difficult to accurately predict. The undulations in the modulus curves are evidence of multiple scattering which is particularly noticeable when $a = 0.3\lambda$. If the surface height is sufficiently large ($a \geq 0.5\lambda$), the surface field near the region of a surface trough is relatively small.

Since the field is so small over most of the concave portions of the surface, it is of interest to see how much the surface field as a whole is affected by the actual geometry of the concavities. We examine this by replacing the concave part ($d/4 \leq x \leq 3d/4$) of a sinusoidal surface by a flat part, and the results are presented in Fig. 3-31 for $a = 0.5\lambda$ and $\theta = 60^{\circ}$. Comparison with Fig. 3-28 shows that the replacement has little effect on the surface field in the illuminated region, but does have a marked effect in the shadow.

Additional data are presented in Figs. 3-32 and 3-33 for a full-wave rectified profile where $d = 0.75\lambda$, $a = 0.6\lambda$ and $\theta = 41.8^{\circ}$, and a triangular profile where $d = 1.75\lambda$, $\theta_1 = 20^{\circ}$, $\theta_2 = 66^{\circ}$ and $\theta = 12.2^{\circ}$. For the rectified profile (Fig. 3-32), the current modulus no longer has a maximum at the surface peaks where $k\rho$ is a minimum. In Fig. 3-33, the current modulus shows clearly the "edge effect" in the neighborhood of the edge, and the physical optics phase agrees relatively well with the exact phase, except near the trough region. In both cases the modulus is zero at the center of the surface trough. Fig. 3-34 represents the case of an inverted full-wave rectified profile with $d = 0.95\lambda$, $a = 0.25\lambda$ and $\theta = 0$.

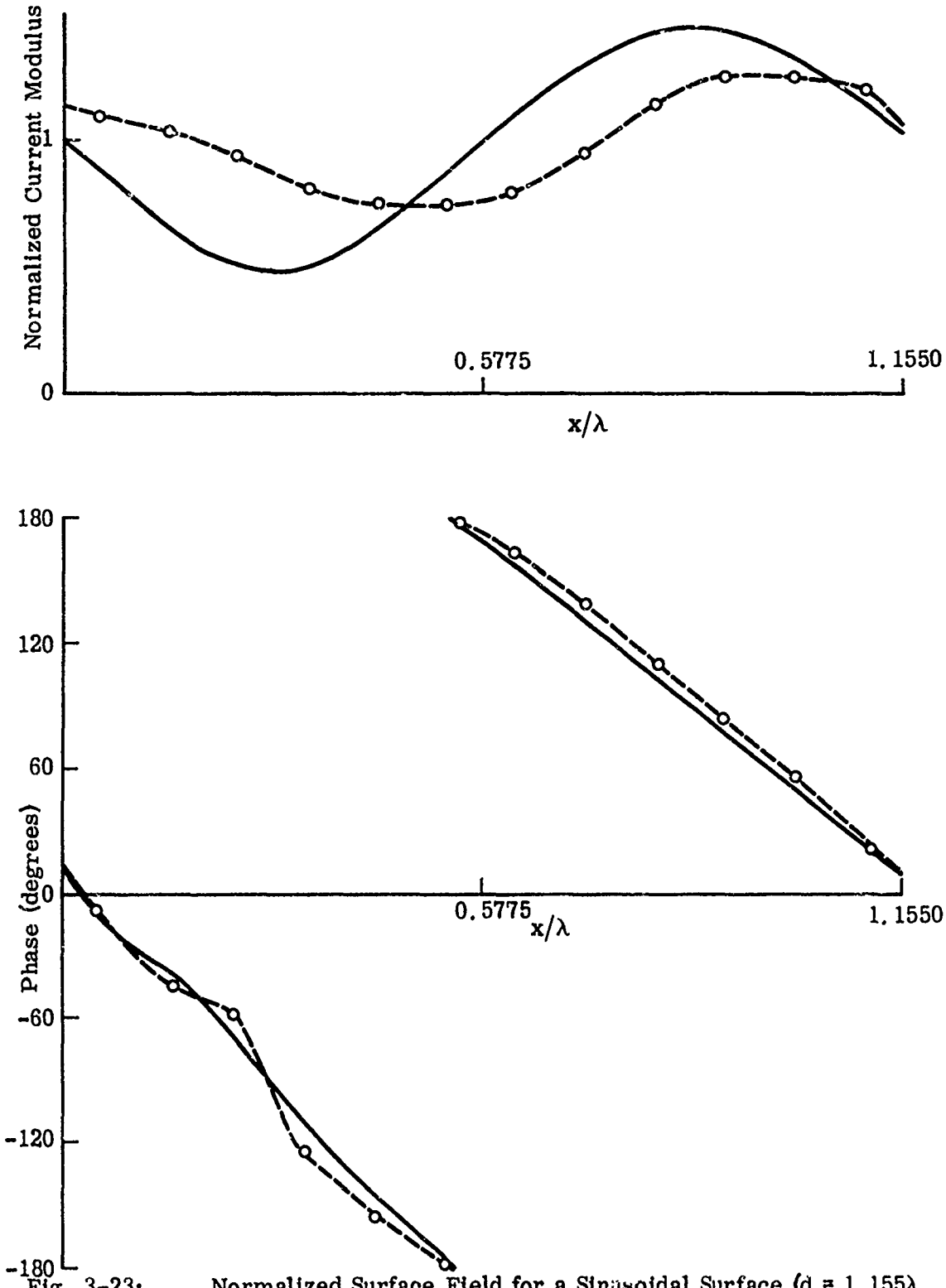

Fig. 3-23: Normalized Surface Field for a Sinusoidal Surface ($d = 1.155\lambda$, $a = 0.05\lambda$ and $\theta = 60^{\circ}$) for E polarization, --o-- exact, — physical optics.

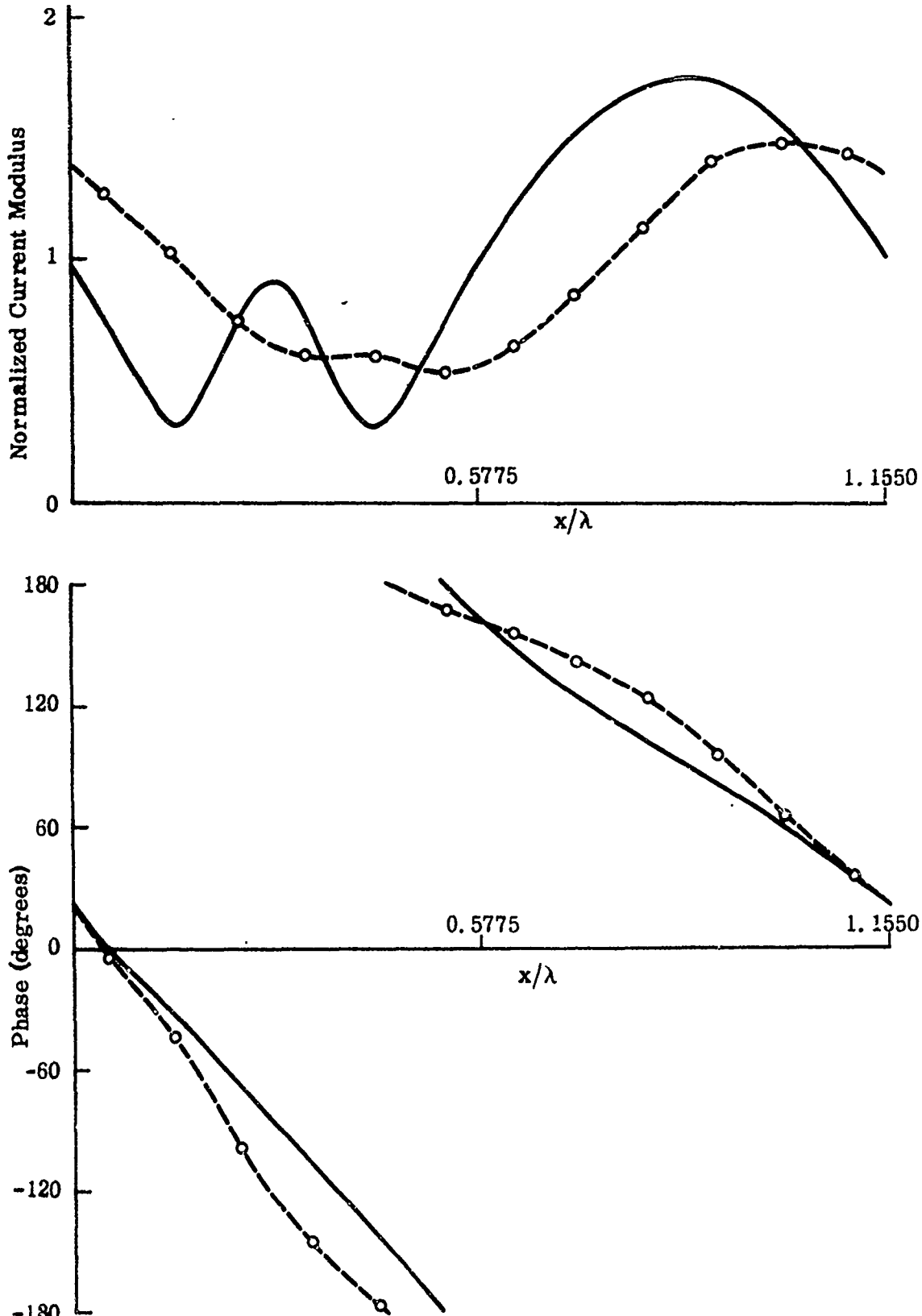

Fig. 3-24: Normalized Surface Field for a Sinusoidal Surface ($d = 1.155\lambda$, $a = 0.1\lambda$ and $\theta = 60^{\circ}$) for E polarization, --o-- exact, — physical optics.

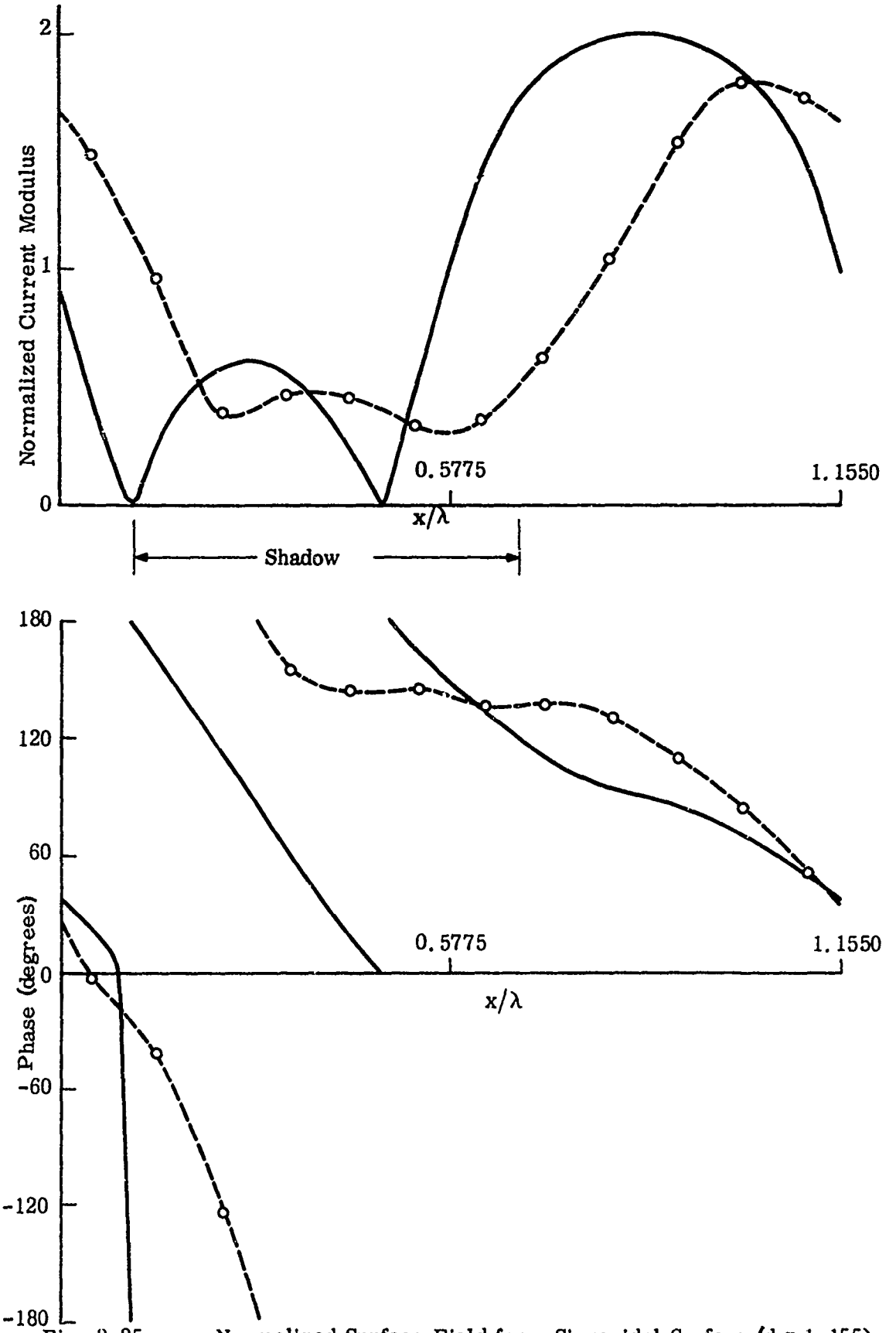

Fig. 3-25: Normalized Surface Field for a Sinusoidal Surface ($d = 1.155\lambda$, $a = 0.2\lambda$ and $\theta = 60^{\circ}$) for E polarization, --o-- exact, — physical optics.

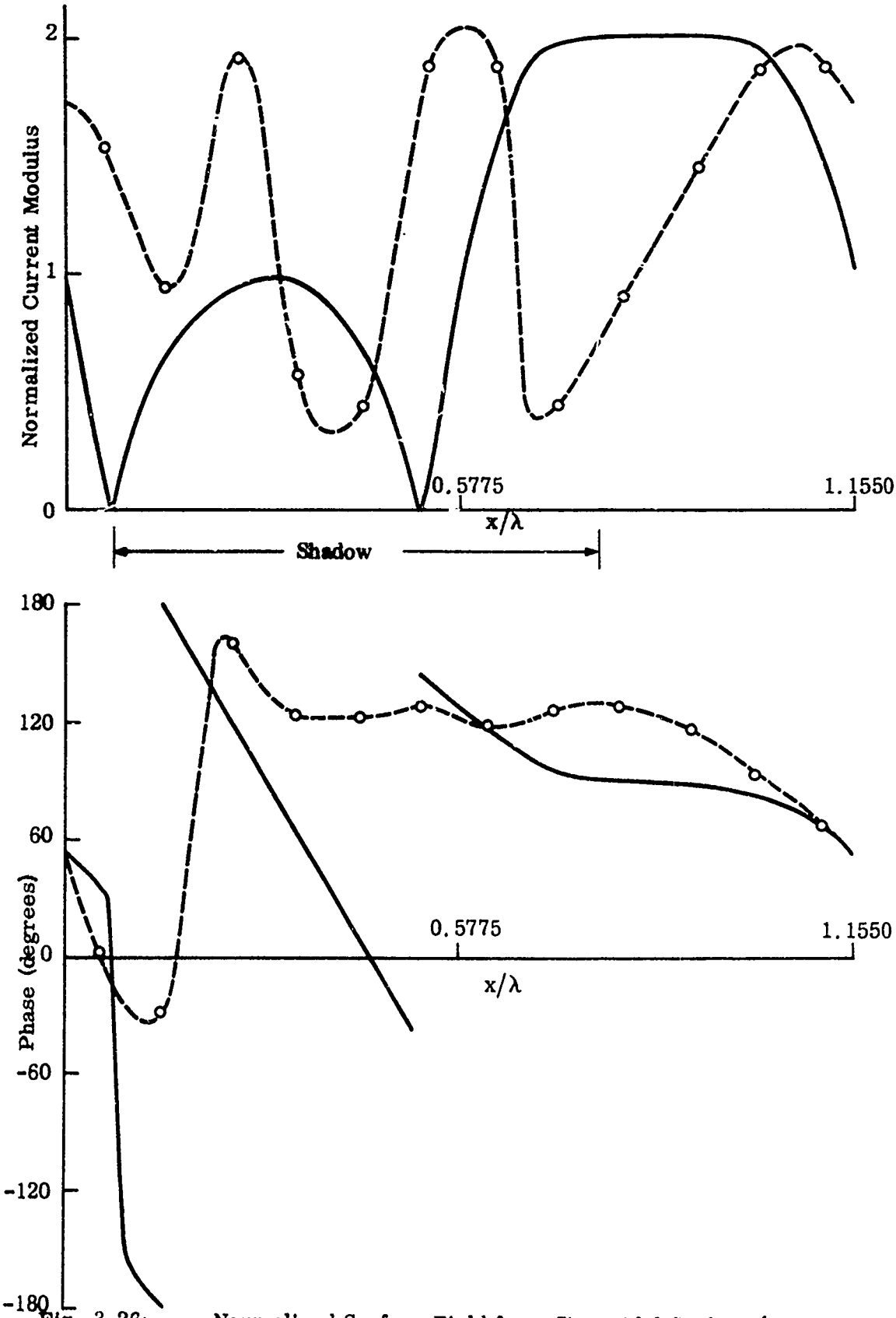

Fig. 3-26: Normalized Surface Field for a Sinusoidal Surface ($d = 1.155\lambda$, $a = 0.3\lambda$ and $\theta = 60^{\circ}$) for E polarization, --o-- exact, — physical optics.

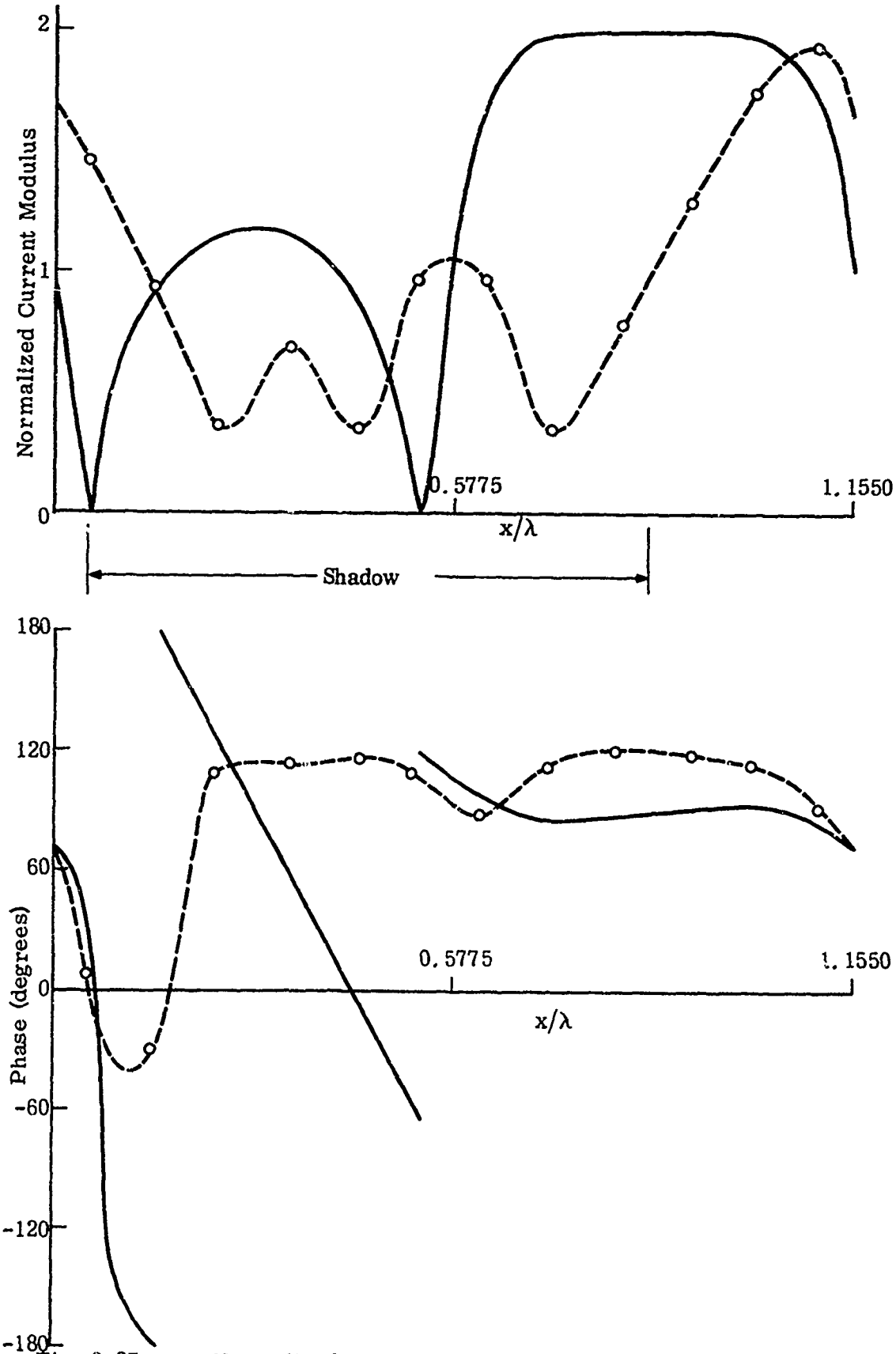

Fig. 3-27: Normalized Surface Field for a Sinusoidal Surface ($d = 1.155\lambda$, $a = 0.4\lambda$ and $\theta = 60^{\circ}$) for E polarization, --o-- exact, — physical optics.

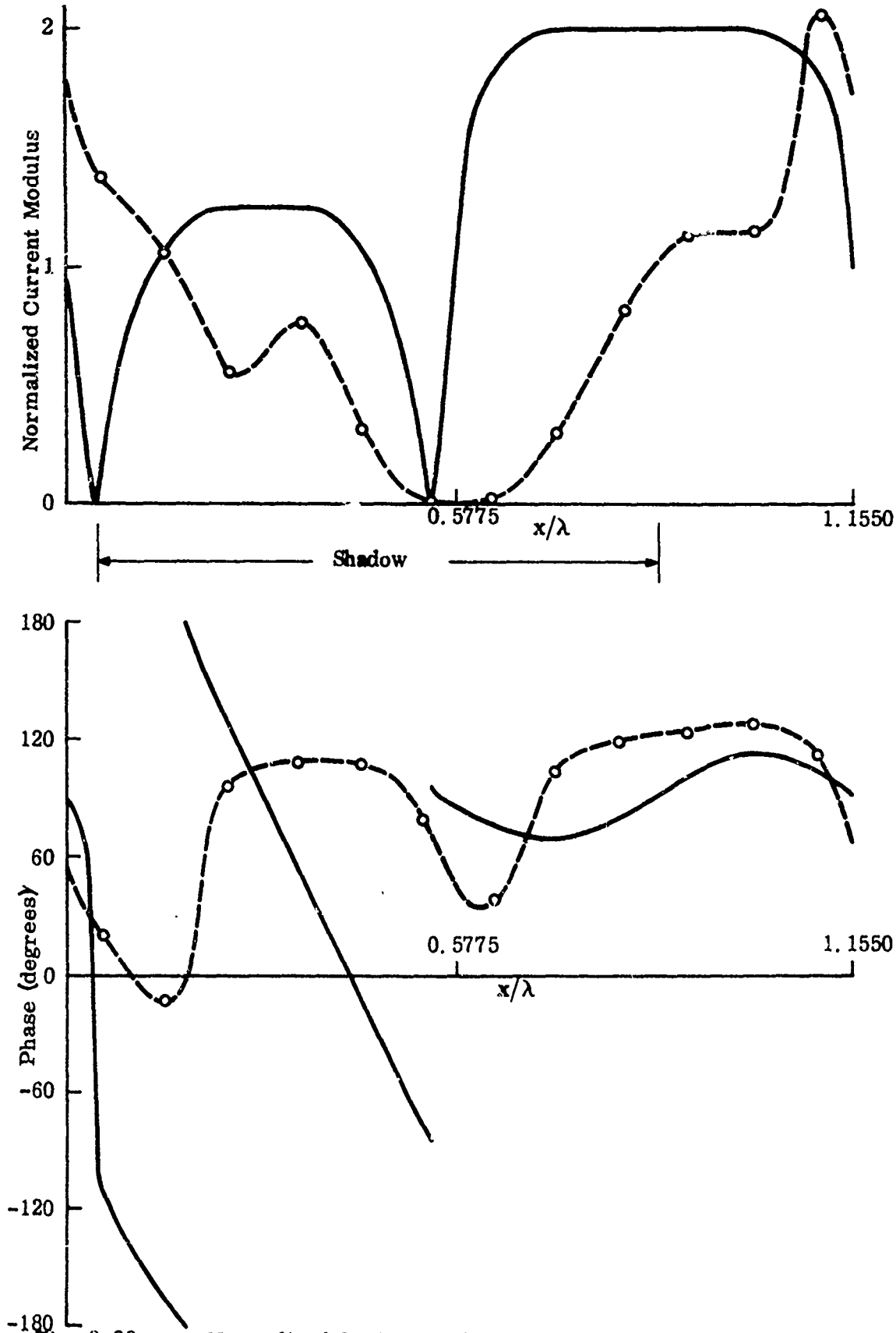

Fig. 3-28: Normalized Surface Field for a Sinusoidal Surface ($d = 1.155\lambda$, $a = 0.5\lambda$ and $\theta = 60^{\circ}$) for E polarization, --o-- exact, — physical optics.

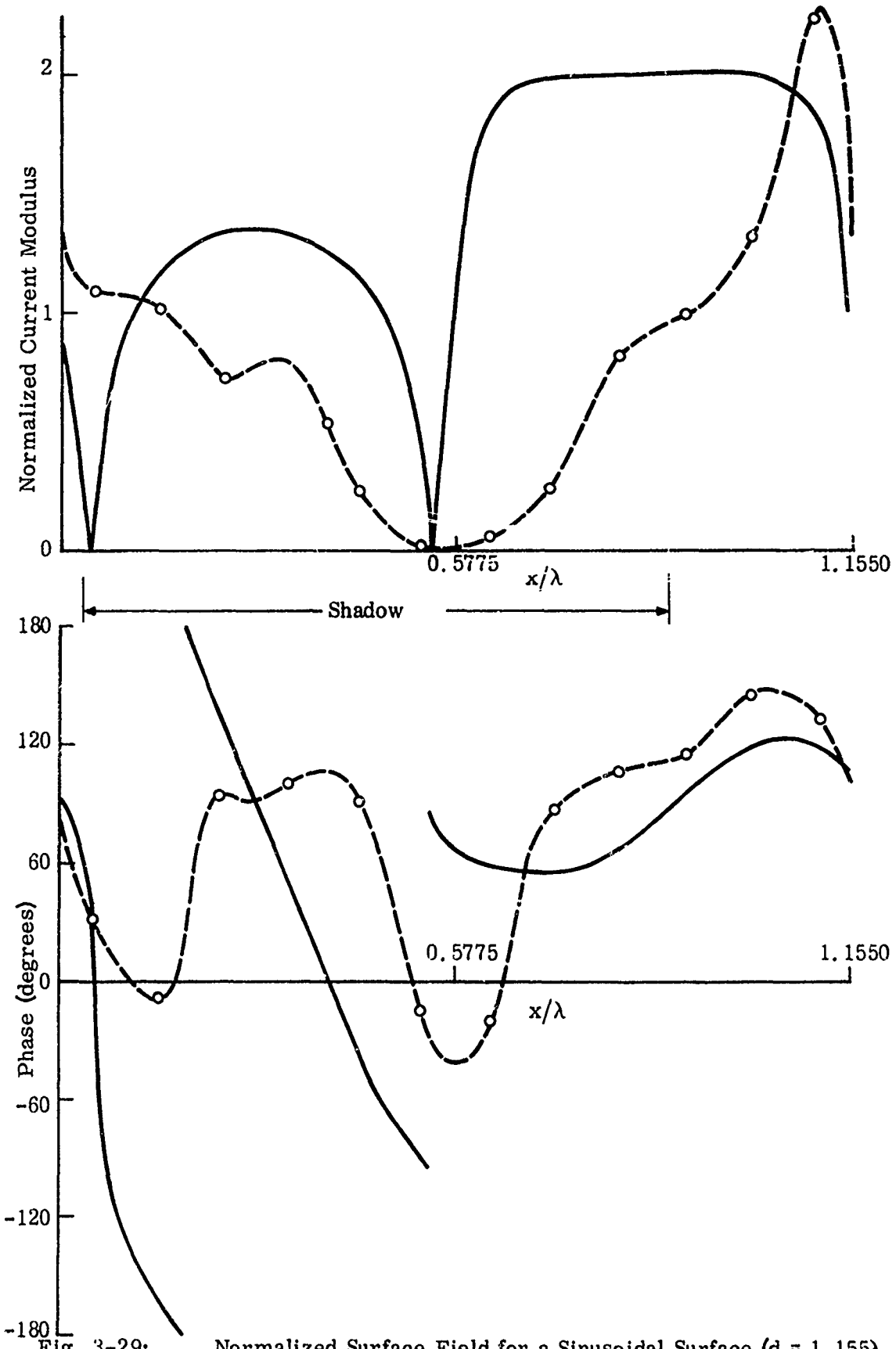

Fig. 3-29: Normalized Surface Field for a Sinusoidal Surface ($d = 1.155\lambda$, $a = 0.6\lambda$ and $\theta = 60^{\circ}$) for E polarization, --o-- exact, — physical optics.

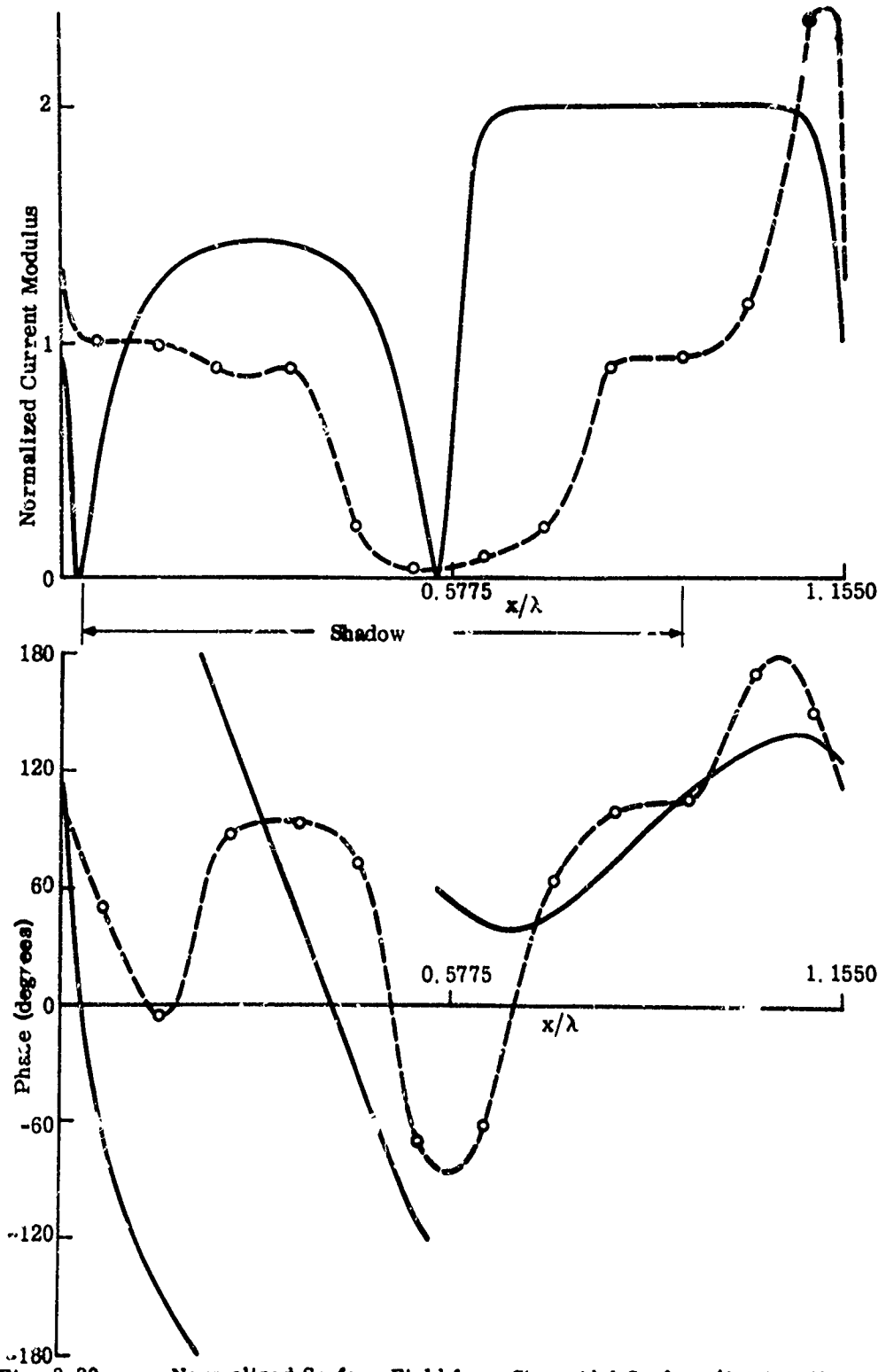

Fig. 3-30: Normalized Surface Field for a Sinusoidal Surface ($d = 1.155\lambda$, $a = 0.7\lambda$ and $\theta = 60^\circ$), for E polarization, --o-- exact, — physical optics.

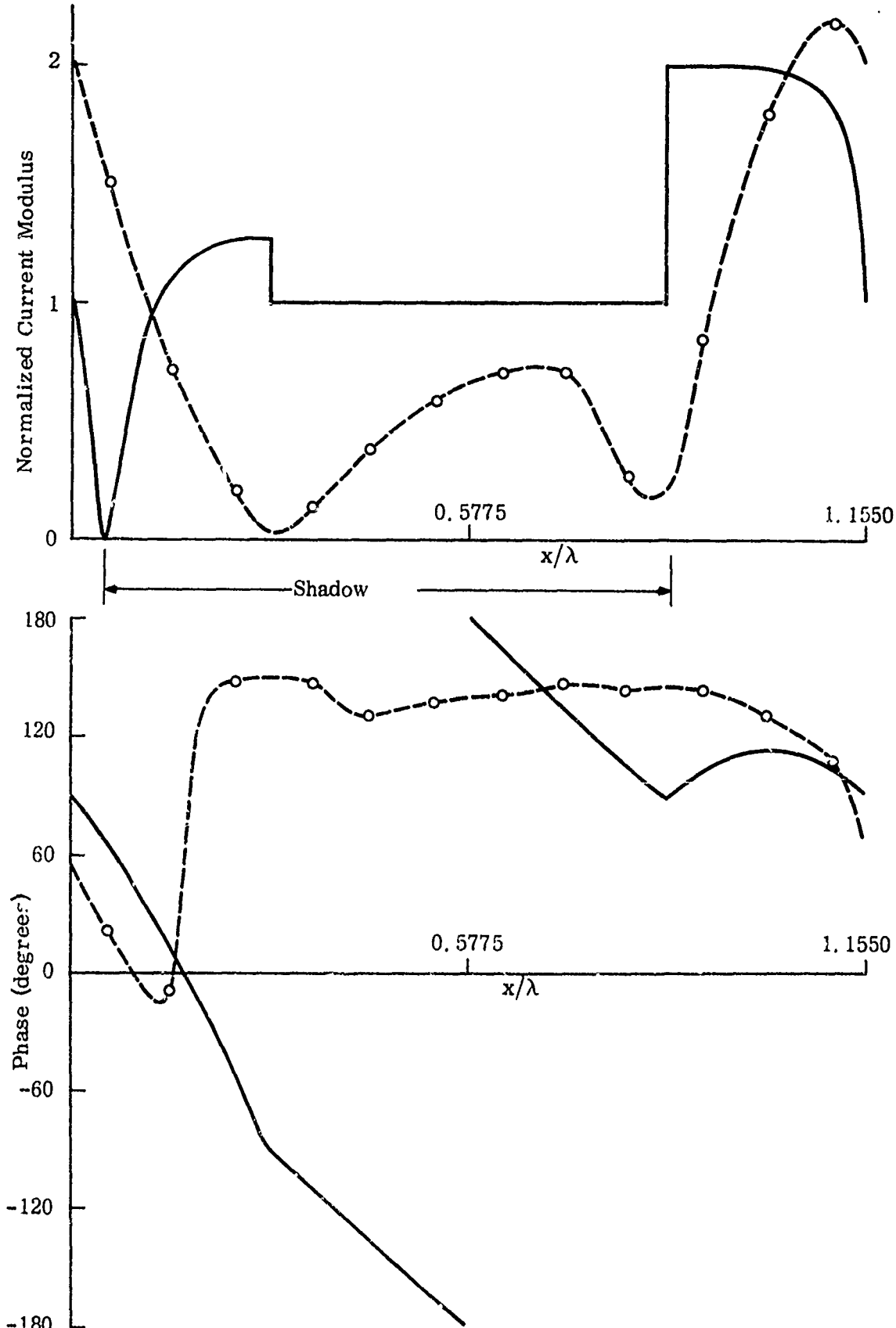

Fig. 3-31: Normalized Surface Field for a Half-Wave Rectified Surface ($d = 1.155\lambda$, $a = 0.5\lambda$ and $\theta = 60^\circ$) for E polarization, --o-- exact, — physical optics.

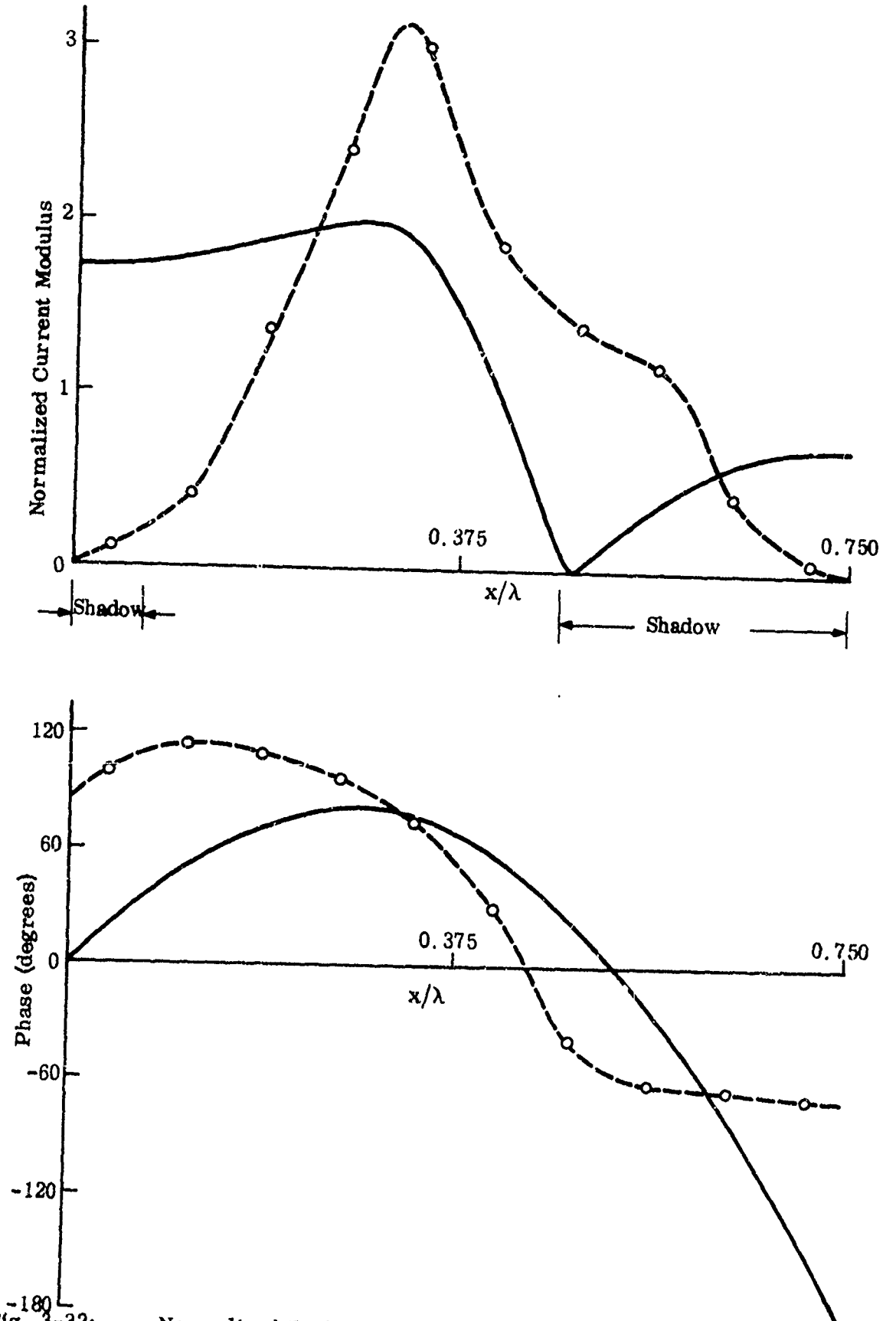

Fig. 3-32: Normalized Surface Field for a Full-Wave Rectified Surface ($d = 0.75\lambda$, $a = 0.6\lambda$ and $\theta = 41.8^{\circ}$) for E polarization, --o-- exact, — physical optics.

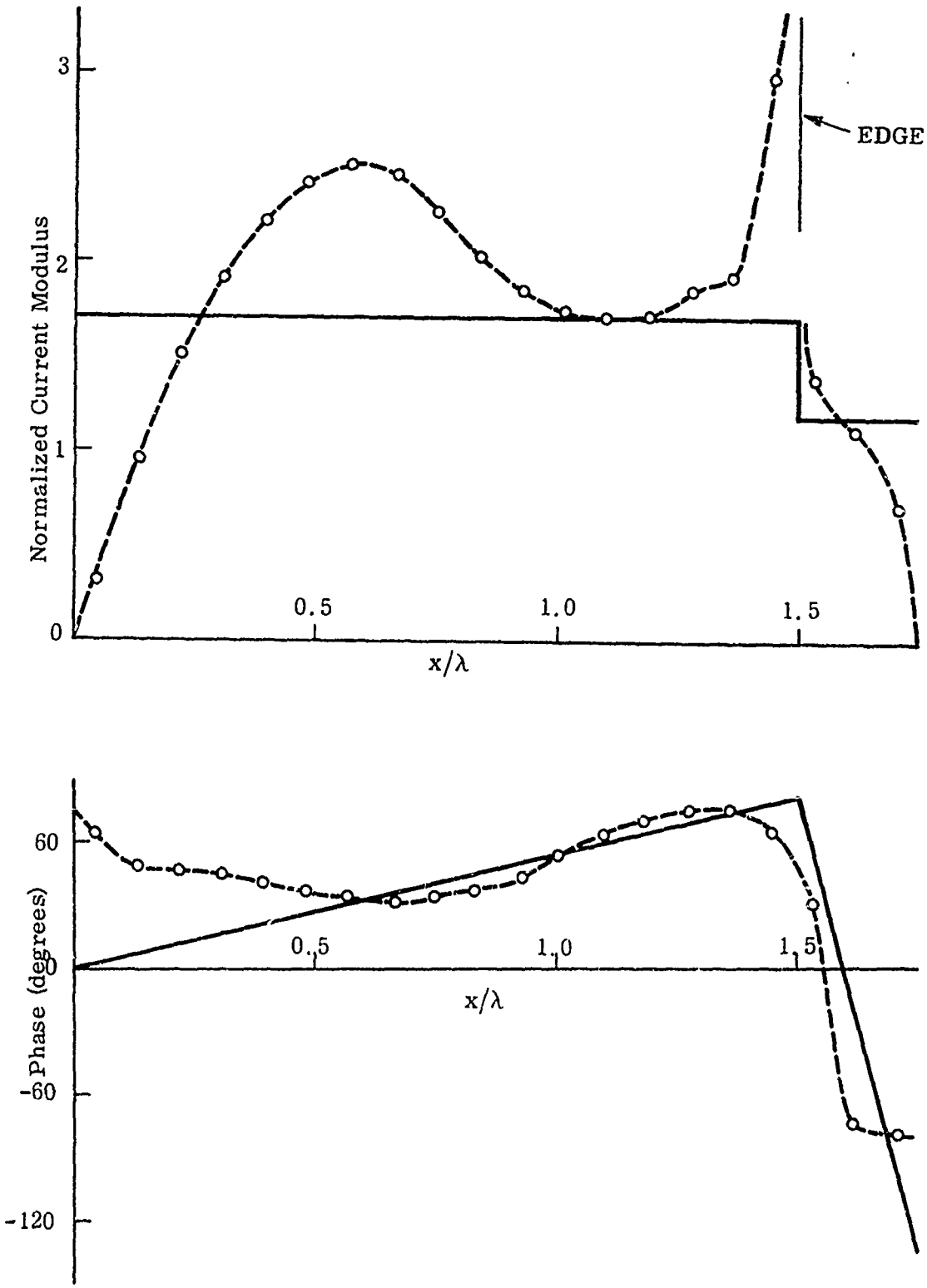

Fig. 3-33: Normalized Surface Field for a Triangular Surface ($d = 1.75\lambda$, $\theta_1 = 20^\circ$, $\theta_2 = 66^\circ$ and $\theta = 12.2^\circ$) for E polarization, --o-- exact, — physical optics.

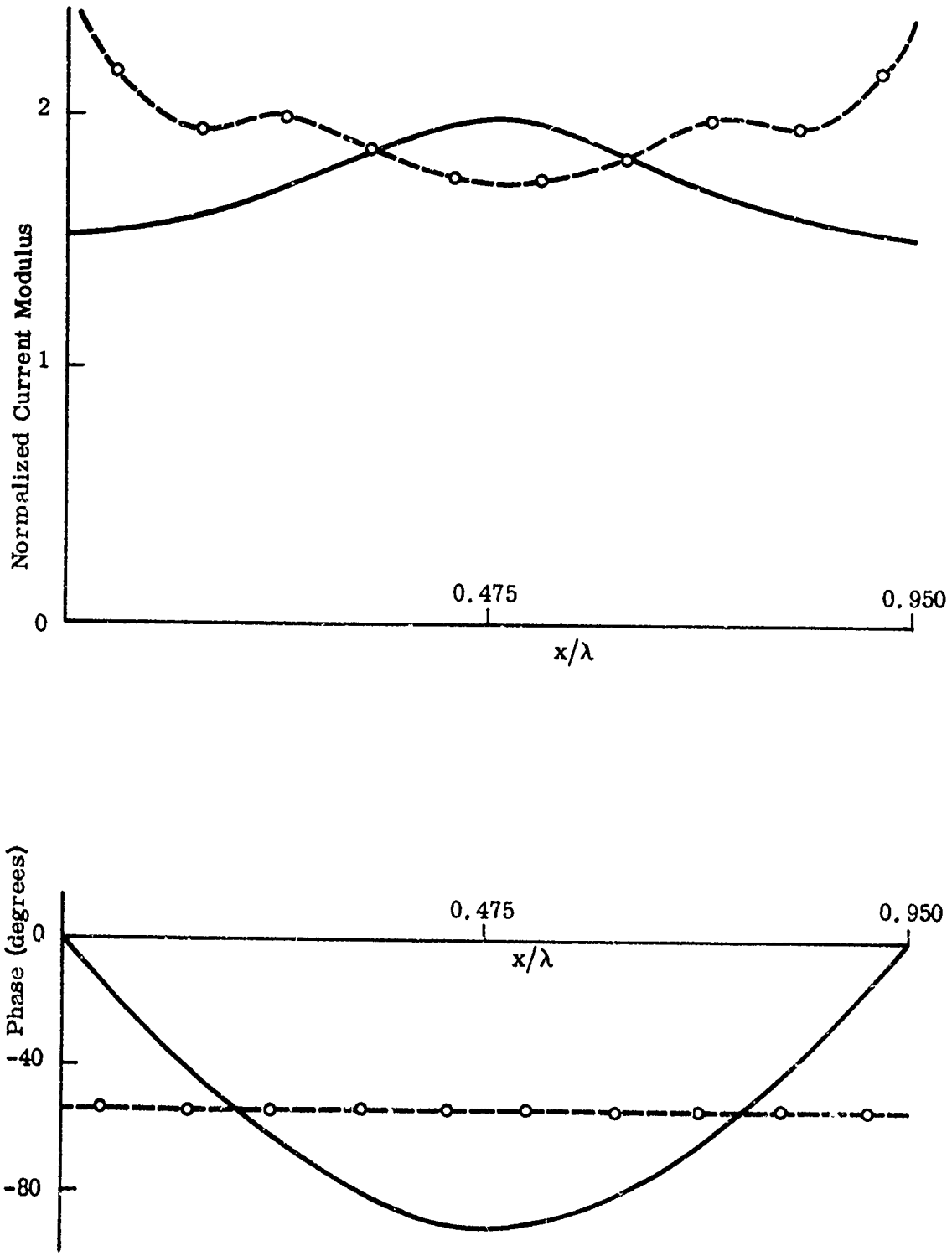

Fig. 3-34: Normalized Surface Field for an Inverted Full-Wave Rectified Surface ($d = 0.95\lambda$, $a = 0.25\lambda$ and $\theta = 0$) for E polarization, --o-- exact, — physical optics.

3.4 Coupling Among Cells

One aspect which has not been looked into so far is the effect on the surface field of a gradual increase in the separation between cells while the other parameters are kept constant. To examine this, we selected a full-wave rectified surface with $a = 0.3\lambda$, $d = 0.3\lambda$, $\theta = 60^{\circ}$ ($k\rho_{min} = 0.0304$) and allowed the distance ℓ between two neighboring periods to increase from 0.3λ to 0.7λ in 0.1λ steps. The results are shown in Figs. 3-35 through 3-39. In the first two figures the modulus curve has the shape characteristic of small periods, while the physical optics phase oscillates about the exact phase. As ℓ gets larger, noticeable changes appear in the modulus curve. One reason for this can be seen from Eqs. (2.29) and (2.30): as ℓ increases, the terms in the infinite series corresponding to higher m's (or higher orders of propagating modes) become more significant, and have a greater effect on the surface current distribution. As ℓ passes through the value 0.535λ, X^{-}_{-1} changes from purely imaginary to real, implying that the $m = -1$ mode becomes propagating. We therefore expect a rather rapid change in the surface field for ℓ near 0.535λ, and this indeed occurs as can be seen by comparing Figs. 3-37 and 3-38. Further increases in ℓ can again produce large changes in the surface field, especially in the shadow region (see Fig. 3-39), but it is worth noting that throughout the illuminated region the modulus is not very sensitive to ℓ.

In all cases considered, the physical optics predictions bear no resemblance to the exact results, although the estimate for the phase is somewhat better than that for the modulus. Examination of the plots also reveals the important fact that the coupling among cells is not very strong even for small periods, and this leads us to conjecture that as regards the surface field the infinite surface can be approximated by a finite surface consisting of only a few cells.

3.5 Accuracy Checks and Computational Time

As mentioned in section 2.5, the numerical results were checked by considering a) the convergence of the numerical solution, b) the limiting approx-

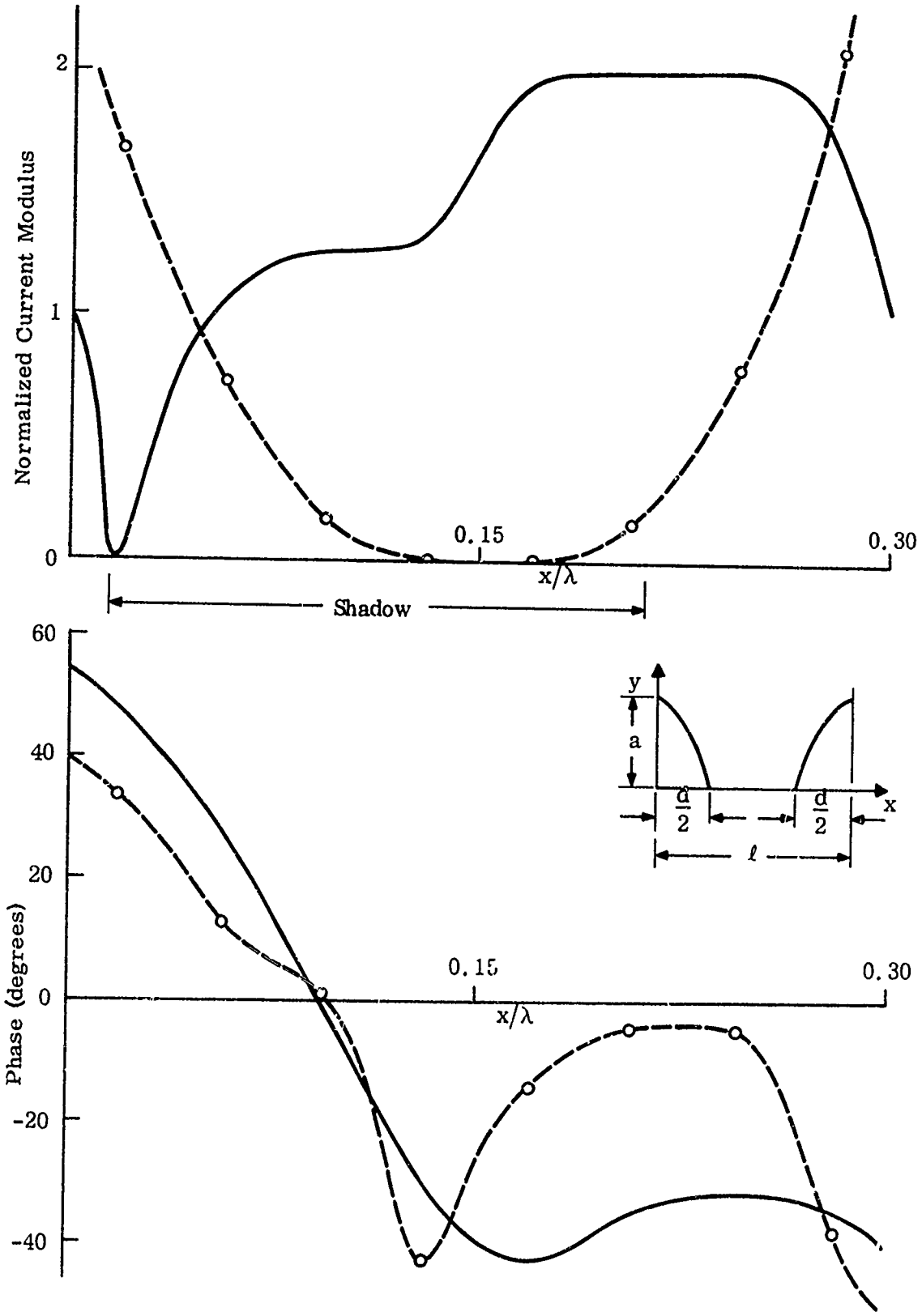

Fig. 3-35: Normalized Surface Field for a Modified Full-Wave Rectified Surface ($d = 0.3\lambda$, $a = 0.3\lambda$, $\theta = 60^{\circ}$ and $\ell = 0.3\lambda$) for E polarization, --o-- exact, — physical optics.

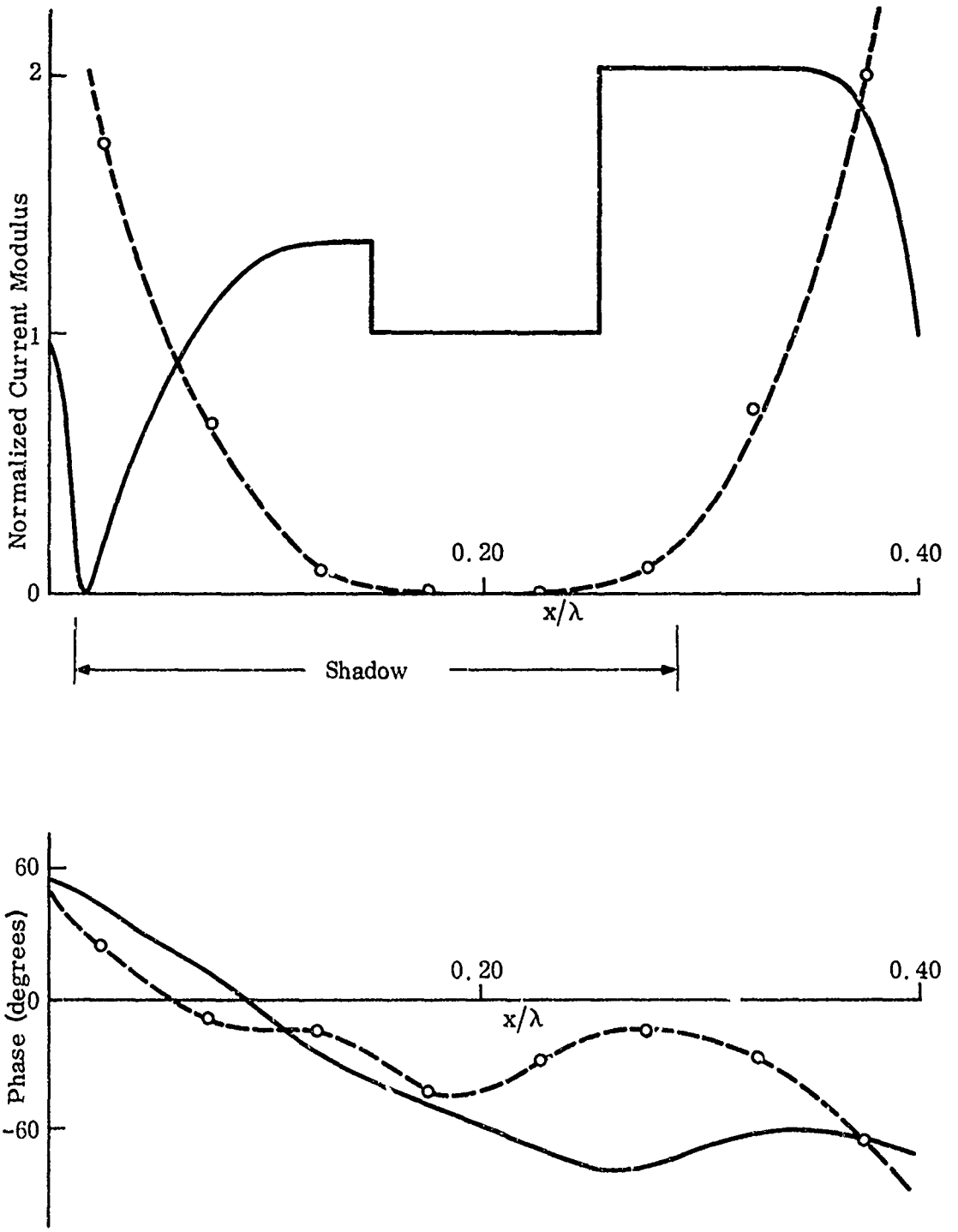

Fig. 3-36: Normalized Surface Field for a Modified Full-Wave Rectified Surface ($d = 0.3\lambda$, $a = 0.3\lambda$, $\theta = 60^{\circ}$ and $\ell = 0.4\lambda$) for E polarization, --o-- exact, — physical optics.

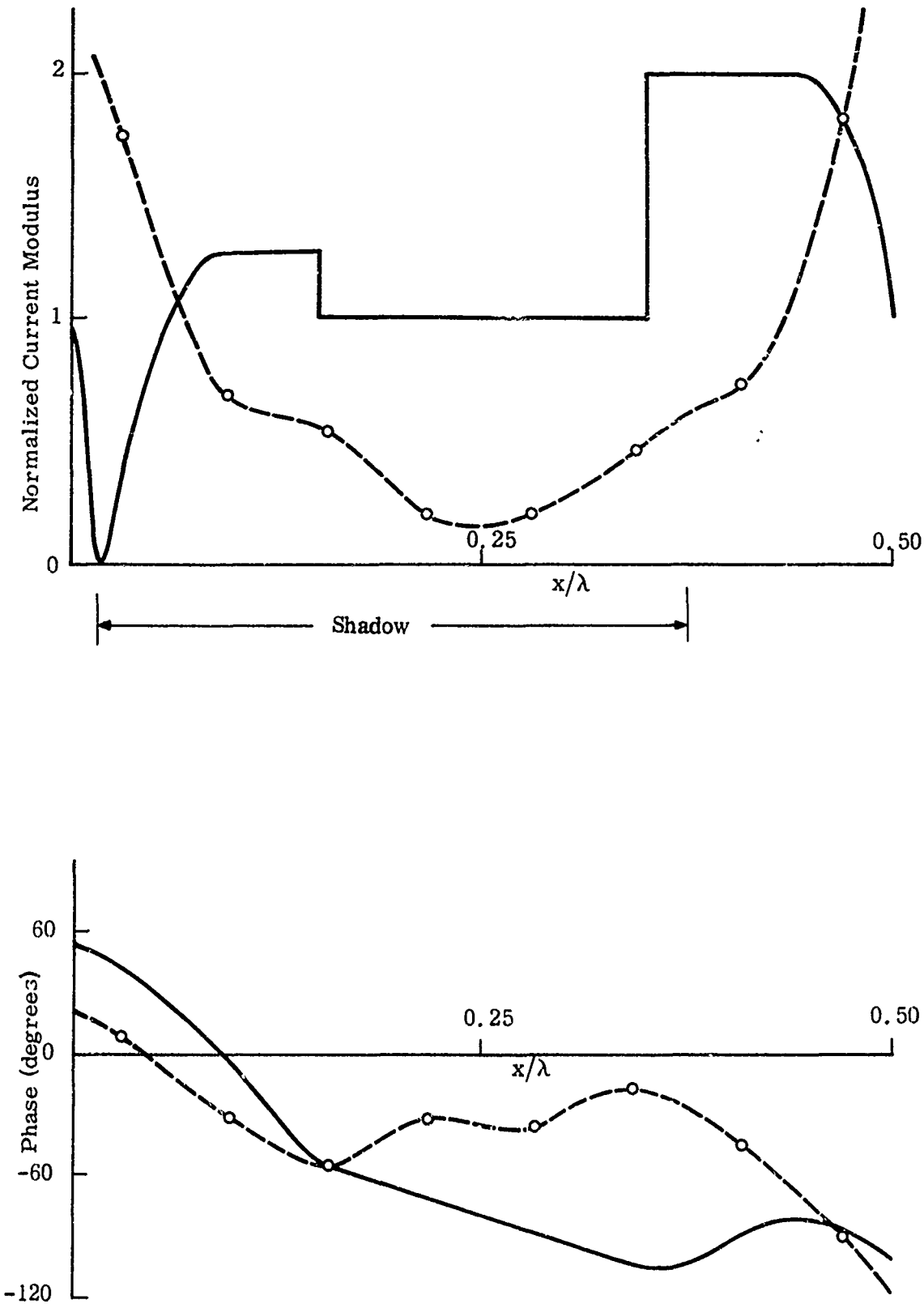

Fig. 3-37: Normalized Surface Field for a Modified Full-Wave Rectified Surface ($d = 0.3\lambda$, $a = 0.3\lambda$, $\theta = 60^{\circ}$ and $\ell = 0.5\lambda$) for E polarization, --o-- exact, — physical optics.

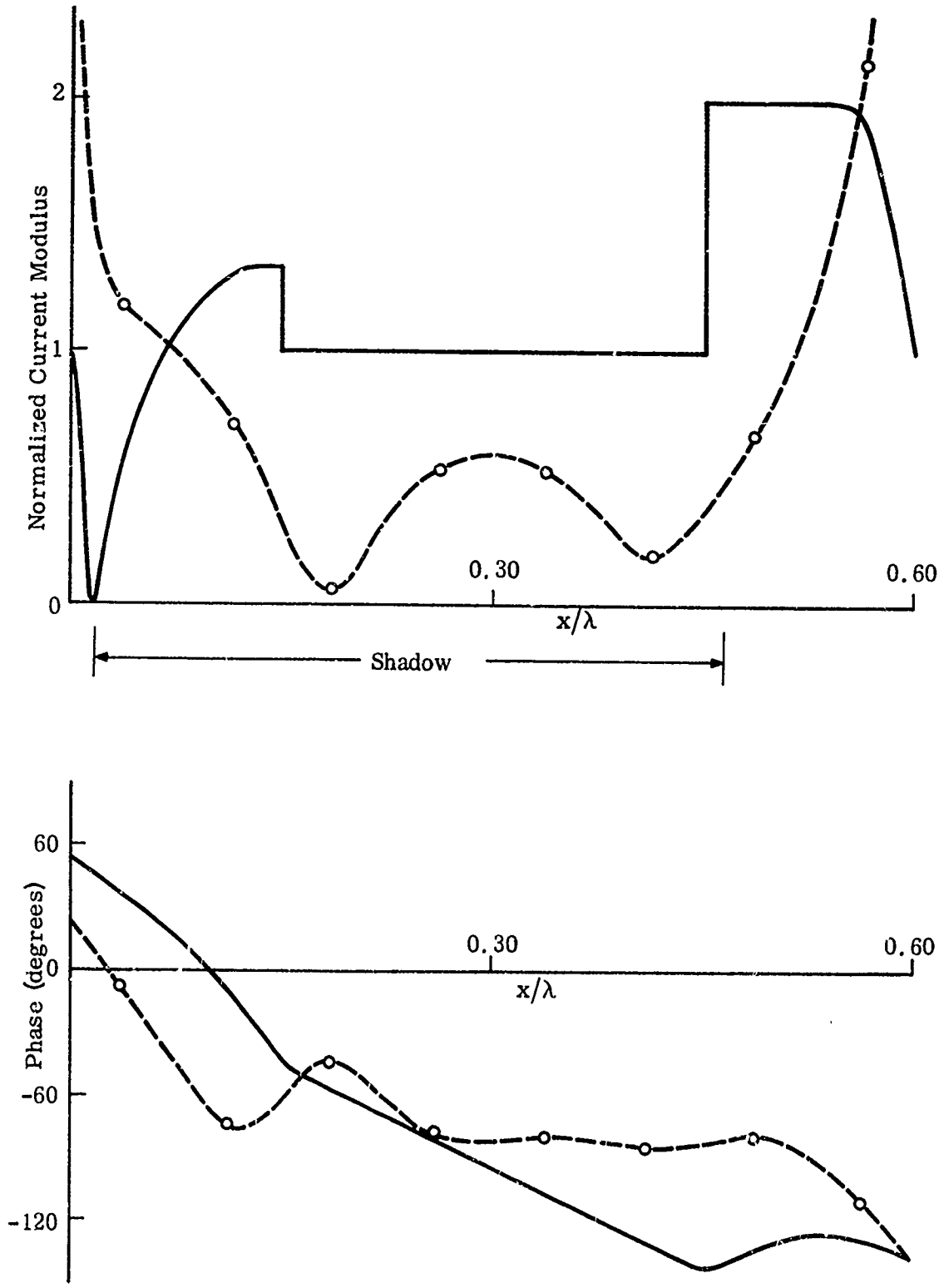

Fig. 3-38: Normalized Surface Field for a Modified Full-Wave Rectified Surface ($d = 0.3\lambda$, $a = 0.3\lambda$, $\theta = 60^\circ$ and $\ell = 0.6\lambda$) for E polarization --o-- exact, — physical optics.

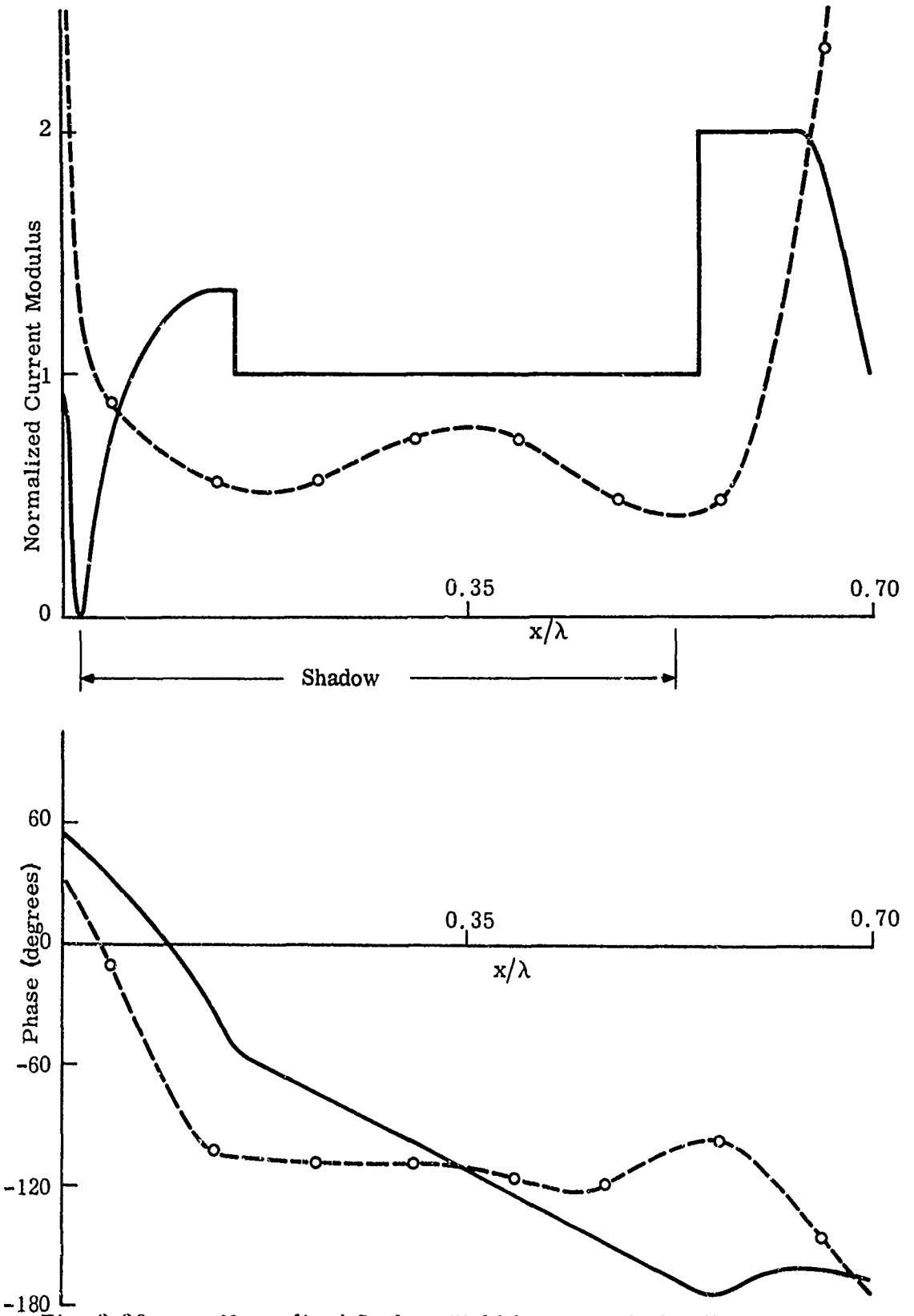

Fig. 3-39: Normalized Surface Field for a Modified Full-Wave Rectified Surface ($d = 0.3\lambda$, $a = 0.3\lambda$, $\theta = 60^{\circ}$ and $\ell = 0.7\lambda$) for E polarization, --o-- exact, — physical optics.

imation of a flat surface, and c) a comparison with results obtained by previous authors. All these will be discussed in this section.

Figure 3-40 shows the result of a convergence test applied to the case of a sinusoidal profile with $d = 0.2\lambda$, $a = 0.1\lambda$ and $\theta = 0$. It can be seen that the solution does appear stable, and that surprisingly good results are obtained even with so few as four sampling points. The limiting approximation of a flat surface is demonstrated with a sinusoidal profile where $d = 0.2\lambda$, $a = 0.05\lambda$ and $\theta = 0$, and the results are shown in Fig. 3-41.

Note that in spite of this relatively small amplitude the modulus still shows significant deviations from the value 2.0 for a flat surface. This is probably due to the rather slow convergence of the infinite series of Eq. (2.29) when the surface height is very small. However, the phase agrees exceptionally well with the exact phase, 0°, for a flat surface.

Comparison of the numerical results with those obtained by previous authors is given in Figs. 3-42 and 3-43. In Fig. 3-42, comparison is made with those by Zaki (1969) for a sinusoidal surface where $d = 1.9\lambda$, $a = 0.25\lambda$ and $\theta = 0$, and in Fig. 3-42 with Green (1970) for a triangular profile where $d = 1.75\lambda$, $\theta_1 = 20^{\circ}$, $\theta_2 = 66^{\circ}$ and $\theta = 12.2^{\circ}$. In both cases good agreement is obtained.

The computational (CPU) time used in each computation depends on the following factors: a) the number of sampling points, b) the number of Fourier terms used to represent the periodic surface, c) the number of terms used in the infinite series summation and d) the accuracy of the numerical integration required. In each case the accuracy of the numerical integration using the Newton-Cotes method was restricted to 1 per cent. A summary of the computational times for various cases is shown in Table III-1.

It should be pointed out that this CPU time includes the computation of the diffracted mode amplitudes, the physical optics approximation, as well as the energy check. In general most of the CPU time is used in filling up the

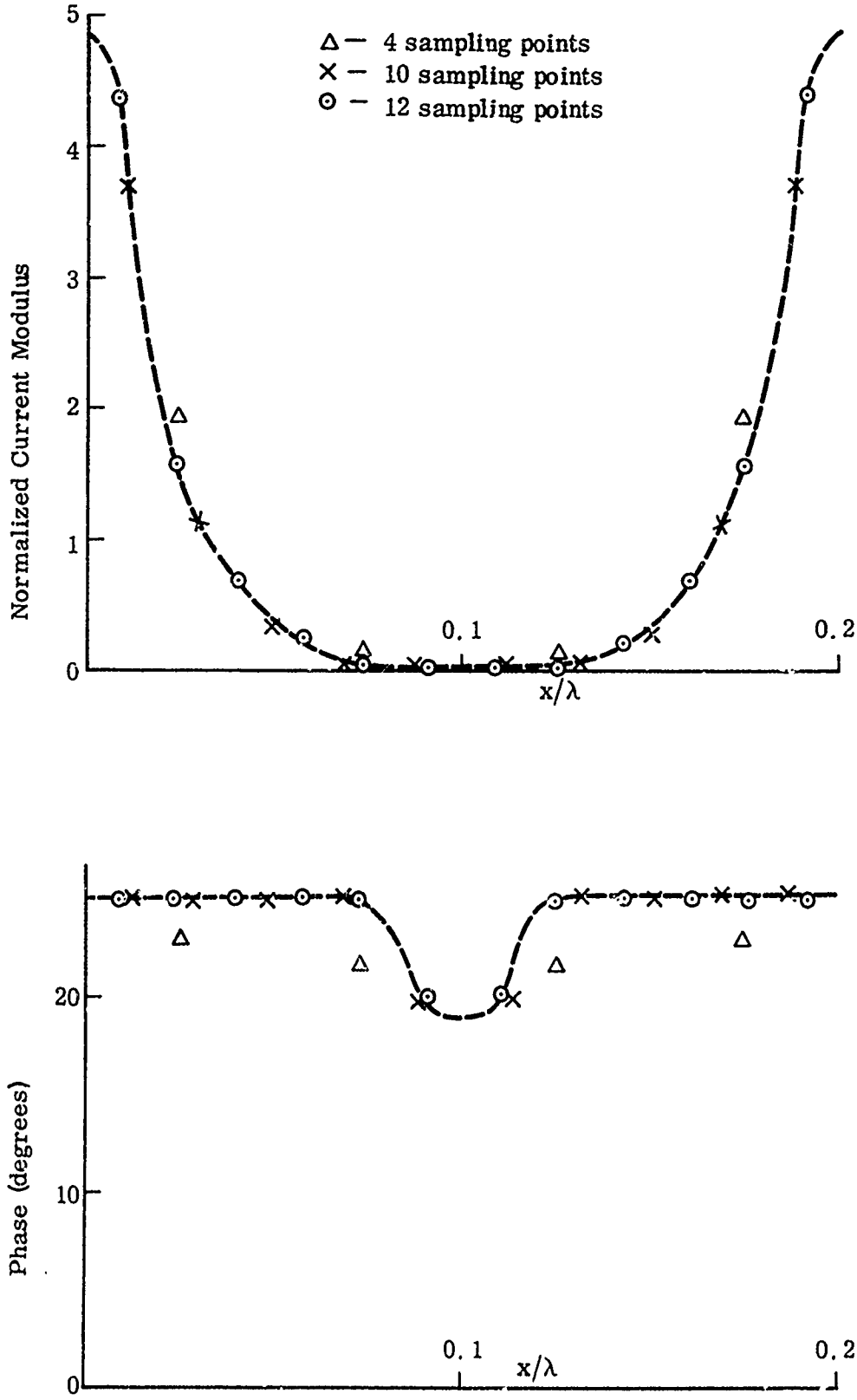

Fig. 3-40: Normalized Surface Field for a Sinusoidal Surface ($d = 0.2\lambda$, $a = 0.1\lambda$ and $\theta = 0$), Computed Using 4, 10 and 12 Sampling Points, for E polarization.

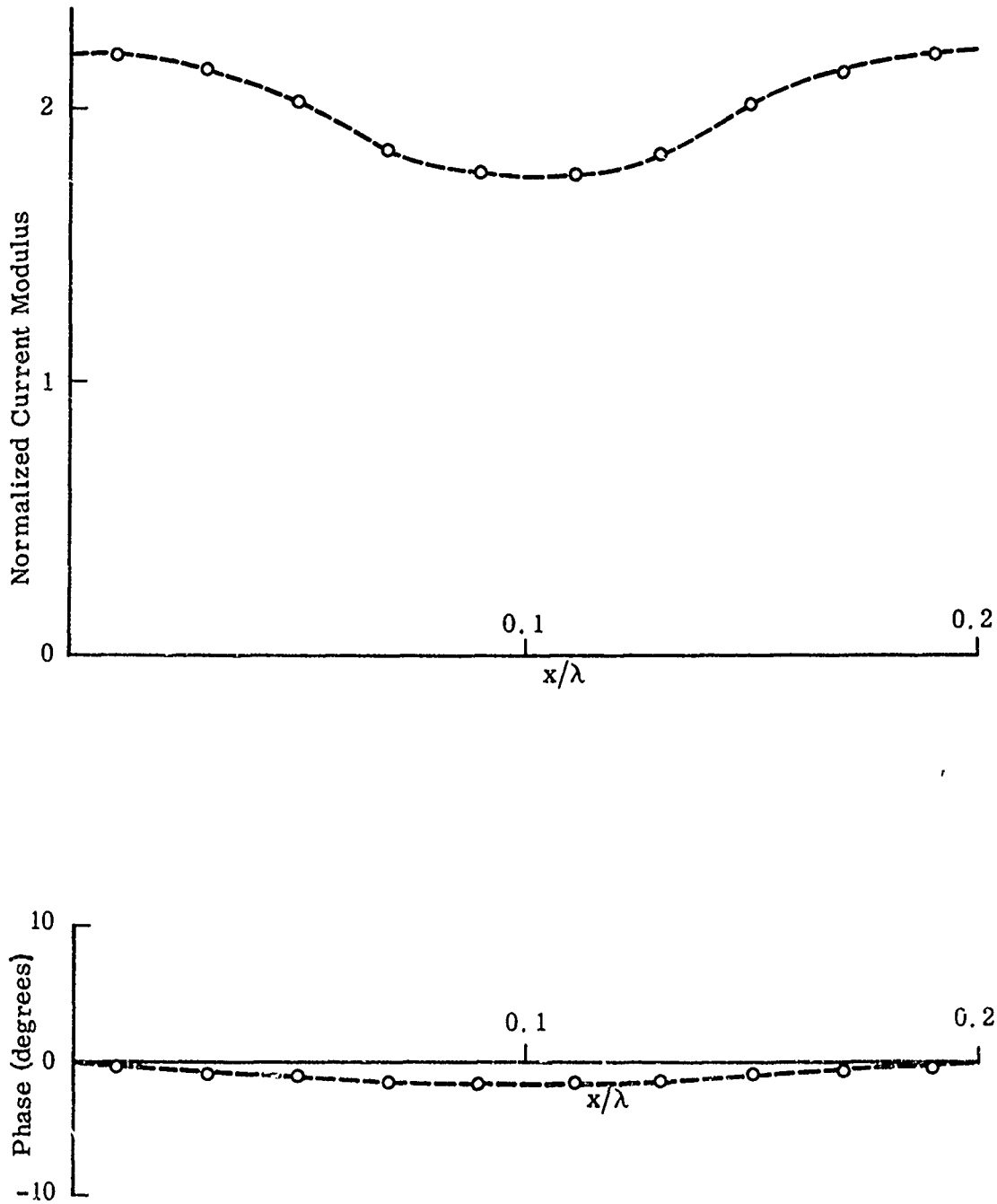

Fig. 3-41: Normalized Surface Field for a Sinusoidal Surface ($d = 0.2\lambda$, $a = 0.005\lambda$ and $\theta = 0$) for E polarization.

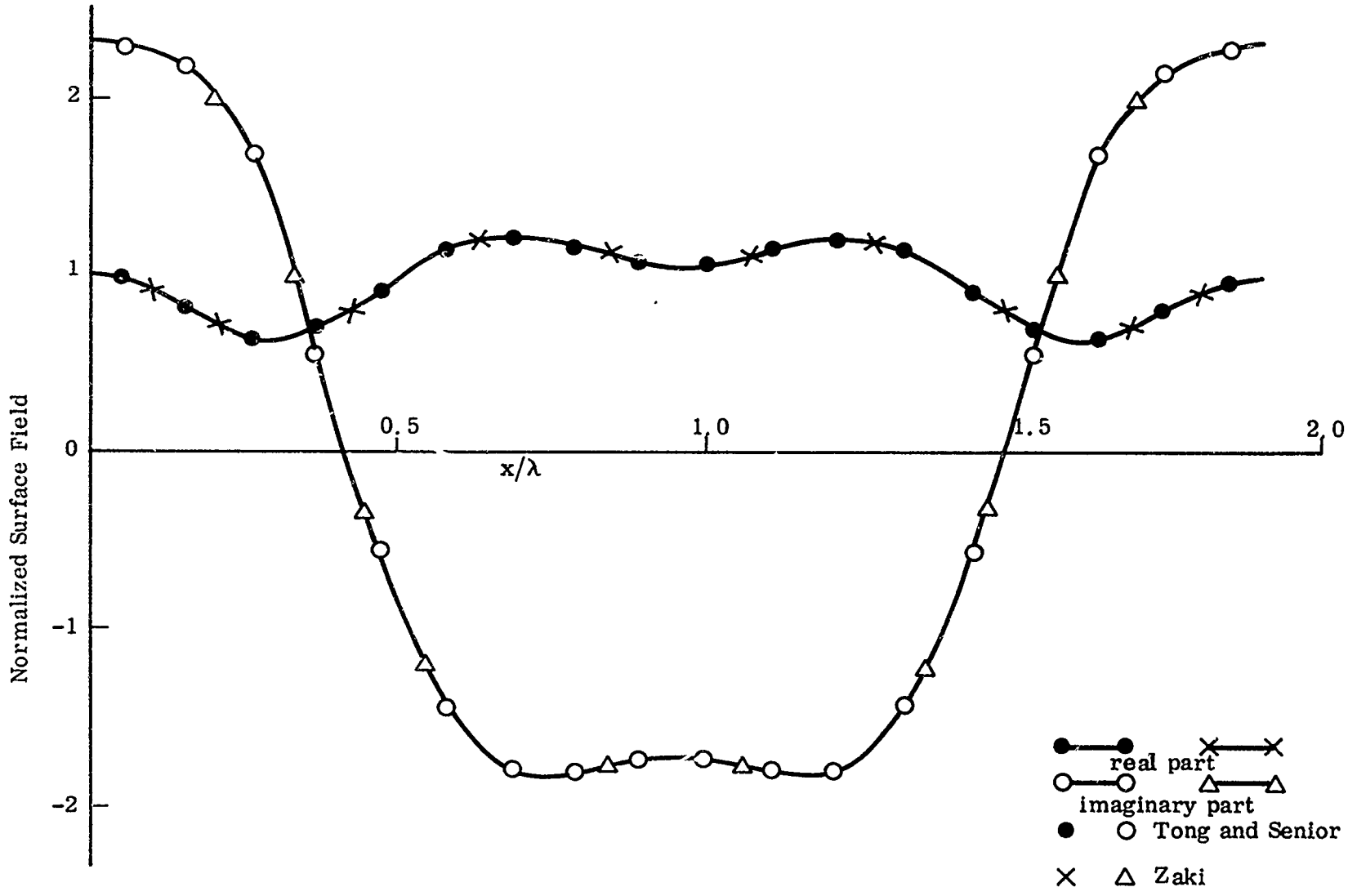

Fig. 3-42: Normalized Surface Field for a Sinusoidal Surface ($d = 1.9$, $a = 0.25\lambda$ and $\theta = 0$) for E polarization.

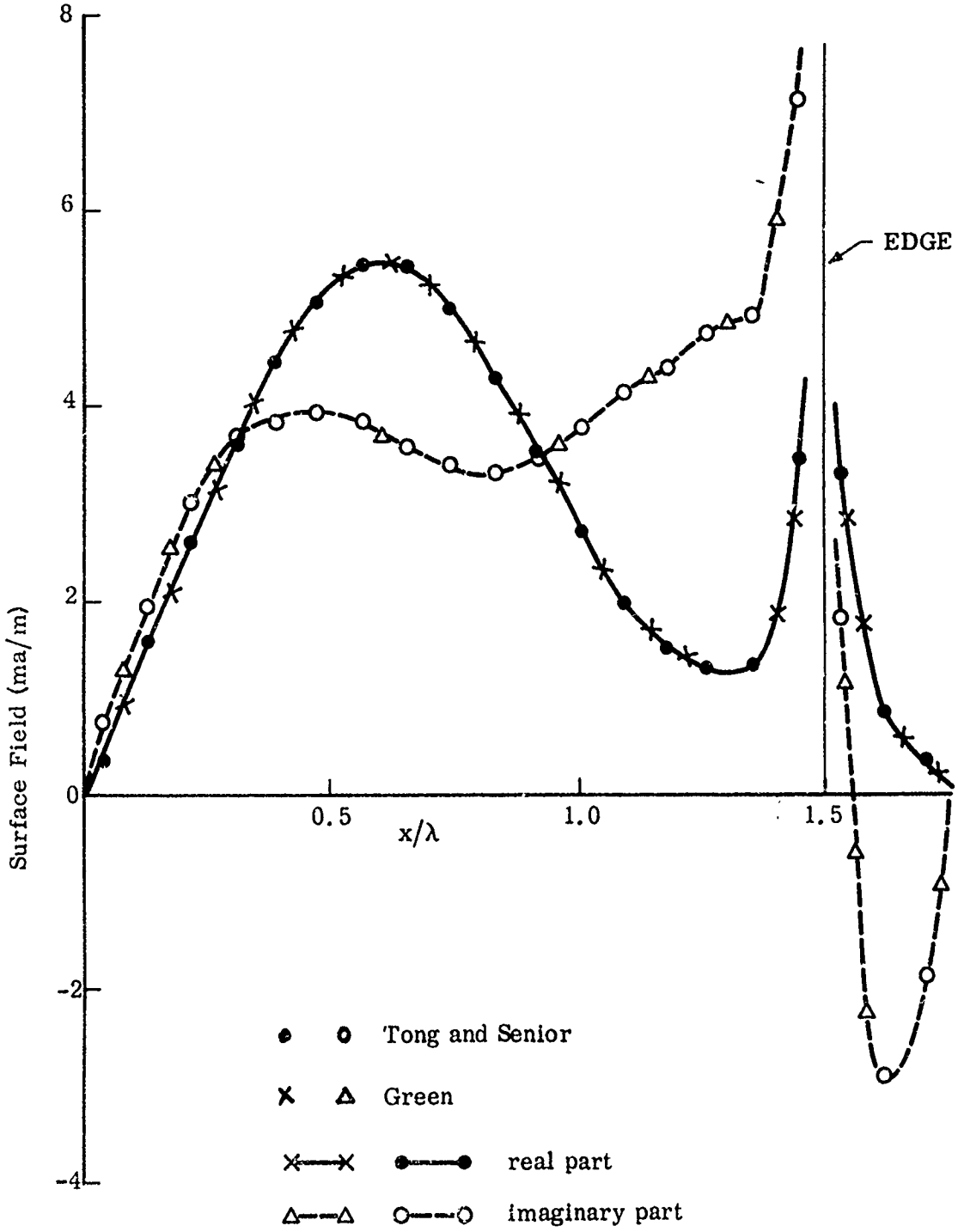

Fig. 3-43: Surface Field for a Triangular Surface ($d = 1.75\lambda$, $\theta_1 = 20^\circ$, $\theta_2 = 66^\circ$ and $\theta = 12.2^\circ$), for E polarization.

Number N of Sampling Points	Number M of Terms in the Infinite Series	Number Q of Fourier terms used to represent the periodic surface	CPU Time (sec) (IBM 360/67)
8	3	1	34.55
10	3	1	47.87
12	3	1	65.55
10	5	1	96.39
8	2	10	49.12
6	2	10	34.58
20	5	15	399.22
12	8	1	168.37
6	1	1	17.13
4	3	1	14.49
18	6	1	199.39
12	3	10	109.03

TABLE III-1: Computational Time for E Polarization

matrix and performing the matrix inversion. For the former operation, the CPU time varies as N^2 while for the latter operation it is proportional to N^3. To see exactly how the CPU time is distributed among the various steps of the computation, let us consider a typical example where $N = 12$, $M = 3$ and $Q = 1$. The distribution of the CPU time is

1. Computation of matrix elements — 44.0 sec.
2. Matrix inversion — 8.3 sec.
3. Physical optics approximation — 5.2 sec.
4. Energy conservation check and diffracted mode amplitude calculations — 8.0 sec.

Chapter IV

SCATTERED FIELD FOR E POLARIZATION

In Chapter III we were primarily concerned with the presentation of numerical data for the surface field. In general, however, the far field is of more direct interest, and the solution of the integral equation for the surface field is then only an intermediate step. In this chapter we will limit our attention to the scattered field, the scattered energy and some interesting physical phenomena known as anomalies associated with the diffracted energy. Comparison is also made with the physical optics approximation, and an approximate technique adequate for prediction, the field backscattered by a sinusoidal surface at oblique incidence is given

4.1 Diffracted Mode Amplitudes

When a plane wave is incident on a periodic surface, the scattered field can be represented as an angular spectrum of plane waves, which spectrum is discrete by virtue of the periodic nature of the boundary condition at the surface. Each of the infinity of waves making up the spectrum has associated with it a diffraction angle which may be real or complex and is determined by the grating law. Whereas the amplitude of the wave is a function of the profile size and shape, and the directions of incidence and diffraction, the diffraction angle depends only on the value of d/λ and the direction of incidence.

A finite number of diffracted waves represent propagating modes and these are the important ones far from the boundary. The remaining modes are evanescent and though these do not serve to carry energy away from the surface, they do play a vital role in affecting the amplitudes of the propagating modes.

The number of modes that propagate can be determined from the expressions for $X_m^{\pm}$ given in Eq. (2.30): if $X_m^{\pm}$ is real, the corresponding mode propagates without attenuation, whereas if $X_m^{\pm}$ is pure imaginary, the mode is evanescent. To find the (complex) amplitudes of the diffracted waves we proceed as follows.

Let $y = f(x)$ be the profile of the surface. Assuming the incident plane wave to be

$$E_z^i = e^{-jk(x\sin\theta - y\cos\theta)} \tag{4.1}$$

(see Eq. (2.20)), and by invoking the periodicity of the surface, the scattered field can be written as

$$E_z^s = \sum_{m=-\infty}^{\infty} A_m e^{-j(\beta_m x + X_m y)} \tag{4.2}$$

for $y \geq \max f(x)$, where

$$\beta_m = \frac{2m\pi}{d} + k\sin\theta \ ,$$

and

$$X_m = \sqrt{k^2 - \beta_m^2} \ .$$

The field arising from the currents induced on the surface is given by

$$E_z^s(x, y) = \frac{\omega\mu}{4} \int_0^d P_1 \sqrt{1 + \{f'(x')\}^2}\, K_z(x')dx' \tag{4.3}$$

where P_1 is as shown in Eq. (2.24). In particular, this is valid for $y \geq \max f(x)$, and hence, by combining Eqs. (2.22), (2.24), (4.2) and (4.3) we have

$$\sum_{m=-\infty}^{\infty} A_m e^{-j(\beta_m x + X_m y)} =$$

$$= \int_0^d \sum_{m=-\infty}^{\infty} \frac{\omega\mu}{2dX_m} e^{-j\left\{\beta_m(x-x') + X_m(y-y')\right\}} \sqrt{1 + \{f'(x')\}^2}\, K_z(x')dx'$$

from which we obtain

$$A_m = \frac{\omega\mu}{2dX_m} \int_0^d e^{j(\beta_m x' + X_m y')} \sqrt{1+\left\{f'(x')\right\}^2}\, K_z(x')dx' \,. \tag{4.4}$$

Notice that the angle of diffraction θ_m for the mth mode is given by

$$\tan\theta_m = \beta_m / X_m \tag{4.5}$$

which, after a little mathematical manipulation, can be reduced to the grating law formula

$$\sin\theta_m = \frac{m\lambda}{d} + \sin\theta \,. \tag{4.6}$$

Having determined the current distributions $K_z(x)$ it is therefore a trivial matter to compute the amplitudes of all the diffracted modes, both propagating and evanescent, and the amplitudes of the propagating waves for several different values of d/λ, a/λ and θ for a sinusoidal surface are given in Tables IV-1 through IV-4. As a basis for comparison, the physical optics approximations are included. In general, the physical optics values, with or without shadowing included, tend to be too small, and we further note that if shadowing is excluded (or is not present), the physical optics estimates are the same for both polarizations (see Appendix A).

TABLE IV-1

Amplitudes of Diffracted Waves for a Sinusoidal Surface ($d = 0.2\lambda$, $a = 0.1\lambda$).

	$\theta = 0^o$		$\theta = 30^o$		$\theta = 60^o$	
	Mag. $\lvert A_0\rvert$	Phase $\phi_0(^o)$	Mag. $\lvert A_0\rvert$	Phase $\phi_0(^o)$	Mag. $\lvert A_0\rvert$	Phase $\phi_0(^o)$
Numerical Solution	1.0050	50.81	0.9940	44.33	1.0000	25.90
Phys. Optics w/o shadow	0.6425	0	0.7251	0	0.9037	0
Phys. Optics w shadow	0.6425	0	0.1253	15.96	0.1770	19.41

TABLE IV-2

Amplitudes of Diffracted Waves for a Sinusoidal Surface
($d = 1.9\lambda$, $a = 0.25\lambda$, $\theta = 0^o$)

	Mag. $\lvert A_0 \rvert$	Phase $\phi_0(^o)$	Mag. $\lvert A_{-1} \rvert = \lvert A_1 \rvert$	Phase $\phi_{-1}(^o) = \phi_1(^o)$
Numerical Solution	0.4920	-160.27	0.6630	107.05
Physical Optics	0.3042	0	0.4389	90

TABLE IV-3

Amplitudes of Diffracted Waves for a Sinusoidal Surface
($d = 0.4\lambda$, $a = 0.2\lambda$).

	$\theta = 0^o$		$\theta = 60^o$	
	Mag. $\lvert A_0 \rvert$	Phase $\phi_0(^o)$	Mag. $\lvert A_0 \rvert$	Phase $\phi_0(^o)$
Numerical Solution	0.9998	-80.81	1.0230	49.89
Physical Optics w/o shadow	0.0549	0	0.6450	0
Physical Optics w shadow	0.0549	0	0.4750	60.37

TABLE IV-4

Amplitudes of Diffracted Waves for a Sinusoidal Surface
($d = 0.2\lambda$, $a = 0.03\lambda$, $\theta = 0^o$).

	Mag. $\lvert A_0 \rvert$	Phase $\phi_0(^o)$
Numerical Solution	1.0000	8.12
Physical Optics	0.9647	0

4.2 Diffracted Energy and Wood Anomalies

4.2.1 Discussion

As mentioned in Section 4.1, when a plane wave is incident on a periodic surface, the scattered field forms a discrete spectrum of plane waves, either propagating or attenuated away from the surface. Only the propagating modes can carry energy away from the surface and are responsible for the far field. Since the surface is perfectly conducting, the diffracted energy as a whole must equal that carried by the incident field.

The problem of determining how the incident energy is distributed among the diffracted waves of various orders is a relatively old one, and has been the subject of numerous theoretical and experimental investigations, many of them motivated by the desire for more efficient optical diffraction. This subject is particularly important in the design of diffraction gratings for use as monochromators in spectroscopy because of their superior properties, such as higher powers of resolution and lower absorption of light, in comparison with prisms.

If we examine the spectrum of light resolved by optical diffraction gratings, we often find rapid variations in the intensity of some diffracted modes over a small range of incidence angles or over a narrow frequency band. These phenomena are termed the Wood anomalies. Unlike ghosts (Rowland or Lyman), anomalies are not caused by errors in the spacing of the rulings, but are due to a type of resonant interaction among the diffracted modes scattered from different periods. An anomaly may appear as a bright or dark band in an otherwise normal spectrum.

Historically, grating anomalies were first observed in reflection grating spectra by Wood in 1902. Since these effects could not be explained by means of ordinary grating theory, Wood termed them "anomalies". At that time, however, he reported that anomalies could occur only if the incident field was H-polarized (S-type anomalies), and there were no anomalies for E polarization (P-type anomalies). Later, experiments by Ingersoll (1920) and Strong (1936) also showed no evidence of P-type anomalies in grating measurements.

The first theoretical treatment was given by Rayleigh (1907). His approach was based on an expansion of the scattered field in terms of outgoing waves only. (Details of this will be given in a later chapter.) Using this assumption, he found that the scattered field was singular at wavelengths for which one of the diffracted modes emerges from the grating at the grazing angle. These wavelengths are now known as the "Rayleigh wavelengths", λ_R:

$$\lambda_{R\pm} = \frac{d}{\pm m}(\pm 1 - \sin\theta) \qquad m = 1, 2, 3, \ldots \quad . \tag{4.7}$$

He also observed that the occurrence of such singularities corresponded to the appearance of the Wood anomalies. Furthermore, these singularities appear only when the incident field is H-polarized, thereby accounting for the S anomalies, and if the incident field is E polarized, the theory predicts a regular behavior near λ_R.

It should be noted that although Rayleigh's theory correctly predicts the major features experimentally observed at that time, it does not give the shape of the bands associated with the S anomalies because of the indicated singularity at the Rayleigh wavelength.

In his later publications, Wood (1935) suggested the existence of the P anomalies, but it was Palmer (1952) who succeeded in detecting these anomalies experimentally, thus proving their existence beyond doubt. Furthermore, Palmer pointed out that the P anomalies (unlike the S-type) occur only for gratings with deep grooves. Since Rayleigh's assumption (chapter VII) is valid for shallow grooves only, no inconsistency is present, but Rayleigh's theory is incomplete. Recent, more sophisticated theoretical treatments by Hessel and Oliner (1965), Wirgin (1969), Itoh and Mittra (1969) and many others also indicate the existence of P anomalies.

The numerical results which we have obtained can also be used to explore the Wood anomalies, and this we shall now do.

4.2.2 Computed Data for the Diffracted Energy

a) Two Radiating Modes. Figure 4-1 shows the plot of normalized diffracted energy versus surface height for a full-wave rectified profile having $d = 0.75\lambda$ with $\theta = 41.8^{\circ}$. Since an equivalent plot for a sinusoidal surface was obtained by Zaki (1969), it is included here for comparison purposes. For this particular choice of parameters, the diffracted modes corresponding to $m = 0$ and $m = -1$ can propagate.

Examination of the curves show that the diffracted energy for either mode displays a standing wave behavior. At a certain value of a/λ depending on the profile shape, there is a complete exchange of energy between the two modes, indicating the existence of a P-type anomaly. When this happens, the total diffracted energy is carried by the $m = -1$ mode, and thus there will be a bright band in the diffraction grating spectrum for the $m = -1$ mode. The value of a/λ for which it occurs is (Fig. 4-1) 0.8 for a sinusoidal surface, but just over 2.4 for the full-wave rectified surface. Note, however, that the actual peak-to-trough depth for the sinusoidal surface is 2a, so that as a function of the total depth the change is not quite so dramatic.

The above data clearly demonstrate the P anomalies are deep-grooved phenomena and dependent on the shape of the grooves. These are consistent with Palmer's experimental observations. Furthermore, the curves show that the band for the full-wave rectified profile is broader than that for the sinusoidal surface, and hence for the former surface the diffracted energy in both modes is less sensitive to a change in surface height.

Note that these P anomalies differ from the classical S anomalies in that they are broader and need not occur near the Rayleigh wavelengths. Under certain conditions, a total (100 per cent) energy conversion takes place between the incident plane wave and the $m = -1$ mode, with the amplitude of the specularly-reflected wave becoming zero at this point. These phenomena were also investigated by Tseng, Hessel and Oliner (1968), and they termed them Brewster-angle

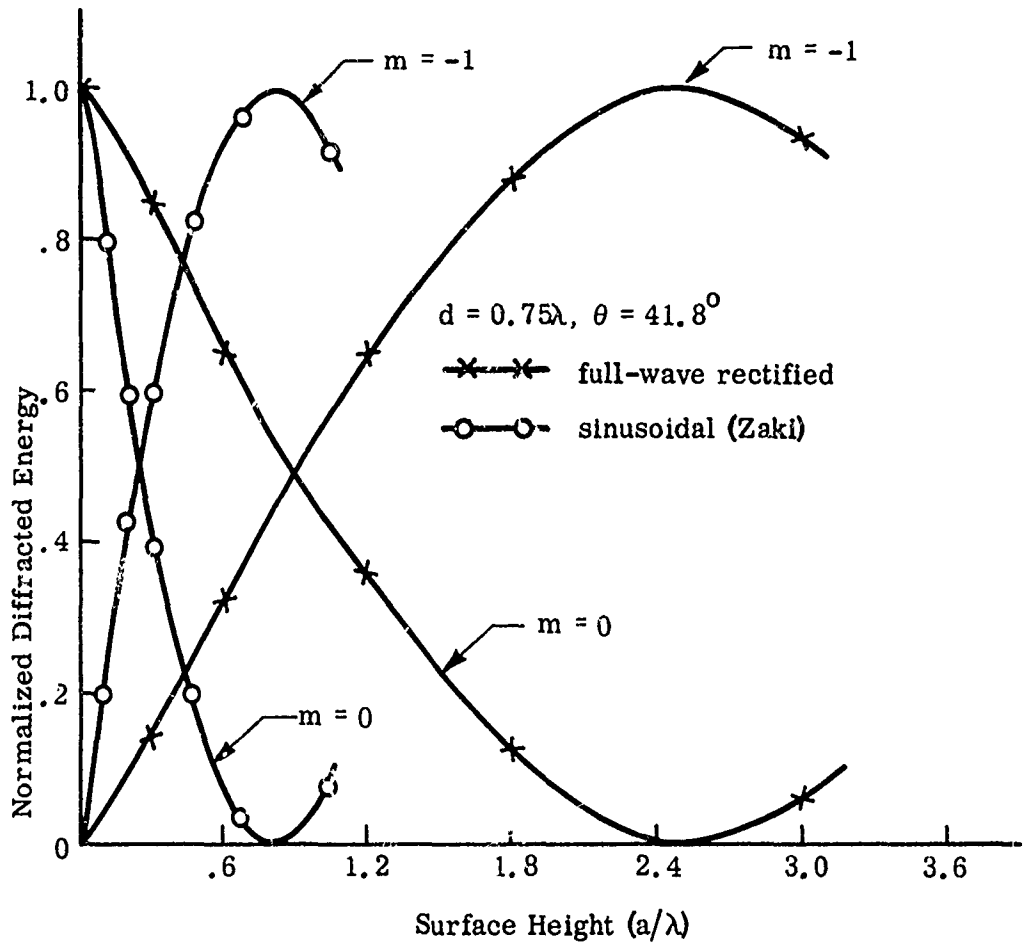

Fig. 4-1: Diffracted Energy for Two Radiating Modes, for E polarization.

effects in an analogue to the well-known Brewster-angle effect for the case of an interface between two different, homogeneous, isotropic media. Furthermore, they pointed out that at the first P anomaly we must have the following condition (Bragg condition):

$$kd \sin\theta = \pi \tag{4.8}$$

Therefore, if we substitute this relation into Eq. (2.21), we obtain

$$K_z(\underline{r} + md\hat{x}) = K_z(\underline{r})e^{-jm\pi} \qquad m = \pm 1, \pm 2, \ldots$$

$$= \begin{cases} K_z(\underline{r}) & \text{if} \quad m = \text{even} \\ -K_z(\underline{r}) & \quad\;\; = \text{odd} \end{cases} \tag{4.9}$$

which shows that at this anomaly the current distribution over any chosen cell (or period) must be in or out of phase with that over the reference cell ($m = 0$) depending on whether the chosen cell is displaced an even or odd number of periods, respectively, from the reference cell. But this is only a necessary condition for the existence of an anomaly. There does not appear to be any rule for predicting the exact depth of groove for an anomaly to occur since this depth is different for different profiles. However, using the condition (4.8), we can derive some information about the nature of the current distribution when the first anomaly occurs. This is done as follows.

From Eqs. (4.2) and (4.8), for the $m = 0$ mode:

$$\begin{aligned} \beta_0 &= k \sin\theta = \pi/d\,, \\ X_0 &= k\cos\theta\,; \end{aligned} \tag{4.10}$$

and for the $m = -1$ mode:

$$\begin{aligned} \beta_{-1} &= -\pi/d\,, \\ X_{-1} &= -k\cos\theta\,. \end{aligned} \tag{4.11}$$

Substituting Eq. (4.10) into Eq. (4.4) we get

$$A_0 = \frac{\omega\mu}{2dk\cos\theta} \int_0^d e^{j(\frac{\pi}{d}x + k\cos\theta y)} \sqrt{1+f'(x)^2}\, K_z(x)dx. \tag{4.12}$$

Similarly, using Eq. (4.11),

$$A_{-1} = \frac{\omega\mu}{2dk\cos\theta} \int_0^d e^{-j(-\frac{\pi}{d}x + k\cos\theta y)} \sqrt{1+f'(x)^2}\, K_z(x)dx\,, \tag{4.13}$$

which can be written as

$$A_{-1} = \frac{\omega\mu}{2dk\cos\theta} \int_0^d e^{-\frac{2\pi}{d}x}\, e^{j(\frac{\pi}{d}x + k\cos\theta y)} \sqrt{1+f'(x)^2}\, K_z(x)dx\,. \tag{4.14}$$

Furthermore, at the first P anomaly:

$$|A_0| = 0\,, \qquad |A_{-1}| = 1\,. \tag{4.15}$$

Observe that Eqs. (4.12) and (4.14) differ only by a factor $\exp(-j\frac{2\pi}{d}x)$ in the kernel, but their magnitudes differ by unity. To show that this is also true if we replace $\exp(-j\frac{2\pi}{d}x)$ by its conjugate $\left(\exp(j\frac{2\pi}{d}x)\right)$, change the variable x to $-x$ to get

$$A_{-1} = -\frac{\omega\mu}{2dk\cos\theta} \int_0^d e^{j(\frac{\pi}{d}x + ky\cos\theta)} \sqrt{1+f'(-x)^2}\, K_z(-x)dx. \tag{4.16}$$

If it is assumed that $f(x)$ is an even function then

$$A_{-1} = -\frac{\omega\mu}{2dk\cos\theta} \int_0^d e^{j(\frac{\pi}{d}x + ky\cos\theta)} \sqrt{1+f'(x)^2}\, K_z(-x)dx\,, \tag{4.17}$$

and using Eq. (2.21)

$$K_z(-x) = K_z(x)\, e^{j2k\sin\theta x}$$

$$= K_z(x)\, e^{j\frac{2\pi}{d}x} \quad . \tag{4.18}$$

Thus Eq. (4.17) becomes

$$A_{-1} = -\frac{\omega\mu}{2dk\cos\theta}\int_0^d e^{j\frac{2\pi}{d}x}\, e^{j(\frac{\pi}{d}x + k\cos\theta y)}\sqrt{1+f'(x)^2}\, K_z(x)dx \tag{4.19}$$

which differs from Eq. (4.14) only in sign. Moreover, if we add Eqs. (4.14) and (4.19), we have

$$A_{-1} = \frac{j\omega\mu}{dk\cos\theta}\int_0^d \sin\left(\frac{2\pi}{d}x\right) e^{j(\frac{\pi}{d}x + k\cos\theta y)}\sqrt{1+f'(x)^2}\, K_z(x)dx\ , \tag{4.20}$$

whereas if we subtract Eq. (4.19) from Eq. (4.14),

$$0 = \frac{\omega\mu}{dk\cos\theta}\int_0^d \cos\left(\frac{2\pi}{d}x\right) e^{j(\frac{\pi}{d}x + k\cos\theta y)}\sqrt{1+f'(x)^2}\, K_z(x)dx \tag{4.21}$$

Therefore from Eqs. (4.12), (4.20) and (4.21) and the orthogonality property of the trigonometric function, we can conclude that

$$K_z(x) = \frac{kd\cos\theta}{j\omega\mu}\,\frac{1}{\sqrt{1+f'(x)^2}}\,\sin\left(\frac{2\pi}{d}x\right)\, e^{-j(\frac{\pi}{d}x + k\cos\theta y)}\ , \tag{4.22}$$

which describes the behavior of the surface field at the first P anomaly. In particular, if we consider a sinusoidal surface, then the modulus of the surface field will exhibit a standing wave pattern showing the propagation of unattenuated surface waves along the x-axis. Once again this phenomenon is seen to be

analogous to the Brewster angle effect which is used in launching a surface wave along an interface of two homogeneous, isotropic media. For a perfectly conducting flat sheet, this Brewster angle is of course equal to 90° (with the normal to the surface), but since the surface is corrugated, it can be modelled by an appropriate reactance surface (see, for example, Hessel and Oliner, 1965), whose Brewster angle can now assume values other than 90°.

Another illustration for two radiating modes is shown in Fig. 4-2 for a full-wave rectified profile at oblique incidence with $\theta = 60^{\circ}$. The parameters of the profile are $a = 0.3\lambda$, $d = 0.30\lambda$, and the period varies from 0 to 0.7λ. The plots show that there is a gradual exchange of diffracted energy between the $m = 0$ and $m = -1$ modes when $d > 0.535\lambda$, which is a Rayleigh wavelength.

b) Three Radiating Modes. As the period becomes larger, more radiating modes are possible. A case of three radiating modes is shown in Fig. 4-3 for a sinusoidal surface at oblique incidence, $\theta = 60^{\circ}$. The parameters of the surface are $d = 1.155\lambda$, and a varies from 0.05 to 0.7λ. The three radiating modes are the $m = 0$, $m = -1$ and $m = -2$ modes, and as computed from the grating law, their diffracted angles are 60° ($m = 0$), 0 ($m = -1$) and -60° ($m = -2$). Thus, the $m = 0$ mode is the specular mode, radiating in the foreward scattered direction, the $m = -1$ mode radiates in the normal direction, and the $m = -2$ mode is the backscattered mode, radiating in the reverse direction of incidence.

The plots show a gradual exchange of the diffracted energy among the three radiating modes. For $a < 0.05\lambda$, the dominant mode is the $m = 0$ mode, which carries almost all the diffracted energy. Thus from the far field point of view, the surface is similar to a flat surface. As the amplitude increases, the other two modes come in, and play an important role in sharing the radiated energy. Since no single mode is observed to carry the whole (or none) of the energy (except, of course, when $a \ll 0.05\lambda$), even for a as large as 0.7λ, it is unlikely that the P anomalies will occur with three radiating modes when the surface height is not very deep (of order λ or less); and if they do occur, it will only be for groove depths much greater than those for two radiating modes.

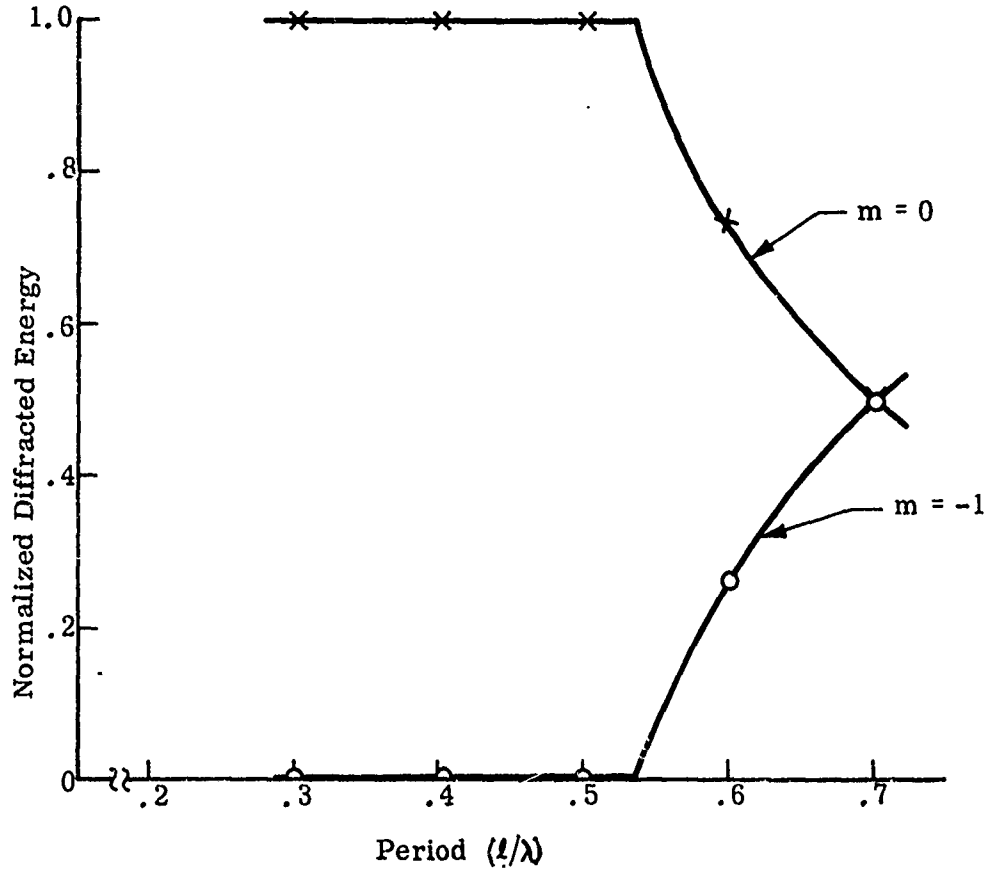

Fig. 4-2: Diffracted Energy for a Modified Full-wave Rectified Surface ($a = 0.3\lambda$, $\theta = 60^\circ$ and $d = 0.30\lambda$) for E polarization.

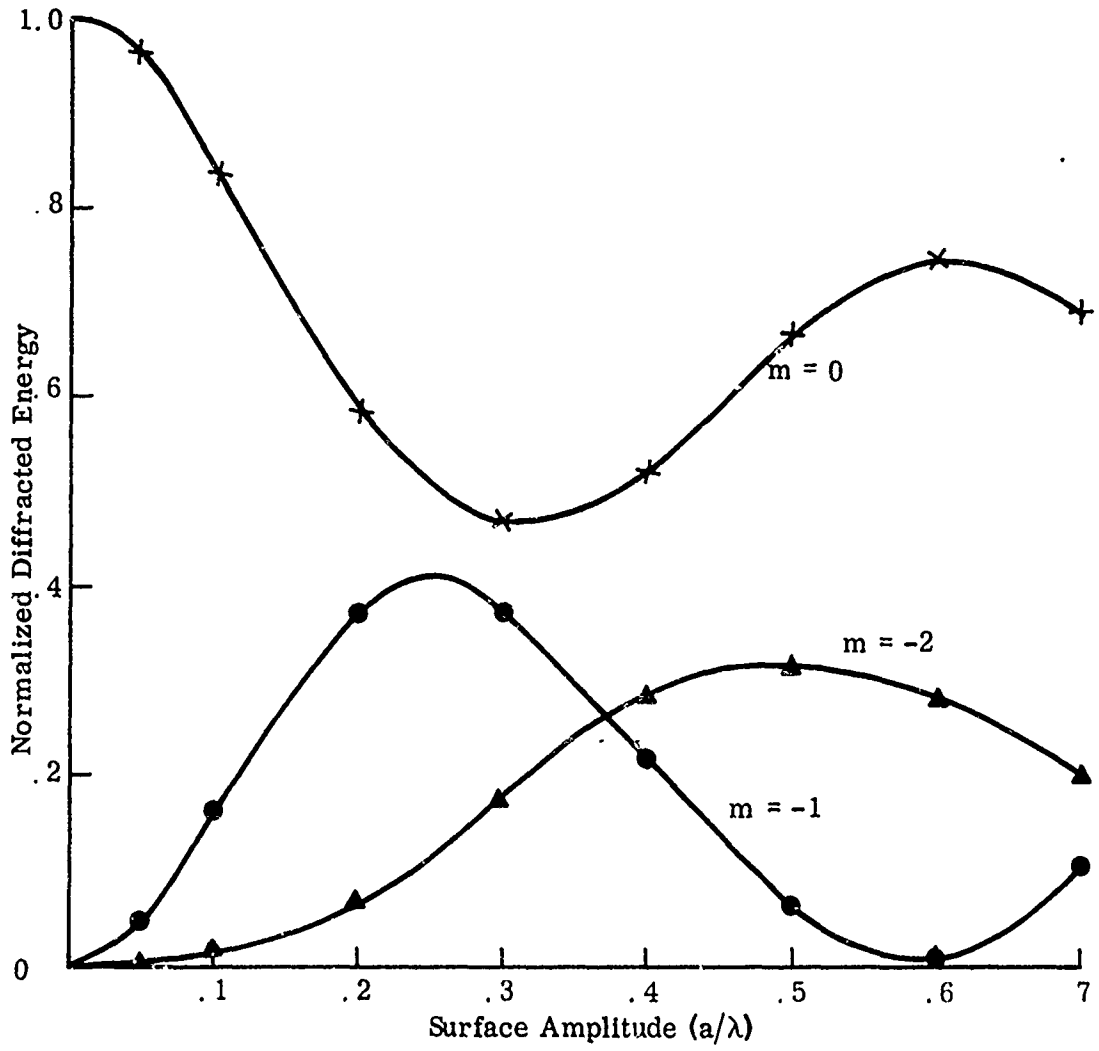

Fig. 4-3: Diffracted Energy for a Sinusoidal Surface ($d = 1.155\lambda$ and $\theta = 60^{\circ}$) for E polarization.

The same kind of plots were also obtained using the physical optics approximation, either with or without shadowing, and they are shown in Figs. 4-4 and 4-5. Comparison with Fig. 4-3 indicates that neither version of the physical optics method gives satisfactory agreement with the exact solution except for the range $a < 0.1\lambda$. For such surface heights, there is no shadow region.

4.3 Conservation of Energy

One criterion that we have used to check the accuracy of the numerical solution is conservation of energy. The numerical results do indeed satisfy this condition, as can be seen from Figs. 4-1 and 4-2 for the two radiating mode case, and from Fig. 4-3 for the three radiating mode case. The results for a single radiating mode are given in Table IV-5.

TABLE IV-5

Conservation of Energy for a Sinusoidal Surface

			Numerical		Physical Optics			
					w/o Shadow		w Shadow	
d/λ	a/λ	$\theta(^o)$	Energy	Error(°/o)	Energy	Error(°/o)	Energy	Error(°/o)
0.2	0.1	0	0.9970	-0.70	0.4128	-58.72	0.4128	-58.72
0.2	0.1	30	0.8564	-1.18	0.4553	-47.50	0.5075	-41.45
0.2	0.1	60	0.5013	0.26	0.4084	-18.32	0.6172	23.44
0.2	0.01	0	0.9990	-0.10	0.9921	- 0.79	0.9921	- 0.79
0.2	0.03	0	1.0042	0.42	0.9308	- 6.92	0.9308	- 6.92
0.4	0.2	0	0.9976	-0.76	0.0030	-99.70	0.0030	-99.70
0.4	0.2	60	0.5068	1.36	0.2061	-58.78	0.1147	-76.47
1.9	0.25	0	0.9996	0.04	0.4202	-57.98	0.4202	-57.98

From Table IV-5 and Figs. 4-4 and 4-5, we see that the physical optics approximations in general do not satisfy the condition of energy conservation.

Another plot showing the relation between the diffracted energy and the minimum radius of curvature (at the surface peak or trough) is shown in Fig. 4-6. It indicates that for $k\rho_{min} > 4.5$, most of the diffracted energy is

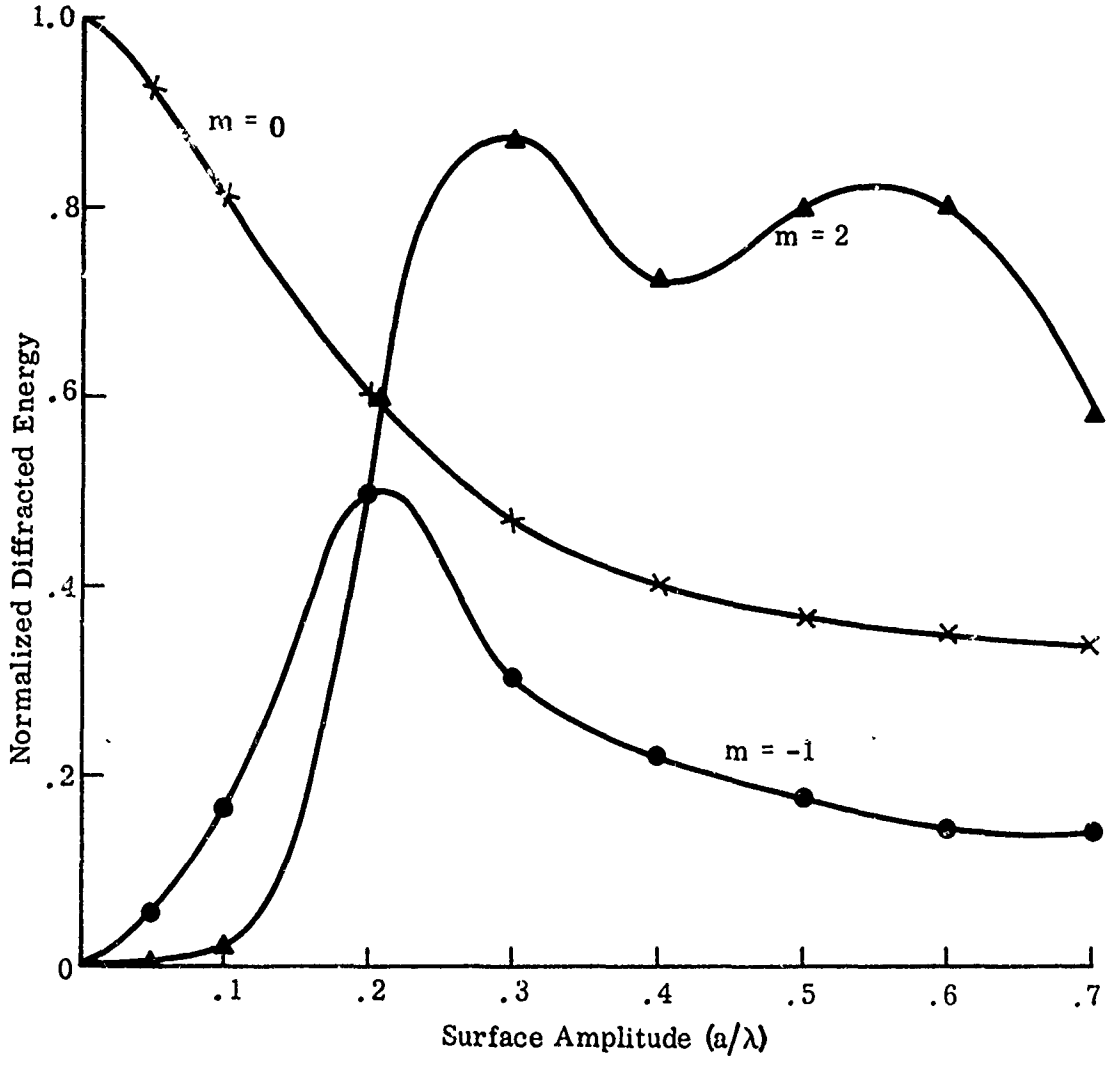

Fig. 4-4: Diffracted Energy for a Sinusoidal Surface ($d = 1.155\lambda$ and $\theta = 60^{\circ}$), Computed Using Physical Optics Method (with shadow), for E polarization.

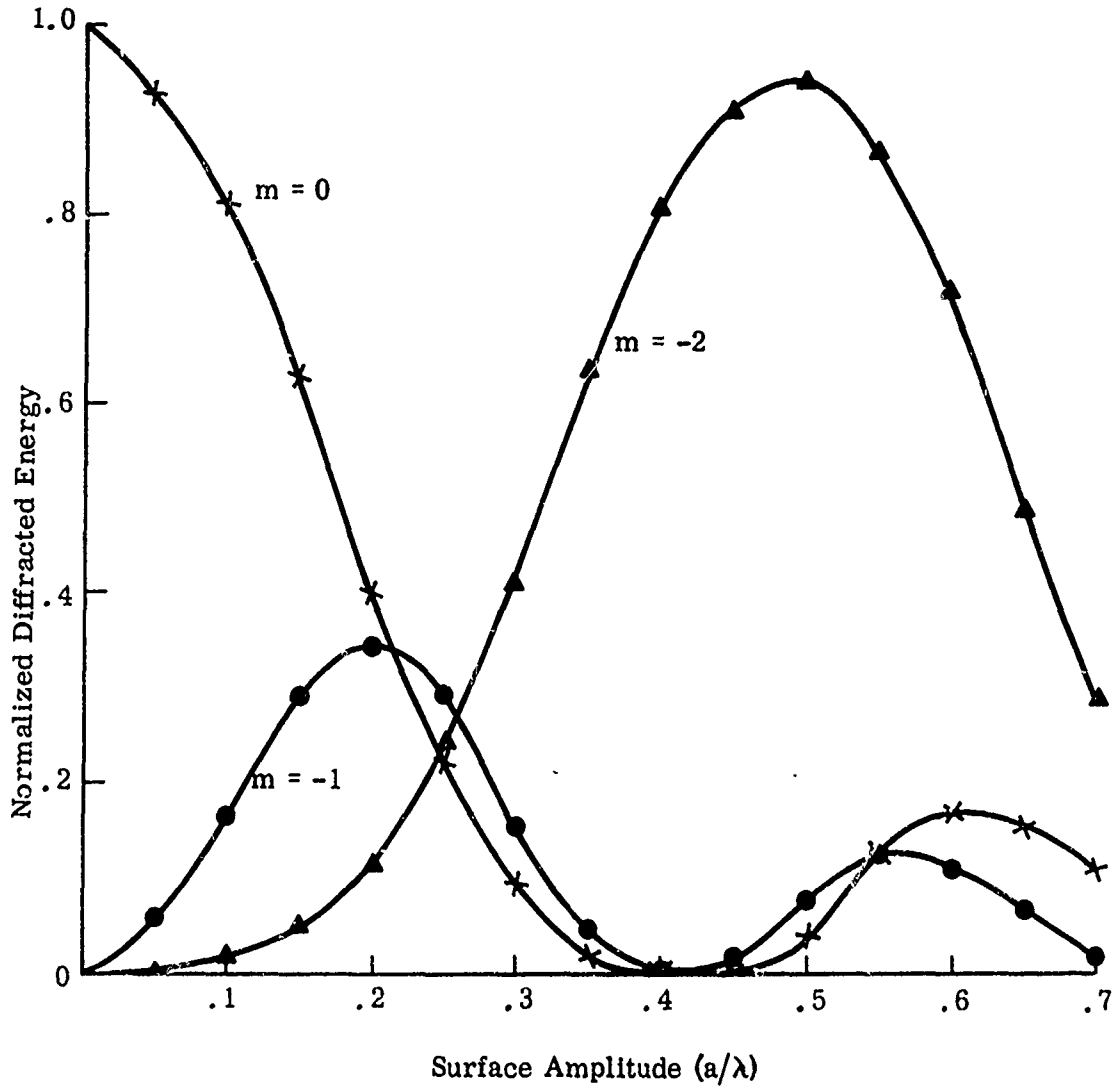

Fig. 4-5: Diffracted Energy for a Sinusoidal Surface ($d = 1.155\lambda$ and $\theta = 60^{\circ}$), Computed Using the Modified Physical Optics Method (without shadow).

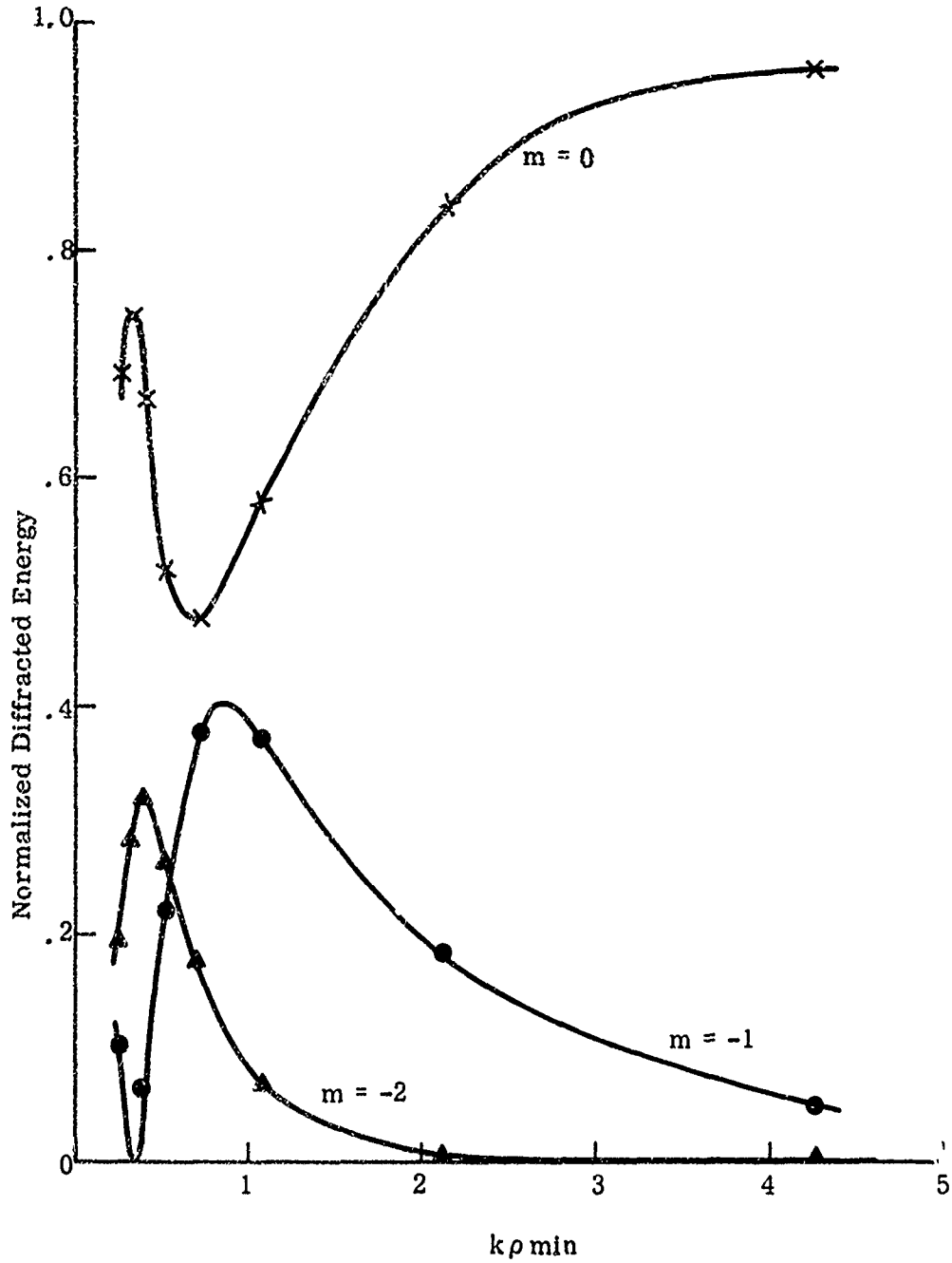

Fig. 4-6: Diffracted Energy for a Sinusoidal Surface ($d = 1.155\lambda$ and $\theta = 60^{\circ}$), for E polarization.

carried away by the $m = 0$ mode so that as far as the radiated field is concerned, the sinusoidal surface can be considered a flat surface if $k\rho_{min} > 4.5$.

4.4 Approximate Techniques

Although the main purpose of this work is to develop numerical procedures for solving the integral equations for scattering from periodic surfaces, a subsidiary objective is to use the understanding gained from our results to treat back-scattering from rough surfaces, with particular reference to oblique angles of incidence. A desirable step in this process is to find more simple methods for predicting the field back-scattered by a periodic surface without resorting to the integral equation.

The method that naturally comes to mind is the physical optics method, but as we have already seen, the predictions are rather poor in the far field and even worse as regards the near field. One reason for this is that the approximation is a local one only, taking no account of the coupling between cells and of the interactions among the diffracted energy.

If we examine the curves shown in Figs. 3-26 through 3-30 for the sinusoidal surface, we notice that over the illuminated portion of the surface and particularly near the surface peak, the current is primarily determined by the local profile shape, and is affected relatively little by the other part of the surface. Furthermore, in most cases the surface field is largest over this region, and the phase does not show the rapid variation which it does in the shadow region. These facts reinforced with some reasoning based on ray optics suggest that it may be possible to estimate the back scattered field with reasonable accuracy using only a knowledge of the current in the illuminated region. This is indeed the case, as was shown by applying the stationary phase method to Eq. (4.4) over the illuminated region and using the exact values for the surface field. The results are presented in Table IV-6 and compared with the exact results.

TABLE IV-6

Comparison of the energy backscattered by a sinusoidal surface: $d = 1.155\lambda$, $\theta = 60^{\circ}$, computed using the exact and stationary phase methods.

Surface Amplitude (a/λ)	Normalized Backscattered Energy Exact Method	Stationary Phase
0.3	0.176	0.152
0.4	0.280	0.320
0.5	0.320	0.360
0.6	0.272	0.344
0.7	0.200	0.216

Since the above computation requires a knowledge of the true surface field, albeit over only a limited portion of the surface, we cannot avoid solving the integral equation unless we can find an approximate method for estimating the surface field in this region. Because of the relatively good agreement between the physical optics phase and the exact phase over the illuminated region, the phase in this region can be simply taken as the incident phase. As for the current modulus, we can approximate it in either of two different ways.

a. Circular cylinder approximation.

For an E-polarized plane wave incident on a circular cylinder of radius a, the modulus of the current induced at the point $P(x,y)$ is

$$\mathrm{mod}\left\{K_z(x)\right\} = \left| -\frac{2}{\omega\mu\pi a} \sum_{n=-\infty}^{\infty} \frac{j^{-n} e^{jnu(x)}}{H_n^{(2)}(ka)} \right| \tag{4.23}$$

where $u(x)$ = obtuse angle between the normal at $P(x,y)$ and the incident ray. Let us now identify a with the local radius of curvature, $\rho(x)$, at the point $P(x,y)$ on the surface (see Fig. 4-7). For a sinusoidal surface, $\rho(x)$ is given by

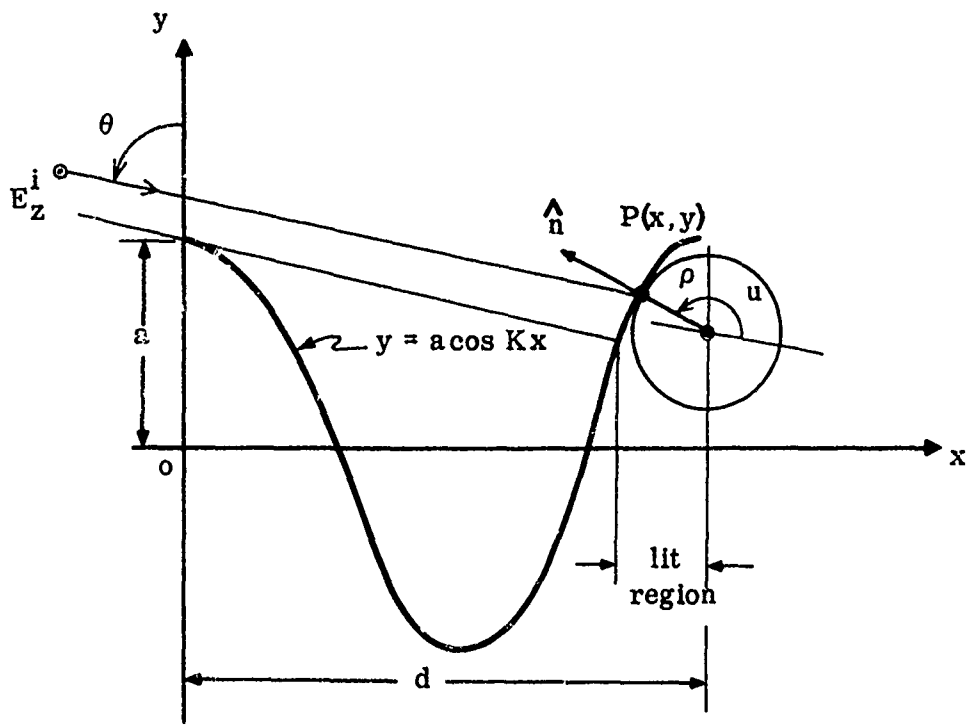

Fig. 4-7: Approximation of the Surface Current Modulus Over the Illuminated Region of the Sinusoidal Surface by that on a Circular Cylinder.

$$\rho(x) = \frac{\left[1+(aK\sin Kx)^2\right]^{3/2}}{aK^2\left|\cos Kx\right|} , \tag{4.24}$$

and

$$u(x) = \frac{3\pi}{4} + \tan^{-1}\left(\frac{1}{aK\sin Kx}\right) - \theta . \tag{4.25}$$

To take account of the deviation of the incident ray from the normal at $P(x,y)$, we multiply Eq. (4.23) by a factor $\cos u$ to give

$$\text{mod}\left\{K_z(x)\right\} = \left| -\frac{2}{\omega\mu\pi\rho} \sum_{n=-\infty}^{\infty} \frac{j^{-n} e^{jnu}}{H_n^{(2)}(k\rho)} \cos u \right| . \tag{4.26}$$

This equation can now be used to compute the current modulus in the illuminated region of the surface.

b. Parabolic cylinder approximation.

Another way of approximating the current modulus over the lit region of the sinusoidal surface is to use our knowledge of the current induced on a perfectly conducting parabolic cylinder whose vertex coincides with the peak of the sinusoidal surface (see Fig. 4-8), and both surfaces have the same radius of curvature at this point. Because of the mathematical complexity of the expression when the cylinder is at oblique incidence, we use instead the normal incidence results and modify it by the factor $\cos u$ defined above.

At normal incidence, the current induced on a parabolic cylinder is

$$K_z(x) = \frac{1}{\omega\mu}\sqrt{\frac{k}{\xi^2+\eta^2}}\,\frac{1}{F(\eta\sqrt{k})}\, e^{-\frac{1}{2}jk(\xi^2+\eta^2)} \tag{4.27}$$

where ξ, η, z are parabolic cylindrical coordinates related to the rectangular Cartesian coordinates by the transformation

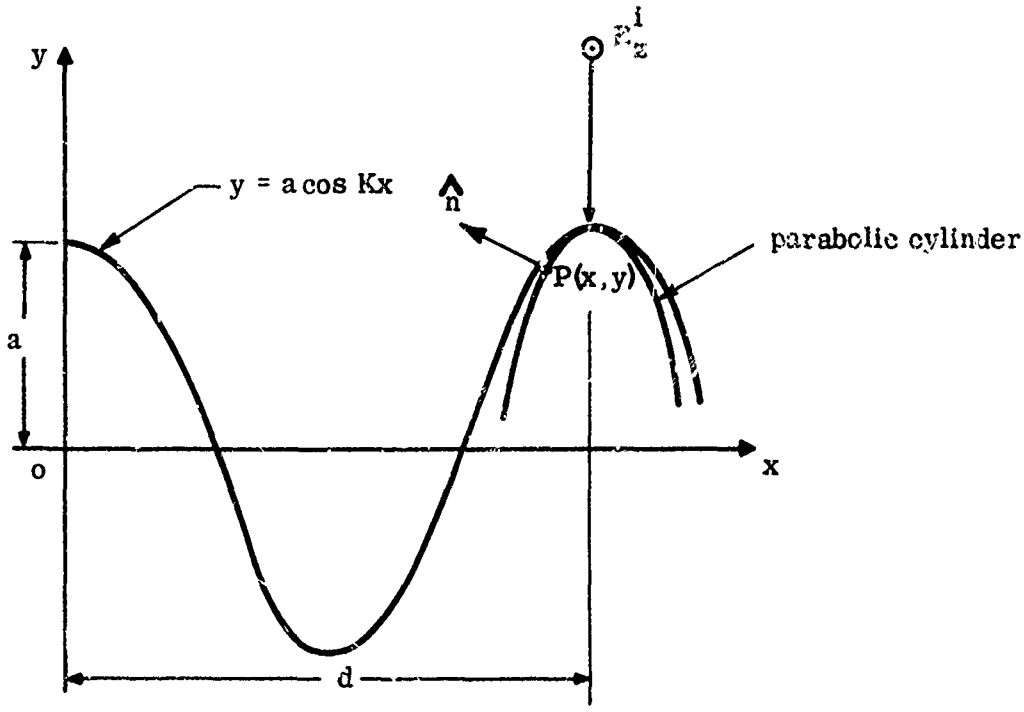

Fig. 4-8: Approximation of the Surface Current Modulus over the Illuminated Region of the Sinusoidal Surface by that on a Parabolic Cylinder.

$$x = \frac{1}{2}(\xi^2 - \eta^2), \qquad y = \eta\xi, \qquad z = z \quad , \tag{4.28}$$

and $F(\eta\sqrt{h})$ is the Fresnel integral which can be computed using

$$F(\omega) = \sqrt{\pi/2}\left[\frac{1}{2} - \int_0^{\sqrt{2/\pi}\,\omega} \cos\left(\frac{1}{2}\pi t^2\right) dt\right] + j\left[\frac{1}{2} - \int_0^{\sqrt{2/\pi}\,\omega} \sin\left(\frac{1}{2}\pi t^2\right) dt\right] \tag{4.29}$$

Thus, multiplying Eq. (4.27) by $\cos u$, we get

$$K_z(x) = \frac{1}{\omega\mu}\sqrt{\frac{k}{\xi^2+\eta^2}}\;\frac{1}{F(\eta\sqrt{k})}\; e^{-\frac{1}{2}jk(\xi^2+\eta^2)} \cos u\,, \tag{4.30}$$

and

$$\left|K_z(x)\right| = \left|\frac{1}{\omega\mu}\sqrt{\frac{k}{\xi^2+\eta^2}}\;\frac{1}{F(\eta\sqrt{k})}\; e^{-\frac{1}{2}jk(\xi^2+\eta^2)} \cos u\right| \tag{4.31}$$

which is the equation used to compute the current modulus in the illuminated region of a sinusoidal surface at oblique incidence.

From experience, it has been found that the parabolic cylinder approximation generally gives results slightly less than the exact values, whereas the circular cylinder approximation gives slightly larger values. The results are shown in Table IV-7, and also compared with the exact values.

TABLE IV-7

Comparison of Normalized Current Modulus over the Illuminated Region for the Sinusoidal Surface with $d = 1.155\lambda$ and $\theta = 60^{\circ}$.

Surface Amplitude a/λ	Location of Point On the Surface, x Coordinate (λ)	Exact Results	Circular Cylinder Approx.	Parabolic Cylinder Approx.
0.3	0.82	0.90	1.66	0.70
	0.92	1.45	1.87	1.20
	1.01	1.88	2.06	1.75
	1.11	1.88	2.10	1.83
0.4	0.92	1.26	1.50	1.00
	1.01	1.75	1.94	1.50
	1.11	1.92	2.15	1.96
0.5	0.92	1.14	1.60	0.96
	1.01	1.15	1.86	1.25
	1.11	2.08	2.20	2.12
0.6	0.92	1.00	1.50	0.70
	1.01	1.33	1.99	1.18
	1.11	2.25	2.30	2.20

Chapter V

SURFACE FIELD DATA FOR H POLARIZATION

In this chapter surface field distributions obtained by numerical solution of the integral equation for H polarization are presented. The particular profiles considered are sinusoidal, full-wave rectified, inverted full-wave rectified, and triangular (see Fig. 3-1) with various periods and angles of incidence. In each case the physical optics approximation is presented as a basis for comparison, and comparison is also made with analogous results for E polarization. Many of the remarks made in Chapter III for E polarization hold for H polarization as well, but the surface field now is generally more complicated and unpredictable even over a small region of the surface.

According to physical optics, the surface current induced on the surface is

$$K_t(x) = 2e^{-jk(x \sin\theta - f(x) \cos\theta)} \tag{5.1}$$

in the illuminated region, and

$$K_t(x) = 0$$

in the shadow.

As in the case of E polarization, however, this approximation is inadequate for many purposes.

5.1 Surfaces of Small Period ($d/\lambda \leq 0.2$)

Figures 5-1 through 5-12 represent the surface fields on periodic surfaces of four different profiles, each having a period $d = 0.2\lambda$ and a maximum amplitude $a = 0.1\lambda$. The angles of incidence are $\theta = 0$, 30°, and 60°.

Let us first examine the results for a sinusoidal surface (Figs. 5-1 through 5-3). The current modulus now has a maximum at the surface trough and a minimum at the peak, and in contrast to the case for E polarization, it remains

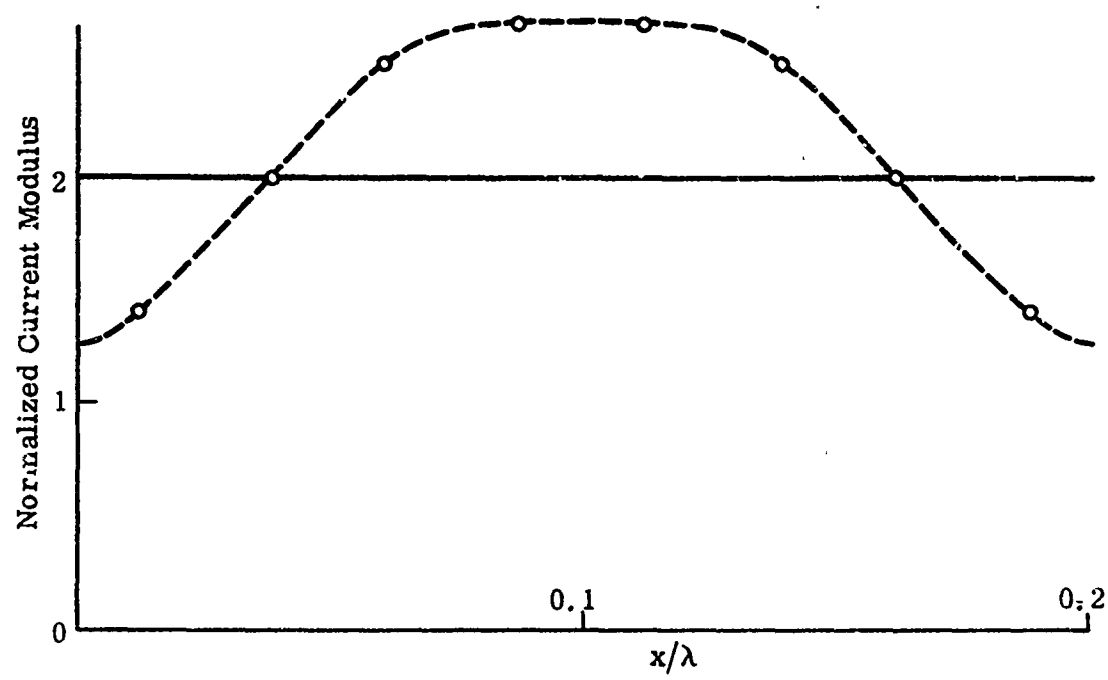

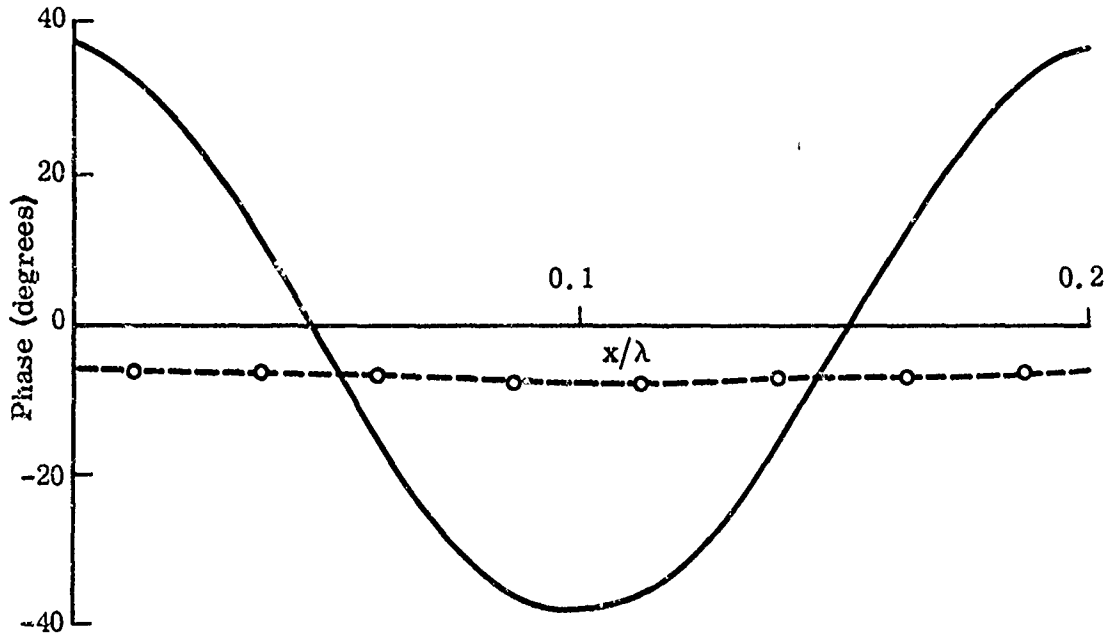

Fig. 5-1: Normalized Surface Field for a Sinusoidal Surface ($d = 0.2\lambda$, $a = 0.1\lambda$ and $\theta = 0$) for H polarization, --o-- exact, — physical optics.

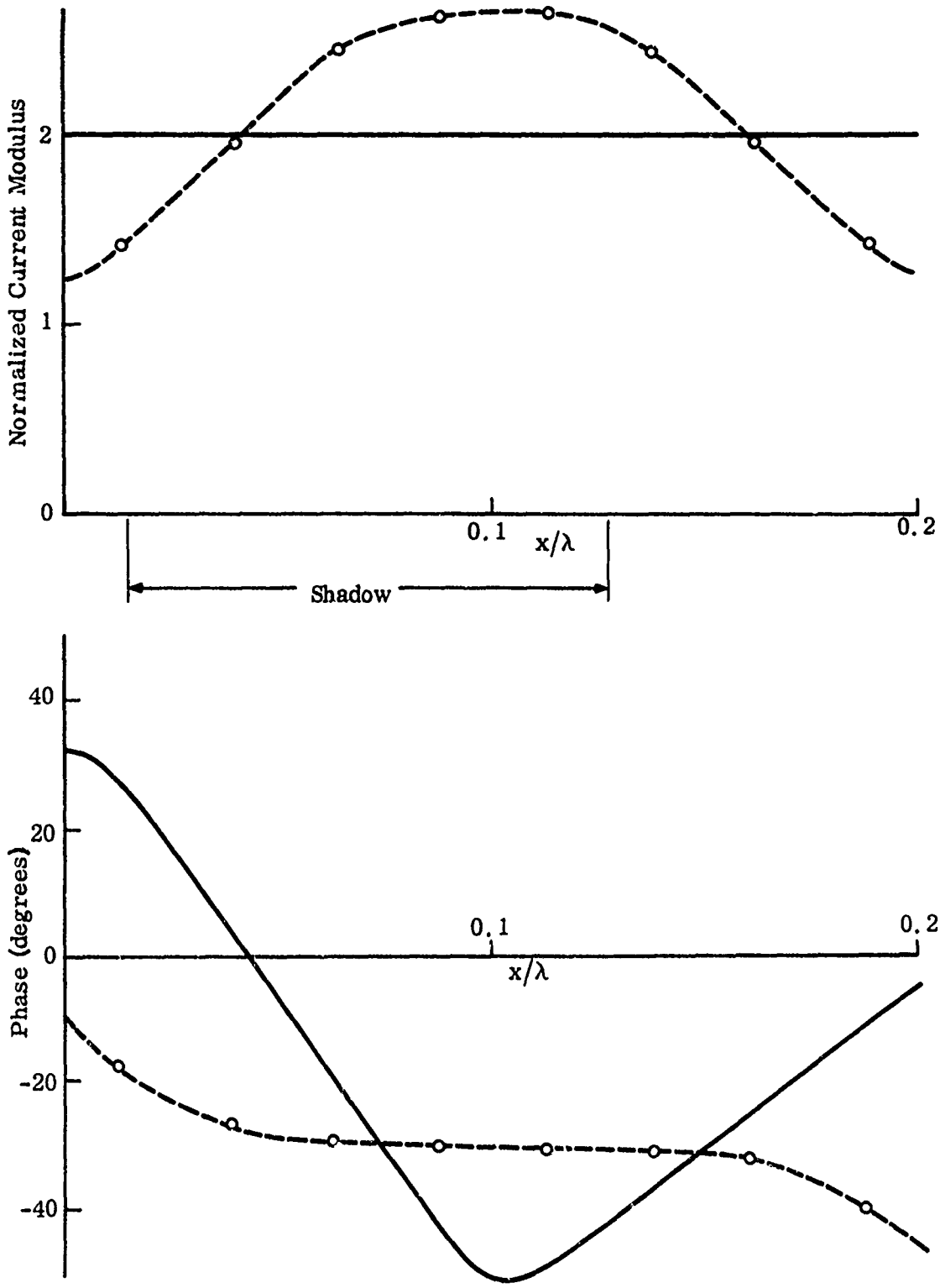

Fig. 5-2: Normalized Surface Field for a Sinusoidal Surface ($d = 0.2\lambda$, $a = 0.1\lambda$ and $\theta = 30^{\circ}$) for H polarization, --o-- exact, — physical optics.

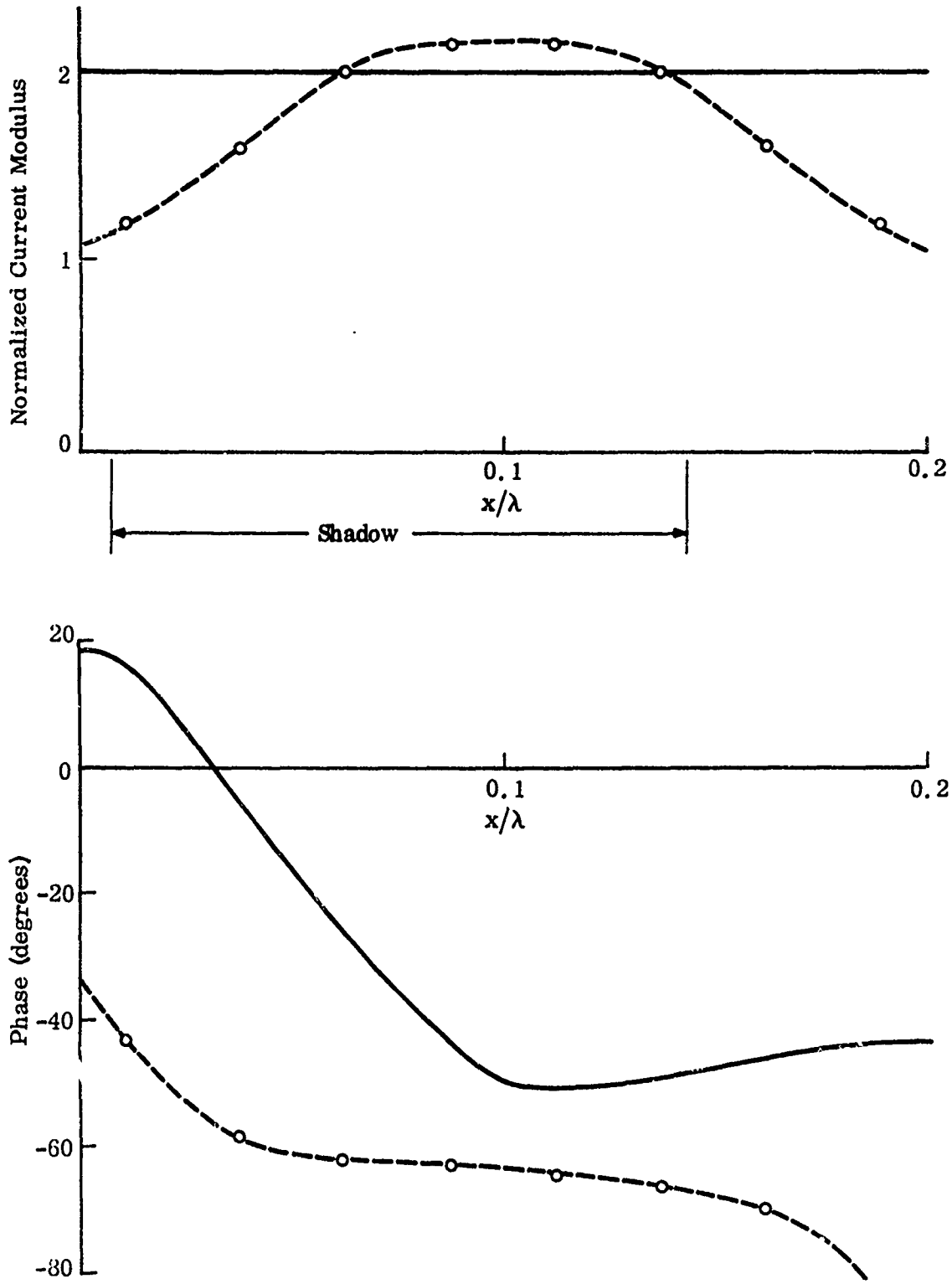

Fig. 5-3: Normalized Surface Field for a Sinusoidal Surface ($d = 0.2\lambda$, $a = 0.1\lambda$ and $\theta = 60^{\circ}$) for H polarization --o-- exact, — physical optics.

substantially unchanged as the angle of incidence is varied. The physical optics approximation is somewhat like the mean of the exact solution. For $\theta = 0$, the phase is almost constant (as for E polarization), but there is more variation, especially near the surface peak, when $\theta \neq 0$.

Figures 5-4 through 5-9 show the surface fields for full-wave rectified and inverted full-wave rectified profiles. Except that there is a slight improvement in the agreement between the exact modulus and the modulus of the physical optics, the general behavior is rather similar to that for a sinusoidal surface. Shadowing has little effect on the current modulus.

The last three figures (Figs. 5-10 through 5-12) are for triangular profiles, and we note only the absence of any "edge effects".

A point worth mentioning is that for all the profiles considered, the exact phase at normal incidence is close (in a mean sense at least) to the physical optics phase. In order to see why the modulus of the surface field is so insensitive to any change in the angle of incidence, let us go back to Eq. (2.35). As in the case of E polarization, if the period is sufficiently small, we can approximate the modified Green's function, Eq. (2.36), by the first two and the last two terms. Thus, the approximate integral equation becomes

$$\int_0^d G_2^*(x, y; x', y')\, K_t(x')dx' \simeq jd\left\{2H_z^i(x) - K_t(x)\right\} , \tag{5.2}$$

where

$$\begin{aligned} G_2^*(x, y; x', y') = {} & -j\,\mathrm{sgn}(y-y') - j\left\{f'(x')\tan\theta - \mathrm{sgn}(y-y')\right\} \times \\ & e^{-jk\sin\theta(x-x') - jk\cos\theta|y-y'|} + \\ & + \frac{j}{2}\left\{f'(x') + j\,\mathrm{sgn}(y-y')\right\}\cot\left\{-\frac{\pi}{d}(x-x') + j\frac{\pi}{d}|y-y'|\right\} + \\ & + \frac{j}{2}\left\{-f'(x') + j\,\mathrm{sgn}(y-y')\right\}\cot\left\{\frac{\pi}{d}(x-x') + j\frac{\pi}{d}|y-y'|\right\} . \end{aligned} \tag{5.3}$$

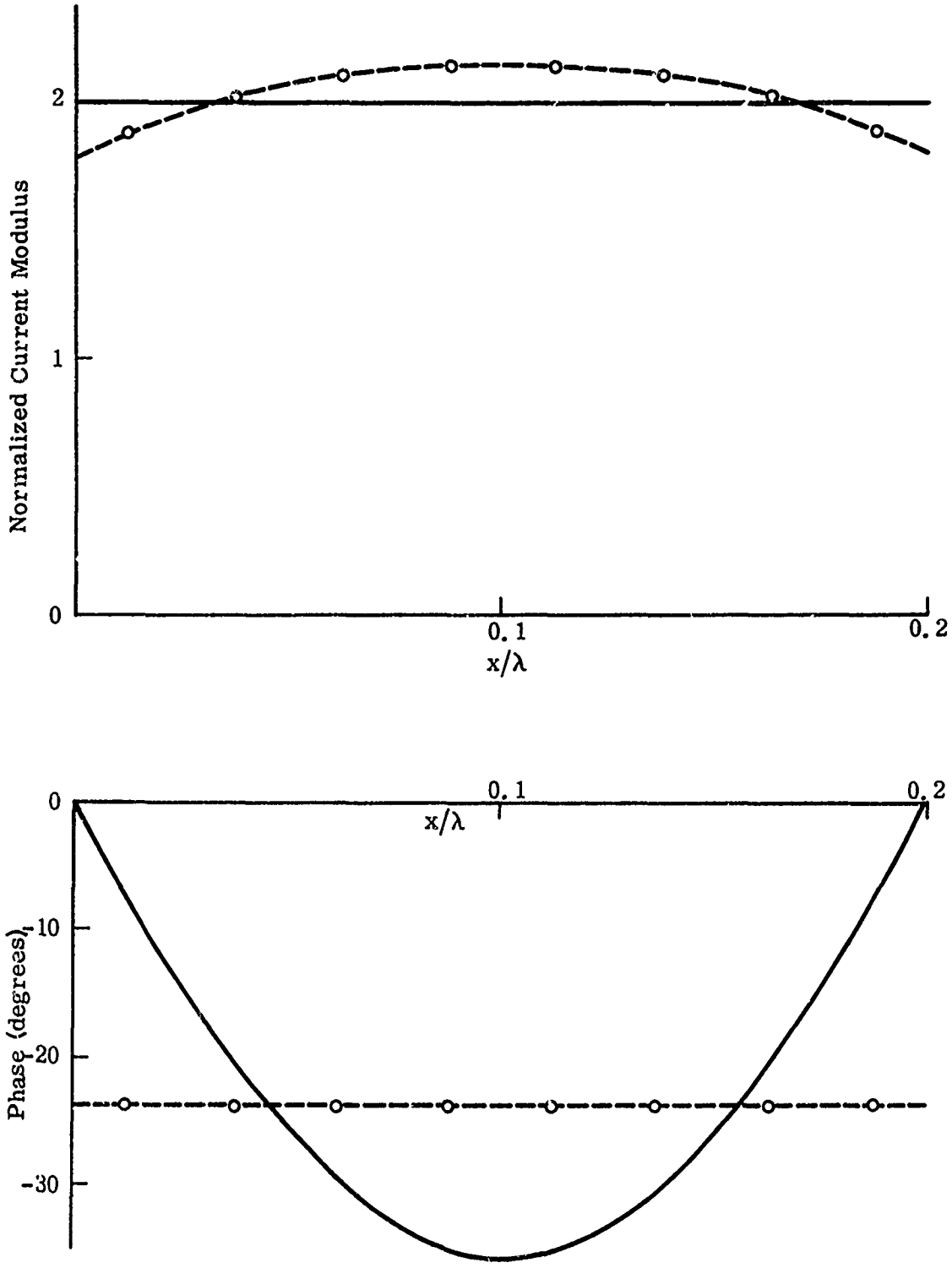

Fig. 5-4: Normalized Surface Field for an Inverted Full-Wave Rectified Surface ($d = 0.2\lambda$, $a = 0.1\lambda$ and $\theta = 0$) for H polarization, --o-- exact, — physical optics.

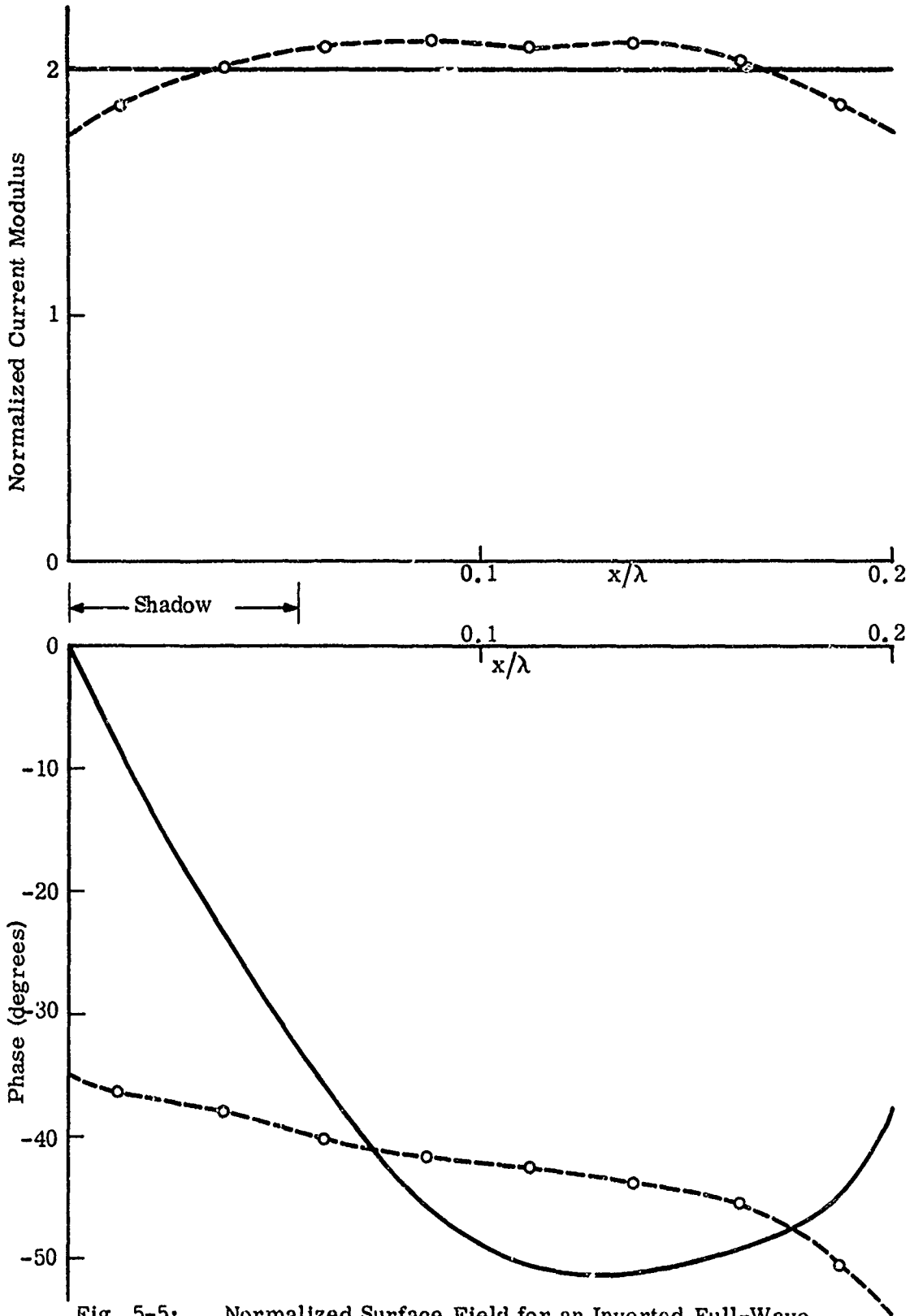

Fig. 5-5: Normalized Surface Field for an Inverted Full-Wave Rectified Surface ($d = 0.2\lambda$, $a = 0.1\lambda$ and $\theta = 30^{\circ}$) for H polarization, --o-- exact, — physical optics.

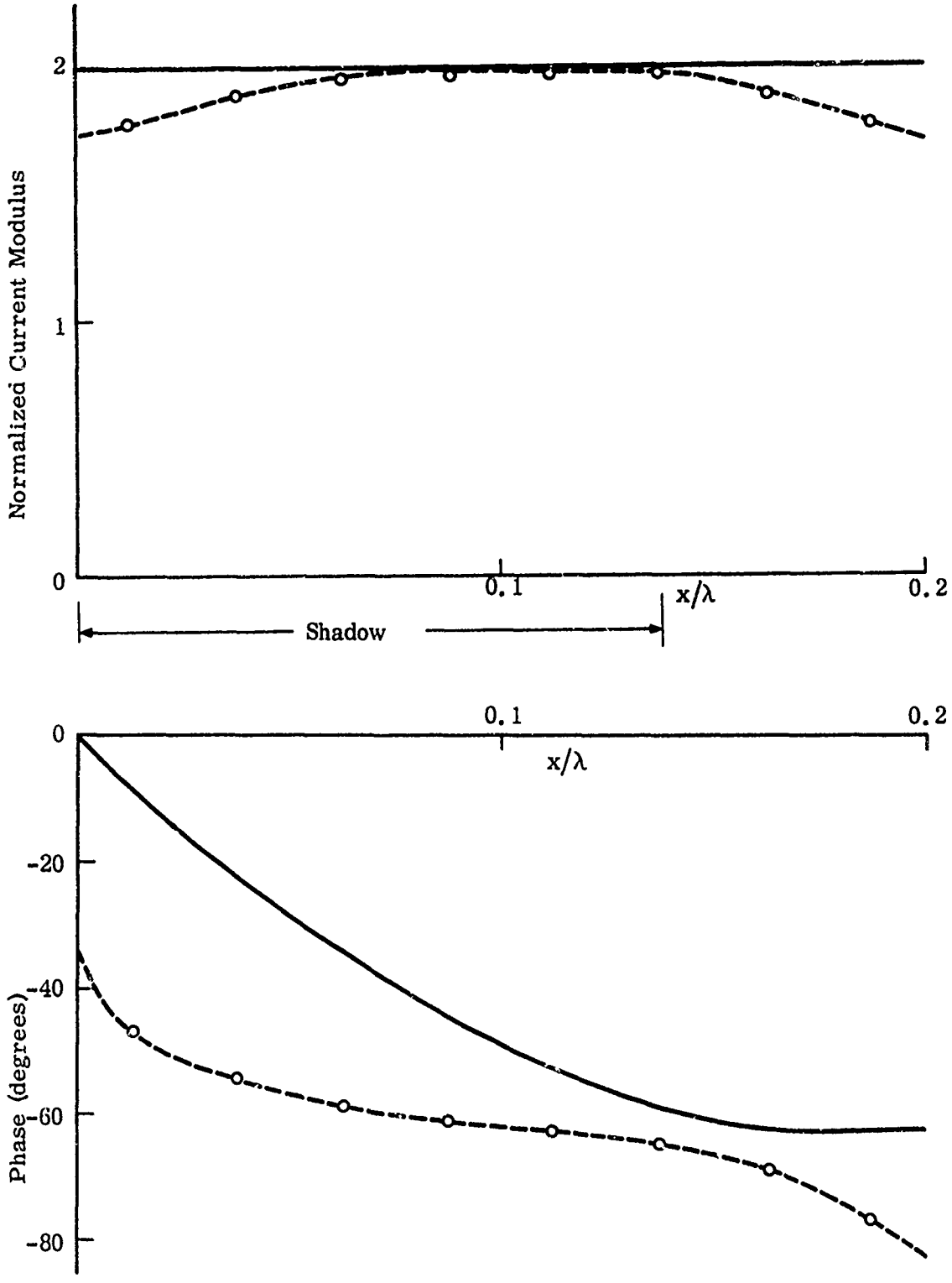

Fig. 5-6: Normalized Surface Field for an Inverted Full-Wave Rectified Surface ($d = 0.2\lambda$, $a = 0.1\lambda$ and $\theta = 60^{\circ}$) for H polarization, --o-- exact, — physical optics.

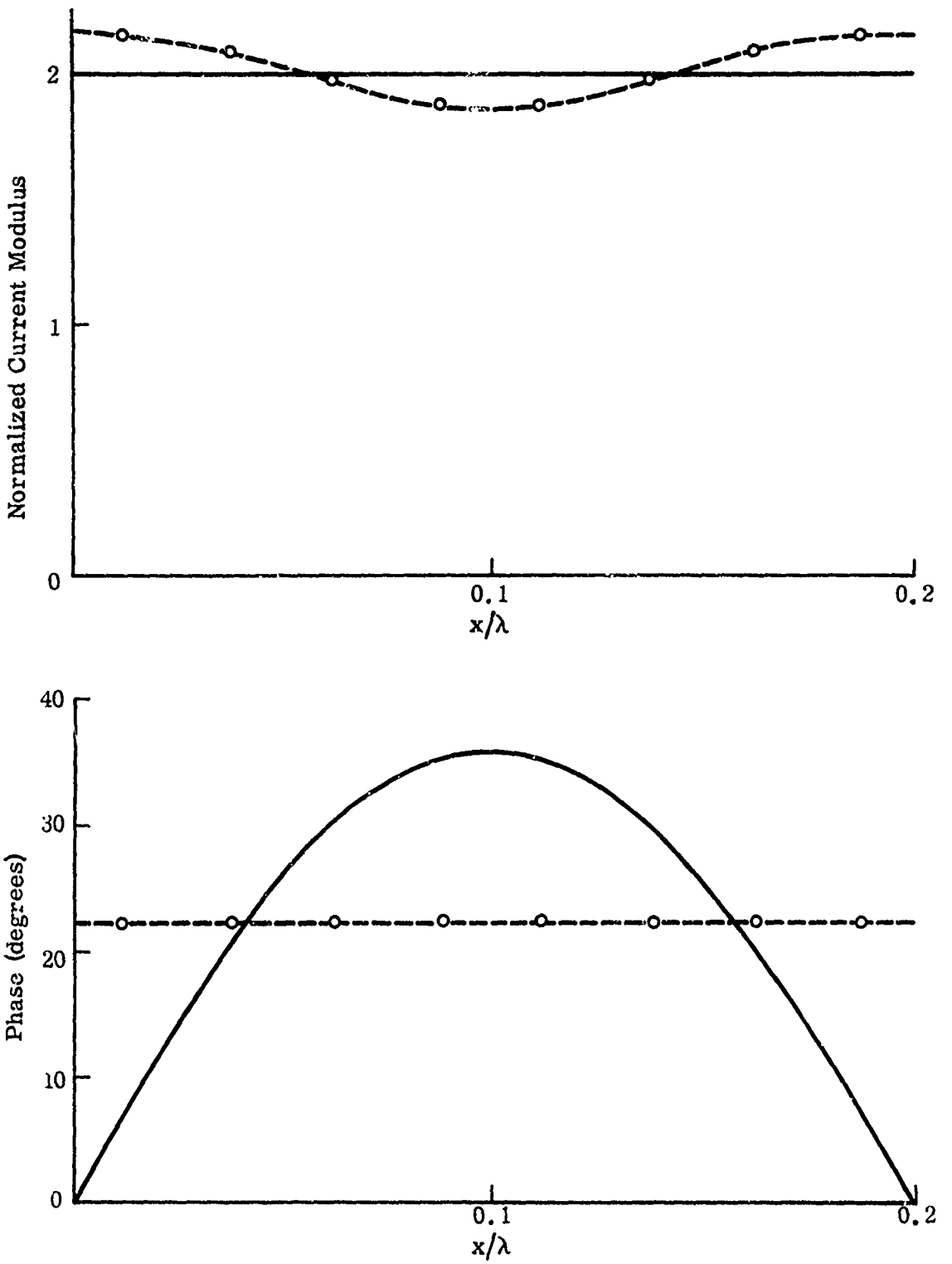

Fig. 5-7: Normalized Surface Field for a Full-Wave Rectified Surface ($d = 0.2\lambda$, $a = 0.1\lambda$ and $\theta = 0$) for H polarization, --o-- exact, — physical optics.

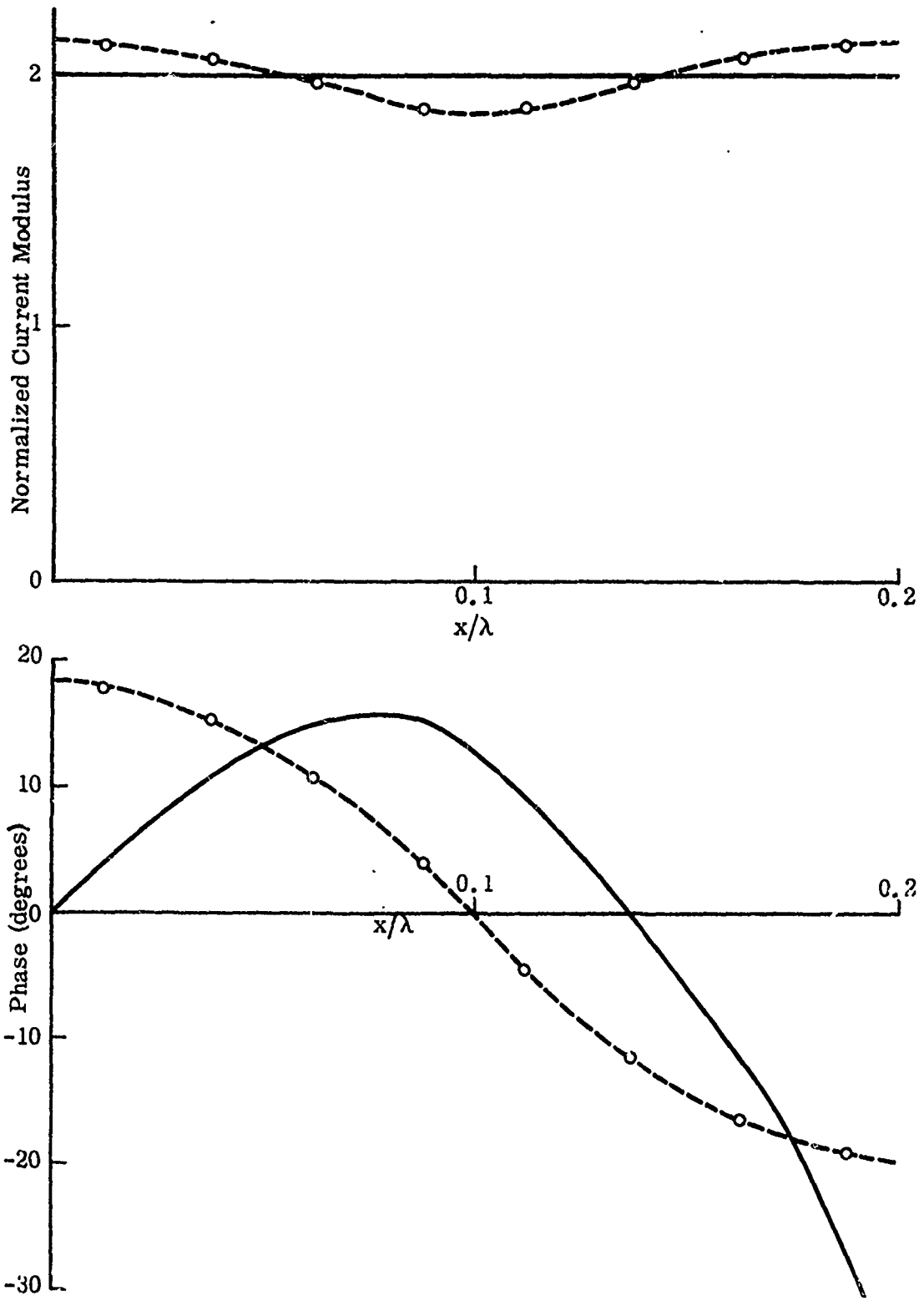

Fig. 5-8: Normalized Surface Field for a Full-Wave Rectified Surface ($d = 0.2\lambda$, $a = 0.1\lambda$ and $\theta = 30^{\circ}$) for H polarization, --o-- exact, — physical optics.

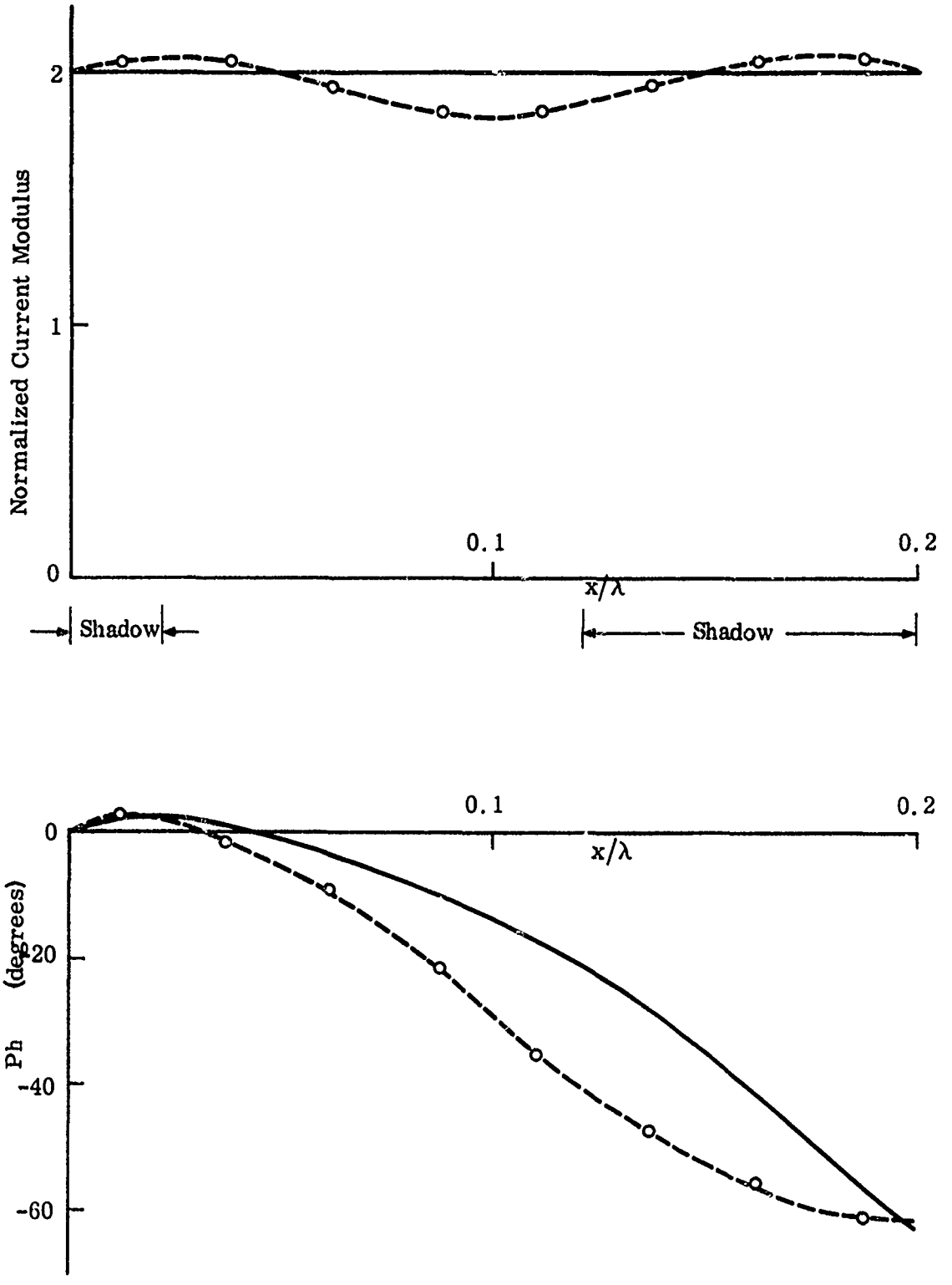

Fig. 5-9: Normalized Surface Field for a Full-Wave Rectified Surface ($d = 0.2\lambda$, $a = 0.1\lambda$ and $\theta = 60^{\circ}$) for H polarization, --o-- exact, — physical optics.

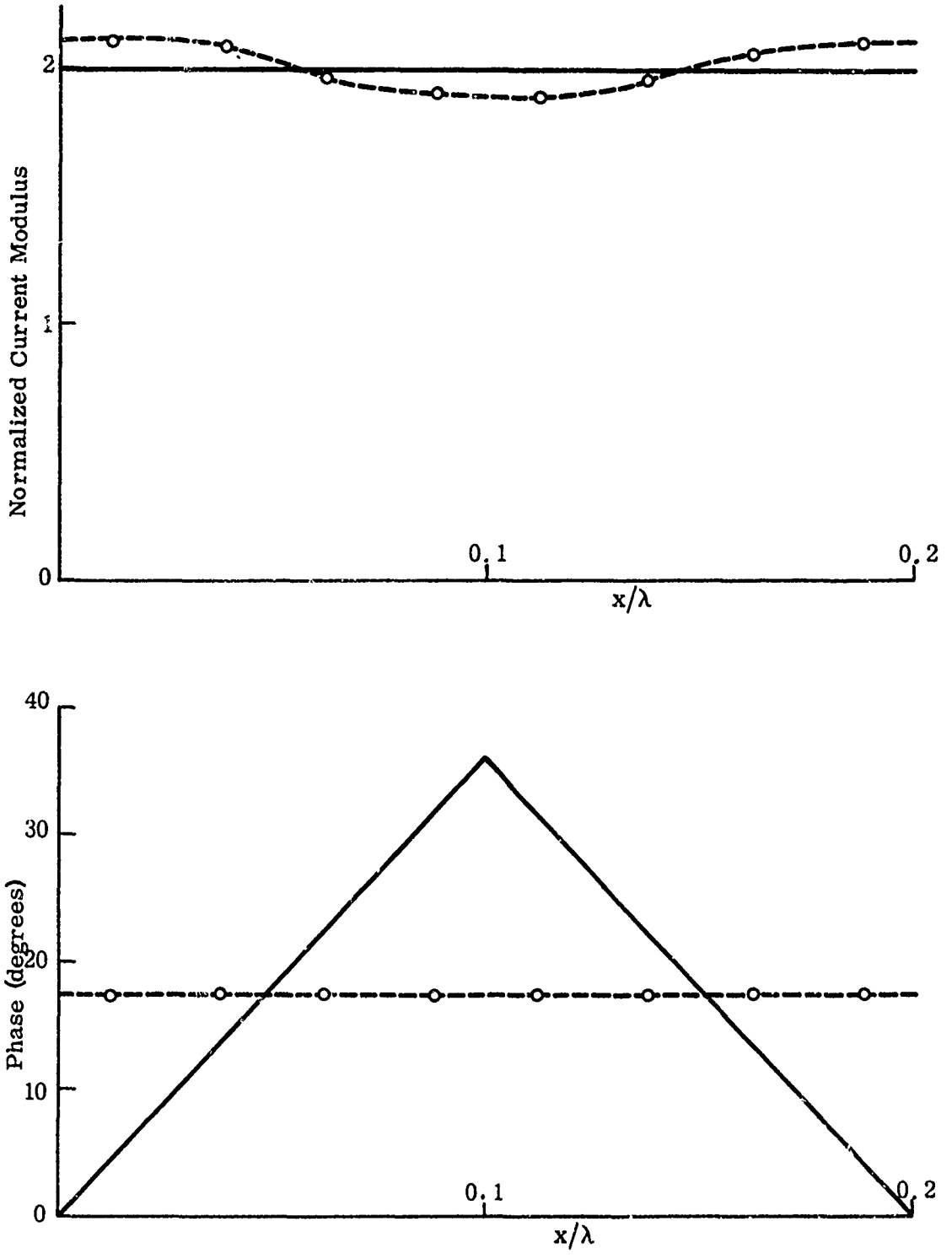

Fig. 5-10: Normalized Surface Field for a Triangular Surface ($d = 0.2\lambda$, $\ell = 0.1\lambda$, $a = 0.1\lambda$ and $\theta = 0$) for H polarization, --o-- exact, — physical optics.

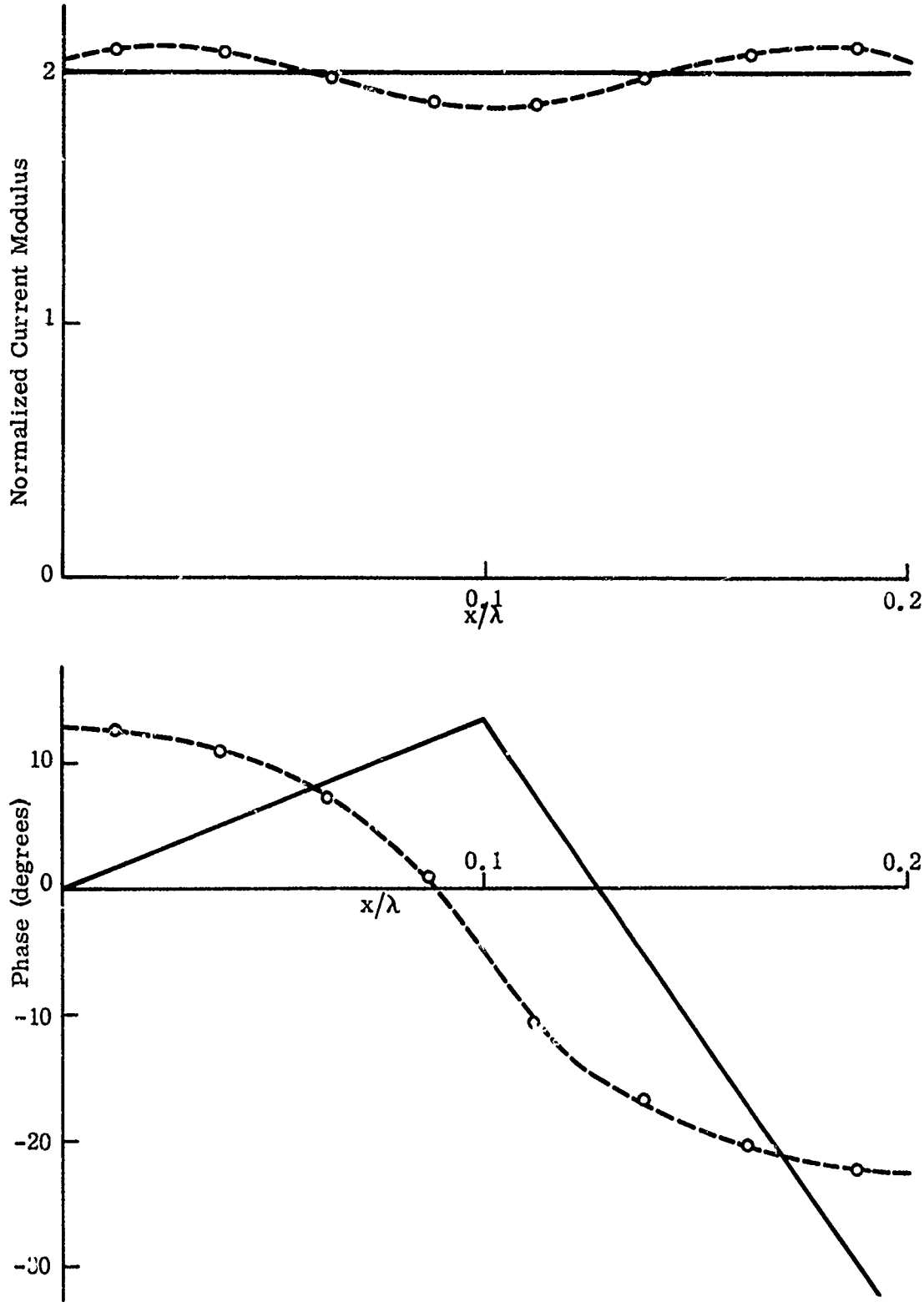

Fig. 5-11: Normalized Surface Field for a Triangular Surface ($d = 0.2\lambda$, $\ell = 0.1\lambda$, $a = 0.1\lambda$ and $\theta = 30^{\circ}$) for H polarization, --o-- exact, — physical optics.

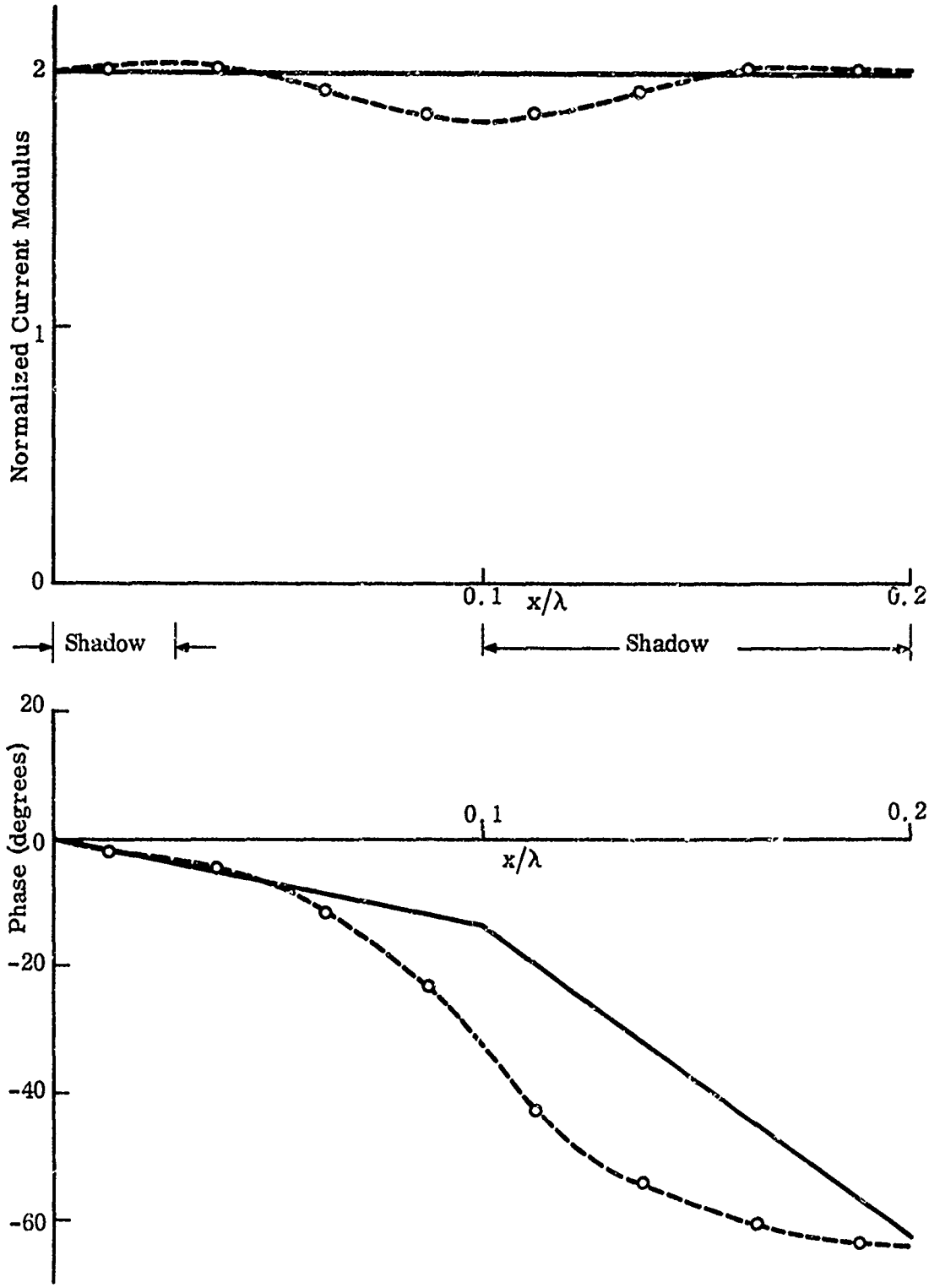

Fig. 5-12: Normalized Surface Field for a Triangular Surface ($d = 0.2\lambda$, $\ell = 0.1\lambda$, $a = 0.1\lambda$ and $\theta = 60^{\circ}$) for H polarization --o-- exact, — physical optics.

Note that of the four terms in G_2^*, only the second contains the angle of incidence explicitly. Since the integral equation is singular, a rough picture of the solution may be obtained if we consider the integral equation in the neighborhood of the singularity. Thus

$$\lim_{\substack{|x-x'|\to 0\\ |y-y'|\to 0}} G_2^*(x,y;x',y') = -j\,\mathrm{sgn}(y-y') - j\left\{f'(x')\tan\theta - \mathrm{sgn}(y-y')\right\} +$$

$$+\frac{j}{2}\left\{f'(x)+j\,\mathrm{sgn}(y-y')\right\}\lim_{\substack{|x-x'|\to 0\\ |y-y'|\to 0}} \cot\left\{-\frac{\pi}{d}(x-x')+j\frac{\pi}{d}|y-y'|\right\} +$$

$$+\frac{j}{2}\left\{-f'(x')+j\,\mathrm{sgn}(y-y')\right\}\lim_{\substack{|x-x'|\to 0\\ |y-y'|\to 0}} \cot\left\{\frac{\pi}{d}(x-x')+j\frac{\pi}{d}|y-y'|\right\}. \quad (5.4)$$

Using the relation

$$\cot(\xi) = j\,\frac{e^{j\xi}+e^{-j\xi}}{e^{j\xi}-e^{-j\xi}}$$

we obtain for the cotangent terms

$$\cot(-a+jb) = j\,\frac{1+e^{2b+j2a}}{1-e^{2b+j2a}}, \quad \text{and} \quad \cot(a+jb) = j\,\frac{1+e^{2b-j2a}}{1-e^{2b-j2a}}, \quad (5.5)$$

where $a = \frac{\pi}{d}(x-x')$, $b = \frac{\pi}{d}|y-y'|$.

Therefore,

$$\lim_{\substack{|x-x'|\to 0\\ |y-y'|\to 0}} \cot\left\{-\frac{\pi}{d}(x-x')+j\frac{\pi}{d}|y-y'|\right\} = \lim_{\substack{|a|\to 0\\ b\to 0}} \frac{j(1+e^{2b+j2a})}{1-e^{2b+j2a}}$$

$$\simeq \lim_{\substack{|a|\to 0\\ b\to 0}} \frac{-(a+jb)}{a^2+b^2}. \quad (5.6)$$

Similarly, for the other term

$$\lim_{\substack{|x-x'|\to 0\\ |y-y'|\to 0}} \cot\left\{\frac{\pi}{d}(x-x')+j\frac{\pi}{d}|y-y'|\right\} \approx \lim_{\substack{|a|\to 0\\ b\to 0}} \frac{(a-jb)}{a^2+b^2} \quad . \tag{5.7}$$

Substituting Eqs. (5.6) and (5.7) into Eq. (5.4), we obtain, after some manipulation,

$$\lim_{\substack{|x-x'|\to 0\\ |y-y'|\to 0}} G_2^*(x,y;x',y') = -j\,\mathrm{sgn}(y-y') - j\left[f'(x')\tan\theta - \mathrm{sgn}(y-y')\right] + \\ + \lim_{\substack{|a|\to 0\\ b\to 0}} \frac{2j}{d(a^2+b^2)}\left[b\,\mathrm{sgn}(y-y')+af'(x')\right] \quad . \tag{5.8}$$

Thus, in the neighborhood of the singularity, Eq. (5.2) becomes

$$\int_{x-\epsilon}^{x+\epsilon} \left\{-j\,\mathrm{sgn}(y-y') - j\left[f'(x')\tan\theta - \mathrm{sgn}(y-y')\right] + \right.$$

$$\left. + \lim_{\substack{|a|\to 0\\ b\to 0}} \frac{2j}{d(a^2+b^2)}\left[b\,\mathrm{sgn}(y-y')+af'(x')\right]\right\} K_t(x')dx'$$

$$\simeq jd\left\{2H_z^i(x) - K_t(x)\right\} \tag{5.9}$$

where $|x-x'|<\epsilon$ with $\epsilon\ (>0)$ an arbitrarily small number.

If we assume $K_t(x)$ to remain constant over this small region of integration, then by the property of $\mathrm{sgn}(y-y')$, all integrations involving $\mathrm{sgn}(y-y')$ vanish. Hence

$$\int_{x-\epsilon}^{x+\epsilon} \left\{-jf'(x')\tan\theta + \lim_{\substack{|a|\to 0\\ b\to 0}} \frac{2jaf'(x')}{d(a^2+b^2)}\right\} K_t(x')dx' \simeq jd\left\{2H_z^i(x) - K_t(x)\right\} \tag{5.10}$$

If the surface amplitude is relatively small, a and b can be assumed to be of the same order of magnitude, in which case Eq. (5.10) becomes

$$\int_{x-\epsilon}^{x+\epsilon} \left\{ -jf'(x')\tan\theta + \frac{jf'(x')}{\pi(x-x')} \right\} K_t(x')dx' \simeq jd\left\{ 2H_z^i(x) - K_t(x) \right\} , \tag{5.11}$$

which can be solved by treating $K_t(x)$ and $f(x)$ as constant over the range of integration. We thus obtain

$$-jf'(x)\tan\theta\, K_t(x)2\epsilon \simeq jd\left\{ 2H_z^i(x) - K_t(x) \right\} , \tag{5.12}$$

and since ϵ is an arbitrarily small number, the left hand side can be neglected in comparison with the second term on the right hand side. Equation (5.12) now reduces to

$$K_t(x) = 2H_z^i(x) , \tag{5.13}$$

which is just the geometrical optics value. This is consistent with the numerical results.

For a sinusoidal profile, the effect on the surface field produced by a change in the surface amplitude as the period is kept constant is shown in Figs. 5-1, 5-13 and 5-14. As the surface height is increased, the numerical results approach those for a flat sheet.

5.2 Surfaces of Slightly Larger Period ($0.2 \lesssim d/\lambda \lesssim 0.6$)

Figures 5-15 and 5-16 show the surface field for a sinusoidal profile with $d = 0.4\lambda$, $a = 0.2\lambda$ and $\theta = 0$, 60° respectively. By comparing these with Figs. 5-1 and 5-3 it is seen that doubling both d and a has a somewhat larger effect on the current modulus than was the case for E polarization. In particular, there is a noticeable change of shape, with minimum no longer

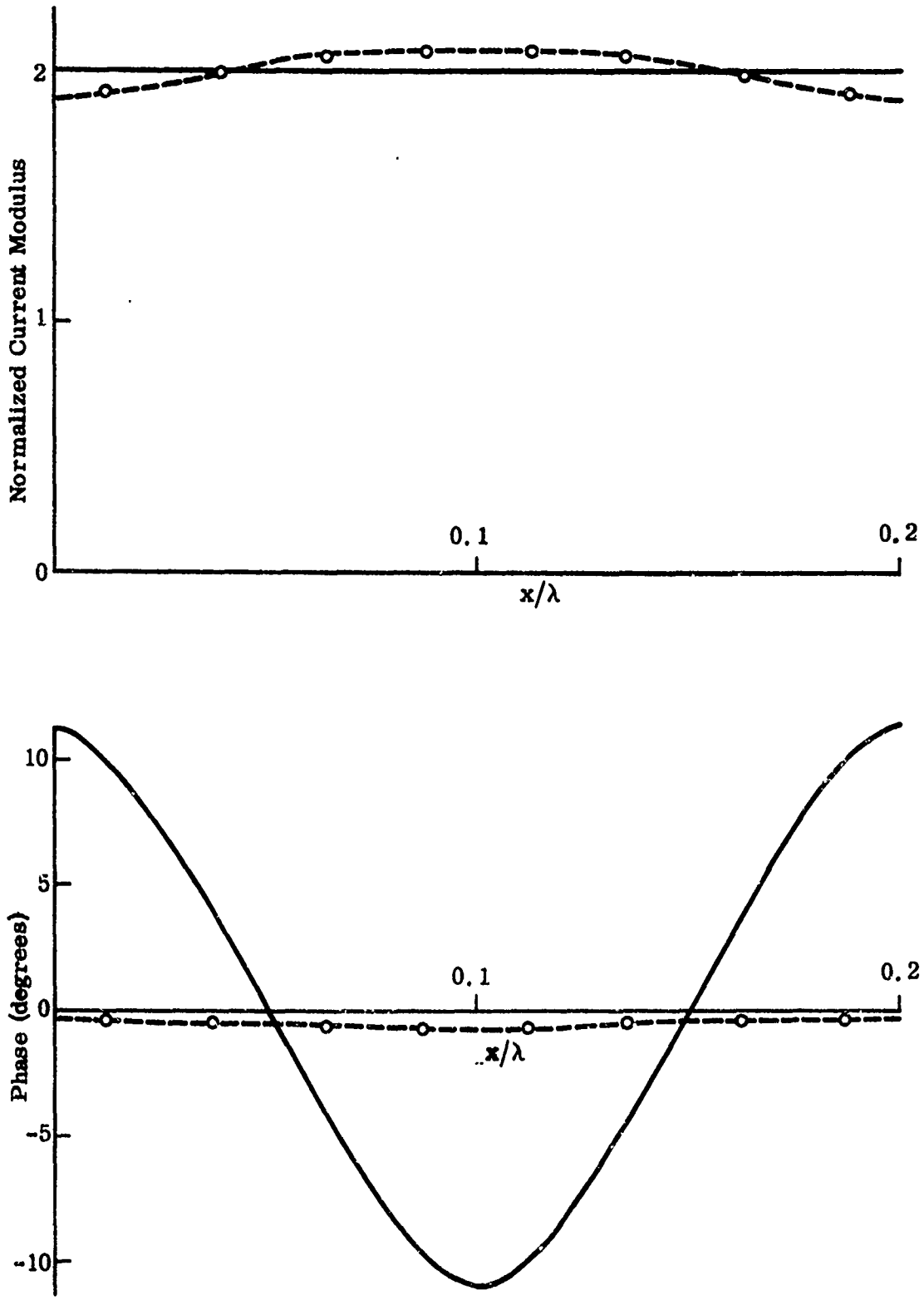

Fig. 5-13: Normalized Surface Field for a Sinusoidal Surface ($d = 0.2\lambda$, $a = 0.03\lambda$ and $\theta = 0$) for H polarization, --o-- exact, — physical optics.

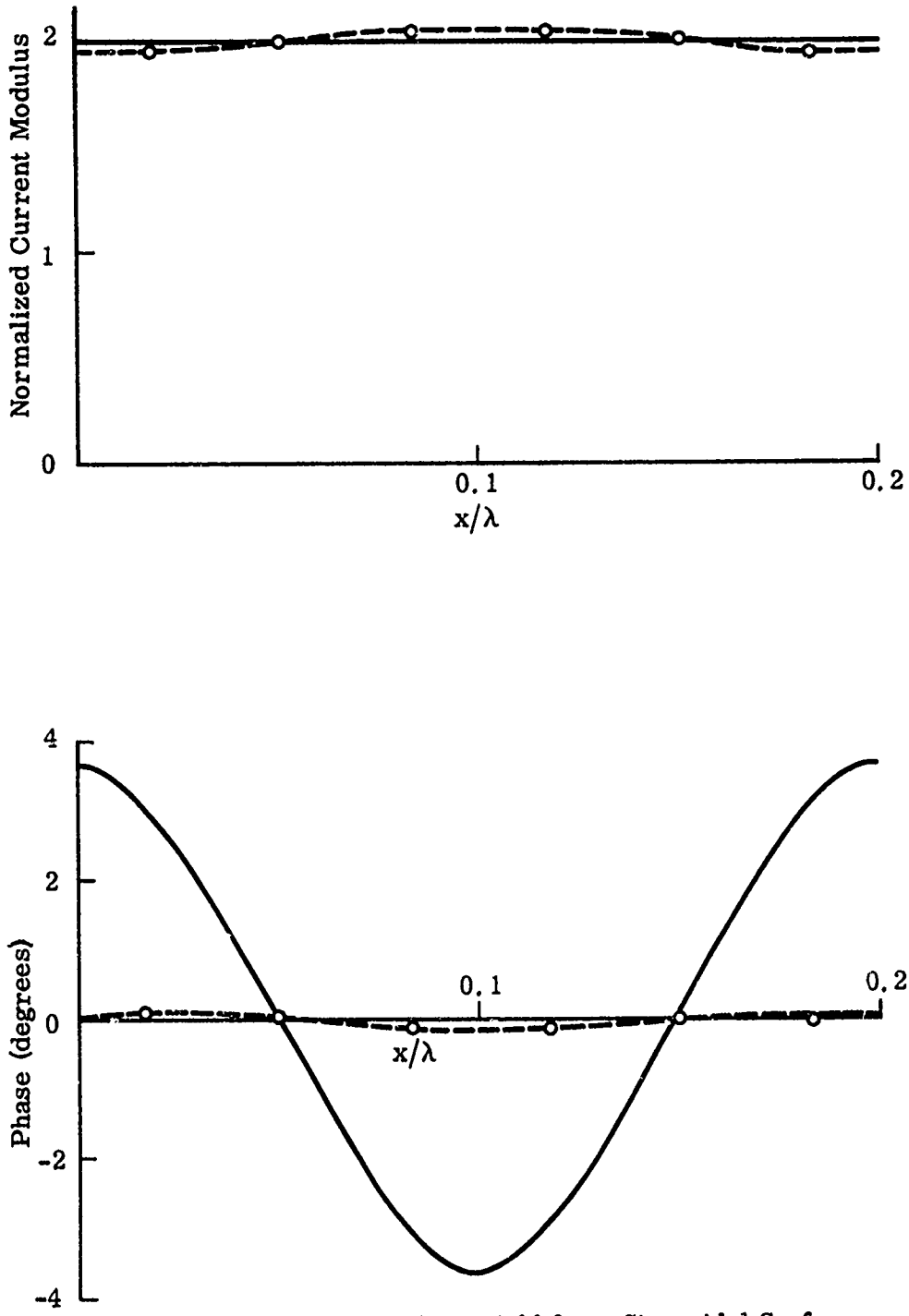

Fig. 5-14: Normalized Surface Field for a Sinusoidal Surface ($d = 0.2\lambda$, $a = 0.01\lambda$ and $\theta = 0$) for H polarization, --o-- exact, — physical optics.

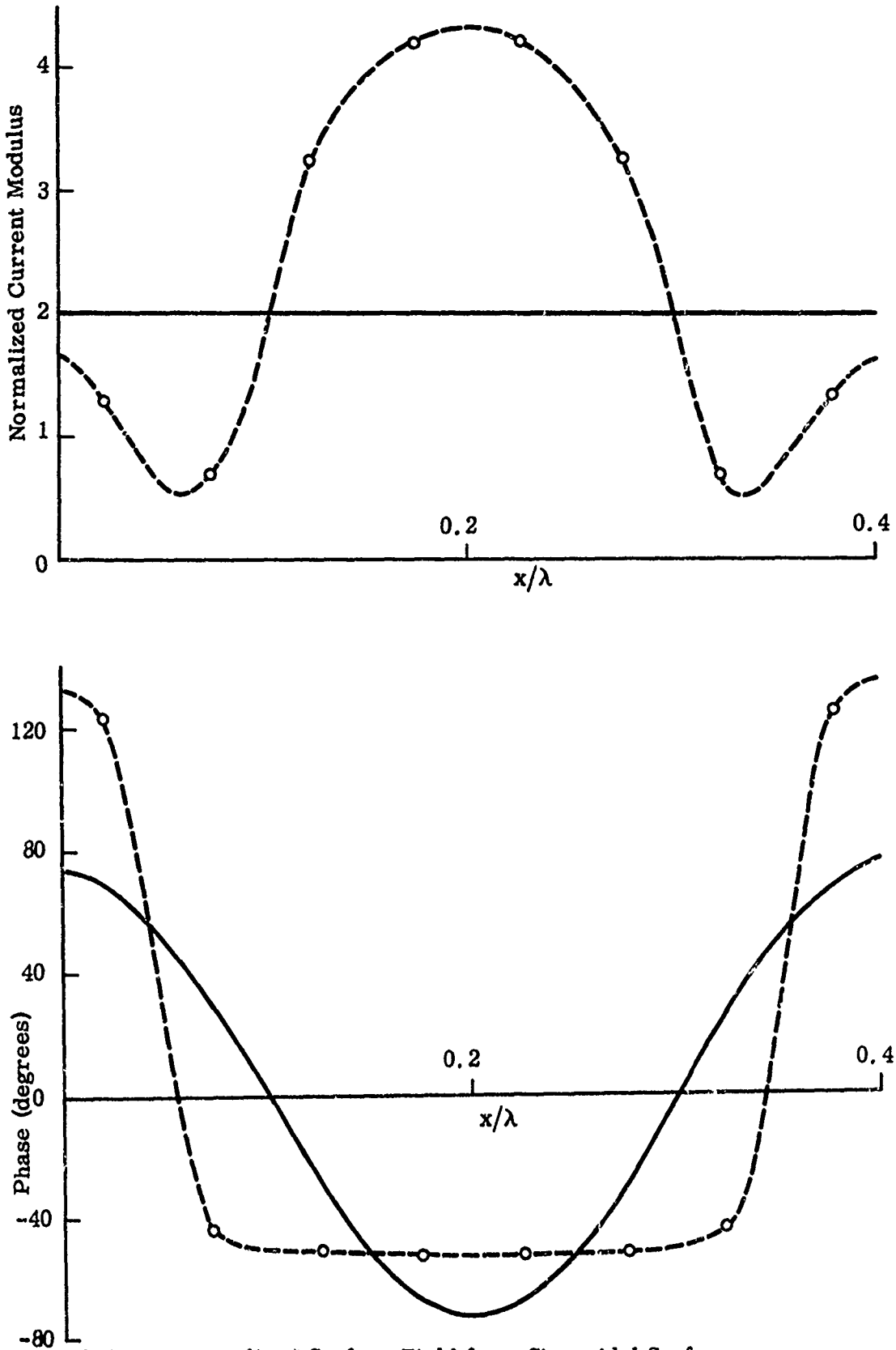

Fig. 5-15: Normalized Surface Field for a Sinusoidal Surface ($d = 0.4\lambda$, $a = 0.2\lambda$ and $\theta = 0$) for H polarization, --o-- exact, — physical optics.

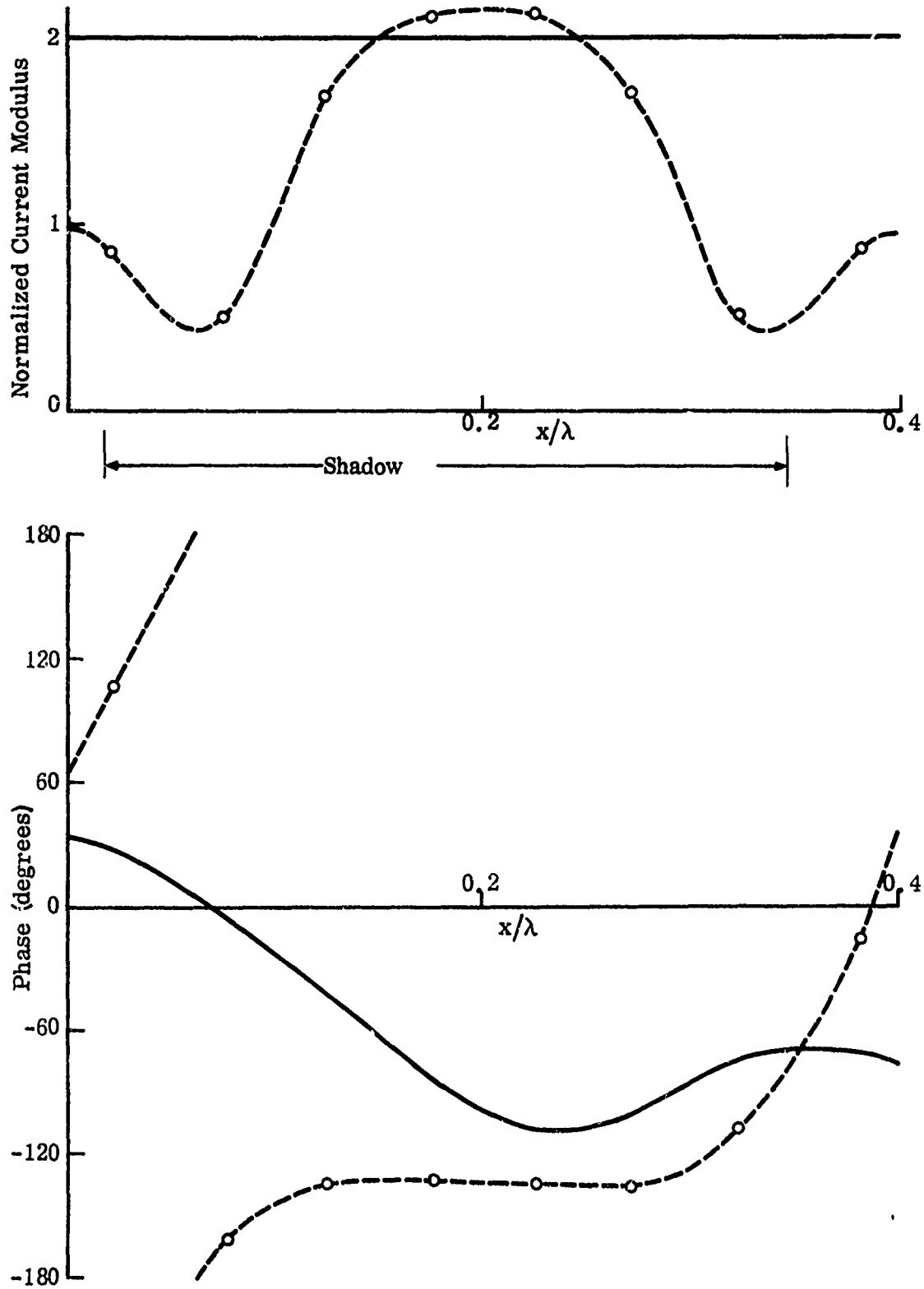

Fig. 5-16: Normalized Surface Field for a Sinusoidal Surface ($d = 0.4\lambda$, $a = 0.2\lambda$ and $\theta = 60^{\circ}$) for H polarization, --o-- exact, — physical optics.

occurring at the surface peak. Once again, there is no agreement between the exact data and physical optics, either in modulus or phase.

Results for a full-wave rectified profile with $d = 0.6\lambda$, $a = 0.3\lambda$ and $\theta = 60^{\circ}$ are given in Fig. 5-17. The undulations of the modulus clearly indicate strong coupling among cells (or multiple scattering among cells). Most of the surface current concentrates in the illuminated region. As the angle of incidence is further increased to $\theta = 75^{\circ}$ (Fig. 5-18), the modulus undergoes a marked change, whereas the phase remains constant over most of the surface.

5.3 Surfaces of Larger Period ($d/\lambda \gtrsim 0.6$)

Surface field distributions for surfaces of large period are generally more complicated than those for surfaces of small period, primarily because of the greater number of radiating modes.

Let us first consider the results for two sinusoidal surfaces whose periods are near the Rayleigh wavelength. The first one (Fig. 5-19) has $d = 0.95\lambda$, $a = 0.25\lambda$ and $\theta = 0$. It is seen that the current modulus curve has a maximum at the surface trough and minima at the places where the surface crosses the x axis. The phase, however, remains fairly constant over the lower part of the concave portion of the surface, but changes rapidly from positive to negative where the modulus has its minimum. The second one is given in Fig. 5-20, where $d = 1.90\lambda$, $a = 0.25\lambda$ and $\theta = 0$. Here the modulus has a marked oscillation, quite distinct from that found for E polarization. One of the maxima is at the surface trough, and the current is again a minimum at the surface peak. The agreement with physical optics is poorer than for E polarization, with neither modulus nor phase being approximated to any real extent.

A careful study of Figs. 5-19, 5-20 and the corresponding ones for E polarization (Figs. 3-20 and 3-21) leads us to conjecture that there are strong surface waves propagating along the x-axis when d is close to 2λ for H polarization, and when d is close to the wavelength for E polarization.

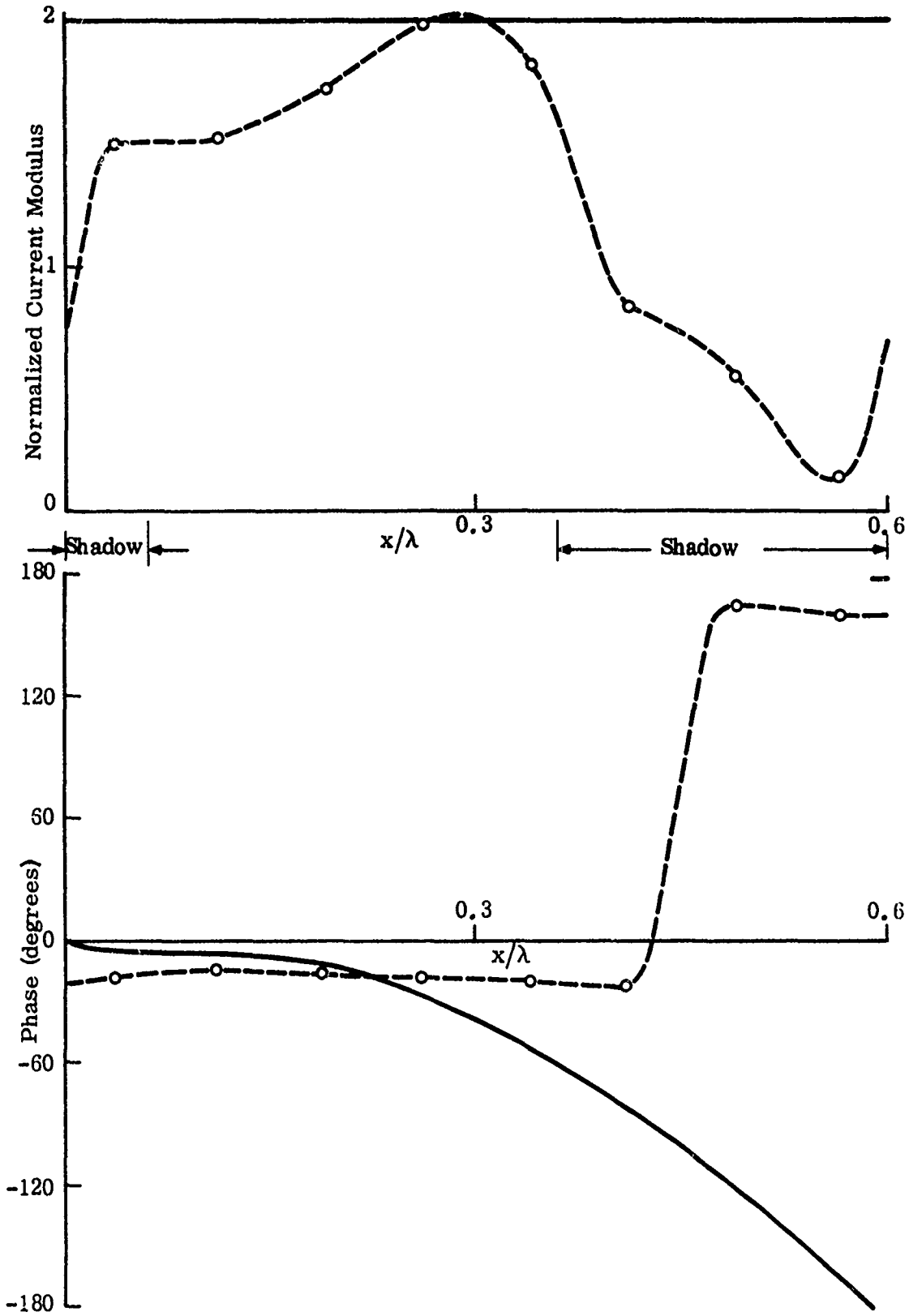

Fig. 5-17: Normalized Surface Field for a Full-Wave Rectified Surface ($d = 0.6\lambda$, $a = 0.3\lambda$ and $\theta = 60^{\circ}$) for H polarization, --o-- exact, — physical optics.

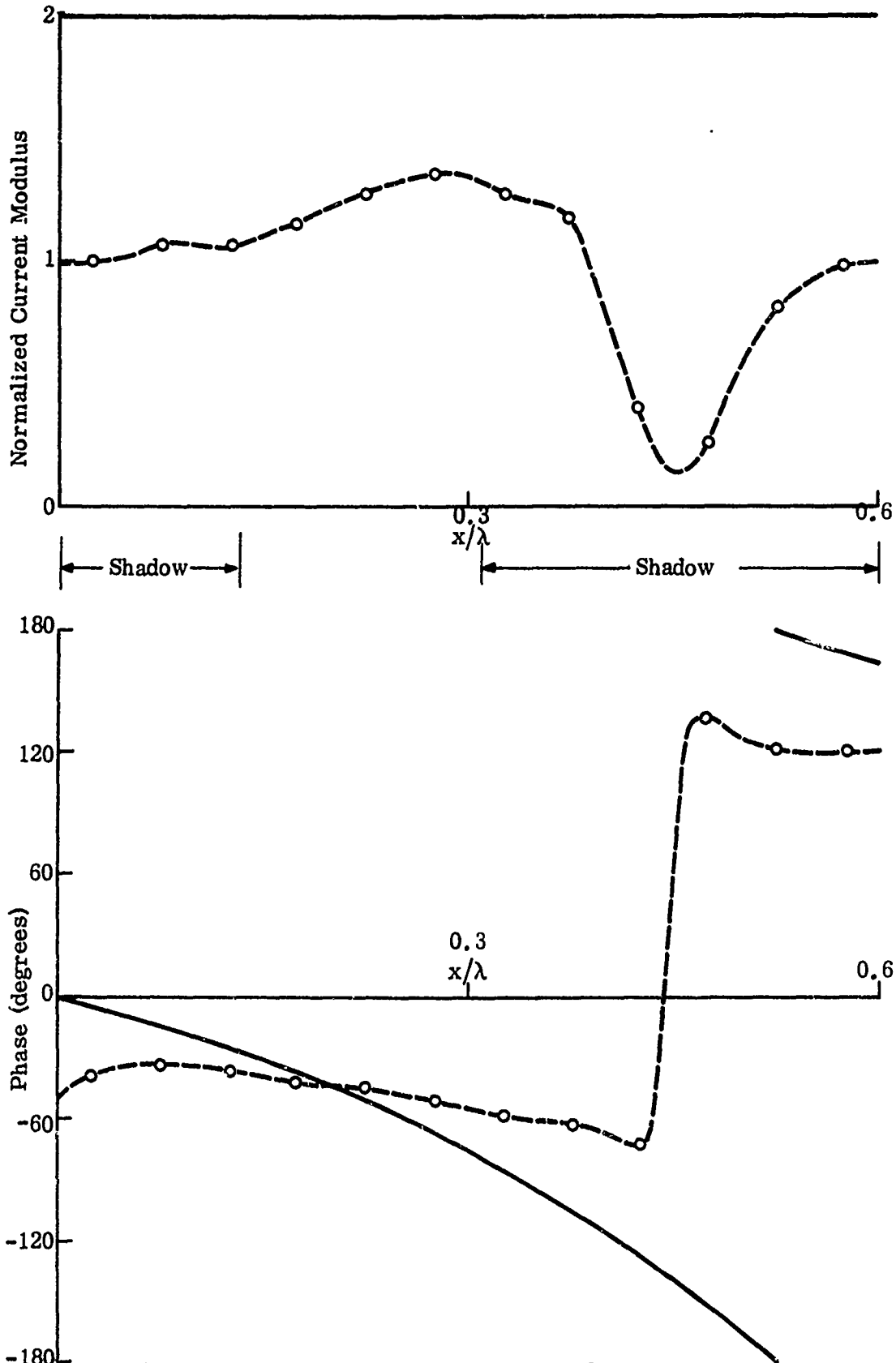

Fig. 5-18: Normalized Surface Field for a Full-Wave Rectified Surface ($d = 0.6\lambda$, $a = 0.3\lambda$ and $\theta = 75^{\circ}$) for H polarization, --o-- exact, — physical optics.

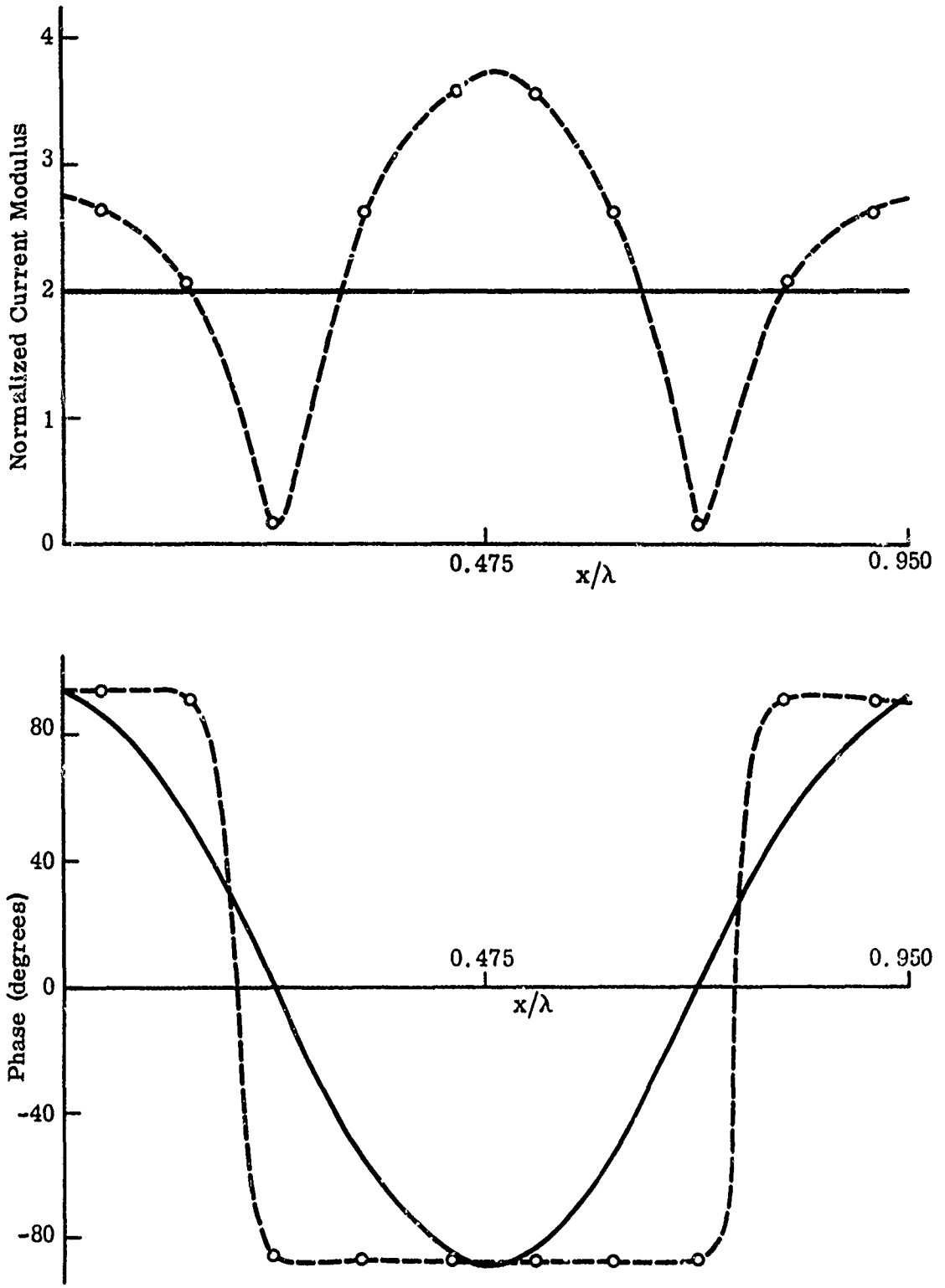

Fig. 5-19: Normalized Surface Field for a Sinusoidal Surface ($d = 0.95\lambda$, $a = 0.25\lambda$ and $\theta = 0$) for H polarization, --o-- exact, — physical optics.

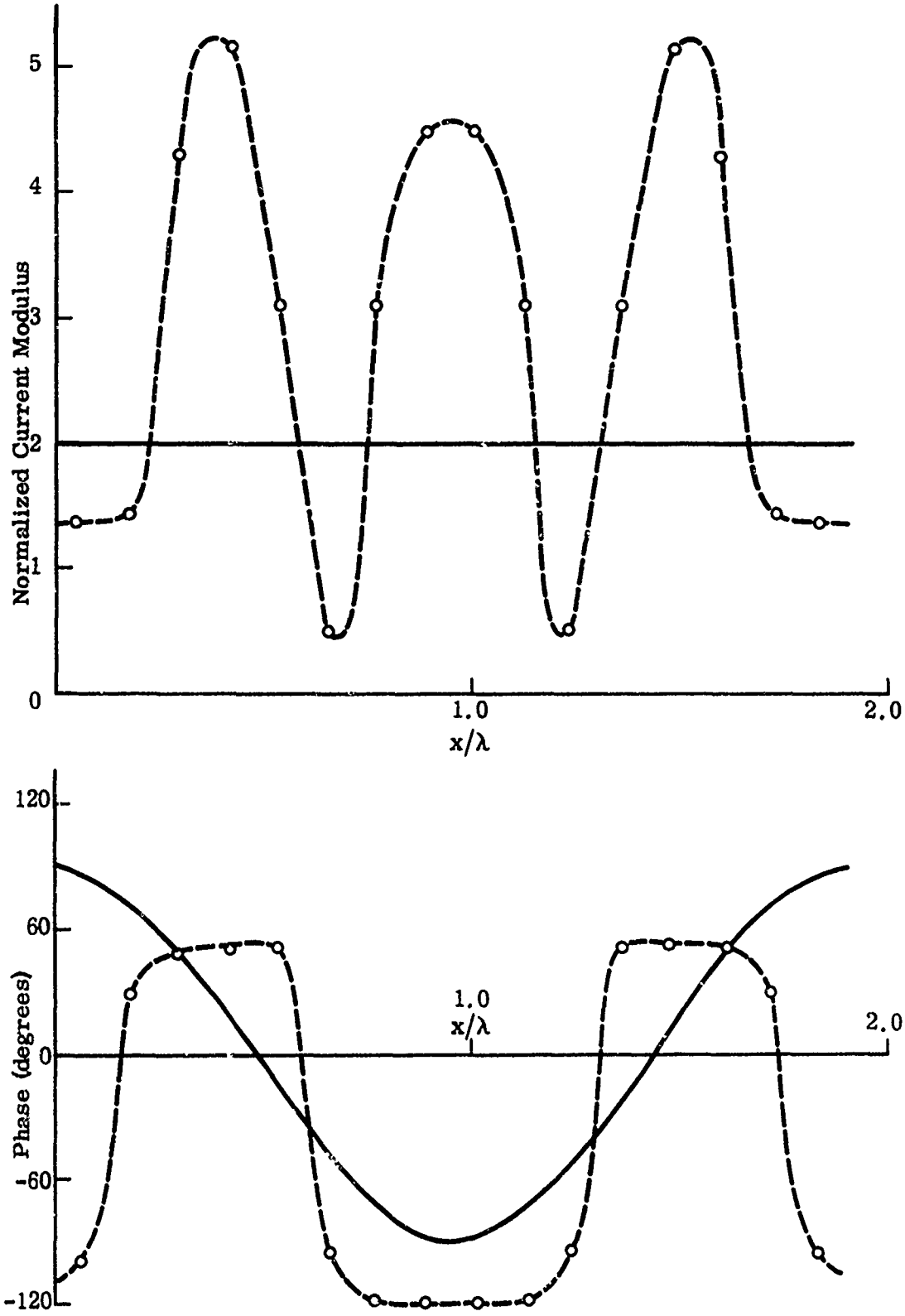

Fig. 5-20: Normalized Surface Field for a Sinusoidal Surface ($d = 1.9\lambda$, $a = 0.25\lambda$ and $\theta = 0$) for H polarization, --o-- exact, — physical optics.

Another case also showing a marked oscillation in the modulus is given in Fig. 5-21 where the surface is a sinusoidal with $d = 1.6\lambda$, $a = 0.25\lambda$ and $\theta = 45^{\circ}$ ($k\rho_{min} = 1.63$). The physical optics phase is in better agreement with the exact phase except in the region where the surface is most likely to receive shadowing.

To examine the effect on the surface field due to a gradual increase in the surface height when the period and angle of incidence are kept fixed, we select a sinusoidal profile with $d = 1.155\lambda$, $\theta = 60^{\circ}$ and allow a to increase from 0.05λ to 0.7λ. The numerical results are shown in Figs. 5-22 through 5-29. Again as in the case of E polarization, the agreement between the exact results and physical optics deteriorates as a is increased. Unlike E polarization, however, this agreement remains exceptionally good for the phase even when the amplitude becomes as large as 0.2λ. Furthermore, the exact phase in the illuminated region is very close to that of the incident field in all cases considered, but physical optics overestimates the modulus.

To see how much of the surface field depends on the concavity of the surface, we replaced the concave portion ($d/4 \leq x \leq 3d/4$) of the sinusoidal surface ($a = 0.5\lambda$) by a flat part. The results are presented in Fig. 5-30. Comparison with Fig. 5-27 shows that this replacement has a marked effect on the surface field in the shadow region, but little effect elsewhere.

Additional data for a full-wave rectified profile ($d = 0.85\lambda$, $a = 0.30\lambda$, and $\theta = 36^{\circ}$), and a triangular profile ($d = 1.75\lambda$, $\theta_1 = 20^{\circ}$, $\theta_2 = 66^{\circ}$, and $\theta = 12.2^{\circ}$) are given in Figs. 5-31 and 5-32. In the former case, the exact modulus and phase are in good agreement with the physical optics values over the left hand portion of the surface, but the agreement (particularly for the modulus) is less good on the right. For the triangular profile, the exact modulus shows an oscillatory variation not predicted by physical optics, and this oscillation is most pronounced on the far right hand portion of the surface. The physical optics phase is again a good approximation to the exact phase.

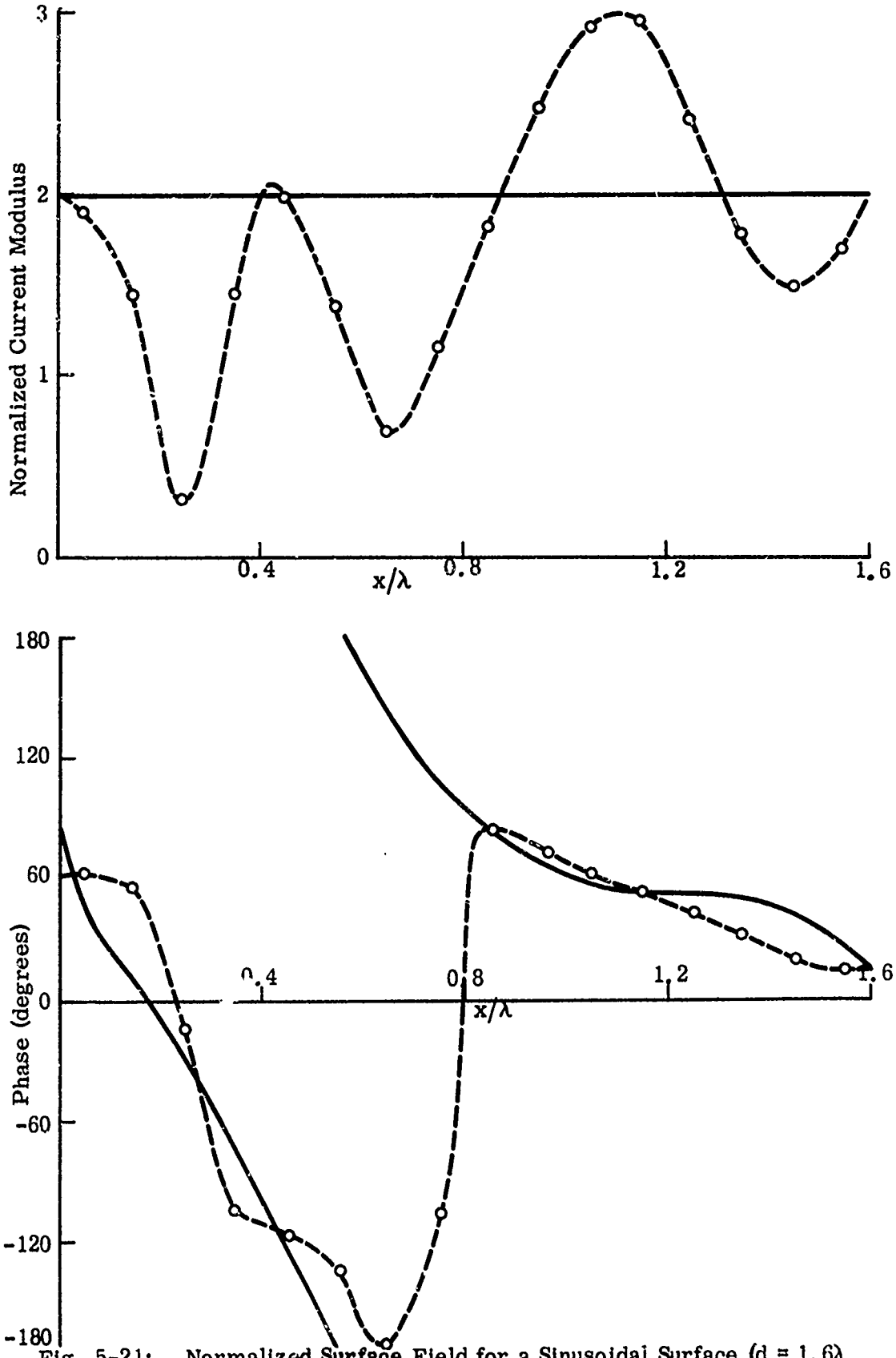

Fig. 5-21: Normalized Surface Field for a Sinusoidal Surface ($d = 1.6\lambda$, $a = 0.25\lambda$ and $\theta = 45^{\circ}$) for H polarization, --o-- exact, — physical optics.

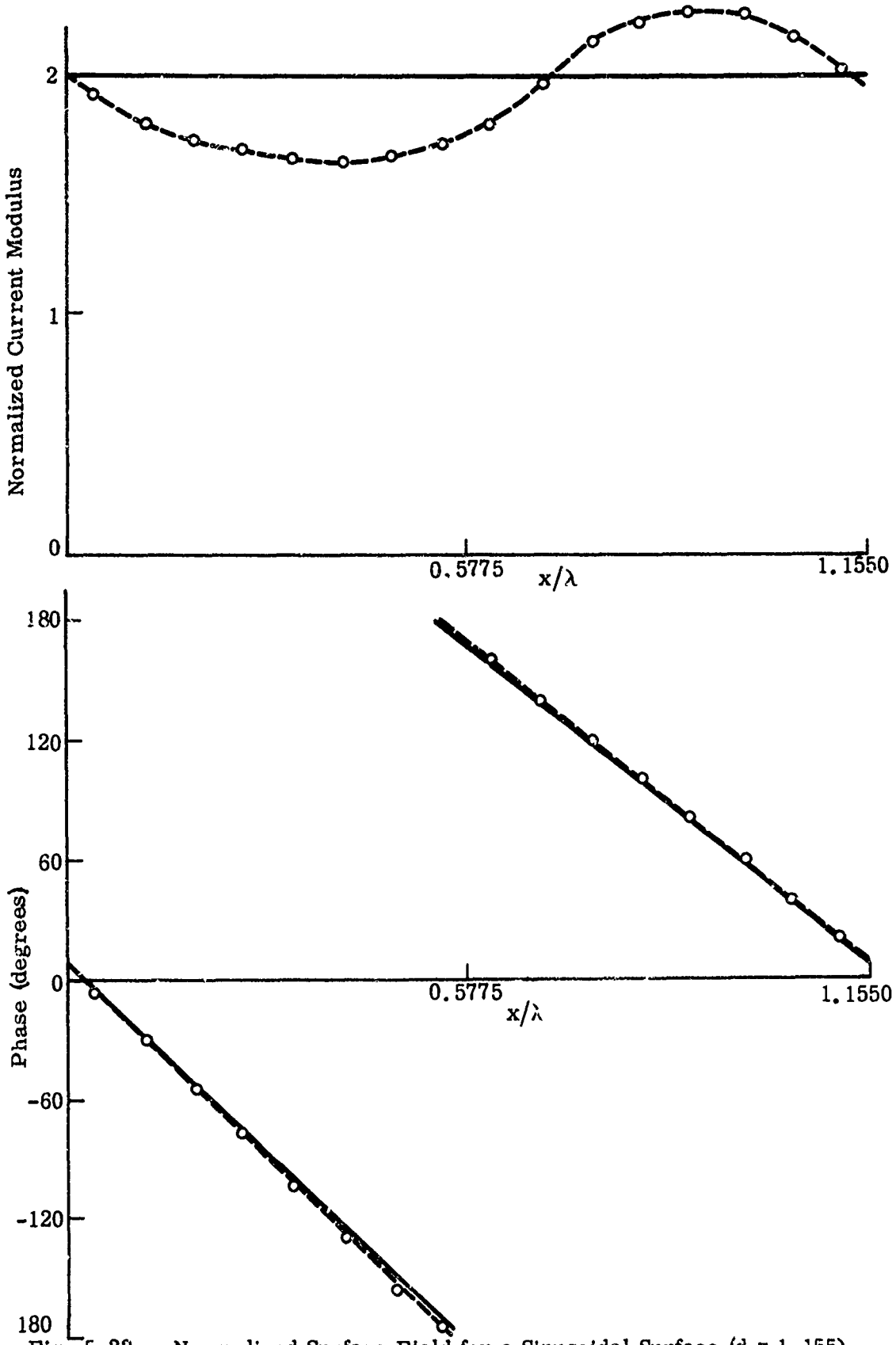

Fig. 5-22: Normalized Surface Field for a Sinusoidal Surface ($d = 1.155\lambda$, $a = 0.05\lambda$ and $\theta = 60^{\circ}$) for H polarization, --o-- exact, — physical optics.

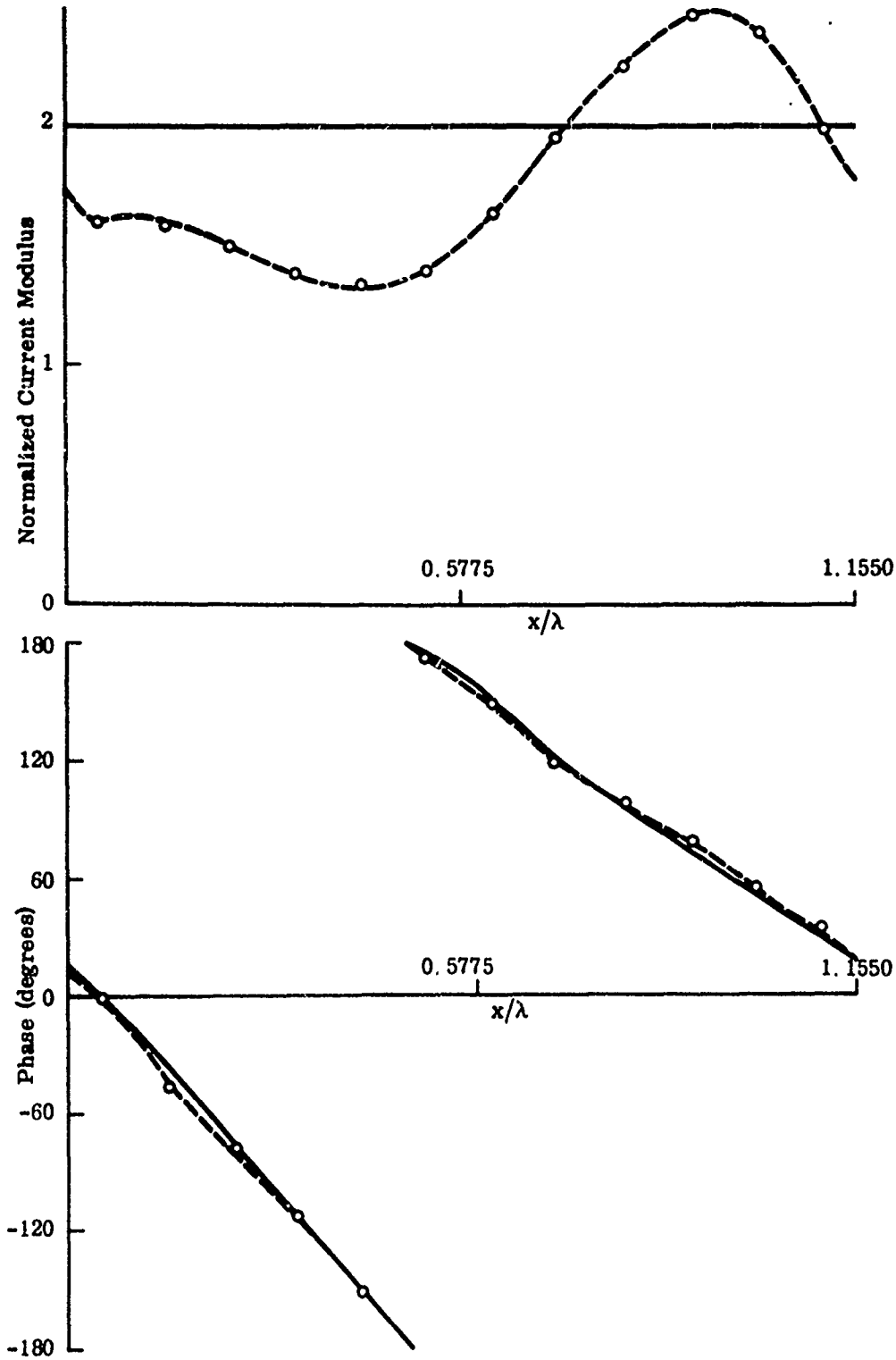

Fig 5-23: Normalized Surface Field for a Sinusoidal Surface ($d = 1.155\lambda$, $a = 0.1\lambda$ and $\theta = 60^{\circ}$), for H polarization, --o-- exact, — physical optics.

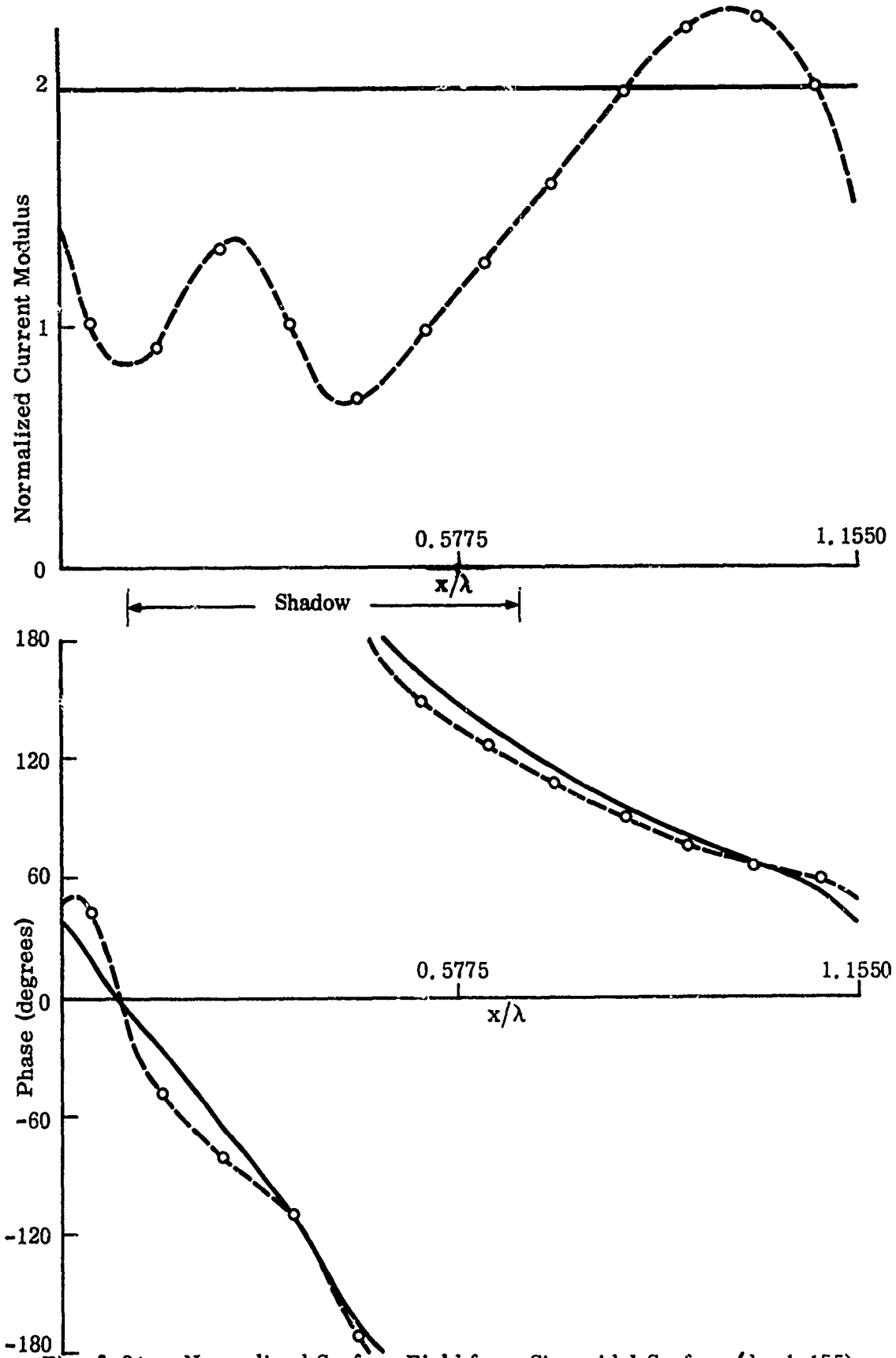

Fig. 5-24: Normalized Surface Field for a Sinusoidal Surface ($d = 1.155\lambda$, $a = 0.2\lambda$ and $\theta = 60^{\circ}$) for H polarization, --o-- exact, — physical optics.

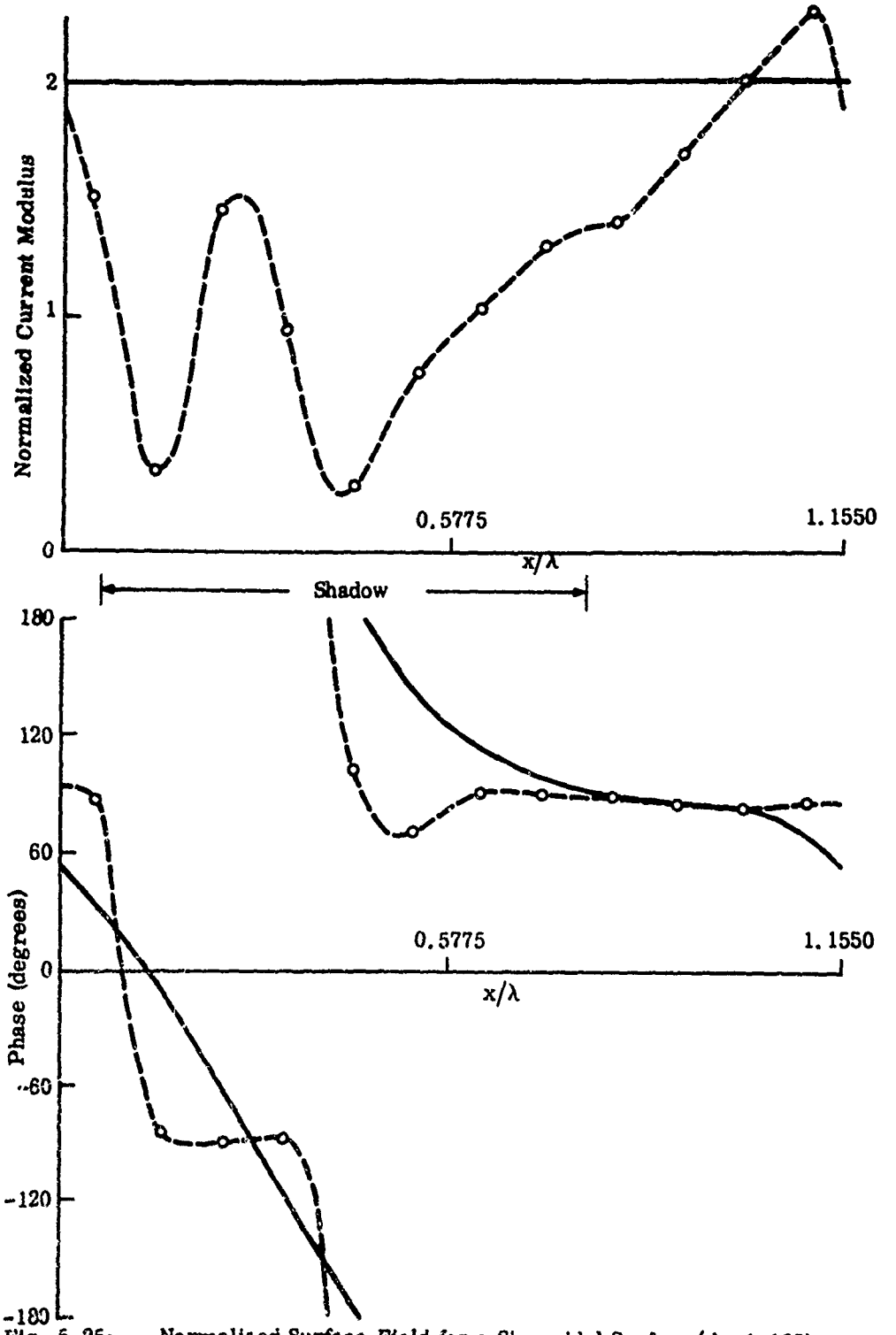

Fig. 5-25: Normalized Surface Field for a Sinusoidal Surface ($d = 1.155\lambda$, $a = 0.3\lambda$ and $\vartheta = 60^{\circ}$) for H polarization, --o-- exact, — physical optics.

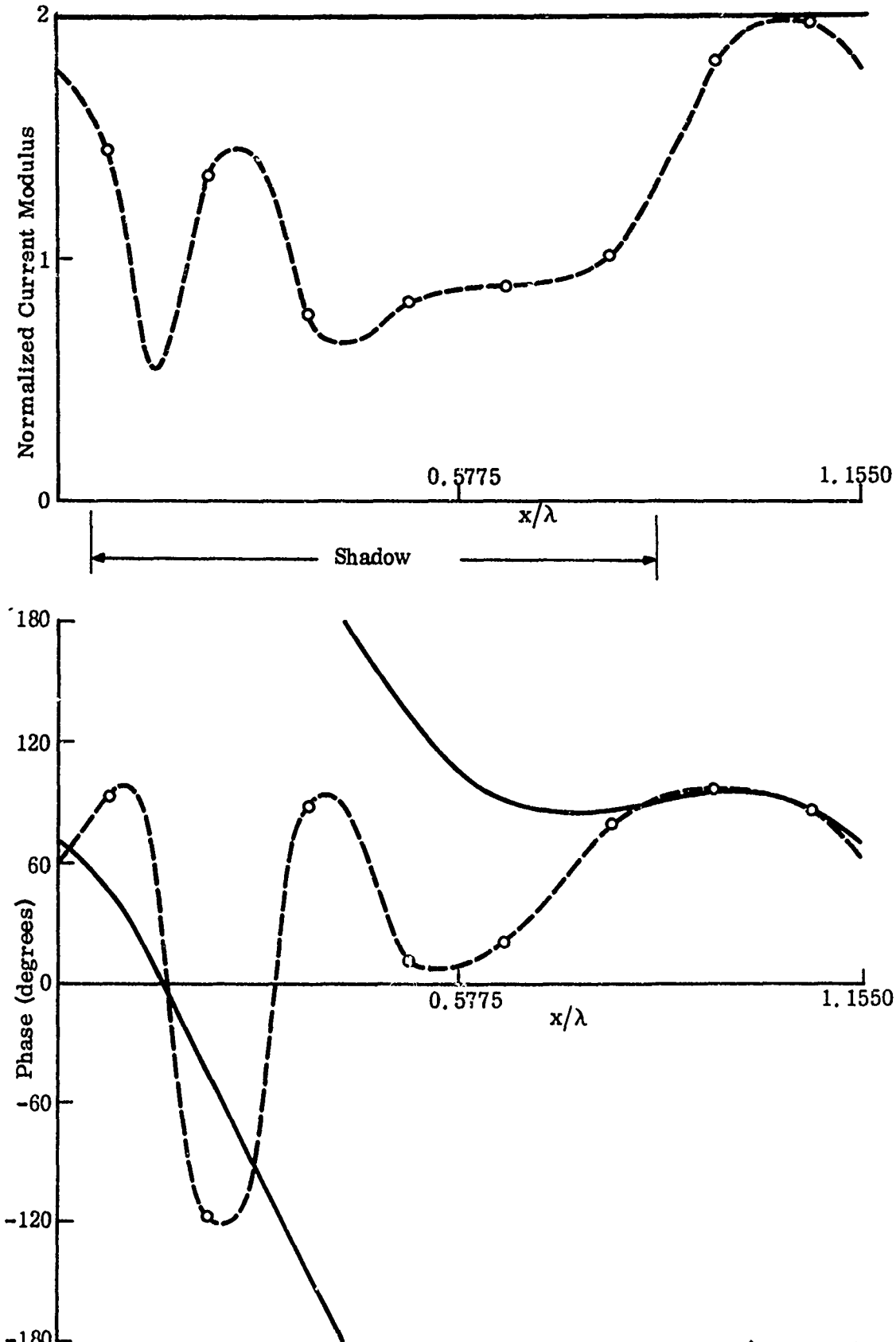

Fig. 5-26: Normalized Surface Field for a Sinusoidal Surface ($d = 1.155\lambda$, $a = 0.4\lambda$ and $\theta = 60^0$) for H polarization, --o-- exact, — physical optics.

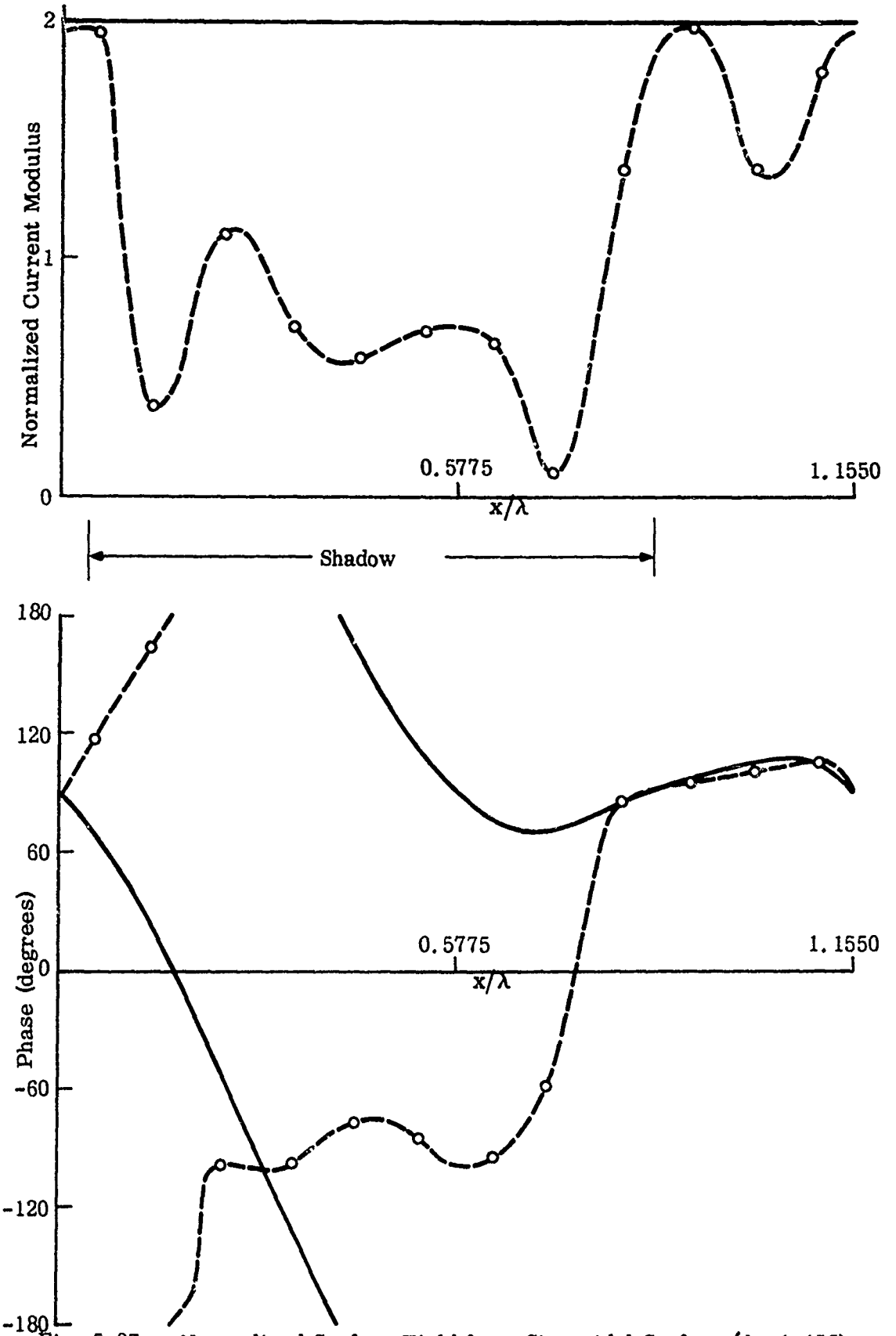

Fig. 5-27: Normalized Surface Field for a Sinusoidal Surface ($d = 1.155\lambda$, $a = 0.5\lambda$ and $\theta = 60^{\circ}$) for H polarization. --o-- exact, — physical optics.

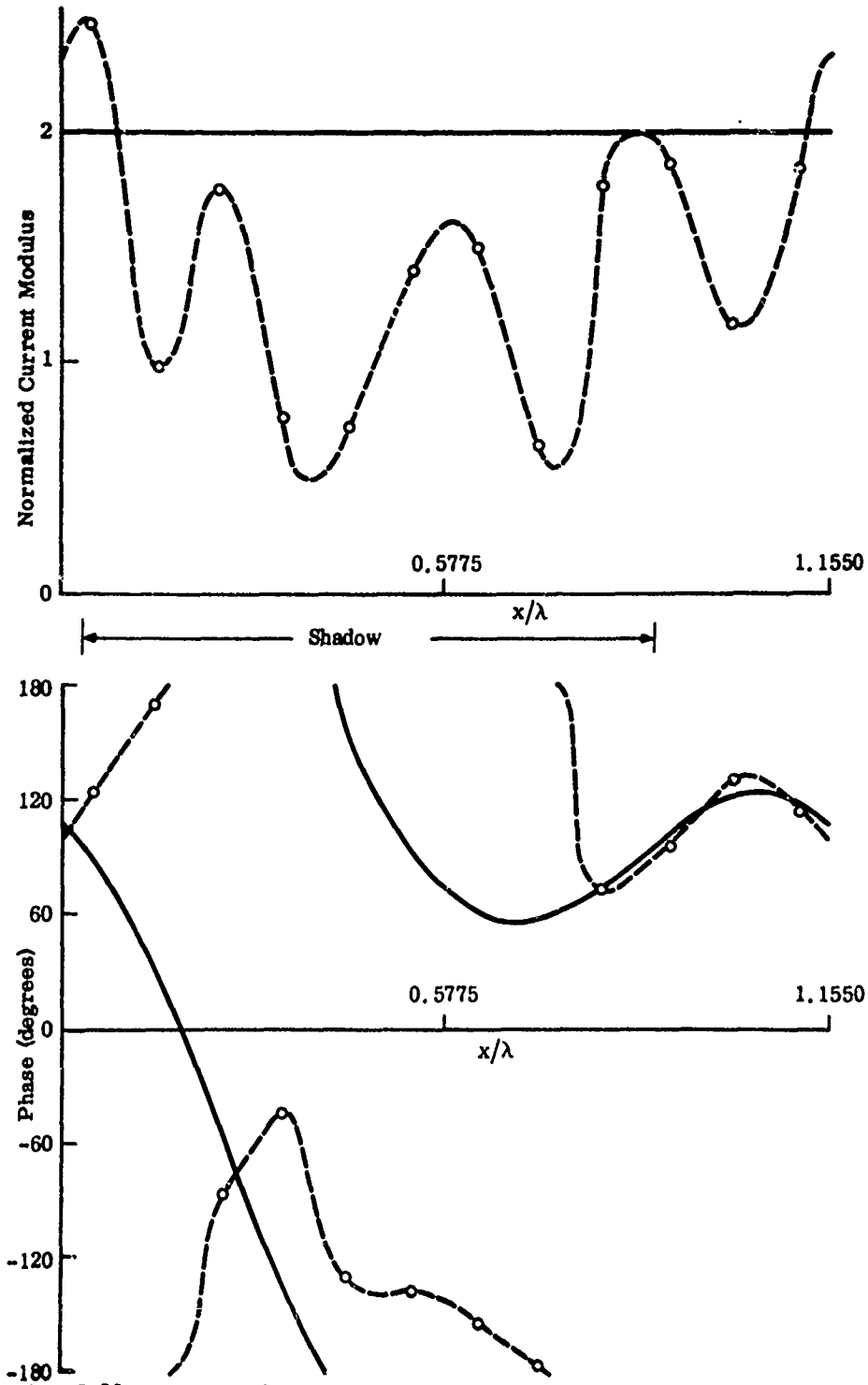

Fig 5-28: Normalized Surface Field for a Sinusoidal Surface ($d = 1.155\lambda$, $a = 0.6\lambda$ and $\theta = 60^\circ$), for H polarization, --o-- exact, — physical optics.

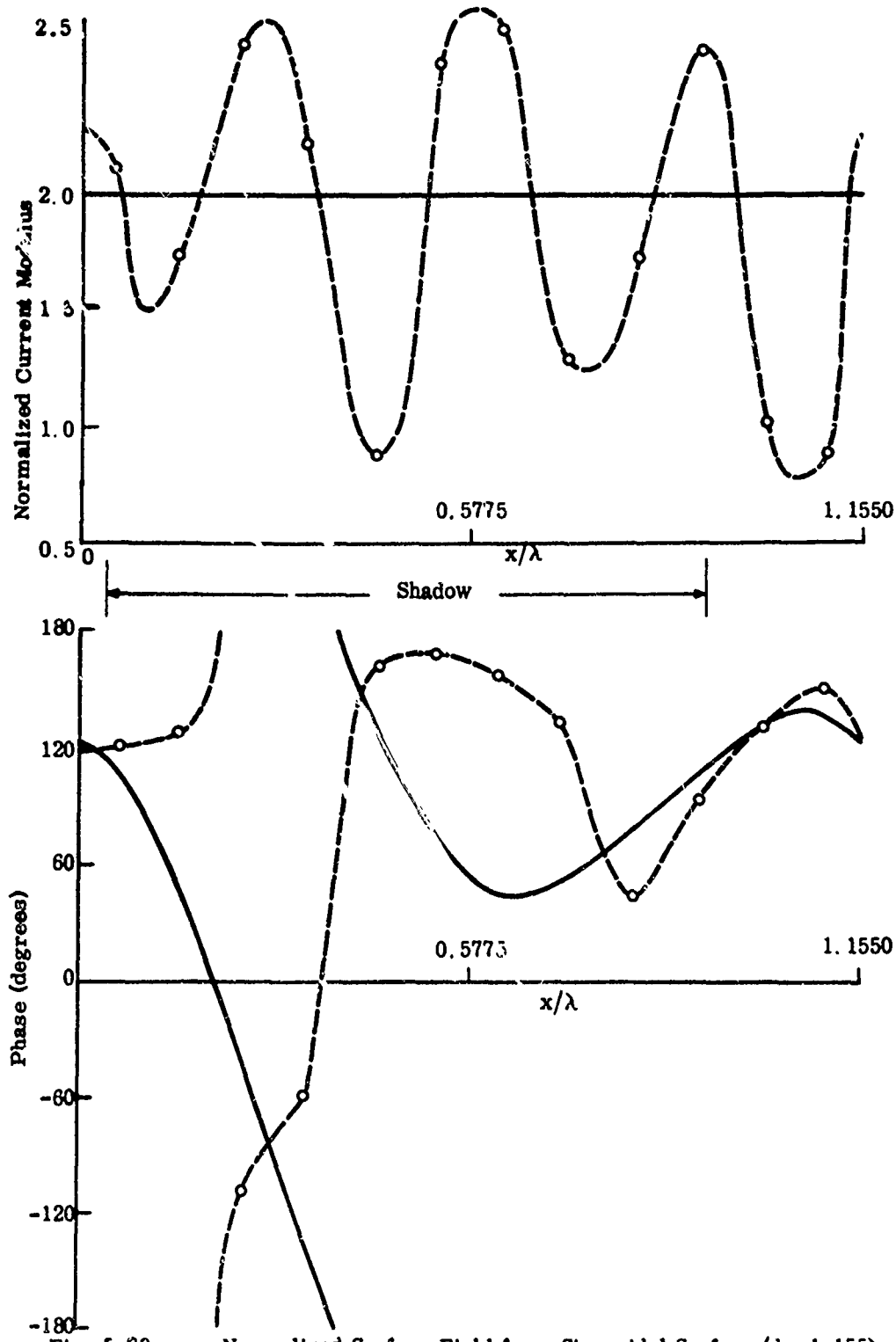

Fig 5-29: Normalized Surface Field for a Sinusoidal Surface ($d = 1.155\lambda$, $a = 0.7\lambda$ and $\theta = 60^{\circ}$), for H polarization, --o-- exact, — physical optics.

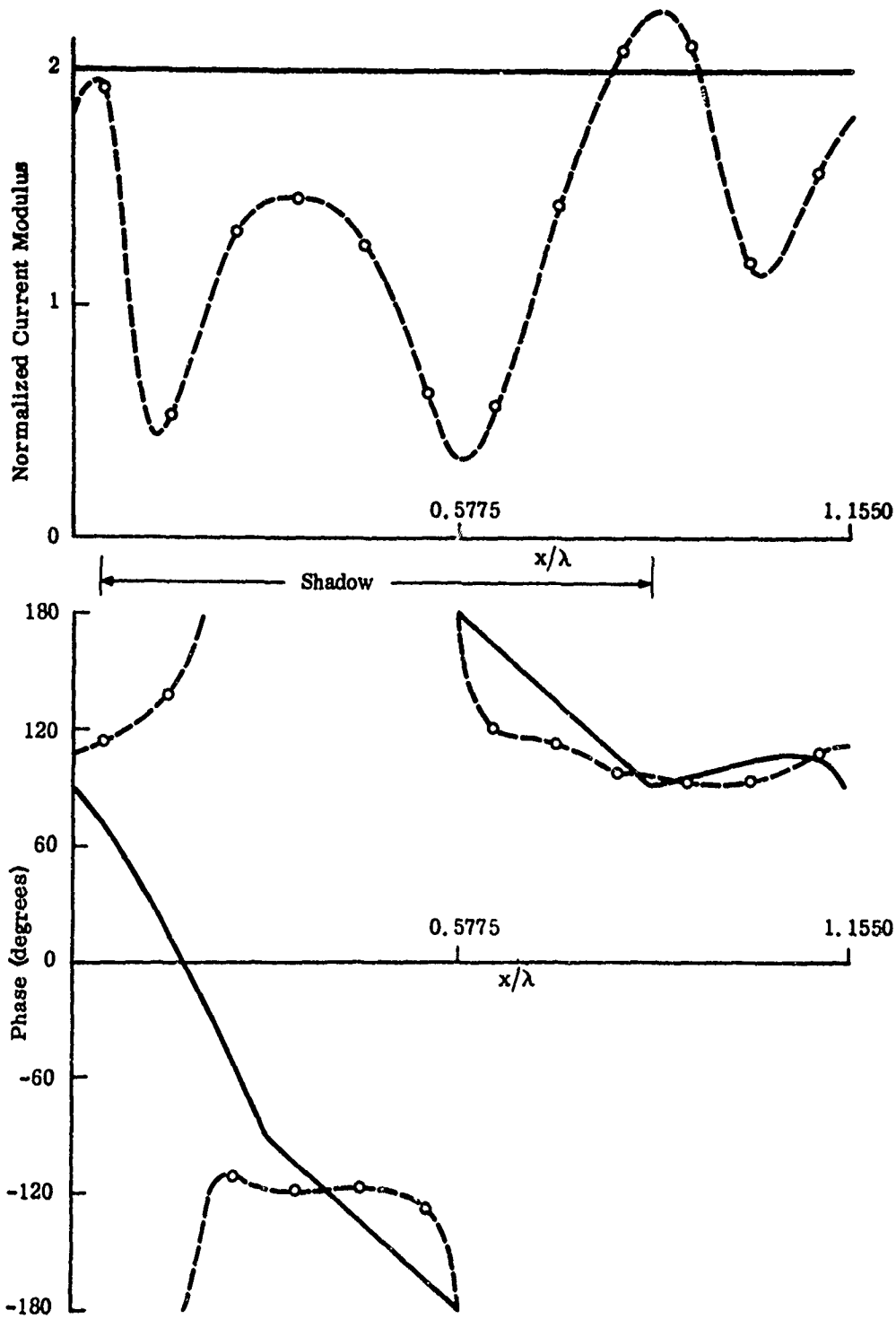

Fig. 5-30: Normalized Surface Field for a Half-Wave Rectified Surface ($d = 1.155\lambda$, $a = 0.5\lambda$ and $\theta = 60^{\circ}$), for H polarization, --o-- exact, — physical optics.

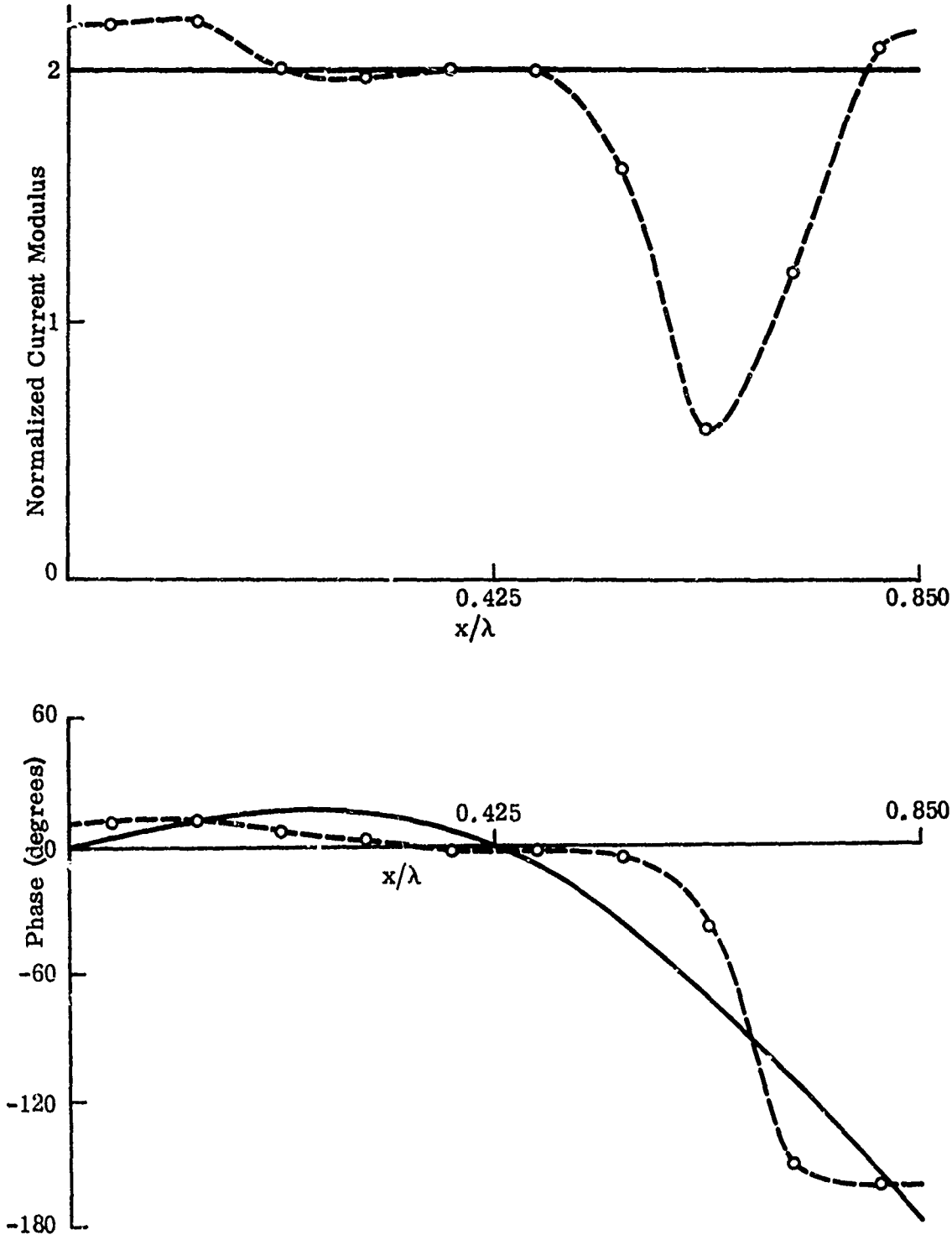

Fig. 5-31: Normalized Surface Field for a Full-Wave Rectified Surface ($d = 0.85\lambda$, $a = 0.3\lambda$ and $\theta = 36^{\circ}$) for H polarization, --o-- exact, — physical optics.

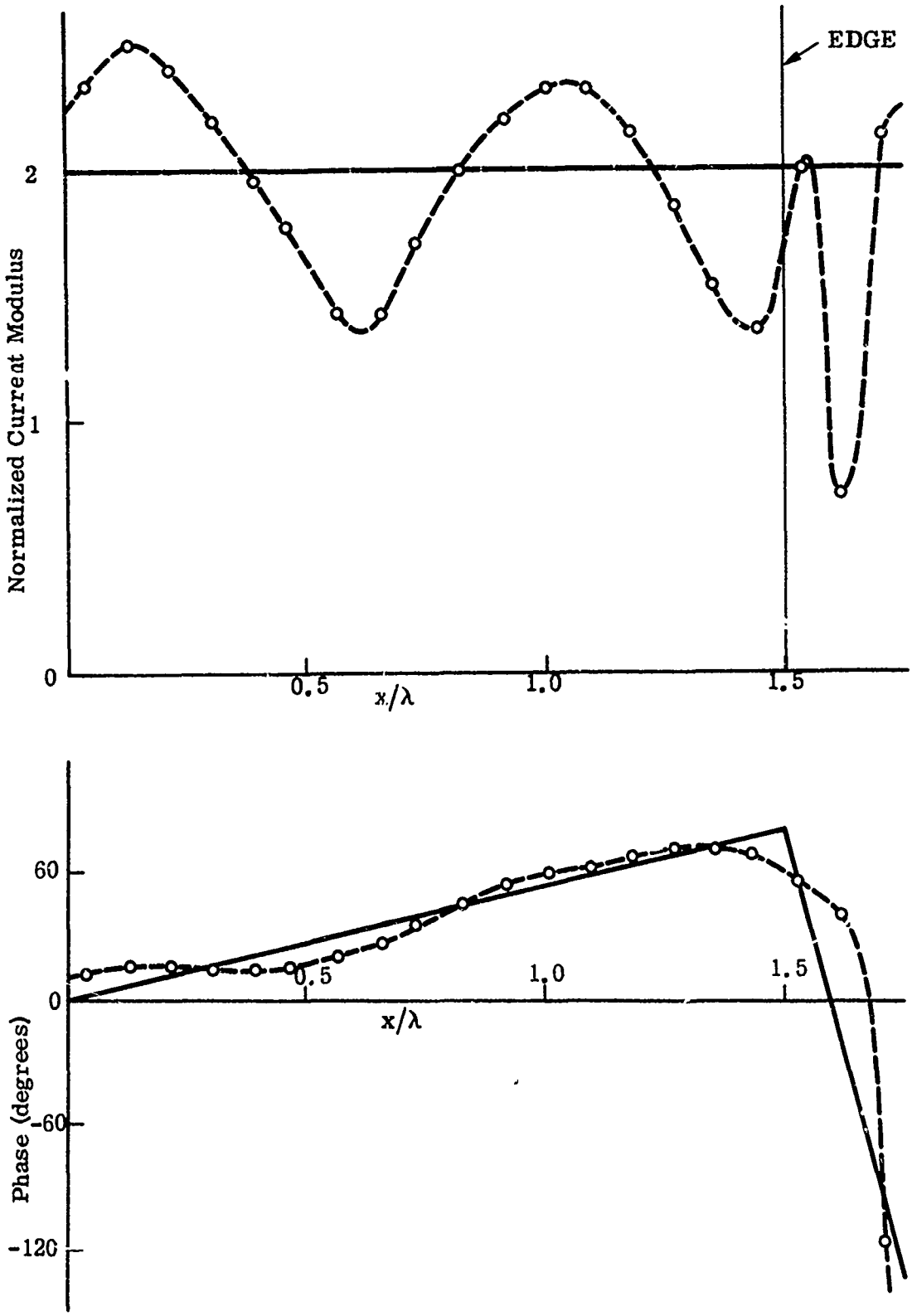

Fig. 5-32: Normalized Surface Field for a Triangular Surface ($d = 1.75\lambda$, $\theta_1 = 20^\circ$, $\theta_2 = 66^\circ$ and $\theta = 12.2^\circ$) for H polarization, --o-- exact, — physical optics.

5.4 Coupling Among Cells

Figures 5-33 through 5-37 illustrate the effect on the surface current distribution produced by a progressive change in the period of the surface while the other parameters are kept fixed. The surface selected is a full-wave rectified surface with $a = 0.3\lambda$, $d = 0.3\lambda$, $\theta = 60^{\circ}$ and ℓ (the distance between two neighboring periods)varying from 0.3λ to 0.7λ in 0.1λ steps. For the first two figures, where $\ell \leq 0.4\lambda$, the modulus shows very good symmetry in spite of shadowing, and over the central portion of the surface at least the phase is almost constant. The physical optics estimates are rather unsatisfactory. As d becomes larger and approaches the Rayleigh wavelength (equal to 0.535λ, according to Eq. (4.7)), the surface field experiences a marked change as shown in Fig. 5-35, but the modulus still preserves its symmetry. Further increase in d again brings noticeable changes in the shape of the modulus (see Figs. 5-36 and 5-37), and in spite of the fact that the radius of curvature is a minimum at the surface peak, the physical optics estimate of the modulus is most accurate in that region. Compared with the analogous results for E-polarization, the surface fields for these relatively small separations between cells are more sensitive to the change in period, suggesting that the coupling between cells is stronger.

5.5 Accuracy Checks and Computational Time

Figure 5-38 shows the results of a convergence test applied to a sinusoidal surface with $d = 0.2\lambda$, $a = 0.1\lambda$ and $\theta = 0$. An indication of the accuracy achieved with an almost flat surface can be had from Fig. 5-14, and because of the nature of the integral equation, this limiting case works better here than it did for E polarization.

Comparison of the results with those obtained by Zaki (1969) for a sinusoidal surface ($d = 1.90\lambda$, $a = 0.25\lambda$ and $\theta = 0$) is shown in Fig. 3-39, and with those of Green (1970) for a triangular profile ($d = 1.75\lambda$, $\theta_1 = 20^{\circ}$, $\theta_2 = 60^{\circ}$, and $\theta = 12.2^{\circ}$) in Fig. 5-40. Good agreement is obtained in both instances.

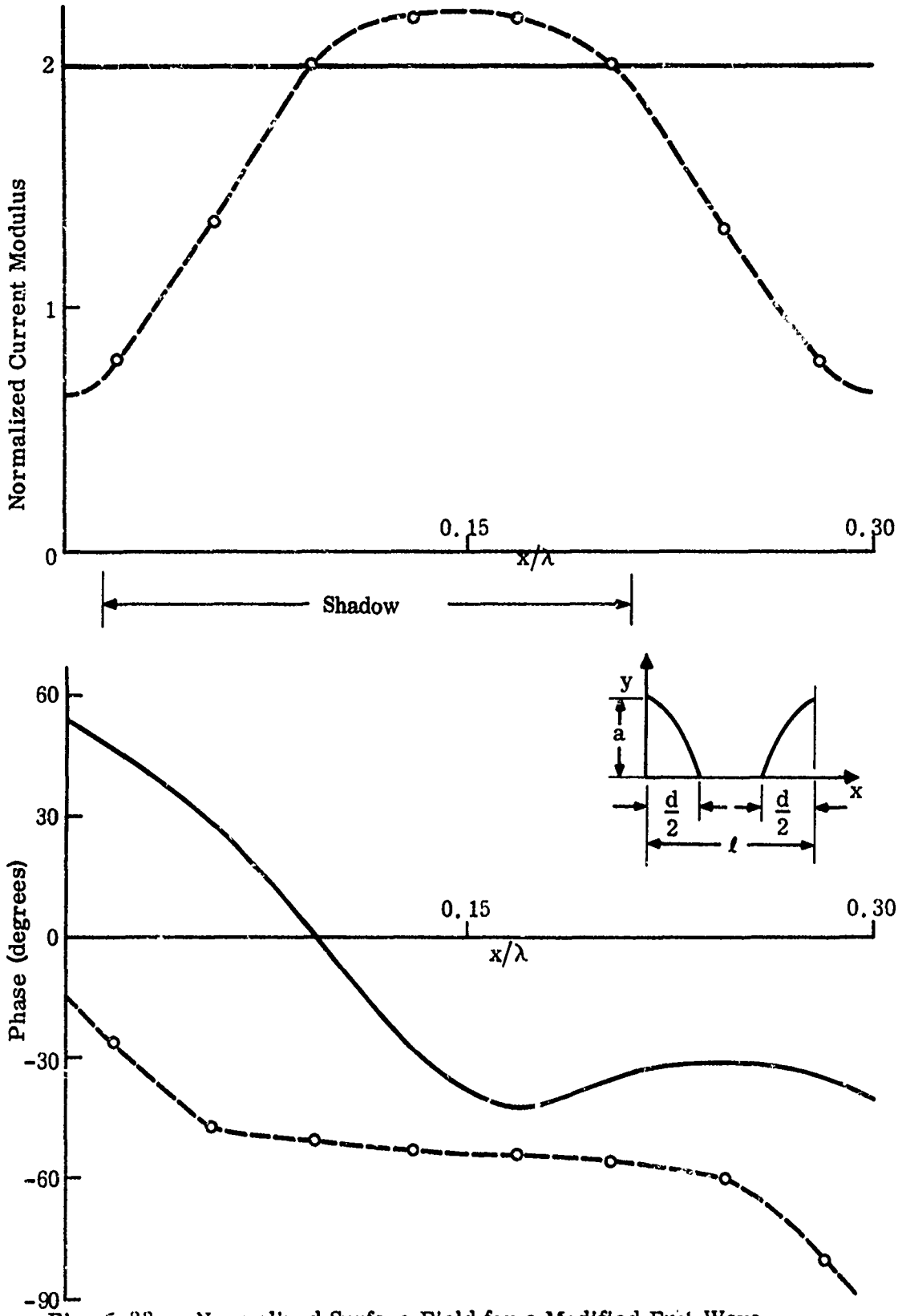

Fig. 5-33: Normalized Surface Field for a Modified Full-Wave Rectified Surface ($d = 0.3\lambda$, $a = 0.3\lambda$, $\theta = 60^{\circ}$ and $\ell = 0.3\lambda$) for H polarization, --o-- exact, — physical optics.

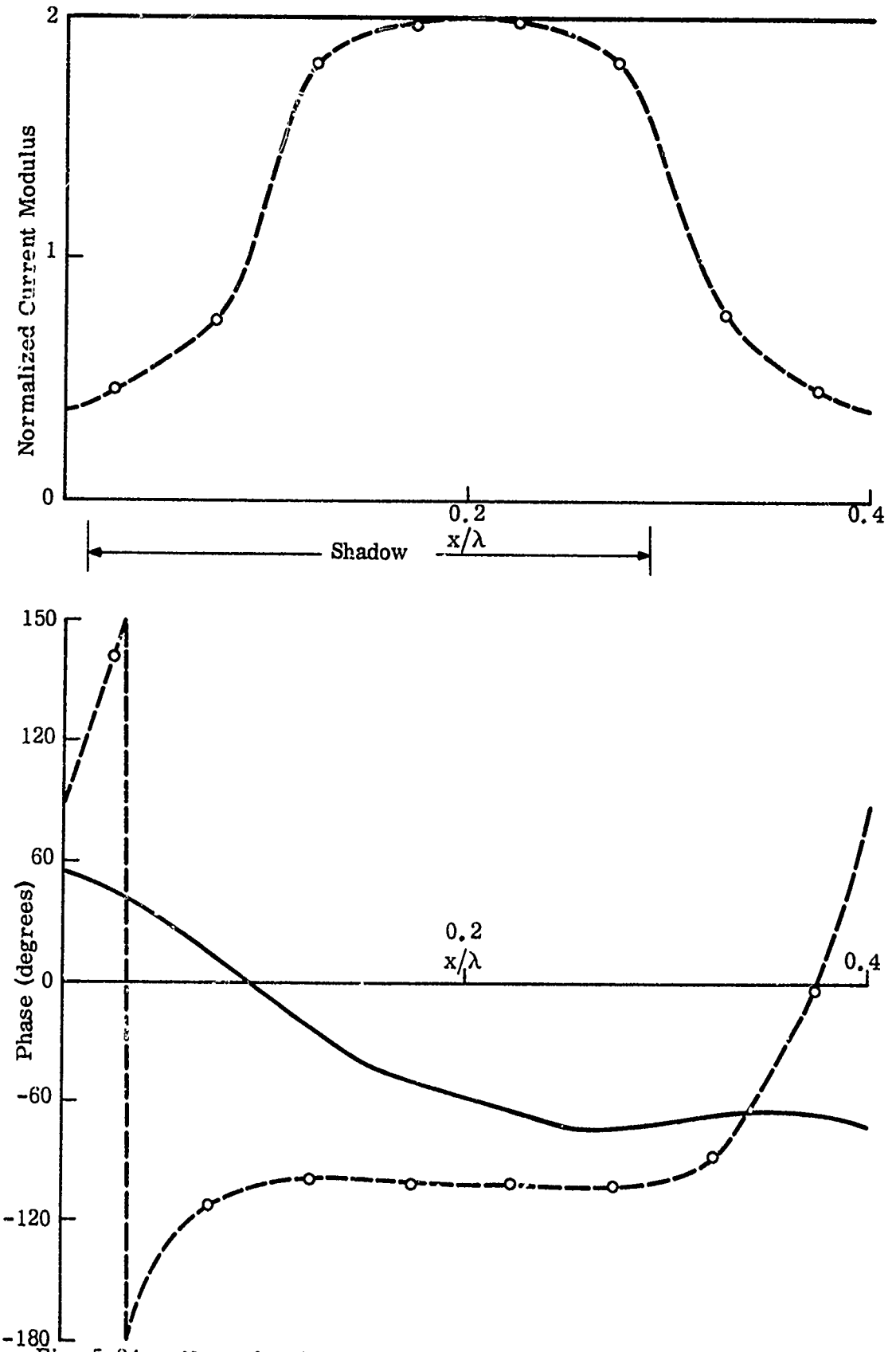

Fig. 5-34: Normalized Surface Field for a Modified Full-Wave Rectified Surface ($d = 0.3\lambda$, $a = 0.3\lambda$, $\theta = 60^\circ$ and $\ell = 0.4\lambda$) for H polarization, --o-- exact, — physical optics.

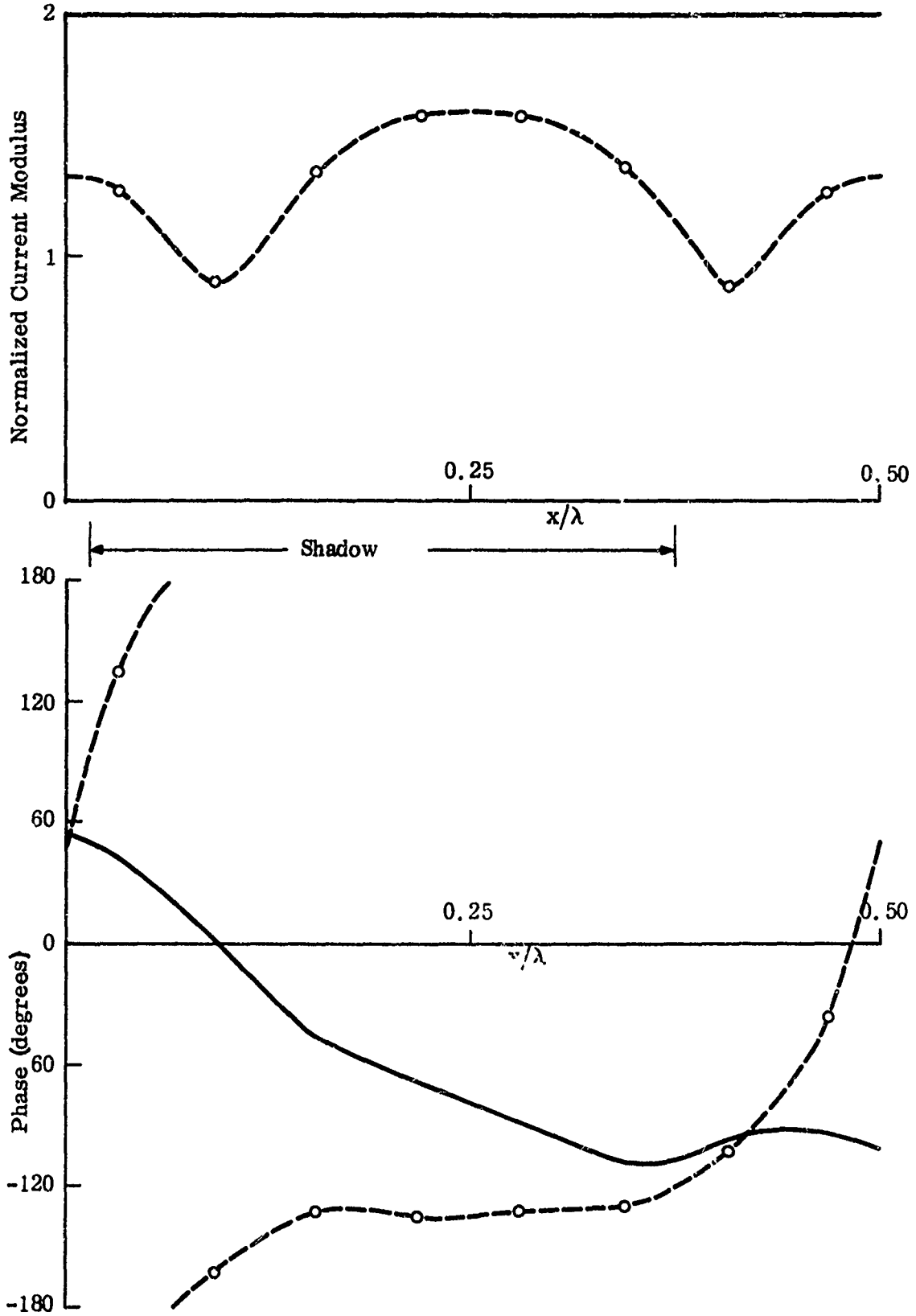

Fig. 5-35: Normalized Surface Field for a Modified Full-Wave Rectified Surface ($d = 0.3\lambda$, $a = 0.3\lambda$, $\theta = 60^{\circ}$ and $\ell = 0.5\lambda$) for H polarization, --o-- exact, — physical optics.

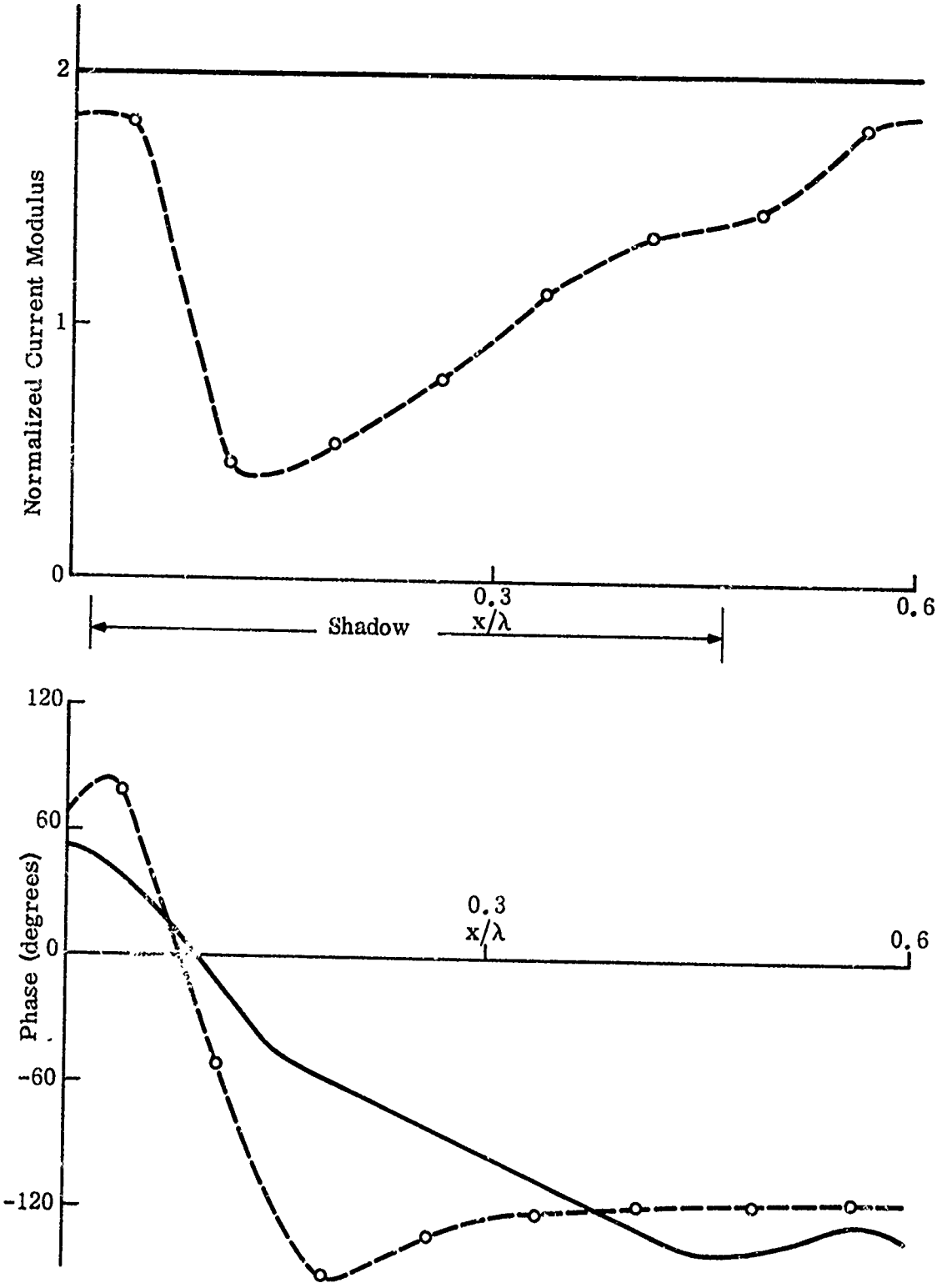

Fig. 5-36: Normalized Surface Field for a Modified Full-Wave Rectified Surface ($d = 0.3\lambda$, $a = 0.3\lambda$, $\theta = 60^{\circ}$ and $\ell = 0.6\lambda$) for H polarization, --o-- exact, — physical optics.

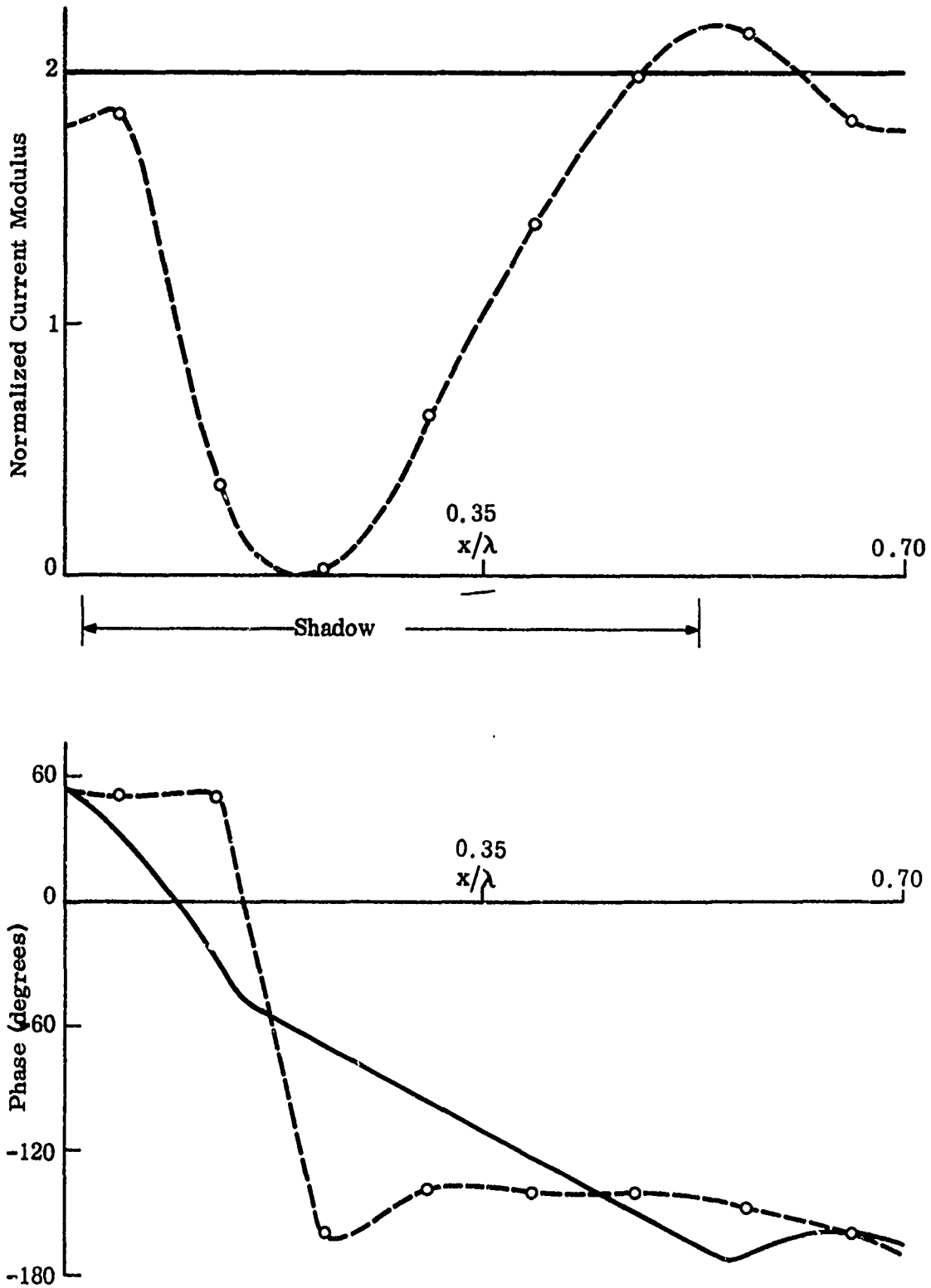

Fig. 5-37: Normalized Surface Field for a Modified Full-Wave Rectified Surface ($d = 0.3\lambda$, $a = 0.3\lambda$, $\theta = 60^{\circ}$ and $\ell = 0.7\lambda$) for H polarization, --o-- exact, — physical optics.

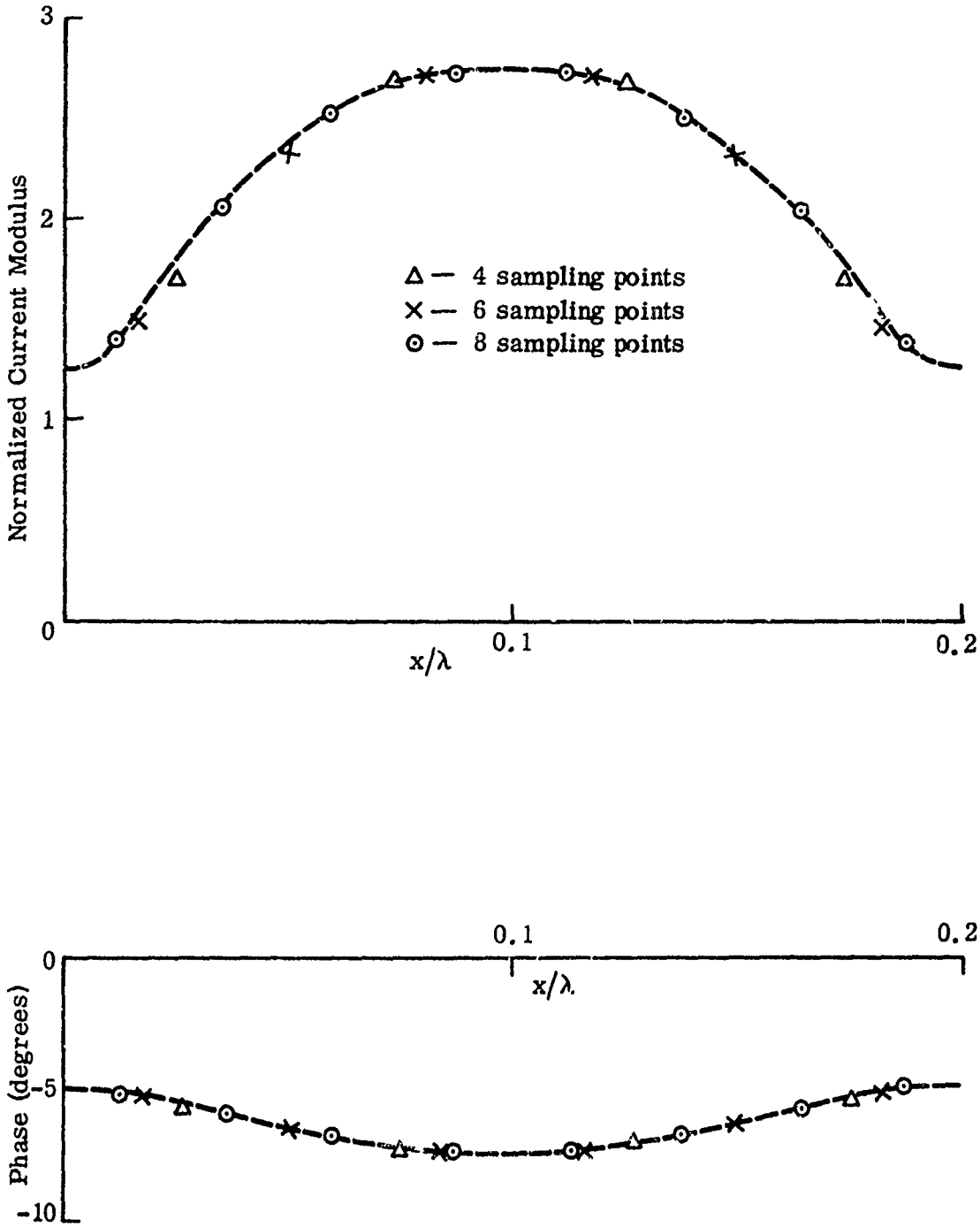

Fig. 5-38: Normalized Surface Field for a Sinusoidal Surface ($d = 0.2\lambda$, $a = 0.1\lambda$ and $\theta = 0$) computed using 4, 6 and 8 sampling points, H polarization

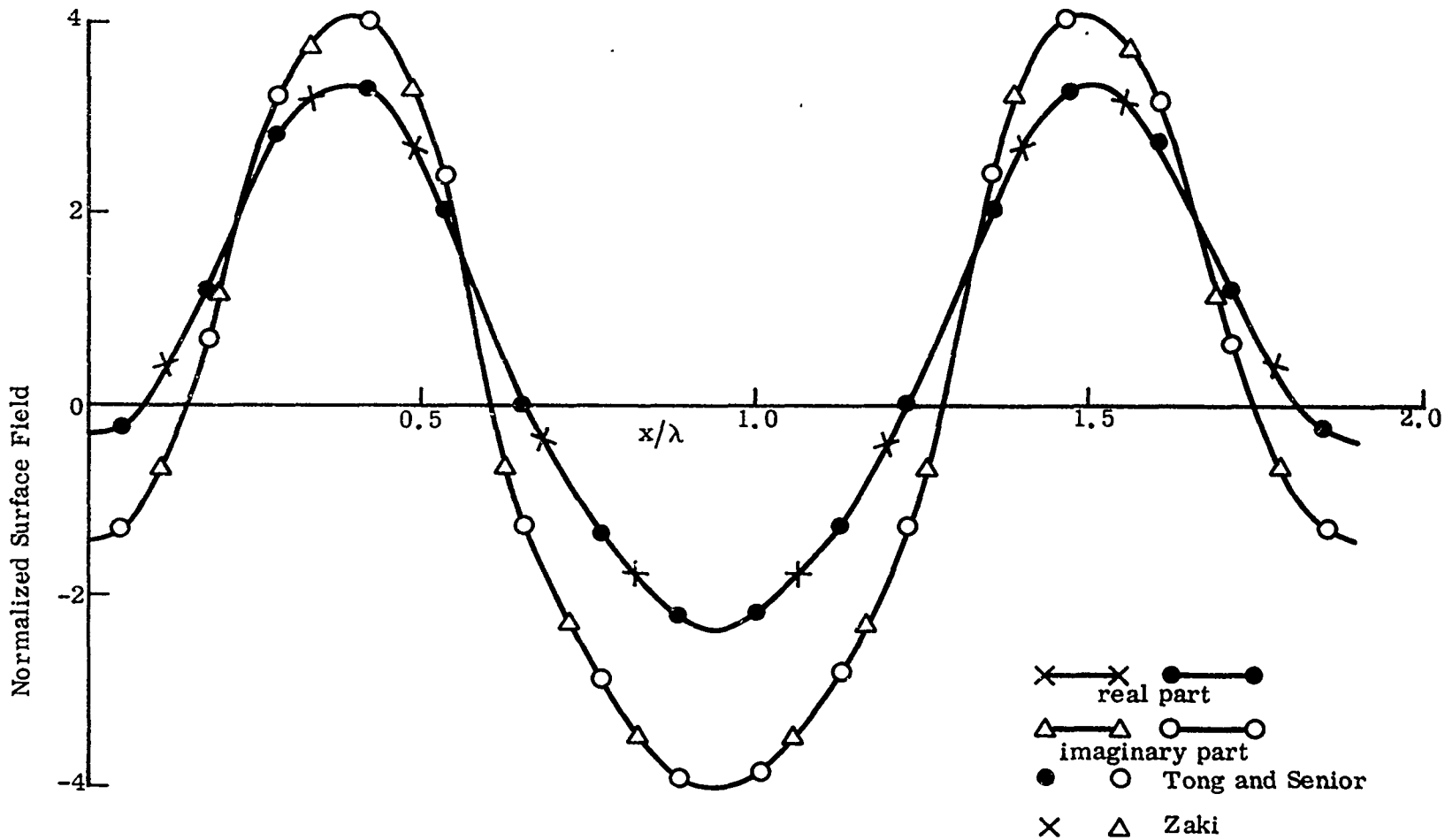

Fig. 5-39: Normalized Surface Field for a Sinusoidal Surface ($d = 1.9\lambda$, $a = 0.25\lambda$ and $\theta = 0$), for H polarization.

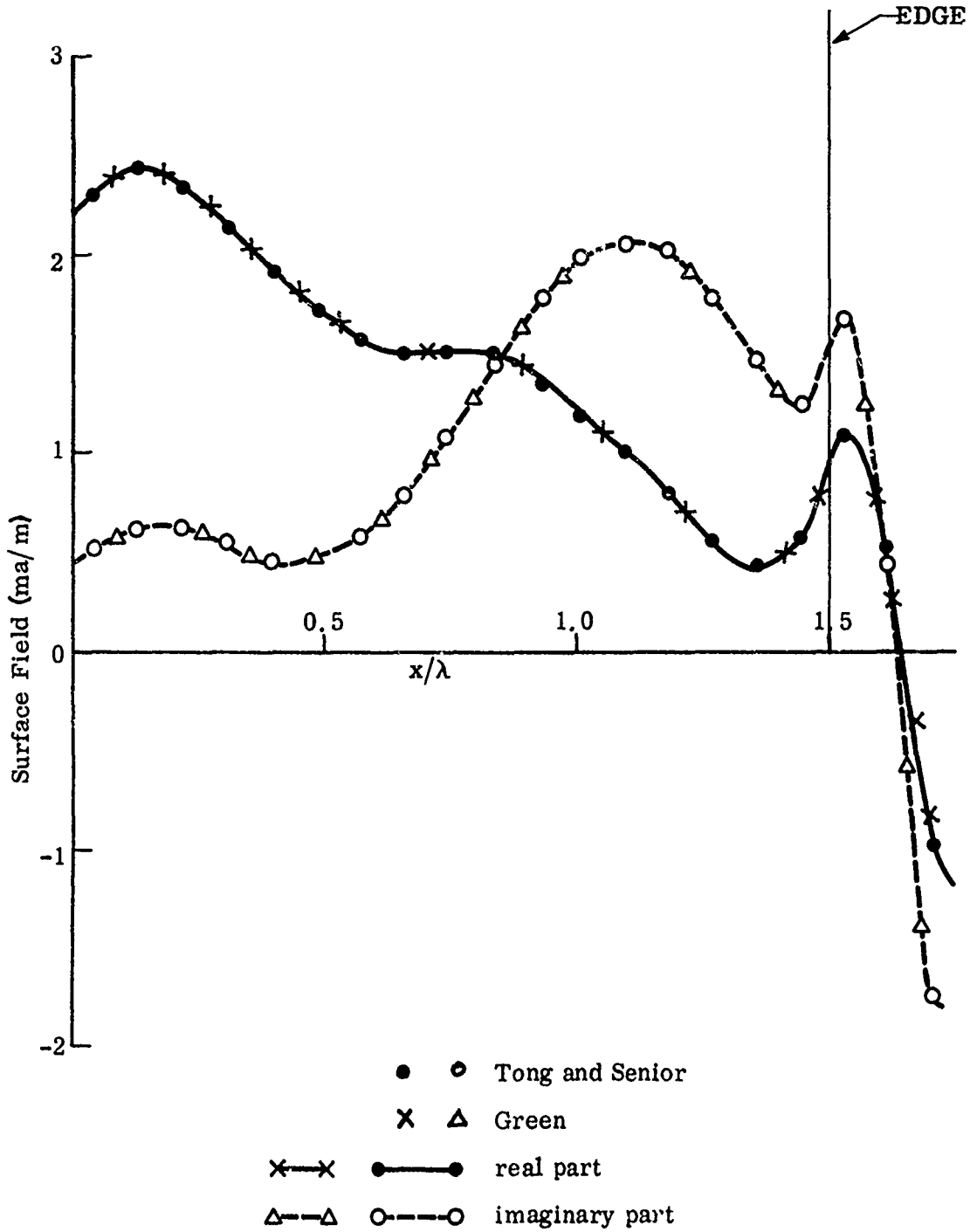

Fig. 5-40: Surface Field for a Triangular Surface ($d = 1.75\lambda$, $\theta_1 = 20^\circ$, $\theta_2 = 66^\circ$ and $\theta = 12.2^\circ$) for H polarization

As in the case of E polarization, the time consumed in each computation depends on several factors (see section 3.5 of Chapter III), but in general the CPU time is larger now because of the more complicated (modified) Green's function. A summary of the CPU times for various combinations of parameters is given in Table V-1.

The distribution of the CPU time for a typical computation where N = 12, M = 3 and Q = 1 is given below:

1. Computation of matrix elements 50.3 sec.
2. Matrix inversion 8.4 sec.
3. Physical optics approximation 4.3 sec.
4. Energy conservation check and calculation of diffracted mode amplitudes 9.0 sec.

TABLE V-1
Computational Time for H Polarization

Number N of Sampling Points	Number M of Terms in the Infinite Series	Number Q of Terms in the Periodic Function Representation	CPU Time (sec) IBM/67
4	3	1	13.00
6	2	10	35.58
6	3	10	41.67
8	3	1	42.47
8	3	10	52.07
8	3	12	61.71
8	8	1	71.87
8	6	1	60.46
10	3	1	67.13
10	8	1	104.84
12	3	1	73.10
12	3	10	120.38
16	6	1	180.21
16	5	1	167.36
20	5	15	424.75

Chapter VI

SCATTERED FIELD FOR H POLARIZATION

In this chapter we consider the scattered field, scattered energy and such associated physical phenomena as the S anomalies. Numerical data are presented to illustrate the discussion, and comparisons are made with the physical optics approximation as well as the results for E polarization.

6.1 Diffracted Mode Amplitudes

Using a procedure directly analogous to that for E polarization, and assuming the incident magnetic field shown in Eq. (2.31), we can write

$$H_z^s(x,y) = \sum_{m=-\infty}^{\infty} A'_m e^{-j(\beta_m x + X_m y)} , \tag{6.1}$$

with

$$A'_m = \frac{1}{2dX_m} \int_0^d e^{j(\beta_m x' + X_m y)} \left\{ X_m - \beta_m f'(x') \right\} K_t(x') dx' \tag{6.2}$$

where X_m and β_m are as given before.

The dependence on X_m and β_m is rather heavier than that displayed by Eq. (4.4).

Once the unknown $K_t(x')$ has been found, it is a simple matter to compute the amplitudes of all the diffracted modes, both propagating ($X_m^{\pm}$ real) and evanescent ($X_m^{\pm}$ purely imaginary), and the amplitudes of the propagating waves for several different values of d/λ, a/λ and θ for a sinusoidal surface are given in Tables VI-1 through VI-4. It is observed that the physical optics approximation, with or without shadowing included, tends to underestimate the amplitudes, and we further note that if shadowing is excluded (or is not present), the physical optics estimate is the same for both polarizations (see Appendix A).

TABLE VI-1

Amplitudes of Diffracted Waves for a Sinusoidal Surface
($d = 0.2\lambda$, $a = 0.1\lambda$).

	$\theta = 0^o$		$\theta = 30^o$		$\theta = 60^o$	
	Mag. $\lvert A'_0 \rvert$	Phase $\phi'_0(^o)$	Mag. $\lvert A'_0 \rvert$	Phase $\phi'_0(^o)$	Mag. $\lvert A'_0 \rvert$	Phase $\phi'_0(^o)$
Numerical Solution	0.9830	-12.45	0.9910	-23.82	1.0640	-67.24
Physical Optics w/o shadow	0.6425	0	0.7251	0	0.9037	0
Physical Optics w/ shadow	0.6425	0	0.1550	-65.17	0.5440	-166.31

TABLE VI-2

Amplitudes of Diffracted Waves for a Sinusoidal Surface
($d = 1.90\lambda$, $a = 0.25\lambda$, $\theta = 0$).

	Mag. $\lvert A'_0 \rvert$	Phase $\phi_0(^o)$	Mag. $\lvert A'_{-1} \rvert = \lvert A'_1 \rvert$	Phase $\phi'_{-1}(^o) = \phi'_0(^o)$
Numerical Solution	0.9040	-80.50	0.3350	52.55
Physical Optics	0.3042	0	0.4389	90

TABLE VI-3

Amplitudes of Diffracted Waves for a Sinusoidal Surface
($d = 0.4\lambda$, $a = 0.2\lambda$).

	$\theta = 0^o$		$\theta = 60^o$	
	Mag. $\lvert A'_0 \rvert$	Phase $\phi'_0(^o)$	Mag. $\lvert A'_0 \rvert$	Phase $\phi'_0(^o)$
Numerical Solution	0.9350	-107.19	1.0140	-145.28
Physical Optics w/o shadow	0.0549	0	0.6450	0
Physical Optics w/ shadow	0.0549	0	0.1290	-131.32

TABLE VI-4

Amplitudes of Diffracted Waves for a Sinusoidal Surface ($d = 0.2\lambda$, $a = 0.03\lambda$, $\theta = 0$).

	Mag. $\lvert A'_0 \rvert$	Phase $\phi'_0(^\circ)$
Numerical Solution	0.9986	-0.55
Physical Optics	0.9647	0

6.2 Diffracted Energy and Wood Anomalies

6.2.1 Discussion

The diffracted energy is the field quantity most frequently measured. It is, of course, directly related to the diffracted mode amplitudes, and the general remarks concerning energy and the Wood anomalies made in section 4.2.1 also apply here. Unlike the P anomalies, however, the S anomalies (which were discovered earlier) have been more widely studied and are more completely understood. According to Rayleigh's theory, the occurrence of the S anomalies corresponds to the singularity of the scattered field at Rayleigh wavelengths. At these wavelengths, a new spectral order appears at grazing angles, and thus causes a sudden rearrangement in the diffracted energy among the other modes. But it should be noted that there are S anomalies other than those which occur at the Rayleigh wavelengths, and these are similar to the "Brewster angle" type discussed in section 4.2.2. A comparison with the P anomalies reveals that the S anomalies are generally much stronger and can occur with structures having relatively shallow grooves.

6.2.2 Computed Data for the Diffracted Energy

a) Two radiating modes. The fields scattered by surfaces of very small (electrical) period are of relatively little interest. Anomalies are observed only when more than one radiating mode is present, and, of course, the simplest cases (also the ones most investigated) are those where there are just two radiating modes.

Figure 6-1 shows a plot of the normalized diffracted energy versus the surface height for a full-wave rectified profile for which $d = 0.85\lambda$ and $\theta = 36^{\circ}$. Since an equivalent plot for a sinusoidal surface was obtained by Zaki (1969), it is included here for the sake of comparison. With this choice of parameters, only the $m = 0$ (specular) and the $m = -1$ (back scattered) modes can propagate. The diffracted energy exchange is continuous, exhibiting maxima and minima in an almost standing wave pattern. The rate of conversion of the diffracted energy is more rapid for the sinusoidal surface than with the full-wave rectified surface. Anomalies occur in both cases, however, with the first appearance being at $a = 0.16\lambda$ for the former surface and at $a = 0.36\lambda$ for the latter. Note that this type of anomaly is different from the classical (Rayleigh) type in that they do not occur at the Rayleigh wavelengths.

Another example for two radiating modes is shown in Fig. 6-2 for a full-wave rectified profile with $a = 0.3\lambda$, $d = 0.30\lambda$, $\theta = 60^{\circ}$ and ℓ varying from 0 to 0.7λ. We note the abrupt exchange of diffracted energy between the $m = 0$ and $m = -1$ modes near the Rayleigh wavelength, $\lambda_R = 0.535\lambda$. This exchange is, however, not complete, but about 50 per cent. A stronger anomaly showing complete conversion of energy is observed at $d = 0.7\lambda$.

The changing division of diffracted energy between two radiating modes as a function of the angle of incidence is illustrated in Fig. 6-3 for a full-wave rectified profile with $d = 0.6\lambda$ and $a = 0.3\lambda$. It is seen that there is a discontinuity in the diffracted energy for both modes at $\theta = 41.8^{\circ}$ corresponding to a Rayleigh wavelength, and for incidence angles greater than 41.8° most of the energy is carried by the $m = -1$ mode.

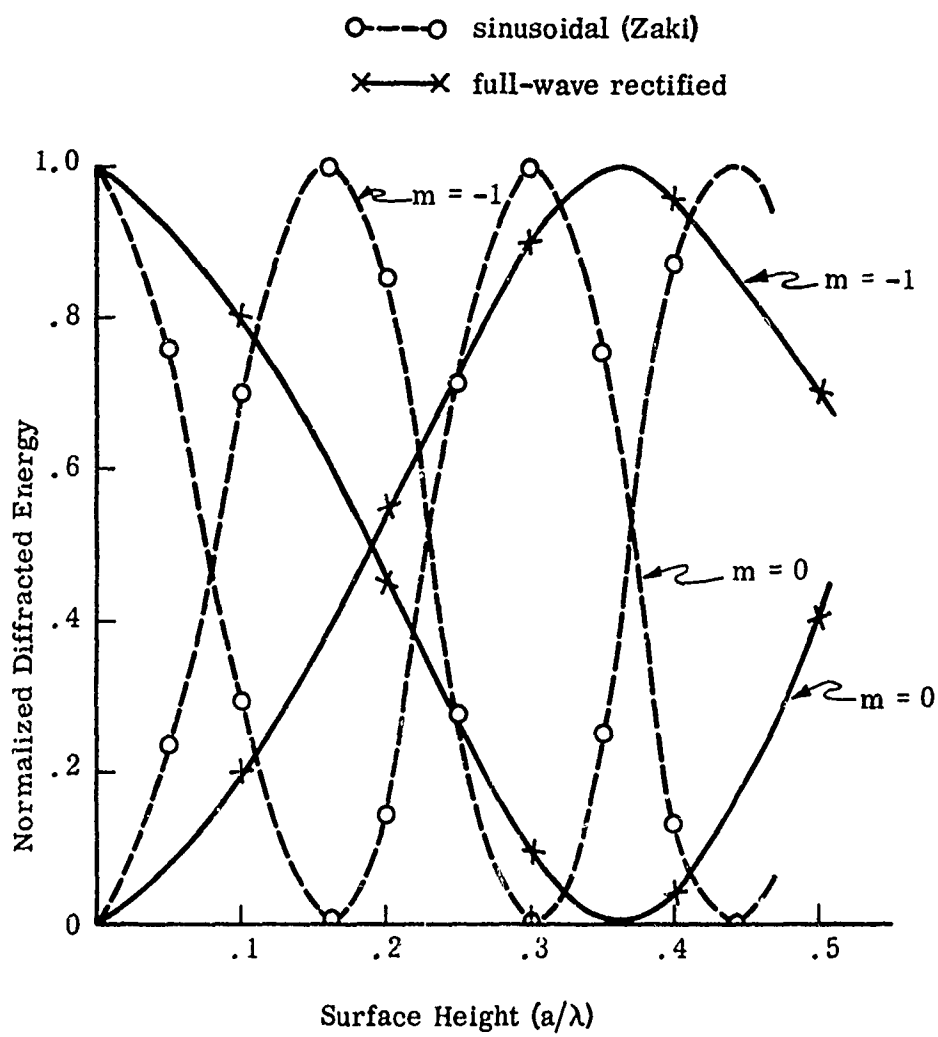

Fig. 6-1: Diffracted Energy for Two Radiating Modes, for H polarization.

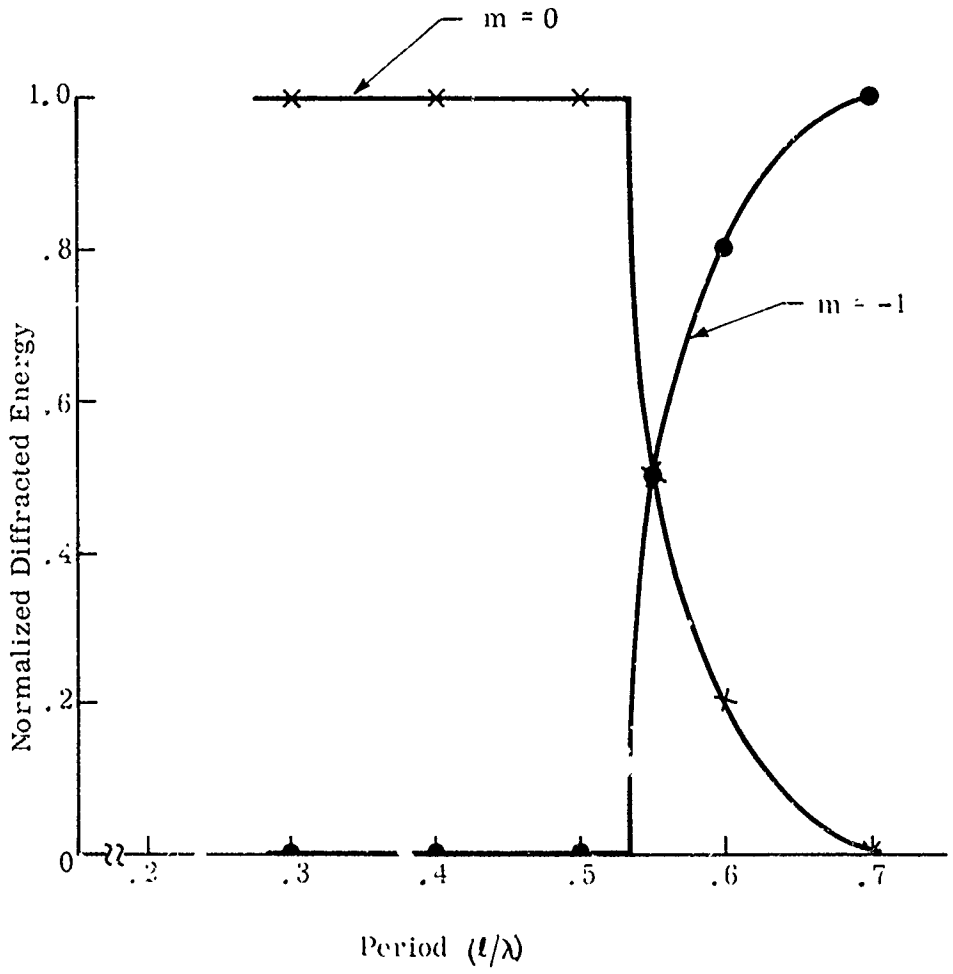

Fig. 6-2: Diffracted Energy for a Modified Full-wave Rectified Surface ($a = 0.3\lambda$, $\theta = 60^\circ$ and $d = 0.30\lambda$), for H polarization.

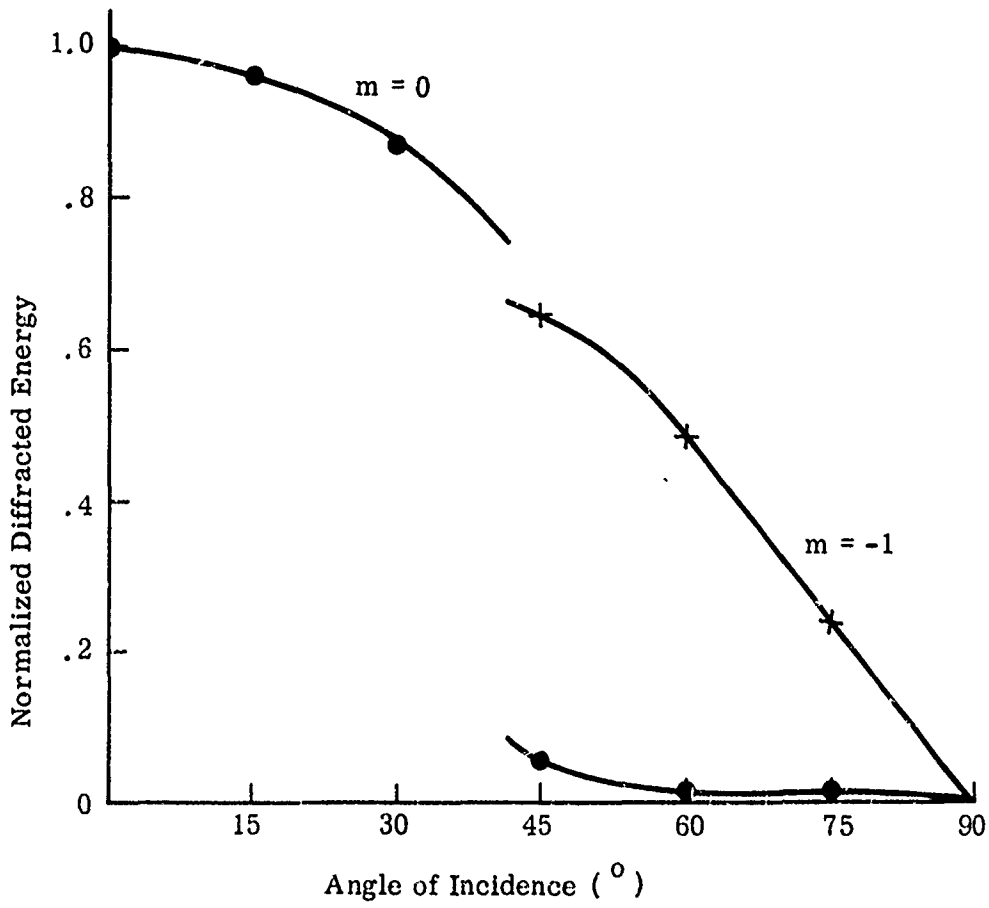

Fig. 6-3: Diffracted Energy for a Full-Wave Rectified Surface ($d = 0.6\lambda$ and $a = 0.3\lambda$), for H polarization.

b) Three radiating modes. As the period of the surface is increased, higher order modes come in, and the distribution of diffracted energy among the radiating modes becomes more complex. This is clearly demonstrated in Fig. 6-4 for a sinusoidal surface where $d = 1.155\lambda$, $\theta = 60^{\circ}$ and a varies from 0 to 0.7λ. With this choice of parameters there are three radiating modes, with the $m = 0$ mode radiating in the specular direction ($\theta_0 = 60^{\circ}$), the $m = -1$ mode radiating in the normal direction ($\theta_{-1} = 0$) and the $m = -2$ mode radiating in the back scattered direction ($\theta_{-2} = -60^{\circ}$). The curves show no resemblance to those for the case of two radiating modes. For $a < 0.05\lambda$, the $m = 0$ mode is the dominant one, carrying at least 80 per cent of the total energy. Once again, we see that the diffracted energy for each mode is more sensitive to a change in the surface height than was the case for E-polarization, and a strong anomaly is observed for even the relatively shallow groove depth, $a = 0.3\lambda$. For this depth, all of the energy is carried by the $m = -2$ mode which produces a correspondingly strong back scattered field.

The same kind of plots were also obtained using the physical optics approximation, either with or without shadowing, and they are shown in Figs. 4-4 (the same for both polarizations) and 6-5. By comparing these with Fig. 6-4, it is apparent that neither version of the physical optics approximation gives satisfactory agreement with the exact solution except perhaps when $a \lesssim 0.05\lambda$.

A plot showing the relation between the diffracted energy and the minimum radius of curvature (at the surface peak or trough) of a sinusoidal surface for which $d = 1.155\lambda$ and $\theta = 60^{\circ}$ is shown in Fig. 6-6. As in the case of E polarization, the dominant mode for $k\rho_{min} \gtrsim 4.5$ is the $m = 0$ (specular) one. Thus, as far as the scattered field is concerned, the surface with $k\rho_{min} \geq 4.5$ can be treated as flat.

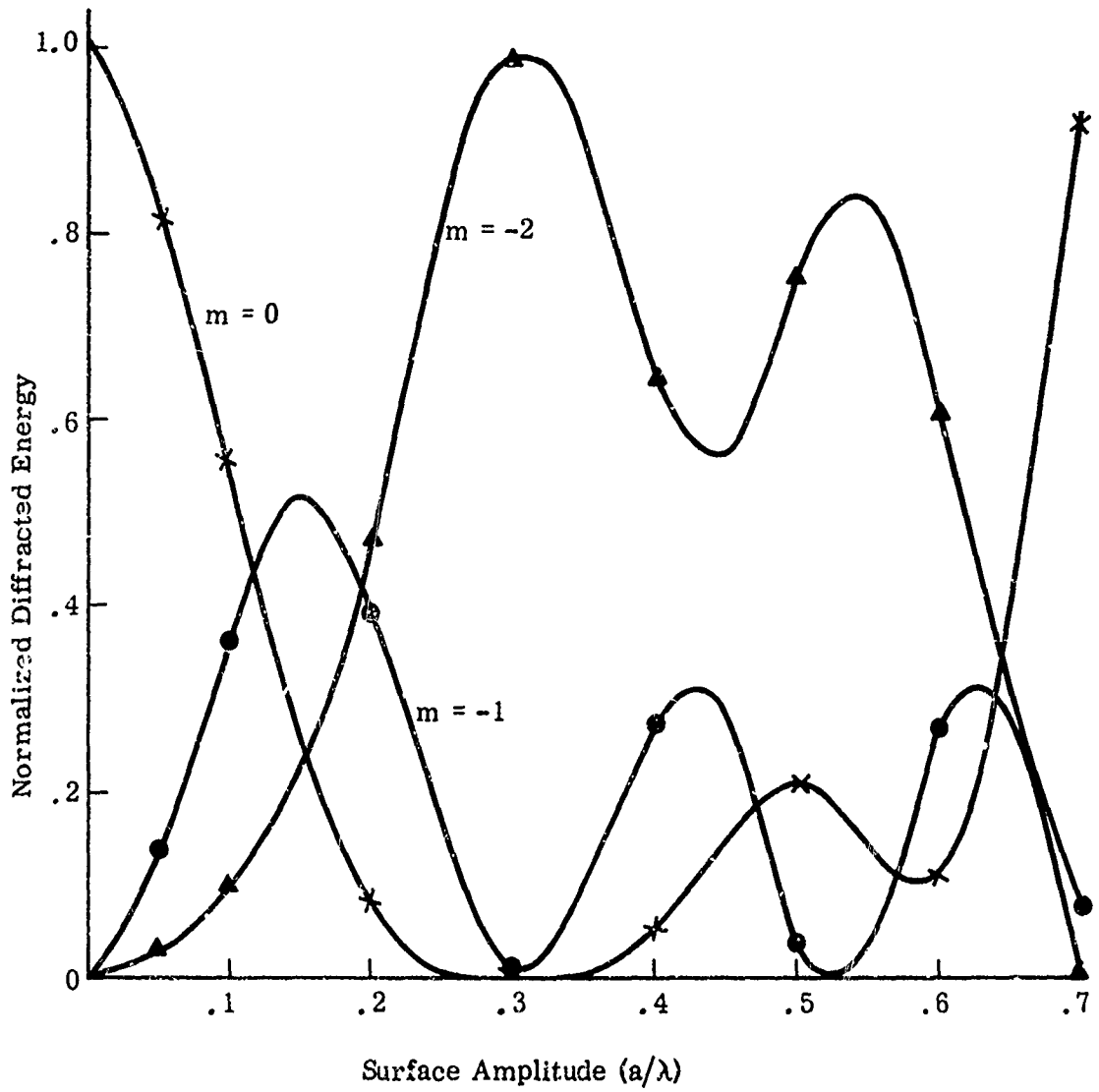

Fig. 6-4: Diffracted Energy for a Sinusoidal Surface ($d = 1.155\lambda$ and $\theta = 60^{\circ}$), for H polarization.

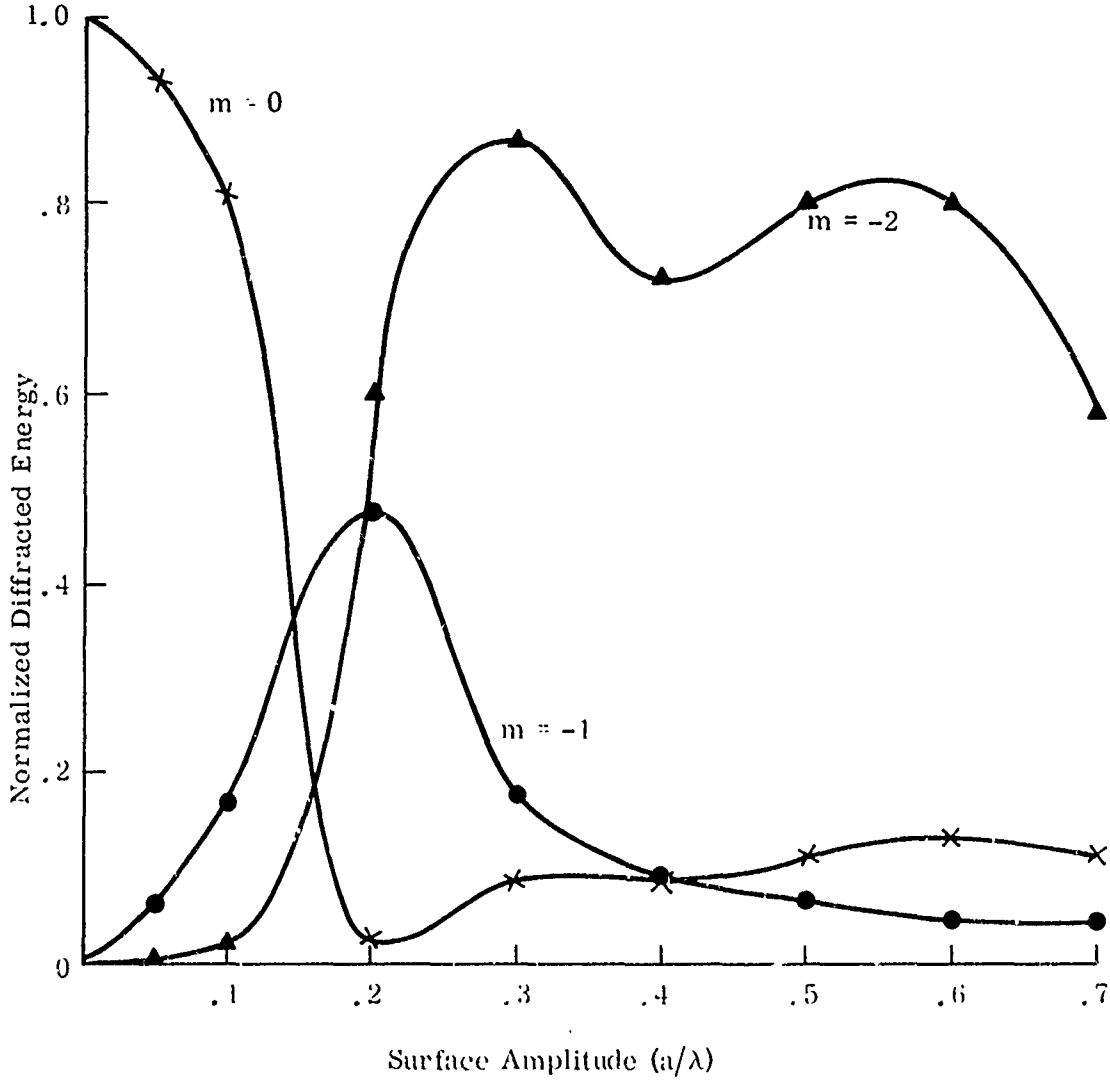

Fig. 6-5: Diffracted Energy for a Sinusoidal Surface ($d = 1.155\lambda$ and $\theta = 60^0$). Computed Using the Physical Optics Method (with shadow), for H polarization.

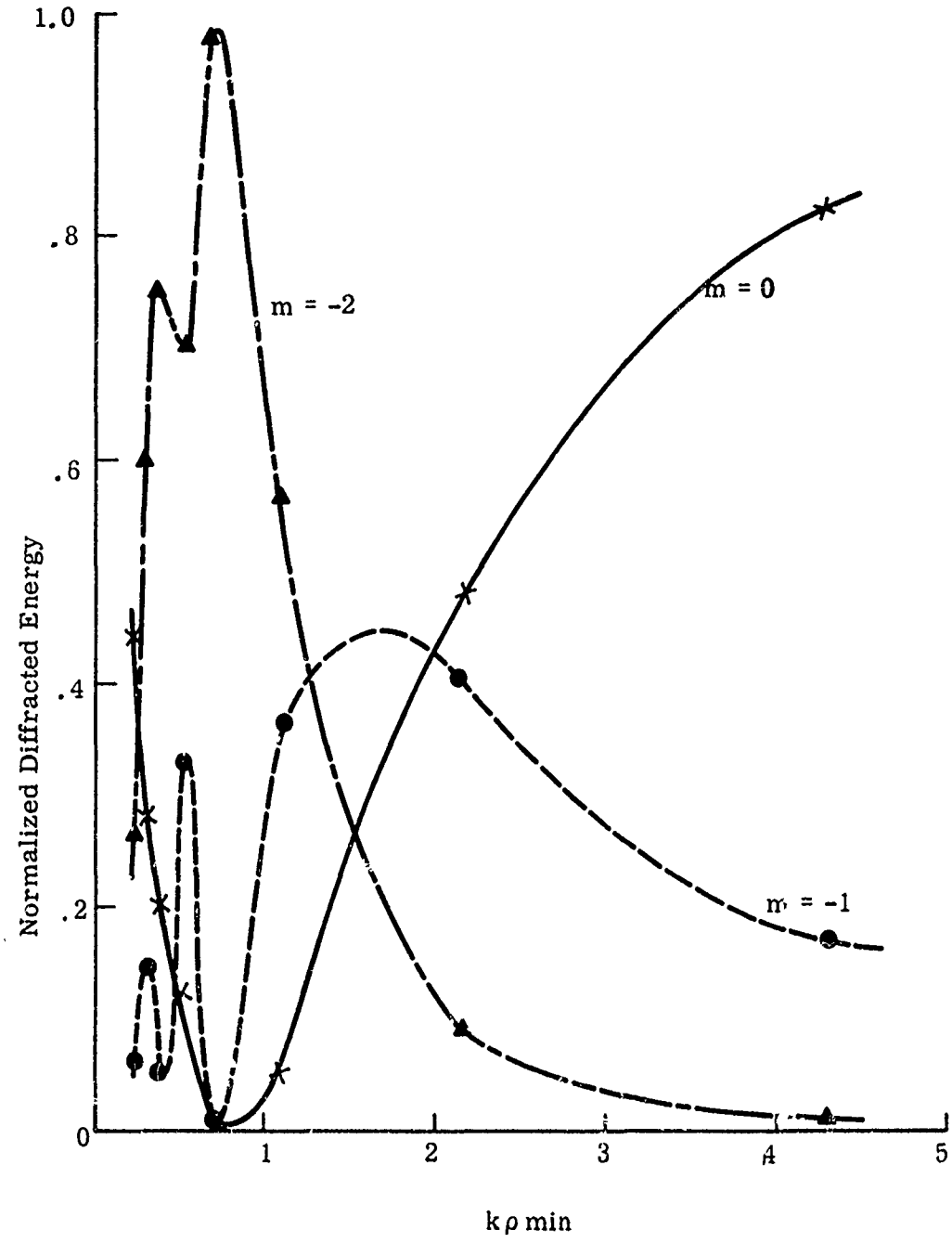

Fig. 6-6: Diffracted Energy for a Sinusoidal Surface ($d = 1.155\lambda$ and $\theta = 60^{\circ}$), for H polarization.

6.2.3 Blazed Gratings

The diffracted energy for various orders of radiating mode can be computed from Eq. (6.2) and used as a basis for the design of blazed gratings (gratings whose profiles are so shaped as to maximize the diffracted energy in a given direction or a given mode).

Blazed gratings find important applications in spectroscopy where the spectrum is observed in only one order at a time, the energy going into the other order modes being completely wasted. It is therefore desirable to have the observed spectrum as luminous as possible, and one way of achieving this is to reduce the number of propagating modes by using smaller periods. Another way is to minimize the amount of energy carried by the other modes, and according to Eq. (6.2) and neglecting the contribution due to the perpendicular side of the surface, the diffracted energy of the mth mode for a right-angled triangular profile will be zero if

$$X_m - \beta_m f'(x) = 0$$

or

$$f'(x) = X_m/\beta_m \,. \tag{6.3}$$

Eq. (6.3) is particularly useful when there are only two radiating modes. However, since this applies only to H polarization, the echelette grating so designed is polarization dependent.

6.3 Conservation of Energy

One feature that is common to perfectly conducting, periodic surfaces regardless of the number of radiating modes involved is the condition of energy conservation, and this can be used as a check on the accuracy of the numerical solution. The results of this check are shown in Table VI-5 for a sinusoidal surface sustaining, in most cases, only one radiating mode. Results for two and three radiating modes are shown in Figs. 6-1 and 6-3. In all cases considered, the numerical results satisfy the condition of energy conservation, but the physical optics approximation, with or without shadowing included, does not.

TABLE VI-5

Conservation of Energy for a Sinusoidal Surface

			Numerical		Physical Optics			
					w/o Shadow		w/ Shadow	
d/λ	a/λ	$\theta(^o)$	Energy	Error(°/o)	Energy	Error(°/o)	Energy	Error(°/o)
0.2	0.1	0	0.9848	-1.52	0.4728	-58.72	0.4728	-58.72
0.2	0.1	30	0.8532	-1.43	0.4554	-47.30	0.0208	-98.00
0.2	0.1	60	0.5075	1.50	0.4083	-18.34	0.1479	-70.42
0.2	0.01	0	0.9980	-0.20	0.9921	- 0.79	0.9921	- 0.79
0.2	0.03	0	0.9987	-0.13	0.9308	- 6.92	0.9308	- 6.92
0.4	0.2	0	0.9823	-1.77	0.0030	-99.70	0.0030	-99.70
0.4	0.2	60	0.5042	0.84	0.2061	-58.78	0.0083	-98.50
1.9	0.25	0	0.9974	-0.26	0.4202	-57.98	0.4202	-57.98

6.4 Approximate Techniques

As in the case of E polarization, an attempt has been made to use the knowledge obtained from the numerical results to develop a simple method for estimating the field back scattered from surfaces at oblique incidence. Were it possible to arrive at a valid approximation technique, it would be very useful in such practical problems as sea surface or terrain scattering.

Naturally the physical optics method was tried, but was abandoned because of its rather poor agreement with exact results. As we have seen in previous sections, the scattered field, involving the conversion of energy among radiating modes, is a very complicated quantity which offers little prospect of simple approximation in any general situation. However, in particular cases such as back scattering by a sinusoidal surface at oblique incidence (Figs. 5-25 through 5-29), there is some hope of developing an approximate technique. In a procedure directly analogous to that for E polarization, the field back scattered by a sinusoidal surface at oblique incidence was computed by the stationary

phase method using the exact surface field over only a restricted portion of the illuminated region of the surface. The results are shown in Table VI-6.

TABLE VI-6

Comparison of the Energy Backscattered by a Sinusoidal Surface: $d = 1.155\lambda$, $\theta = 60^{\circ}$, Computed Using the Exact and Stationary Phase Methods.

Surface Amplitude (a/λ)	Normalized Back Scattered Energy	
	Exact Method	Stationary Phase Method
0.3	0.98	1.06
0.4	0.64	0.69
0.5	0.75	0.70
0.6	0.60	0.64
0.7	0	0.16

Although the agreement with the exact values is excellent, the approximate method still requires a knowledge of the true surface field over a small region of the surface, and in order to avoid solving the integral equation numerically, it is necessary to find some other means for estimating this field. As regards the phase, the physical optics value turns out to be adequate; unfortunately, the modulus is a much more complicated quantity and, unlike E polarization, is not dependent on the local surface properties. Many different methods using combinations of ray optics and surface wave theory have been tried. For example, one method considered the interaction of two rays: the incident ray and the ray reflected from the opposite face of the surface; another method considered forward and backward traveling waves whose amplitudes we sought to choose to fit the exact data. However, neither of these methods alone (or even in combination) was satisfactory, though it was noted that a rough estimate for the modulus was provided by the imaginary part of the physical optics approximation. Though there is no physical basis for this

whatsoever, the corresponding estimates of the back scattered field were computed, and a comparison with the exact values is given in Table VI-7.

TABLE VI-7

Comparison of the Current Modulus over the Illuminated Region Of a Sinusoidal Surface, Computed Using the Exact Method and The Imaginary Part of the Physical Optics Approximation. ($d = 1.155\lambda$, $\theta = 60^{\circ}$).

Surface Amplitude (a/λ)	Location of Point, x Coordinate (λ)	Normalized Current Modulus	
		Exact Method	Approximation Using The Imaginary Part of The Phys. Optics Values
0.3	0.915	1.75	2.00
	1.010	2.05	1.92
	1.109	2.30	1.84
0.4	0.938	1.84	1.96
	1.082	1.99	2.00
0.5	0.915	2.00	1.97
	1.010	1.42	1.90
	1.109	1.84	1.96
0.6	0.915	1.85	1.90
	1.010	1.17	1.70
	1.109	1.84	1.70
0.7	1.010	1.04	1.43
	1.109	0.90	1.37

Chapter VII

RAYLEIGH'S METHOD

As mentioned in Chapter IV in connection with Wood anomalies, Rayleigh's work was one of the early attempts to theoretically investigate scattering (electromagnetic or acoustic) by a periodic surface. His approach, now termed "Rayleigh's method", is indeed an important one, and has been used, with or without refinement, by many subsequent investigators. We shall now examine his method in some detail and compare exact data with data obtained using his assumption.

7.1 History

In 1907 Lord Rayleigh studied the scattering of sound waves by corrugated surfaces and sought to solve the wave equation in combination with the appropriate boundary condition. His method is an intuitive one that has been used by many investigators and is based on the following two assumptions: a) the scattered field may be represented by a linear combination of discrete plane waves, either propagating or attenuated from the surface, and b) this representation holds everywhere above and on the boundary. A simple and straightforward description of the Rayleigh method for a periodic boundary is given by Beckmann and Spizzichino (1963). The second assumption, which is often termed the "Rayleigh assumption," has been a controversial subject for many years.

As first observed by Lippmann (1953), a choice of scattered field consisting only of outgoing waves is not the most general, and may not completely represent the field within the grooves; at any point in this region, one would expect the field to include waves propagating (or exponentially damped) in both directions, since there are currents on those parts of the grating above and below the given point. Meecham (1956b) studied reflection from irregular surfaces with a method based on Fourier transforms, and obtained numerical

results for the distribution of energy reflected from a sinusoidal surface. By comparing these with experimental results and also with the ones obtained using Rayleigh's method, he concluded that errors were of the same order as those in the physical optics approximation.

Heaps (1957) attacked the validity of the "Rayleigh assumption" in another way. He studied the reflection of plane acoustic waves at a sinusoidal surface of zero pressure and investigated the least possible value of the surface pressure consistent with the assumption that all the reflected radiation is in the form of undamped plane waves. After comparing his results with the experimental data of LaCasce and Tamarkin (1956), he concluded that "if all reflected energy has the form of undamped plane waves then the surface is necessarily sound absorbing and of pressure significantly different from zero. Thus, in the neighborhood of the corrugated surface of zero pressure, it is necessary to take into account other forms of radiation and such forms play a significant part in satisfying the boundary condition." Murphy and Lord (1964) have also criticized the Rayleigh assumption. By making a direct comparison of the results obtained from an exact representation of the field with those based on Rayleigh's formulation, they concluded that the latter is inadequate.

On the defense side, there are people who support Rayleigh's assumption. Marsh (1963) has generalized Rayleigh's method, and considered the scattering of acoustic waves from a sinusoidal surface ($y = a \cos Kx$) with a Dirichlet boundary condition. He showed that the boundary condition can be satisfied using only outgoing waves. Numerical data were obtained for the amplitudes of diffraction which, upon substitution into the energy relation, indicated conservation of energy. However, it must be noted that the values of Ka used were relatively small, and as shown later, the Rayleigh assumption is indeed valid in this case. Additional support of Rayleigh's assumption comes from Millar (1963), who argued from the viewpoint of analytic continuation. He remarked that if the boundary values are analytic, "the exterior

field may be continued into the grating from above, and that the exterior plane wave representation will converge everywhere above a plane parallel to $y = 0$. Likewise the interior field may be continued into the upper half-space from below, and the interior plane wave representation will be convergent below a plane parallel to $y = 0$. If the two half-spaces of convergence so defined contain a common layer which, in turn, completely contains the reflecting surface $y = a \cos Kx$, then the two representations, each outgoing or attenuated in its own half-space, may be matched on the reflecting surface where both are valid." This remark seems very reasonable.

Possibly the most significant step toward the resolution of the controversy (with Dirichlet condition) was taken by Petit and Cadilhac (1966). They demonstrated (using analytic continuation) that for the profile $y = a \cos Kx$ $(-\infty < x < \infty)$ Rayleigh's assumption could not be valid if $Ka > 0.448$; for $Ka < 0.448$, the question remained open. Recently Millar (1969) used a technique developed to locate singularities of solutions to the Helmholtz equation. By applying this to the sinusoidal profile, he was able to show that Rayleigh's assumption is indeed valid if $Ka \leq 0.448$ and is not valid if $Ka > 0.448$.

In order to shed some light on this remark, let us compute the scattered field using the exact representation and under the Rayleigh assumption.

7.2 Numerical Results by the Exact and Rayleigh Methods

For E polarization we have, from Eq. (2.22),

$$E_z^s(x, y) = \frac{\omega\mu}{4} \int_0^d P_1 \sqrt{1 + f'(x')^2}\, K_z(x')dx' \quad . \tag{7.1}$$

Using the exact representation we can expand the field in terms of incoming and outgoing waves, thus

$$E_z^s(x,y) = \sum_{m=-\infty}^{\infty} \left[B_m e^{-j(\beta_m x + X_m y)} + C_m e^{-j(\beta_m x - X_m y)} \right] . \tag{7.2}$$

From Eqs. (7.1) and (7.2) we get

$$B_m = \frac{\omega\mu}{2dX_m} \int_{S^-} e^{j(\beta_m x + X_m y)} \sqrt{1+f'(x)^2}\; K_z(x)dx \;, \tag{7.3}$$

$$C_m = \frac{\omega\mu}{2dX_m} \int_{S^+} e^{j(\beta_m x - X_m y)} \sqrt{1+f'(x)^2}\; K_z(x)dx \tag{7.4}$$

where S^+ and S^- represent the portions of the surface above and below a plane through the point $P(x,y)$ (see Fig. 7-1). Of course, when y is above the grating, i.e. $y \geq \max f(x)$, then

$$B_m = A_m \qquad \text{and} \qquad C_m = 0 \;,$$

where A_m is defined by Eq. (4.4)

On the other hand using Rayleigh's assumption, we can expand the field everywhere in terms of outgoing waves alone, viz.

$$\tilde{E}_z^s(x,y) = \sum_{m=-\infty}^{\infty} \tilde{B}_m e^{-j(\beta_m x + X_m y)} \;. \tag{7.5}$$

If we now substitute

$$P_1 = \sum_{m=-\infty}^{\infty} \frac{2}{X_m d} e^{-j\left[\beta_m (x-x') + X_m |y-y'|\right]}$$

into Eq. (7.1), we get

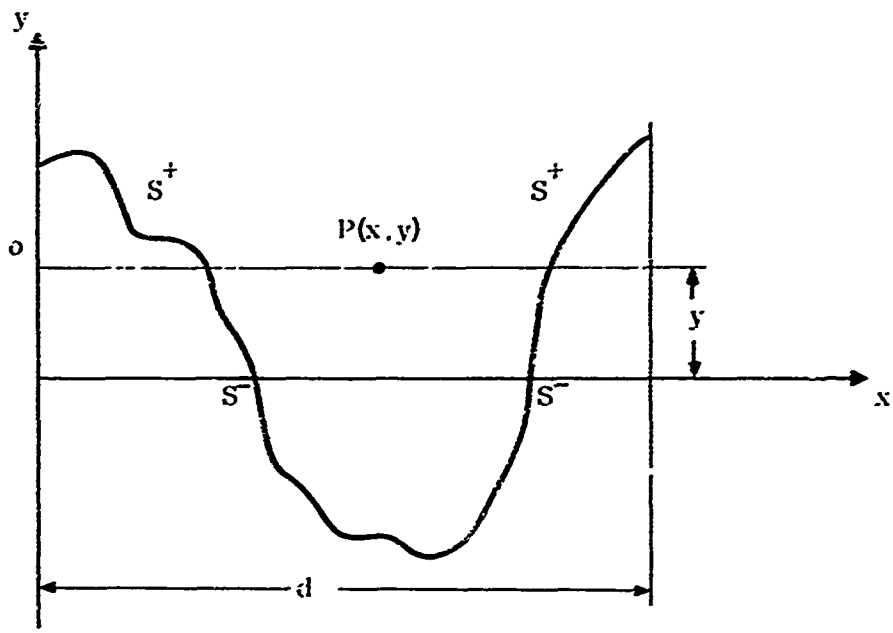

Fig. 7-1: Partitioning the Periodic Surface into Two Parts, S^+ and S^-

$$E_z^s(x,y) = \frac{\omega\mu}{2d} \int_0^d \sum_{m=-\infty}^{\infty} \frac{1}{X_m} e^{-j\left[\beta_m(x-x') + X_m|y-y'|\right]} \sqrt{1+f'(x')^2}\, K_z(x')dx' . \tag{7.6}$$

In order to make Eq. (7.5) equal to Eq. (7.6) everywhere on the surface, we must remove the modulus sign in the kernel. Thus, equating Eqs. (7.5) and (7.6), we obtain

$$\tilde{B}_m = \int_0^d e^{j(\beta_m x + X_m y)} \sqrt{1+f'(x)^2}\, K_z(x)dx \tag{7.7}$$

$$= \int_{S^+} e^{j(\beta_m x + X_m y)} \sqrt{1+f'(x)^2}\, K_z(x)dx$$

$$+ \int_{S^-} e^{j(\beta_m x + X_m y)} \sqrt{1+f'(x)^2}\, K_z(x)dx . \tag{7.8}$$

Intuitively we expect the discrepancy between Eqs. (7.2) and (7.5) to be greatest when $S^- = 0$, that is when the point $P(x,y)$ is in the surface trough. Thus, letting $S^- = 0$, we get from Eq. (7.2)

$$E_z^s(d/2, -a) = \sum_{m=-\infty}^{\infty} C_m e^{-j(\frac{d}{2}\beta_m + aX_m)} \tag{7.9}$$

where

$$C_m = \frac{\omega\mu}{2dX_m} \int_0^d e^{j(\beta_m x - X_m y)} \sqrt{1+f'(x)^2}\, K_z(x)dx ,$$

and from Eq. (7.5)

$$\tilde{E}_z^s(d/2, -a) = \sum_{m=-\infty}^{\infty} \tilde{B}_m e^{-j(\frac{d}{2}\beta_m - aX_m)} \tag{7.10}$$

where

$$\tilde{B}_m = \int_0^d e^{j(\beta_m x - X_m y)} \sqrt{1+f'(x)^2}\, K_z(x)dx \quad .$$

Using Eqs. (7.9) and (7.10), numerical results for the scattered field were computed for a sinusoidal and an inverted full-wave rectified surface, and these are shown in Table VII-1.

TABLE VII-1

E-polarization. Comparison of Scattered Fields at the Surface Trough Obtained by the Exact and Rayleigh Methods.

Type of Surface	Ka	Scattered Field	
		Exact Representation	Rayleigh's Method
Sinusoidal	0.314	2.27440 - j0.22657	2.27420 - j0.22664
	0.942	1.96310 - j0.48310	1.95450 - j0.48166
	1.884	1.86610 - j0.52445	1.75170 - j0.54162
Inverted Full-wave Rectified	0.314	2.42170 - j0.18443	2.42180 - j0.17913
	0.942	2.22550 - j0.49810	2.22720 - j0.46486

Table VII-1 shows that, for sufficiently small values of Ka, the scattered fields based on the exact and Rayleigh methods agree extremely well for a sinusoidal surface. This is consistent with Millar's remark. In

the case of the inverted full-wave rectified surface, agreement is not so good for the same values of Ka. This is probably due to the fact that the inverted full-wave rectified profile is not an analytic function as is required in Millar's analysis.

Turning now to H-polarization, we have

$$H_z^s(x,y) = \frac{1}{4j}\int_0^d P_2 K_t(x')dx' . \tag{7.11}$$

Using the exact representation we get

$$H_z^s(x,y) = \sum_{m=-\infty}^{\infty}\left[B'_m e^{-j(\beta_m x + X_m y)} + C'_m e^{-j(\beta_m x - X_m y)}\right] \tag{7.12}$$

where

$$B'_m = \frac{1}{2dX_m}\int_{S^-} e^{j(\beta_m x + X_m y)}\left\{X_m - \beta_m f'(x)\right\} K_t(x)dx , \tag{7.13}$$

and

$$C'_m = \frac{1}{2dX_m}\int_{S^+} e^{j(\beta_m x - X_m y)}\left\{X_m - \beta_m f'(x)\right\} K_t(x)dx , \tag{7.14}$$

and when

$$y \geq \max\left[f(x)\right] ,$$

then $\qquad B'_m = A'_m \qquad$ and $\qquad C'_m = 0 \quad ,$

where A'_m is defined by Eq. (6-2).

On the other hand, using Rayleigh's assumption, we have

$$\tilde{H}_z^s(x,y) = \sum_{m=-\infty}^{\infty} \tilde{B}'_m e^{-j(\beta_m x + X_m y)} \tag{7.15}$$

If we now substitute the expression

$$P_2 = \sum_{m=-\infty}^{\infty} \frac{j2}{dX_m} \left\{ f'(x)\left(\frac{2m\pi}{d} + k\sin\theta\right) - X_m \operatorname{sgn}(y-y') \right\} \times$$

$$\times\ e^{-j\left(\frac{2m\pi}{d} + k\sin\theta\right)(x-x')}\ e^{-j|y-y'|X_m}$$

into Eq. (7.11) we get

$$H_z^s(x,y) = \frac{1}{2dX_m} \int_0^d \sum_{m=-\infty}^{\infty} \left\{ f'(x')\left(\frac{2m\pi}{d} + k\sin\theta\right) - X_m \operatorname{sgn}(y-y') \right\} \times$$

$$e^{-j\left(\frac{2m\pi}{d} + k\sin\theta\right)(x-x')}\ e^{-j|y-y'|X_m} K_t(x')dx'. \tag{7.16}$$

Again, in order to make Eq. (7.15) equal to Eq. (7.16) everywhere on the surface, we require the modulus sign in the kernel to be removed. Thus, equating Eqs. (7.15) and (7.16),

$$\tilde{B}'_m = \int_0^d e^{j(\beta_m x + X_m y)} \left\{ X_m - \beta_m f'(x) \right\} K_t(x)dx \tag{7.17}$$

$$= \int_{S^+} e^{j(\beta_m x + X_m y)} \left\{ X_m - \beta_m f'(x) \right\} K_t(x)dx +$$

$$+ \int_{S^-} e^{j(\beta_m x + X_m y)} \left\{ X_m - \beta_m f'(x) \right\} K_t(x)dx\ ; \tag{7.18}$$

and if we examine the field at the surface trough (so that $S^- = 0$), then

$$H_z^s(d/2, -a) = \sum_{m=-\infty}^{\infty} C'_m e^{-j(\frac{d}{2}\beta_m + aX_m)} \tag{7.19}$$

where

$$C'_m = \frac{1}{2dX_m} \int_0^d e^{j(\beta_m x - X_m y)} \left\{ X_m - \beta_m f'(x) \right\} K_t(x) dx ,$$

and from Eq. (7.15)

$$H_z^s(x, y) = \sum_{m=-\infty}^{\infty} \tilde{B}'_m e^{-j(\frac{d}{2}\beta_m - X_m a)} \tag{7.20}$$

where

$$\tilde{B}'_m = \int_0^d e^{j(\beta_m x + X_m y)} \left\{ X_m - \beta_m f'(x) \right\} K_t(x) dx .$$

Numerical values computed using Eqs. (7.19) and (7.20) for a sinusoidal surface and an inverted full-wave rectified surface with $d = 0.2\lambda$, $\theta = 0$ and different values of Ka are shown in Table VII-2.

TABLE VII-2

H-polarization. Comparison of Scattered Fields at Surface Trough Obtained by the Exact and Rayleigh Methods

Type of Surface	Ka	Scattered Field	
		Exact Representation	Rayleigh's Method
Sinusoidal	0.314	0.74072 - j0.63363	0.75254 - j0.62012
	0.157	0.87126 - j0.31756	0.87870 - j0.31196
Inverted Full-wave Rectified	0.314	0.79608 - j0.34601	0.92741 - j0.34870
	0.942	-0.07901 - j0.90223	1.07230 - j1.00060

It is interesting to note that the criterion under which the Rayleigh assumption holds seems different for H-polarization, with all data suggesting that Ka must be smaller than the value 0.448 appropriate to E-polarization. However, the exact figure for H-polarization is unknown. Again the agreement between the exact representation method and the Rayleigh method becomes worse if the periodic surface is not an analytic function (such as an inverted full-wave rectified profile).

From the above computed data for E and H polarizations, we therefore conclude that Rayleigh's method can be used, with sufficient accuracy, for estimating the field scattered by a periodic surface provided that it is analytic and has a small value of Ka (say less than 0.5). If the surface is not an analytic curve (in practice, a grating profile cannot be shaped to coincide with an analytic curve), Rayleigh's method provides us better results if the incident field is E-polarized.

Chapter VIII

APPLICATION TO ROUGH SURFACE SCATTERING

8.1 Discussion

Although the main purpose of this work is concerned with scattering by a periodic surface of arbitrary shape, it is appropriate to consider the application of our results to scattering from rough surfaces.

In the past decade or so, a great number of papers have been published dealing with this type of scattering. A few of the more important references are Rice (1951), Hoffman (1955), Beckmann (1963) and Fung and Chen (1969), and if there is one feature that almost all such theoretical treatments have in common, it is their reliance on the physical optics approximation which, in effect, reduces the determination of the scattered field to quadratures. Of course, there exist many differences of detail, both conceptual and analytical, depending, for example, on whether the perturbed surface is defined specifically or statistically, the nature of the statistical variations assumed, the stage at which averaging is performed, the method of evaluating the remaining surface integral, whether shadowing is taken into account, etc. However, the results obtained are still limited by the physical optics approximation, which takes no account of any multiple scattering, is invalid for surfaces of curvature small compared to the wavelength (small scale roughness), and provides a false estimate of shadowing.

If the surface is illuminated near normal incidence, these deficiencies are of little consequence, primarily because the base surface provides a strong return. As we depart from normal incidence, the surface concentrates the return in the forward (specular) direction, where the estimated scattering from the perturbed surface may remain valid, but in other directions (e.g. back scattering) all of the observed return is a consequence of roughness, and any perturbation based on physical optics is of doubtful accuracy.

In order to treat adequately the case of oblique incidence on a rough surface, it is desirable to postulate a base surface which will itself generate a back scattered return at these angles; to devise a means for accurately estimating this scattering; and then to handle by a perturbation technique such small scale roughness as it may be desirable to include. In order to simulate actual rough surfaces, the small scale roughness will be assumed statistical in character. From the viewpoint of optical gratings, the effect of this kind of roughness is equivalent to degrading a diffraction grating with small random errors. For this reason, the results obtained here are also applicable to the study of grating imperfections which may cause phenomena such as "ghosts" and wave-front aberrations.

8.2. Perturbation of the Surface Field

Consider a plane wave of either polarization incident in a direction making an angle θ with the positive y axis, as shown in Fig. 8-1. We represent the rough surface by a small scale roughness superimposed on a sinusoidal base simulating large scale roughness. The surface height is then

$$\bar{y} = \bar{f}(x) = a\cos\left(\frac{2\pi}{d}x\right) + \delta(x)\,, \qquad -\infty < x < \infty \tag{8.1}$$

with $a \gg |\delta(x)|$.

Furthermore we assume that $\delta(x)$ is a random variable obeying a Gaussian distribution with zero mean, such that

$$g\left\{\delta(x)\right\} = \frac{1}{\sigma\sqrt{2\pi}}\exp\left\{-\frac{\delta(x)^2}{2\sigma^2}\right\}\,, \tag{8.2}$$

$$\langle\delta(x)\rangle = 0$$

where σ is the standard deviation, and the bracket sign $\langle\,\rangle$ represents a statistical average process.

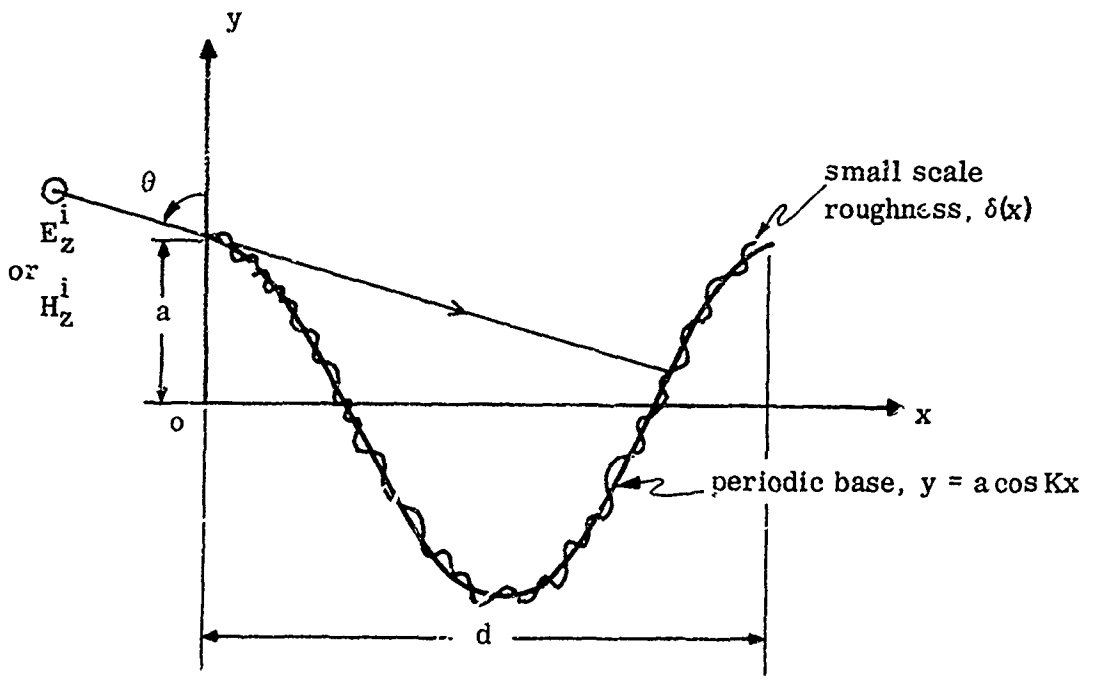

Fig. 8-1: Geometry of a Rough Surface Consisting of a Periodic Base and a Small Scale Random Roughness.

In accordance with the boundary conditions, the wave induces on the surface a current density $\underline{F}(\underline{r})$ which is the actual source of the scattered field. Application of Green's second identity and the appropriate boundary conditions then yields the following expressions for the scattered field:

$$E_z^s(\underline{r}) = j\omega \int_S G(\underline{r}, \underline{r}')F_z(\underline{r}')d\ell$$

$$H_z^s(\underline{r}) = -\int_S \frac{\partial G(\underline{r}, \underline{r}')}{\partial n'} F_t(\underline{r}')d\ell' \tag{8.3}$$

for E and H polarization respectively, where

$$G(\underline{r}, \underline{r}') = -\frac{j}{4} H_0^{(2)}(k|\underline{r} - \underline{r}'|) ,$$

and $\hat{n}'$ is the unit outward normal to the surface.

If the observation point is far from the nearest point on the surface, the asymptotic form of the Hankel function may be introduced; viz.

$$H_0^{(2)}(kR) \sim \sqrt{\frac{2j}{\pi kr}}\, e^{-jkr} \exp\left\{jk(x\cos\phi + \bar{y}\sin\phi)\right\} \tag{8.4}$$

where

$$R = \left\{(x - x')^2 + (\bar{y} - \bar{y}')^2\right\}^{1/2}$$

and ϕ is the angle of diffraction, made with the positive x axis.

Combining Eqs. (8.3) and (8.4) we get

$$E_z^s(\underline{r}) = q(r) \int_{-\infty}^{\infty} e^{jk(x\cos\phi + \bar{y}\sin\phi)} \sqrt{1 + f'(x)^2}\, F_z(x)dx \tag{8.5}$$

for E-polarization and

$$H_z^s(\underline{r}) = -\frac{kq(r)}{\omega\mu}\int_{-\infty}^{\infty} e^{jk(x\cos\phi+\bar{y}\sin\phi)}\cos(\hat{n},\underline{r})\sqrt{1+f'(x)^2}\,F_t(x)dx$$

$$= -\frac{kq(r)}{\omega\mu}\int_{-\infty}^{\infty} e^{jk(x\cos\phi+\bar{y}\sin\phi)}\left\{f'(x)\cos\phi-\sin\phi\right\}F_t(x)dx \tag{8.6}$$

for H-polarization

where $$q(r) = \left(\frac{2j}{\pi kr}\right)^{1/2} e^{-jkr} .$$

Since the perturbation is, by assumption, small, the perturbation on the periodic base is equivalent to a perturbation on the surface current. Moreover, by using the fact that the modulus of the surface field is less sensitive to a small change in the surface height than the phase, we can assume that the perturbation on the surface field produces only a small change in the phase of the unperturbed surface field. This allows us to replace the rough surface by its periodic base. Let

$$\bar{y} = f(x) = a\cos\left(\frac{2\pi}{d}x\right) ,$$

and

$$F_z(x) = K_z(x)e^{jk\delta(x)} \tag{8.7}$$

for E-polarization,

$$F_t(x) = K_t(x)e^{jk\delta(x)} \tag{8.8}$$

for H-polarization, where $K_z(x)$ and $K_t(x)$ are the surface fields for the unperturbed surface.

Substituting Eq. (8.7) into Eq. (8.5) we get

$$E_z^s(r,\phi) = q(r)\int_{-\infty}^{\infty} e^{jk(x\cos\phi + y\sin\phi)}\sqrt{1+f'(x)^2}\,K_z(x)e^{jk\delta(x)}dx \qquad (8.9)$$

The intensity is then

$$\left|E_z^s(r,\phi)\right|^2 = E_z^s(r,\phi)\cdot E_z^{s*}(r,\phi)$$

$$= |q(r)|^2\int_{-\infty}^{\infty}\int_{-\infty}^{\infty} e^{jk\left[(x_1-x_2)\cos\phi+(y_1-y_2)\sin\phi\right]} \times$$

$$\sqrt{1+f'(x_1)^2}\,\sqrt{1+f'(x_2)^2}\,K_z(x_1)K_z^*(x_2)\,e^{jk\left[\delta(x_1)-\delta(x_2)\right]}dx_1dx_2, \qquad (8.10)$$

which has the average value

$$<\left|E_z^s(r,\phi)\right|^2> = |q(r)|^2\int_{-\infty}^{\infty}\int_{-\infty}^{\infty} e^{jk\left[(x_1-x_2)\cos\phi+(y_1-y_2)\sin\phi\right]}\sqrt{1+f'(x_1)^2}\,\sqrt{1+f'(x_2)^2}\,\times$$

$$K_z(x_1)K_z^*(x_2)<e^{jk\left[\delta(x_1)-\delta(x_2)\right]}>dx_1dx_2 \qquad (8.11)$$

From our knowledge of statistics it is known that if $\delta(x_1)$ and $\delta(x_2)$ are two random variables of normal distribution with zero mean, variance σ^2 and correlation coefficient $c(\tau)$, their joint probability function is (see, for example, Middleton, 1960)

$$f\left\{\delta(x_1),\delta(x_2)\right\} = \frac{1}{2\pi\sigma^2(1-c^2)^{1/2}}\exp\left\{-\frac{\delta(x_1)^2-2c\delta(x_1)\delta(x_2)+\delta(x_2)^2}{2\sigma^2(1-c^2)}\right\}. \qquad (8.12)$$

The factor < > in Eq. (8.11) can now be evaluated and is (Beckmann and Spizzichino, 1963)

$$<e^{jk[\delta(x_1)-\delta(x_2)]}> = \exp\left\{-k^2\sigma^2(1-c)\right\} \quad . \tag{8.13}$$

and when this is substituted into Eq. (8.11), we obtain

$$<\left|E_z^s(r,\phi)\right|^2> = |q(r)|^2 \int_{-\infty}^{\infty}\int_{-\infty}^{\infty} e^{jk[(x_1-x_2)\cos\phi+(y_1-y_2)\sin\phi]} \sqrt{1+f'(x_1)^2}\,\sqrt{1+f'(x_2)^2}\ \times$$

$$\times K_z(x_1)K_z^*(x_2)\exp\left[-k^2\sigma^2(1-c)\right]dx_1dx_2 \tag{8.14}$$

For convenience, the normalized correlation coefficient will be used

$$c(\tau) = \exp(-\tau^2/T^2) \tag{8.15}$$

where $\tau = x_1 - x_2$ (assuming stationary process) and T is the correlation distance.

Using the expansion

$$\exp\left[-k^2\sigma^2(1-c)\right] = e^{-\sigma^2k^2}\sum_{n=0}^{\infty}\frac{(k\sigma)^{2n}}{n!}\ e^{-n\tau^2/T^2} \quad ,$$

a little mathematical manipulation is sufficient to convert Eq. (8.14) into

$$<\left|E_z^s(r,\phi)\right|^2> = v(r)(T/k\sigma)^2\left|\int_{-\infty}^{\infty}u(x,\phi)dx\right|^2 + 2v(r)\left|\int_{-\infty}^{\infty}u(x,\phi)x\,e^{-x^2/T^2}dx\right|^2$$

$$+\ 2v(r)\left|\int_{-\infty}^{\infty}u(x,\phi)x^2e^{-x^2/T^2}dx\right|^2 + \ldots \tag{8.16}$$

where

$$v(r) = |q(r)|^2 e^{-\sigma^2 k^2} (k\sigma/T)^2 ,$$

$$u(x, \phi) = e^{jk(x\cos\phi + y\sin\phi)} \sqrt{1+f'(x)^2}\, K_z(x) .$$

To evaluate Eq. (8.16) numerically, we must reduce the limit of integration from infinity to a finite value. This can be done by noting that $K_z(x)$ is a periodic function. Thus, using Eq. (2.21),

$$< |E_z^s(r, \phi)|^2 > = v(r)(T/k\sigma)^2 \left| \int_0^d u(x, \phi) \sum_{m=-\infty}^{\infty} \left\{ e^{jkmd(\cos\phi - \sin\phi)} \right\} dx \right|^2$$

$$+ 2v(r) \left| \int_0^d u(x, \phi) \sum_{m=-\infty}^{\infty} \left\{ e^{jkmd(\cos\phi - \sin\phi)} (x+md) e^{-(x+md)^2/T^2} \right\} dx \right|^2$$

$$+ 2v(r) \left| \int_0^d u(x, \phi) \sum_{m=-\infty}^{\infty} \left\{ e^{jkmd(\cos\phi - \sin\phi)} (x+md)^2 e^{-(x+md)^2/T^2} \right\} dx \right|^2$$

$$+ \ldots \qquad (8.17)$$

which can be evaluated by truncating the infinite series. On examining Eq. (8.17), it is observed that for small values of σ the first term dominates and represents contributions coming mainly from the periodic base, while the second and higher order terms are the contributions from the perturbations.

Numerical results showing the scattered field pattern for a sinusoidal profile ($d = 1.155\lambda$, $a = 0.3\lambda$ and $\theta = 60^\circ$) are shown in Figs. 8.2 through 8.4 with $\sigma = 0.05\lambda$ and T varying from 0.5d to 3d. It is seen that the diffracted energy spectrum has broadened slightly into a shape like a pencil beam around

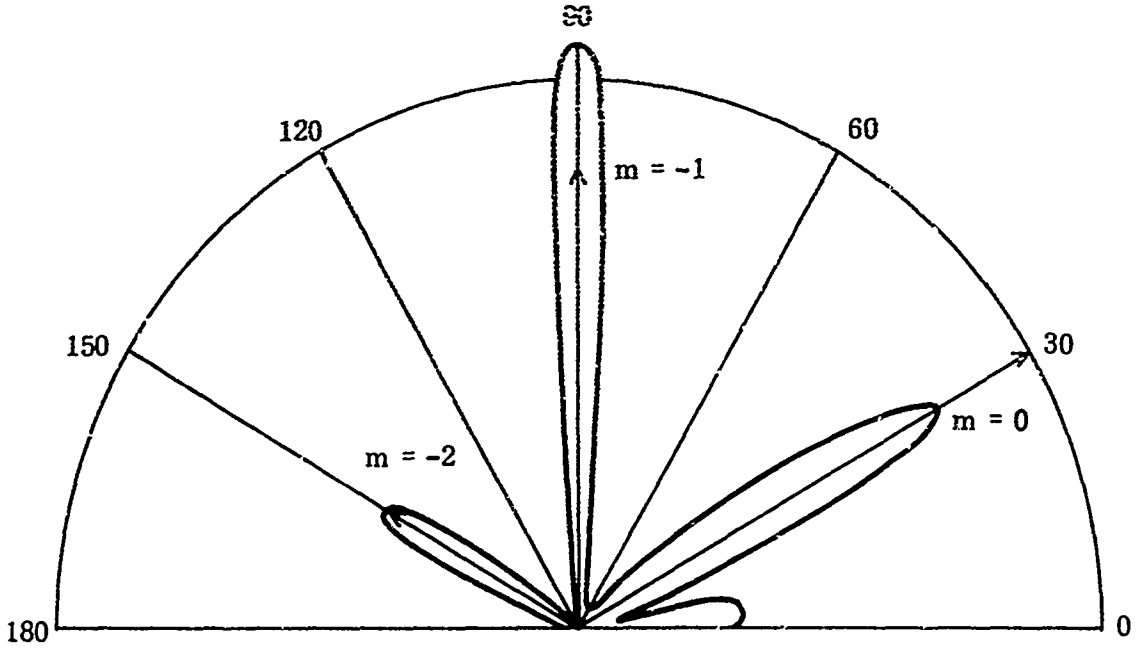

Fig. 8-2: Scattered Intensity Pattern (T = 0.5d), for E polarization.

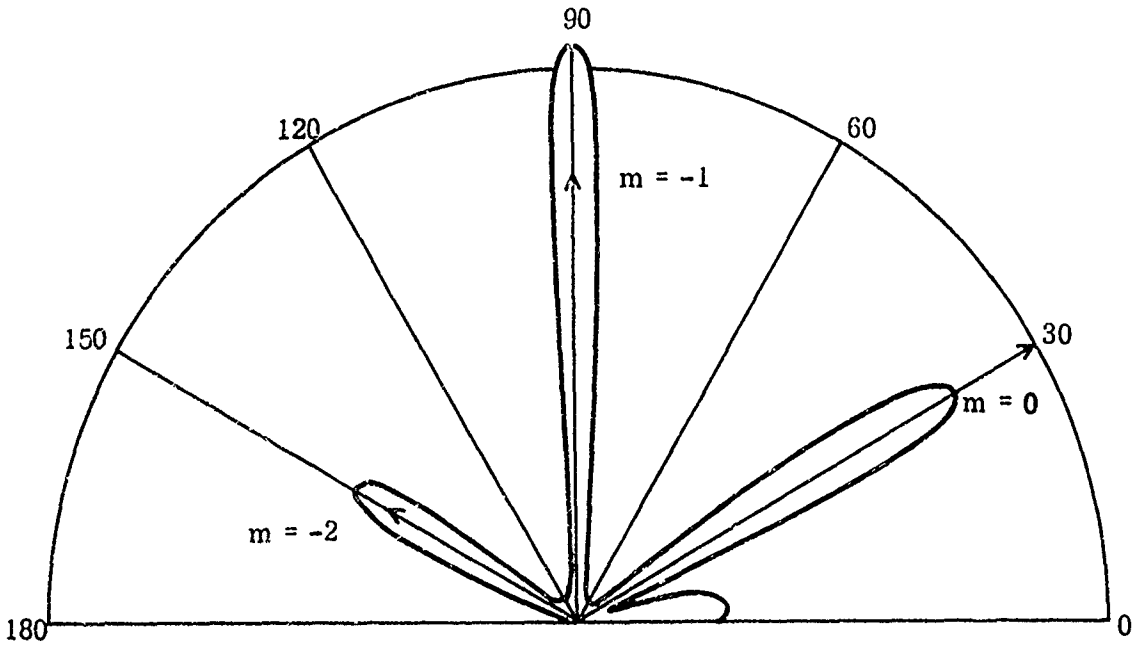

Fig. 8-3: Scattered Intensity Pattern (T = d), for E polarization.

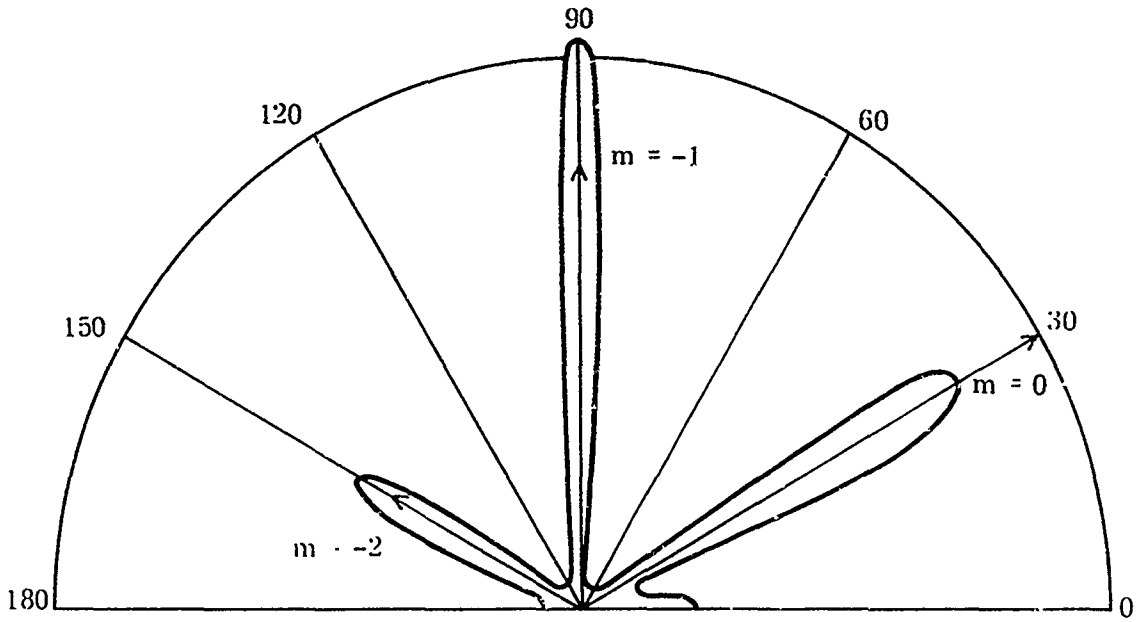

Fig. 8-4: Scattered Intensity Pattern (T = 3d), for E polarization.

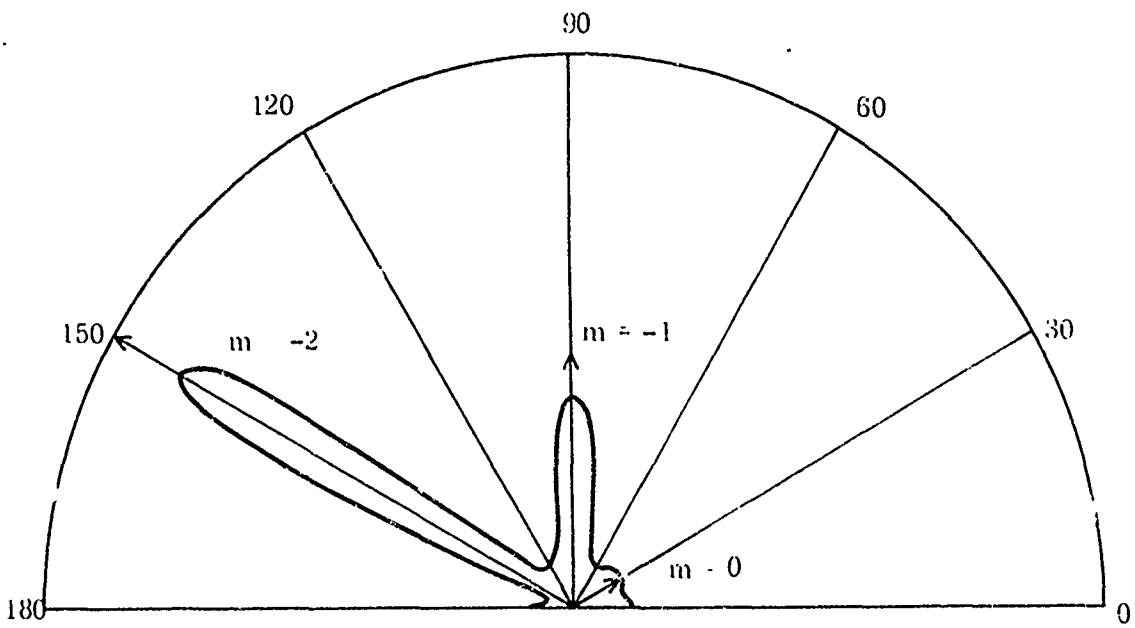

Fig. 8-5: Scattered Intensity Pattern (T = 0.5d), for H polarization.

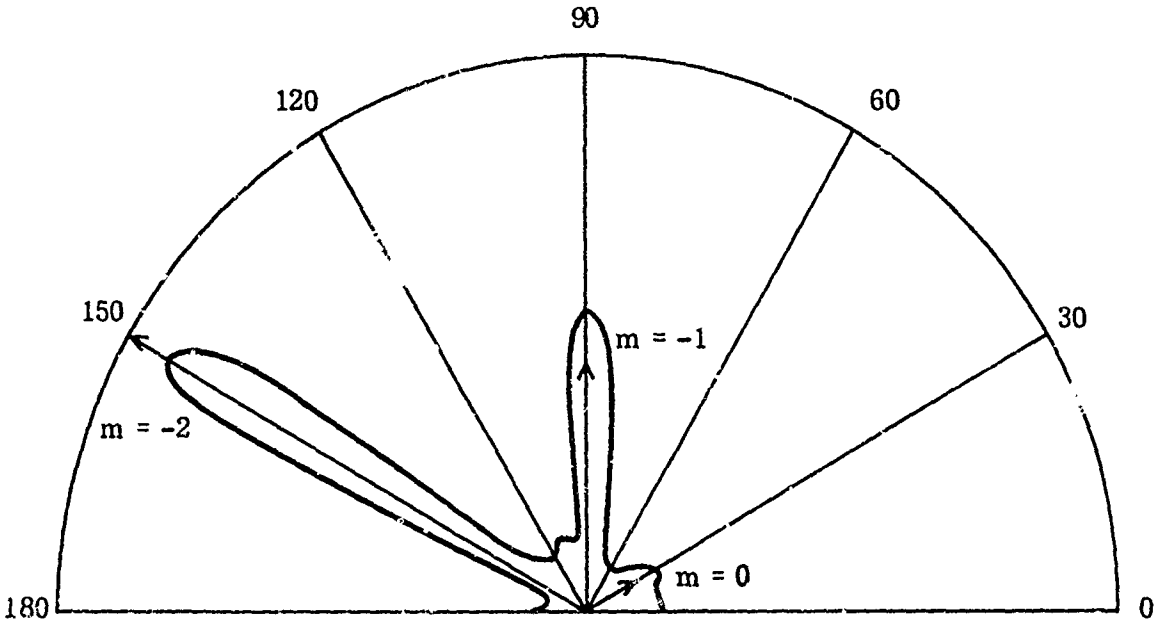

Fig. 8-6: Scattered Intensity Pattern (T = d), for H polarization.

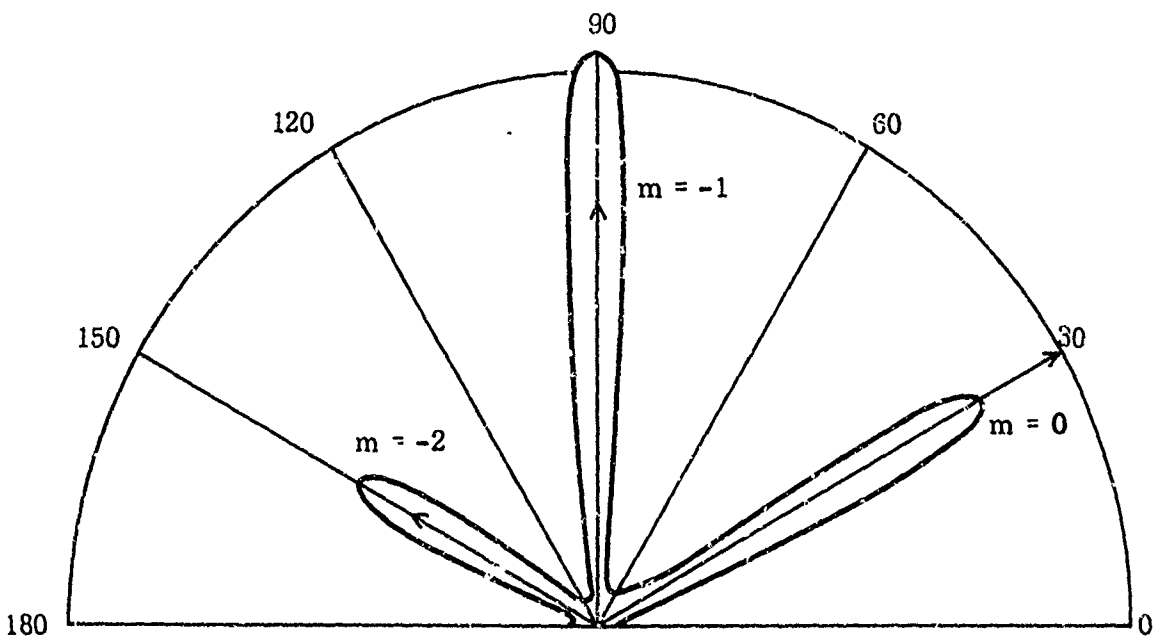

Fig. 8-7: Scattered Intensity Pattern with Finite Source Illumination (p = 3d, T = d), for E polarization.

the discrete (unperturbed) spectrum. In all cases considered, there is a decrease of diffracted energy in the specular and normal directions when the surface is perturbed. There is also some evidence of surface wave radiation for small ϕ. In the back scattered direction, however, the energy is relatively unaffected.

In an analogous way, using Eq. (8.6) we get for H-polarization

$$<\left|H_z^s(r,\phi)\right|^2> = v'(r)(T/k\sigma)^2\left|\int_0^d u'(x,\phi)\sum_{m=-\infty}^{\infty}\left\{e^{jkmd(\cos\phi-\sin\phi)}\right\}dx\right|^2$$

$$+2v'(r)\left|\int_0^d u'(x,\phi)\sum_{m=-\infty}^{\infty}\left\{e^{jkmd(\cos\phi-\sin\phi)}(x+md)e^{-(x+md)^2/T^2}\right\}dx\right|^2$$

$$+2v'(r)\left|\int_0^d u'(x,\phi)\sum_{m=-\infty}^{\infty}\left\{e^{jkmd(\cos\phi-\sin\phi)}(x+md)^2 e^{-(x+md)^2/T^2}\right\}dx\right|^2$$

$$+\ldots\ldots \tag{8.18}$$

where

$$v'(r) = (k/\omega)^2 v(r)$$

$$u'(x,\phi) = e^{jk(x\cos\phi+y\sin\phi)}\left\{f'(x)\cos\phi-\sin\phi\right\}K_t(x)\ ,$$

in which the first term represents the dominant contribution from the periodic base surface, and the second and higher order terms show the effect of the small scale roughness. Numerical results for the scattered field pattern for a sinusoidal surface ($d = 1.155\lambda$, $a = 0.4\lambda$ and $\theta = 60^\circ$) are presented in Figs. 8-5 and 8-6, where $\sigma = 0.05\lambda$ and T varies from 0.5d to d. It is seen that they bear the same features as those for E-polarization; however, we observe now there is a decrease of diffracted energy in the back scattered direction.

In the above study we have assumed an unlimited illumination area which means that the entire infinite rough surface is exposed to the incident wave (whether there is shadowing involved is another matter). However, in a more practical situation, it is likely that not all of the rough surface will be illuminated (limiting illumination area) because of the finite aperture of the illuminating source. Thus let us assume the incident wave to be a plane wave whose amplitude is given by a Gaussian distribution as

$$E_z^i(\underline{r}) = I(x)\, e^{-jk(x \sin\theta - y \cos\theta)} \tag{8.19}$$

for E-polarization, and

$$H_z^i(x) = I(x) e^{-jk(x \sin\theta - y \cos\theta)} \tag{8.20}$$

for H-polarization, where

$$I(x) = \frac{1}{p\sqrt{2\pi}} \exp(-x^2/2p^2) \tag{8.21}$$

and p is the standard deviation.

Rigorously speaking, in order to find the current distributions on the rough surface due to the finite source illuminations Eq. (8.19) or (8.20), it is necessary to solve two other problems whose integral equations are

$$\int_S K_z(\underline{r}') H_0^{(2)}(k|\underline{r} - \underline{r}'|)\, d\ell' = \frac{4}{\omega\mu}\, I(x) e^{-jk(x \sin\theta - y \cos\theta)} \tag{8.22}$$

for E-polarization, and

$$\int_S K_t(\underline{r}') \frac{\partial}{\partial n'} H_0^{(2)}(k|\underline{r} - \underline{r}'|)\, d\ell' = 4j \left\{ I(x)\, e^{-jk(x \sin\theta - y \cos\theta)} - \frac{1}{2} K_t(\underline{r}) \right\} \tag{8.23}$$

for H-polarization.

But if the amplitude of the incident wave does not decrease very rapidly with respect to x, the current distribution for the finite source illumination can be approximated by the current distribution for the non-limiting source illumination after multiplication by the factor given in Eq. (8.21). Thus from Eq. (8.16)

$$<\left|E_x^s(r,\phi)\right|^2> = v(r)(T/k\sigma)^2\left|\int_{-\infty}^{\infty}\tilde{u}(x,\phi)dx\right|^2$$

$$+ 2v(r)\left|\int_{-\infty}^{\infty}\tilde{u}(x,\phi)x\,e^{-x^2/T^2}\,dx\right|^2$$

$$+ 2v(r)\left|\int_{-\infty}^{\infty}\tilde{u}(x,\phi)x^2\,e^{-x^2/T^2}\,dx\right|^2 + \ldots \qquad (8.24)$$

where $\tilde{u}(x,\phi) = u(x,\phi)I(x)$.

Eq. (8.24) can be computed numerically by considering only that part of the surface where the amplitude of the incident wave is significant. The numerical results for a sinusoidal surface ($d = 1.155\lambda$, $a = 0.3\lambda$, and $\theta = 60^\circ$) with $p = 3d$ and the limit of integration varying from $-10d$ to $+10d$ are shown in Fig. 8-7. It is seen that the results are very similar to those obtained previously for an infinite illumination area.

In an analogous way, we obtain for H-polarization

$$<\left|H_z^s(r,\phi)\right|^2> = v'(r)(T/k\sigma)^2 \left|\int_{-\infty}^{\infty} \tilde{u}'(x,\phi)dx\right|^2$$

$$+ 2v'(r)\left|\int_{-\infty}^{\infty} \tilde{u}'(x,\phi)x\, e^{-x^2/T^2}\, dx\right|^2$$

$$+ 2v'(r)\left|\int_{-\infty}^{\infty} \tilde{u}'(x,\phi)x^2 e^{x^2/T^2}\, dx\right|^2 + \ldots \qquad (8.25)$$

where $\tilde{u}'(x,\phi) = u'(x,\phi)I(x)$.

The numerical results are shown in Fig. 8.8 (using the same parameters as for E-polarization). Again it is seen that the scattered field intensity pattern has the same characteristics as the pattern for an infinite illumination source.

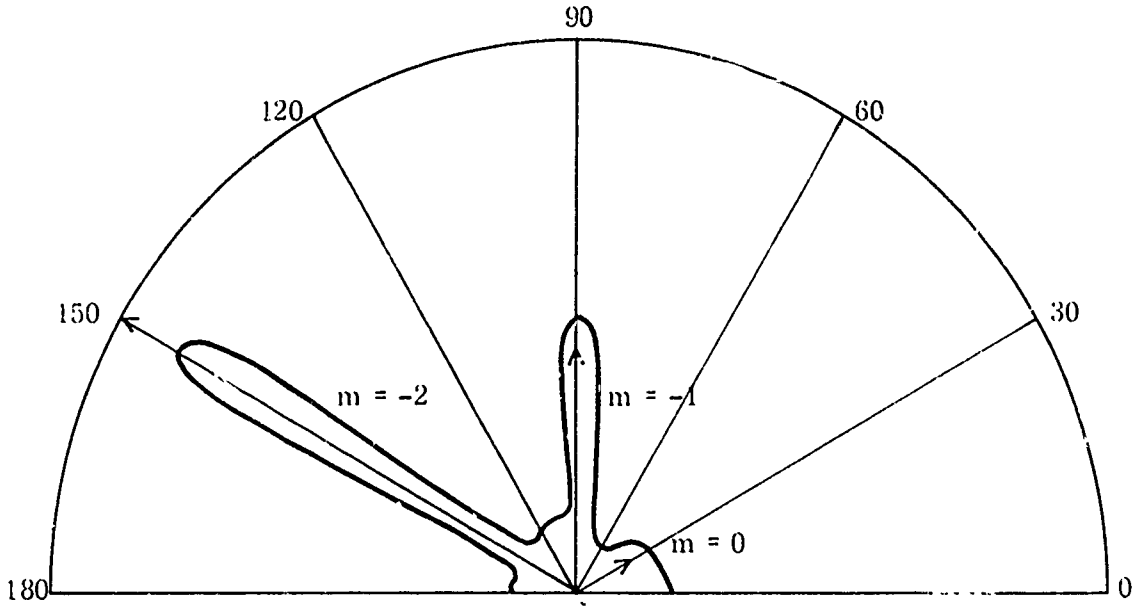

Fig. 8-8: Scattered Intensity Pattern with Finite Source Illumination (p - 3d, T = 1d), for H polarization.

Chapter IX

CONCLUSION

We have here considered the problem of a plane electromagnetic wave incident on a perfectly conducting, two dimensional periodic surface, and have developed numerical procedures for the direct digital solution of the integral equations for the surface fields. By using special summation techniques followed by the subtraction of the dc term to improve the convergence of the series for the modified Green's function, a relatively efficient procedure has been arrived at, and this has been programmed for a computer.

For both polarizations (E and H), data have been obtained for the surface fields on a variety of profiles representing sinusoidal, full-wave rectified, inverted full-wave rectified and triangular surfaces having different periods, amplitudes and angles of incidence. In each case the physical optics approximation is included for comparison and to aid in developing a simpler method for predicting scattering from a periodic surface. It was found that the polarization has a marked effect on the surface field, and the current distribution is strongly dependent on the number of radiating modes. In general the physical optics method fails to give an accurate prediction.

Knowing the surface field, the amplitudes of the diffracted waves in the discrete angular spectrum representation of the scattered field can be computed, and this has been done using the exact surface fields as well as the physical optics estimates with shadowing either included or ignored. Here again the physical optics predictions are deficient, and whereas the results derived from the numerical program satisfy the conservation of energy law, the physical optics values do not.

The numerical results have been used to explore the physical phenomena associated with the diffracted energy of the radiating modes and known as Wood anomalies. Both the S and P anomalies were observed. It was found that there

are anomalies which do not occur at the Rayleigh wavelengths, and the S-type anomalies are generally stronger than the P-type and can occur on structures having relatively shallow grooves.

Consideration has also been given to the Rayleigh assumption. Numerical data for the scattered field were obtained for surfaces of different profiles using the exact and Rayleigh methods. The results are consistent with Millar's remark, and indicate that the criteria under which the Rayleigh assumption holds are different for different polarizations.

Lastly the knowledge gained from the study of periodic surfaces was applied to a study of rough-surface scattering. The rough surface was considered as a small scale roughness superimposed on a sinusoidal periodic base (large scale roughness), the small scale roughness having a Gaussian distribution. The numerical results obtained show that the main effect of a small perturbation is to broaden slightly the discrete (unperturbed) spectrum.

REFERENCES

Adachi, S. (1965), "The Nose-on Echo Area of Axially Symmetric Thin Bodies Having Sharp Apices", Proc. IEEE, 53, 1067-1068.

Amitay, N. and V. Galindo (1969), "On Energy Conservation and the Method of Moments in Scattering Problems", IEEE Trans., AP-17, 747-751.

Andreasen, M.G. (1964), "Scattering from Parallel Metallic Cylinders with Arbitrary Cross Sections", IRE Trans., AP-12, 746-754.

Beckmann, P. and A. Spizzichino (1963), The Scattering of Electromagnetic Waves from Rough Surfaces, Macmillan, New York.

Bousquet, P. (1963), "Diffraction des ondes électromagnétiques par un réseau à profil triangulaire", C.R. Acad. Sci., Paris, 257, 80-83.

Brekhovskikh, L.M. (1952), "Diffraction of Electromagnetic Waves at Uneven Surfaces", J. Exp. Theor. Phys., USSR, 23, 275-304.

Collin, R.E. (1960), Field Theory of Guided Waves, McGraw-Hill Book Co., Inc., New York.

Eckart, C. (1953), "The Scattering of Sound from the Sea Surface", J. Acoust. Soc. Am., 25, 566-570.

Fung, A.K. and H.L. Chan (1969), "Backscattering of Waves by Composite Rough Surfaces", IEEE Trans., AP-17, 590-597.

Green, R.B. (1970), "Diffraction Efficiences for Infinite Perfectly Conducting Gratings of Arbitrary Profile", IEEE Trans., MTT-18, 313-318.

Harrington, R.F. (1968), Field Computation by Moment Methods, The Macmillan Co., New York.

Heaps, H.S. (1957), "Reflection of Plane Waves of Sound from a Sinusoidal Surface", J. Appl. Phys., 28, 815-818.

Hessel, A. and A.A. Oliner (1965), "A New Theory of Wood's Anomalies on Optical Grating", Appl. Optics, 4, 1275-1297.

Hoffman, W.C. (1955), "Scattering of Electromagnetic Waves from a Random Surface", Quart. Appl. Math., 13, 291-304.

Ingersoll, L.R. (1921), "Some Peculiarities of Polarization and Energy Distribution by Specular Gratings", Phys. Rev., 17, 493-501.

Itoh, T. and R. Mittra (1969), "An Analytical Study of the Echelette Grating with Application to Open Resonators", IEEE Trans., MTT-17, 319-327.

Jones, D.S. (1952), "Removal of an Inconsistency in the Theory of Diffraction", Proc. Camb. Phil. Soc., 48, 733-741.

Kalos, H.A. and A.R. Neureuther (1971), "Numerical Method for the Analysis of Diffraction Gratings", J. Opt. Soc. Amer., 61, 43-48.

Katsenelenbaum, B.A. (1955), "The Perturbation of an Electromagnetic Field for Small Deformations of a Metal Surface", J. Tech. Phys. (USSR), 25, 546.

LaCasce, E.O. and P. Tamarkin (1956), "Underwater Sound Reflection from a Corrugated Surface", J. Appl. Phys., 27, 138-148.

Lee, S.W., W.R. Jones and J. Campbell (1971), "Convergence of Numerical Solutions of Iris-Type Discontinuity Problems", IEEE Trans., MTT-19, 528-536.

Lippmann, B.A. (1953), "Note on the Theory of Gratings", J. Opt. Soc. Amer., 43, 408.

Lysanov, Iu. P. (1958), "Theory of the Scattering of Waves at Periodically Uneven Surfaces," Soviet Phys., 4, 1-10.

Marsh, H.W. (1963), "In Defense of Rayleigh's Scattering from Corrugated Surfaces", J. Acoust. Soc. Amer., 35, 1835-1836.

Maue, A.W. (1949), "Zur Formulierung eines Allgemeinen Beugungsproblems durch eine Integralgleichung" Z. Physik, 126, 601-618.

Meecham, W.C. (1956a),"Variational Method for the Calculation of the Distribution of Energy Reflected from a Periodic Surface", J. Appl. Phys., 27, 361-367.

Meecham, W.C. (1956b), "Fourier Transform Method for the Treatment of the Problem of the Reflection of Radiation from Irregular Surfaces", J. Acoust. Soc. Amer., 28, 370-377.

Middleton, D. (1960), An Introduction to Statistical Communication Theory, McGraw-Hill Book Co., Inc., New York.

Miles, J.W. (1954), "On Nonspecular Reflection at a Rough Surface", J. Acoust. Soc. Amer., 26, 191-199.

Millar, R.F. (1963), "Plane Wave Spectra in Grating Theory, II. Scattering by an Infinite Grating of Identical Cylinders", Canad. J. Phys., 41, 2135-2154.

Millar, R.F. (1969), "On the Rayleigh Assumption in Scattering by a Periodic Surface", Proc. Camb. Phil. Soc., 65, 773-791.

Millar, R.F. (1971), "On the Rayleigh Assumption in Scattering by a Periodic Surface - II", Proc. Camb. Phil. Soc., 69, 217-225.

Morse, P.M. and H. Feshbach (1953), Methods of Theoretical Physics, Part II, McGraw-Hill Book Co., Inc., New York.

Murphy, S.R. and G.E. Lord (1964), "Scattering from a Sinusoidal Surface - a Direct Comparison of the Results of Marsh and Uretsky", J. Acoust. Soc. Amer., 36, 1598-1599.

Neureuther, A. and K. Zaki (1968), "Numerical Methods for the Analysis of Scattering from Nonplanar Periodic Structures", Alta Frequenza, 38, Special Issure on the URSI Symposium on Electromagnetic Waves, Stresa, Italy.

Palmer, C.H. Jr. (1952), "Parallel Diffraction Grating Anomalies", J. Opt. Soc. Amer., 42, 269-276

Palmer, C.H. Jr. (1956), "Diffraction Grating Anomalies, II. Course Gratings", J. Opt. Soc. Amer., 46, 50-53.

Pavageau, J. (1967), "Équation intégral pour la diffraction électromagnétique par des conducteurs parfaits dans les problèmes à deaux dimensions; application aux reseaux", C.R. Acad. Soc., Paris, 264B, 424-427.

Pavageau, J. (1968), "Sur la méthode des spectres d'ondes planes dan les problèmes de diffraction", C.R. Acad. Sci., Paris, 266B, 1352-1355.

Pavageau, J. and J. Bousquet (1969), "Nouvelle méthod générale pour la détermination de la répartition angulaire de l'énergie diffractée par un réseau conducteur", C.R. Acad. Sci., Paris, 268B, 776-778.

Petit, R (1963), "Diffraction d'une onde plane monochromatique par un reseau periodique infiniment conducteur", Comptes Rendes, 257, 2018-2021.

Petit, R. and M. Cadilhac (1964), "Etude théorique de la diffraction par un réseau", C.R. Acad. Sci., Paris, 259, 2077-2080.

Petit, R. and M. Cadilhac (1966), "Sur la diffraction d'une onde plane par un réseau infiniment conducteur", C.R. Acad. Sci., Paris, 262B, 468-471.

Petit, R. and M. Cadilhac (1967), "Sur la diffraction d'une onde plane par un réseau, infiniment conducteur", Comptes Rendes, 264, 1441-1444.

Lord Rayleigh (1878), The Theory of Sound, Vol. II, Dover Publications, New York (1945).

Lord Rayleigh (1907), "On the Dynamical Theory of Gratings", Proc. Roy. Soc., 79A, 399-416.

Riblet, H.J. (1952), "Geometrical-Optical Currents", Microwave Development Laboratories Report (Contract AF 19(122)-167), Waltham, Mass.

Rice, S.O. (1951), "Reflection of Electromagnetic Waves from Slightly Rough Surfaces", Comm. Pure Appl. Math., 4, 351-378.

Senior, T.B.A. (1959), "The Scattering of Electromagnetic Waves by a Corrugated Sheet", Canad. J. Phys., 37, 787-797 and 1572.

Sivov, A.N. (1964), "Reflection of Electromagnetic Waves from Corrugated Surfaces with Small Periods", Radio Eng. and Elect. Phys., 10, 1509-1515.

Stratton, J.A. (1941), Electromagnetic Theory, McGraw-Hill Book Co., Inc., New York.

Strong, J. (1936), "Effects of Evaporated Films on Energy Distribution in Grating Spectra", Phys. Rev., 49, 291-296.

Tai, C-T (1948), "Reflection and Refraction of a Plane Electromagnetic Wave at a Periodic Surface", Harvard University, Cruft Laboratory Technical Report No. 28, Cambridge, Massachusetts.

Tseng, D.Y., A. Hessel and A.A. Oliner (1968), "Scattering by a Multimode Corrugated Structure with Application to P Type Wood Anomalies", Alta Frequenza, 38, Special Issue on the URSI Symposium on Electromagnetic Waves, Stresa, Italy.

Uretsky, J.L. (1965), "The Scattering of Plane Waves from Periodic Surfaces", Ann. Phys., 33, 400-427.

Wirgin, A. (1966), "Diffraction par un réseau de profil rectangulaire illuminé par une onde plane associée à un vecteur champ électrique polarisé parallèlement aux sillons", C.R. Acad. Sci., Paris, 262, 385-388.

Wirgin, A. (1969), "Theoretical and Experimental Investigation of a New Type of Blazed Grating", J. Opt. Soc. Amer., 59, 1348-1357.

Wood, R.W. (1902), "On a Remarkable Case of Uneven Distribution of Light in a Distribution in a Diffraction Grating Spectrum", Phil. Mag., 4, 396-402.

Wood, R.W. (1912), "Diffraction Gratings with Controlled Groove Form and Abnormal Distribution of Intensity", Phil. Mag., 23, 310-317.

Wood, R.W. (1935), "Anomalous Diffraction Gratings", Phys. Rev., 48, 928-936.

Yen, J.L. (1962), "Multiple Scattering and Wave Propagation in Periodic Structures", IRE Trans., AP-10, 769-775.

Zaki, K. (1969), "Numerical Methods for the Analysis of Scattering from Nonplanar Periodic Structures," Ph.D. Dissertation, University of California, Berkeley.

Zaki, K. and A. Neureuther (1971a), "Scattering from a Perfectly Conducting Surface with a Sinusoidal Height Profile: TE Polarization", IEEE Trans., AP-19, 208-214

Zaki, K. and A. Neureuther (1971b), "Scattering from a Perfectly Conducting Surface with a Sinusoidal Height Profile: TM Polarization", IEEE Trans., AP-19, 747-751.

Appendix A

PHYSICAL OPTICS APPROXIMATION

Although the main purpose of this work is the development of a numerical technique for the determination of exact values for the surface and, hence, scattered fields, we have found it desirable to compare the results obtained with those provided by the physical optics approximation. This approximation is a physically-based one which postulates an explicit form for the surface field arrived at by assuming each element of the surface to bear that current which it would carry were it part of the local tangent plane. The calculation of the scattered field is then reduced to quadratures.

In many instances, however, and a periodic sheet is one, an analytical evaluation of the physical optics integral is a difficult procedure, particularly in such cases where part of the surface is shadowed, and some of the shortcomings of physical optics estimates in general certainly arise from sloppiness in the evaluation of the integral. In still other cases, the physical optics result proves to be more accurate if shadowing is ignored* (see, for example, Adachi, 1965) and it is of interest to observe that for a sinusoidal sheet it is then possible to produce an exact evaluation of the integral. Needless to say, however, the resulting scattered field is still subject to the unknown errors inherent in the use of the physical optics approximation, and to the neglect (if present) of all shadowing effects.

The procedure is directly analogous to that given by Senior (1959) for the particular case of an H polarized plane wave at normal incidence on a sinusoidal sheet and consists of three steps:

(i) writing down the physical optics integral for the scattered field without any shadowing included;

---

*This modified method is sometimes called "extended physical optics".

(ii) asymptotically evaluating this expression appropriate to an observation point at large distances from the sheet; and

(iii) matching this expression to a discrete angular spectrum of waves to obtain their amplitudes. Since these amplitudes are independent of the field point we have, in effect, produced an exact evaluation of the integral valid certainly in the half space above the sheet.

Let us take the equation of the perfectly conducting sheet to be

$$y = a\cos Kx \tag{A.1}$$

where a is the amplitude of the corrugations and $2\pi/K = d$ is the period. If the incident field is E-polarized, we write

$$\underline{E}^i = \hat{z}e^{-jk(x\sin\theta - y\cos\theta)} \tag{A.2}$$

(cf. Eq. 2.20), implying

$$\underline{H}^i = -Y(\cos\theta\hat{x} + \sin\theta\hat{y})e^{-jk(x\sin\theta - y\cos\theta)} \tag{A.3}$$

where Y is the intrinsic admittance of free space.

By virtue of the periodicity of the sheet and, hence, of the problem as a whole, the scattered field can be expressed as a discrete spectrum of waves which waves are certainly outgoing as regards $y \geq a$. Thus, we have

$$\underline{E}^s = \hat{z}\sum_{m=-\infty}^{\infty} A_m e^{-jk(x\sin\theta_m + y\cos\theta_m)} \tag{A.4}$$

where

$$\begin{aligned} k\sin\theta_m &= mK + k\sin\theta\,, \\ k\cos\theta_m &= \sqrt{k^2 - (mK + k\sin\theta)^2} \end{aligned} \tag{A.5}$$

and that branch of the square root is chosen having imaginary part non-positive. Application of the physical optics approximation, followed by steps (i) through (iii) above now gives

$$A_m = -j^m \frac{k}{\sqrt{k^2-(mK+k\sin\theta)^2}} \left\{ \cos\theta - \frac{mKa}{\mu_m} \sin\theta \right\} J_m(\mu_m) \quad (A.6)$$

where

$$\mu_m = a\left(k\cos\theta + \sqrt{k^2-(mK+k\sin\theta)^2}\right). \quad (A.7)$$

In particular,

$$A_0 = -J_0(2ak\cos\theta),$$

and as $a \longrightarrow 0$,

$$A_0 \longrightarrow 1, \quad A_m \longrightarrow 0, \quad m \neq 0,$$

in agreement with the known solution for a flat sheet.

If the incident field is H-polarized, we take

$$\underline{H}^i = \hat{z} e^{-jk(x\sin\theta - y\cos\theta)}, \quad (A.8)$$

implying

$$\underline{E}^i = \frac{1}{Y}(\cos\theta\hat{x} + \sin\theta\hat{y}) e^{-jk(x\sin\theta - y\cos\theta)}, \quad (A.9)$$

and expand the scattered magnetic field as

$$\underline{H}^s = \hat{z} \sum_{m=-\infty}^{\infty} A'_m e^{-jk(x\sin\theta_m + y\cos\theta_m)} \quad (A.10)$$

where θ_m is as before. On evaluation of the physical optics integral, we now obtain

$$A'_m = A_m \quad . \tag{A.11}$$

The equivalence of the results for the two polarizations is consistent with the known fact that the physical optics approximation for a perfect conductor is inherently polarization insensitive.

Results computed from Eqs. (A.6) and (A.11) agree with those given in the appropriate columns of Tables III-1 through III-4, Tables V-1 through V-4, and obtained from a numerical evaluation of the integrals in Eqs. (4.4) and (6.2).

APPENDIX B

An Alternative Integral Equation for E Polarization

Another integral equation for the surface current on a periodic conducting surface can be derived. It is different from Eq. (2.11), and since it is a Fredholm equation of the second kind with a weakly singular kernel, it can be solved using an iterative scheme such as a Neumann series.

Consider the perfectly conducting cylindrical surface of Fig. B-1. The equation of the surface is $y = f(x)$, where $f(x)$ may or may not be a periodic function of x at this stage of the discussion. The incident plane electromagnetic wave propagates in the direction of the unit vector

$$\hat{k} = \sin\phi\,\hat{x} - \cos\phi\,\hat{y} \quad , \tag{B.1}$$

and the incident electric field is parallel to the generators of the surface:

$$\underline{E}^i = e^{-jk(x\sin\phi - y\cos\phi)} \quad . \tag{B.2}$$

The time dependence factor $e^{j\omega t}$ is omitted.

The scattered field is (Stratton, 1941)

$$\underline{E}^s(\underline{r} + z\hat{z}) = -\frac{1}{4\pi}\int_v j\omega\mu_0 \underline{I}\,\frac{e^{-jkR_1}}{R_1}\,dv \tag{B.3}$$

where

$$R_1 = \left|\underline{r} - \underline{r}' + (z - z')\hat{z}\right| \quad , \tag{B.4}$$

$P(x, y, z)$ and $P'(x', y', z')$ are the field and integration points respectively, $\underline{I}$ is the volume current density, and v is a volume containing both the field point and the scattering surface. The vectors $\underline{r}$ and $\underline{r}'$ lying in the plane $z = 0$ are shown in Fig. B-1 and are given by

$$\underline{r} = x\hat{x} + y\hat{y}, \qquad \underline{r}' = x'\hat{x} + y'\hat{y} \quad . \tag{B.5}$$

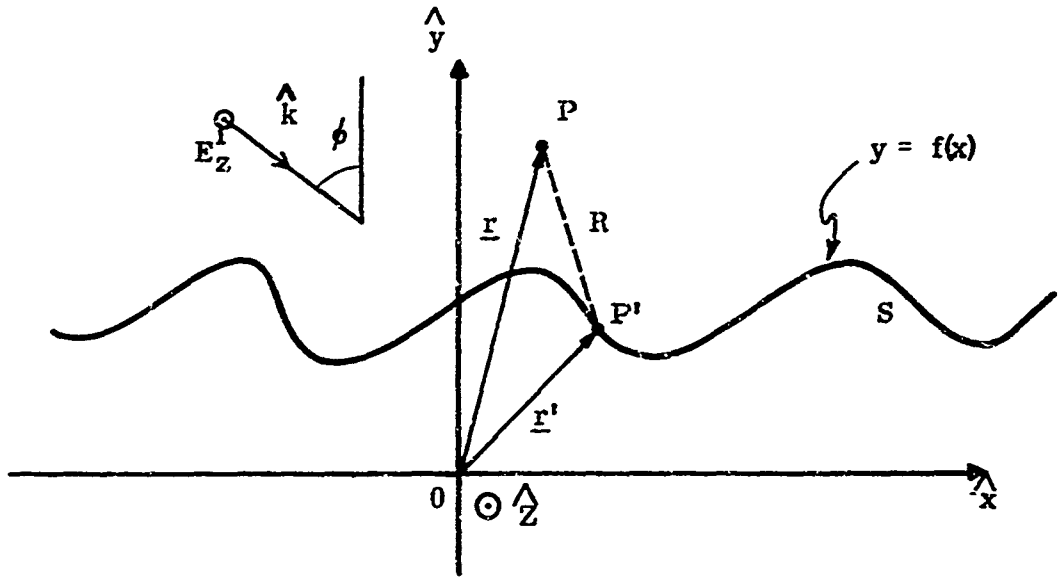

Fig. B-1: Scattering by a Cylindrical Surface.

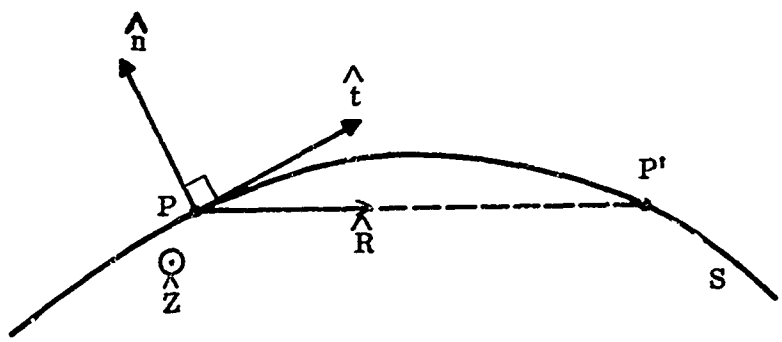

Fig. B-2: Geometry of Orthogonal Vectors.

If $\underline{K}$ is the surface current density, then

$$\underline{K}ds = \underline{I}dv \ , \tag{B.6}$$

and therefore

$$\underline{E}_z^s(\underline{r}+z\hat{z}) = -\frac{j\omega\mu_0}{4\pi}\int_S \frac{e^{-jkR_1}}{R_1} K_z ds$$

$$= -\frac{j\omega\mu_0}{4\pi}\int_{S'} K_z(\underline{r}')dx' \int_{-\infty}^{\infty} \frac{e^{-jkR_1}}{R_1} dz' \tag{B.7}$$

where S' is the scattering surface, and S is its profile in the $z = 0$ plane. Now

$$\int_{-\infty}^{\infty} \frac{e^{-jkR_1}}{R_1} dz' = j\pi H_0^{(2)}(kR) \tag{B.8}$$

where $$R = \sqrt{(x-x')^2+(y-y')^2} \ . \tag{B.9}$$

Substitution of Eq. (B.8) into Eq. (B.7) yields

$$E_z^s(\underline{r}+z\hat{z}) = E_z^s(x) = -\frac{\omega\mu_0}{4}\int_S H_0^{(2)}(kR)K_z(\underline{r}')ds' \tag{B.10}$$

where $$ds' = \sqrt{1+f'(x')^2}\ dx' \ . \tag{B.11}$$

The kernel $H_0^{(2)}(kR)\sqrt{1+f'(x')^2}$ is nonsymmetric and weakly singular at $R = 0$, due to the logarithmic singularity of $H_0^{(2)}(kR)$.

Let the normal n to the surface S' at the fixed point P be as shown in Fig. B-2; differentiating both sides of Eq. (B.10) with respect to n, as P approaches the surface S', we obtain

$$\left\{\frac{\partial E_z^s(\underline{r})}{\partial n}\right\}_{P \text{ on } S} = -\frac{\omega\mu_0}{4}\frac{\partial}{\partial n}\int_S H_0^{(2)}(kR)K_z(\underline{r}')ds' \quad . \tag{B.12}$$

To evaluate the left-hand side, observe that with the three basis vectors $\hat{t}$, $\hat{n}$ and $\hat{z}$ of Fig. B-2, Maxwell's equation $\nabla \times \underline{E} = -j\omega\mu_0\underline{H}$ with $\underline{E} = E_z$ gives ($H_n \equiv 0$ on S')

$$\frac{\partial E_z}{\partial n}\hat{t} - \frac{\partial E_z}{\partial t}\hat{n} = -j\omega\mu_0(H_t\hat{t} + H_z\hat{z}) \quad , \tag{B.13}$$

and therefore,

$$H_z = 0 \ , \qquad \frac{\partial E_z}{\partial t} = 0$$

$$\frac{\partial E_z}{\partial n} = -j\omega\mu_0 H_t \quad . \tag{B.14}$$

Since $\underline{K} = \hat{n} \times \underline{H}$ and $E_z = E_z^i + E_z^s$, Eq. (B.14) becomes

$$\frac{\partial E_z^s}{\partial n} = -\frac{\partial E_z^i}{\partial n} + j\omega\mu_0 K_z \ , \qquad \text{on } S \ . \tag{B.15}$$

Now

$$\frac{\partial E_z^i}{\partial n} = jk\left(\frac{\partial x}{\partial n}\sin\phi - \frac{\partial y}{\partial n}\cos\phi\right)e^{-jk(x\sin\phi - y\cos\phi)} \ , \tag{B.16}$$

and making use of the relations

$$\frac{\partial x}{\partial n} = (\nabla x)\cdot\hat{n} = \hat{x}\cdot\hat{n} \ , \qquad \frac{\partial y}{\partial n} = (\nabla y)\cdot\hat{n} = \hat{y}\cdot\hat{n} \ , \tag{B.17}$$

and Eq. (B.1), Eq. (B.16) gives

$$\frac{\partial E_z^i}{\partial n} = -jk\hat{k}\cdot\hat{n}\, e^{-jk(x\sin\phi - y\cos\phi)} \quad . \tag{B.18}$$

Substitution of Eqs. (B.15) and (B.18) into Eq. (b.12) yields

$$K_z(\underline{r}) = -\sqrt{\frac{\epsilon_0}{\mu_0}}\, \hat{k}\cdot\hat{n}\, e^{-jk(x\sin\phi - y\cos\phi)} + \frac{j}{4}\frac{\partial}{\partial n}\int_S H_0^{(2)}(kR) K_z(\underline{r}')ds' \quad . \tag{B.19}$$

Since the integrand in Eq. (B.19) is singular, when $P \equiv P'$, particular care must be taken in interchanging the differentiation with respect to n and the integration with respect to x'. This difficulty was previously encountered by Maue (1949) and Riblet (1952), among others, and can be overcome in the manner that they adopted. The procedure consists of interchanging $\partial/\partial n$ and $\int_{S'}$, but in replacing $K_z(\underline{r})$ on the left-hand side with $\frac{1}{2}K_z(\underline{r})$: for a detailed justification of this step, see Maue (1949). The result is

$$\frac{1}{2}K_z(\underline{r}) = -\sqrt{\frac{\epsilon_0}{\mu_0}}\, k\cdot n\, e^{-jk(x\sin\phi - y\cos\phi)} + \frac{j}{4}\int_S \left\{\frac{\partial}{\partial n} H_0^{(2)}(kR)\right\} K_z(\underline{r}')ds' \quad . \tag{B.20}$$

It now remains to evaluate the partial derivative in the integrand, viz.

$$\frac{\partial}{\partial n} H_0^{(2)}(kR) = \frac{\partial H_0^{(2)}}{\partial(kR)}\, k\, \frac{\partial R}{\partial n} \tag{B.21}$$

where

$$\frac{\partial H_0^{(2)}(kR)}{\partial(kR)} = -H_1^{(2)}(kR) \quad , \tag{B.22}$$

$$\frac{\partial R}{\partial n} = \frac{\partial R}{\partial x}\frac{\partial x}{\partial n} + \frac{\partial R}{\partial y}\frac{\partial y}{\partial n} = \frac{x-x'}{R}\,\hat{x}\cdot\hat{n} + \frac{y-y'}{R}\,\hat{y}\cdot\hat{n} = -\frac{(\underline{r}'-\underline{r})\cdot\hat{n}}{R}$$

$$= -\hat{R}\cdot\hat{n}\,, \qquad \text{(B.23)}$$

with

$$\hat{R} = \frac{\underline{r}'-\underline{r}}{R} \qquad \text{(B.24)}$$

which is a unit vector directed from the fixed point P towards the integrand point P'. When Eqs. (B.21), (B.22) and (B.23) are inserted into Eq. (B.20), we have

$$K_z(\underline{r}) = -2\sqrt{\frac{\epsilon_0}{\mu_0}}\,\hat{k}\cdot\hat{n}\,e^{-jk(x\sin\phi - y\cos\phi)} + \frac{jk}{2}\int_S (\hat{R}\cdot\hat{n})H_1^{(2)}(kR)K_z(r')ds' \qquad \text{(B.25)}$$

which is a weakly singular one-dimensional Fredholm integral equation of the second kind for the unknown surface current density K_z.

As a simple check, let us take $f(x) = 0$. Then $\hat{R}\cdot\hat{n} = 0$ and

$$K_z = 2\sqrt{\frac{\epsilon_0}{\mu_0}}\,\cos\phi\,e^{-jkx\sin\phi}\,, \qquad \text{(B.26)}$$

which is the expected geometric optics result.

Equation (B.25) is valid for any cylindrical surface and thus can be applied to the case of a periodic surface.